Dynamic wetting with superspreading surfactants.

Thesis submitted in accordance with the requirements of the University of Liverpool for the degree of Doctor of Philosophy

Kevin Hugh Williams

Supervisors: Dr Volfango Bertola, and Dr David Martin.

May 2018

Engineering school (Fluid Dynamics Group), at the University of Liverpool

Acknowledgements

Thanks to Volfango for his support, guidance and insight and for introducing me to the interesting subject of fluid dynamics. Thanks to David for his assistance with the RAS and AFM techniques and organising with Volfango the 2 trips to the Synchrotron to perform the GISAXS experiments. At the synchrotron we were assisted by Dr Oier Bikondoa who worked round the clock to help us. I would also like to thank the E.P.S.R.C for the PhD studentship. Finally I would like to thank my Mother, Father and brother without whose help and support this work would not have been possible.

Abstract

Dynamic wetting with superspreading surfactants.

Kevin Hugh Williams

The moving contact line of a liquid that advances over or recedes from a solid substrate, is a fundamental problem of fluid dynamics with important practical applications, including coating and thin deposition processes, sprays, bio and micro fluidics. Certain trisiloxane surfactants have the ability to promote rapid spreading of liquids on low energy surfaces which is known as "superspreading". The project aims at studying experimentally the dynamic behaviour of the contact line during wetting and de-wetting when the fluid contains small amounts of superspreader surfactants.

We intend to look at trisiloxane surfactants, (S240 (0.1%) (aq)) and compare them to water and the non superspreader S233 (0.1%) (aq), we will also use different substrates (parafilm (pf), polypropylene (pp) and poly carbonate plastic sheet (pcp)). The approach adopted is to study the superspreading phenomenon macroscopically (video imaging) and microscopically (RAS and GISAXS).

It was found using high speed imaging that for the pp, pf and pcp substrates the S240 (0.1%) (aq) superspreading solution drop spreads to a larger diameter and smaller contact angle more rapidly than the S233 (0.1%) (aq) non superspreading solution. The pcp substrate reached a larger final drop diameter and smaller final contact angle more rapidly than the pp and pf substrates which behaved very similarly.

It is important to remark that the two surfactants used in the present work, S240 and S233, both prepared by Evonik Industries GmbH (Germany), have an almost identical chemical structure, however the former exhibits superspreading properties while the latter doesn't. Thus, the present work is one of the few examples in the literature in which there is a direct comparison between superspreading and non-superspreading trisiloxane surfactants.

Drop diameter versus time data was plotted on a log scale and there was evidence that the S240 (0.1%) (aq) and S233 (0.1%) (aq) drop on pp does exhibit 2 regimes. The S233 (0.1%) (aq) drop on pf and pcp has two regimes when the diameter and time axis are plotted with a log scale. The S240 (0.1%) (aq) drop on pf and pcp both have 1 regime when the diameter and time are plotted on log scales.

Using Reflection Anisotropy Spectroscopy (RAS) for the first time we looked at spreading drops of surfactant solution and "dipping" experiments. There was no evidence of adsorbed micelle structures at the contact line of the evaporated drop of the superspreading S240 (0.1%) (aq) solution on any pp, pf or pcp substrate. In the dipping experiment there is evidence that the descending film of S240 (0.1%) (aq) contains anisotropic structures and/or a preferred alignment of structures in the solution. It is not known if this is at the contact line or if this is related to superspreading in detail. However, the descending films of S233 (0.1%) (aq) and water had flat featureless RA time scans, indicating isotropic behaviour. This could lead to the conclusion that anisotropic supporting RAS signals could be related to superspreading. Atomic Force Microscopy (AFM) did not find any evidence of micelles at the evaporated contact line of the pp, pf and pcp substrates which could aid superspreading.

Grazing Incidence Small Angle X-ray Scattering (GISAXS), used for the first time, revealed the presence of molecular layering for the S240 (0.1%) (aq) drop on pp with a thickness of

10nm. In comparison, the S233 (0.1%) (aq) solutions, exhibit a large scatter with a standard deviation comparable to the mean value which suggests no layering occurs. The data was found to support Ruckenstein's bi-layer model.

List of Publications.

1. Williams K, Bertola V, Martin D S, (2016), Experimental investigation of a flowing superspreader solution using reflection anisotropy spectroscopy. Results in Physics 6: 277-279.
2. Martin D S, Williams K, Bikondoa O, Dennis D, Bertola V (2014), Superspreading fluids investigated by GISAXS. GISAXS, XMaS Newsletter, European Synchrotron Radiation Facility, p. 10.

Contents

List of Figures.

List of Tables

Notation

RAS – Reflection Anisotropy Spectroscopy.

AFM – Atomic Force Microscopy.

GISAXS – Grazing Incidence Small Angle X-ray Scattering.

CMC – Critical Micelle Concentration.

V_H – Volume occupied by the hydrophilic group in the micellar core.

l_c - Length of the hydrophobic group in the core.

a_0 - The cross sectional area occupied by the hydrophilic group at the micelle-solution interface.

γ - The surface or interfacial tension, or surface free energy per unit area.

γ_a - The surface free energy per unit area/ surface tension of pure liquid a

γ_b - The surface free energy per unit area/ surface tension of pure liquid b.

γ_{ab} - The interaction energy per unit area across the interface of a/ b liquids.

γ_{SA}/γ_{SG} - The interfacial free energy per unit area of the substrate/liquid saturated air surface/interface

γ_{SL} -The interfacial free energy per unit area of the liquid/substrate interface.

γ_{LA}/γ_{LG} - The interfacial free energy per unit area of the liquid/air interface.

$S_{L/S}$ - The spreading coefficient.

θ - The contact angle.

η - The viscosity of the liquid.

d – drop diameter in chapter 3 or bi-layer dimension in chapter 5

t – time

c – constant

C_A – contact angle

Δr - The difference in reflectance (of normal incidence plane-polarised light between two orthogonal directions in the surface plane (x,y)

r – The mean reflectance.

r_x – The reflectance of normal incidence plane polarised light along the x axis of the surface plane.

r_y - The reflectance of normal incidence plane polarised light along the y axis of the surface plane.

c – The speed of light.

ν - The frequency of the wave.

λ - The wavelength of the wave.

E – The energy of a photon.

h – The Planck constant.

n – refractive index

β – absorption properties of material

δ - scattering properties of material

ESRF – European Synchrotron Radiation Facility

BM – Bending Magnet

ID – Insertion Device

rf – radio frequency cavity

Linac – Linear Accelerator

Q_{xy} – in plane scattering vector

Q_z – out of plane scattering vector

α_i - incident angle of X-ray

α_f – scattering angle

θ_f – scattering angle

Q – absolute wave vector transfer

d – bi layer spacing

L_{sd} – calibrated sample to detector distance

I(q) – The scattering intensity*)* for a lateral electron density fluctuation on the surface.

F - The form factor.

S(q)- The total interference function.

$\frac{d\sigma}{d\Omega}$ - The total incoherent cross section.

DWBA The Distorted Wave Born Approximation.

F_{DWBA} - Form factor within the DWBA (distorted wave Born Approximation).

Chapter 1 – Introduction

1.1: Superspreading.

"Superspreading", or "superwetting", is the process by which a small droplet of an aqueous diluted solution of certain trisiloxane surfactants (typically ~0.1wt %), spreads on a moderately hydrophobic surface to a very large area, usually in a short time period (~ tens of seconds). (1) Compared with water spreading, the surfactant solution drop is larger in terms of the wetted area it produces by 100 times, and 25 times bigger then conventional surfactants. Trisiloxane-ethoxylate surfactants can reduce the surface tension at room temperature from 72mN/m to 21-22mN/m (2), however this is not sufficient to explain the exceptionally large spreading ratios, therefore superspreading remains poorly understood to date.

Superspreading was first observed over 20 years ago with dilute solutions of trisiloxane surfactants on hydrophobic substrates, with the first physiochemical paper on superspreading written by Ananthapadmanabhan in 1990 (2).

The interest in studying superspreading is motivated by a number of important practical and industrial applications. Surfactants are used in the chemical industry in motor oils, in detergents used in cleaning laundry and homes, in agrochemical formulations to improve the deposition of pesticides, in drilling muds used in petroleum prospecting and in additives for enhanced oil recovery. Recent applications include electronic printing, magnetic recording, micro-electronics biotechnology and viral research.

Knowing about superspreading is useful in any process involving wetting or capillary phenomenon. Capillary action is the ability of a liquid to flow in narrow spaces without the assistance of, or even in opposition to external forces like gravity, eg the drawing up of paint between the hairs of a paint brush, or liquid in a thin tube. As well as superspreading being useful in understanding the capillarity of the paint it also effects how far the paint spreads on a surface. The aim of using the surfactant is to maximise the area covered by the paint drop thus decreasing costs.

The scientific motivation to study superspreading lies in the challenge to understand the underlying physical mechanisms of superspreading and how this particular type of surfactants work. Allthough there has been a lot of research which has advanced the understanding of superspreading, the reasons why only a few trisiloxane surfactants are superspreaders while other chemically similar trisiloxane surfactants are not, is still unanswered. To address this challenge, this work investigates model fluids prepared using two surfactants which have a

similar chemical structure but exhibit different superspreading properties, namely the Evonik Break – Thru S240 (0.1%) (aq) superspreader and the non-superspreading Evonik Break – Thru S233 (0.1%) (aq).

1.2: Applications of Evonik Break Thru S240 superspreader.

The main application of the surfactants studied in this work is in the formulation of agrochemicals. In general, spreading and wetting agents optimise the performance of agricultural chemicals by minimising the spray droplets tendency to rebound of a plant's leaf, by increasing foliar uptake of the spreading agent through the plant pathways and by encouraging the spreading of the agent to bigger leaf surfaces.

Trisiloxane surfactants can lower the surface tension of the water to 22 mN/m, (which is a low surface tension) allowing the rapid coverage and penetration of cuticular waxes on hydrophobic leaf surfaces and causes an effect known as stomatal flooding; The almost instantaneous entrance of the solution into the openings in the plant surfaces. This fast penetration results in "rainfastness" as the delivery of the pesticide into the plant has occurred and further rainfall cannot remove the residue.

An aqueous solution spray droplet of superspreading S240 (0.1%) (aq) spreads immediately when it hits the leaf surface and no droplet can be seen, this is in contrast to aqueous solutions of conventional surfactants. Coverage of the leaf is fast and total, and the low surface tension and fast spreading allows the spray to reach locations inaccessible to conventional surfactants.

An example of an application of Break-Thru S240 is being added to insecticides, this causes the complete wetting of aphids on the plant crop foliage caused by the properties of the superspreading agent. Spray coverage is so improved compared to just water that spray volumes can be decreased by 30%. Economically, this is advantageous as less water is required per area thereby reducing energy cost or allowing the extending of the area treated by a single spray tank.

Evonik Break Thru S240 has been shown in field trials to be used successfully with:

- Herbicides
- Fungicides
- Insecticides & acaracides
- Plant growth regulators
- Micronutrients.

Break – Thru S240 has several advantages when used. Break Thru S240 safeguards the performance of pesticides and foliar fertilizers, by:

- Delivering the active under hot and dry conditions.
- Making sure of the penetration and coverage of mature and hardened weeds.
- Penetrating the target plant's dust covered surface.
- Penetrating and wetting the waxy surface of weather-hardened plants.
- When penetration is very difficult providing wetting.
- Stopping the treatment being ruined by sudden rain after treatment.
- Increasing coverage when spray volumes are decreased.
- By improving the dissolution of solid formulations in the tank.

To summarise Break – Thru S240 has a multitude of uses and can be used in pesticide formulations, tank adjuvant to improve the control of pests, diseases and weeds. In particular hard to control weeds such as gorse. Break -Thru S240 is not phytotoxic to crops when used correctly. Additional technical and commercial information can be found at www.break-thru.com.

1.3: Overview of this work.

Superspreading is to be investigated by looking at the surfactant drop's contact line for evidence of micelle structures which could aid this phenomenon. The two surfactant solutions of S240 (0.1%) (aq) and S233 (0.1%) (aq), with the latter being a superspreader, and the former being a non-superspreader with a similar chemical formula will be investigated. Three different substrates will be tested, (only a small number of substrates are known to allow superspreading on them), these are parafilm (pf), polypropylene (pp) and polycarbonate plastic sheet. Macroscopic analysis will be carried out using video imaging while microscopic analysis will be carried out using Reflection Anisotropy Spectroscopy (RAS), (chapter 4), and Grazing Incidence Small Angle X-ray Scattering (GISAXS), (chapter 5).

This work's approach was to compare a novel superspreading trisiloxane surfactant solution with a non superspreading trisiloxane surfactant solution with an almost identical chemical structure. This approach of directly comparing these two surfactant solutions has not been carried out in the literature before.

1.4: Key terms and concepts in superspreading.

Typical droplet sizes for the S240 (0.1%) (aq) and S233 (0.1%) (aq) have a radius of 5mm and a volume (if we assume the drop is a sphere $V = \frac{4}{3}\pi \cdot r^3$) of 5.24×10^{-7} m^3. Comparing this to a typical molecule of surfactant we have a length of around 5 – 10 nm, while a water molecule has a length of 2.75 Angstroms.

Micelle formation by Surfactants.

Micelle formation (or "micellization") is a fundamental property of surfactants ranking alongside the important property of being absorbed at interfaces. It refers to the surface-active solutes forming colloidal-sized clusters in solution. Micellization is important as quite a few interfacial phenomenon depend on the presence of micelles, these include detergency and solubilisation, while it also affects other properties such as surface or interfacial tension reduction that do not depend on micelles directly.

The Critical Micelle Concentration (CMC)

It has been known for a long time that surfactant solutions have peculiar bulk properties that support the idea that colloidal particles are present in the solution. The critical micelle concentration is the concentration at which there is a clear break in the relation of equivalent conductivity versus the square root of normality of solution. It is the concentration at which micelles are formed from surfactant molecules.

Micellar structure and shape

Properties of surfactant solutions, such as viscosity, are dependent on the shape of the micelle. There are a number of main types of micelles:

1. Small spherical structures with an aggregation number < 100.
2. Elongated rod like cylindrical micelles with hemispherical ends (prolate ellipsoids).
3. Big flat lamellar disk like extended oblate spheroids micelles.
4. Vesicles which are basically spherical structures made from bilayer lamellar micelles arranged in more one or more concentric spheres.

5.

Value of $V_H/l_c a_0$	Structure of the Micelle
$0-\frac{1}{3}$	Spheroidal in (aq) media
$\frac{1}{3}-\frac{1}{2}$	Cylindrical in (aq) media
$\frac{1}{2}-1$	Lamellar in (aq) media
>1	Inverse (reversed) micelles in nonpolar media

Table 1.1 – Table of packing parameter versus structure of the Micelle

Table 1.1 can be found in (5). Where V_H is the volume occupied by the hydrophobic group in the micellar core, l_c is the length of the hydrophobic group in the core, and a_0 is the cross sectional area occupied by the hydrophilic group at the micelle-solution interface. When combined, $V_H/l_c a_0$ is a packing parameter which tell us the shape of the micelle. This approach was developed by (6) and (7).(i)

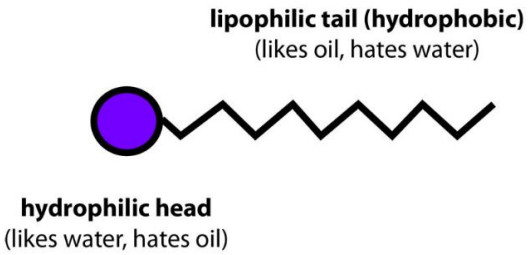

(i)

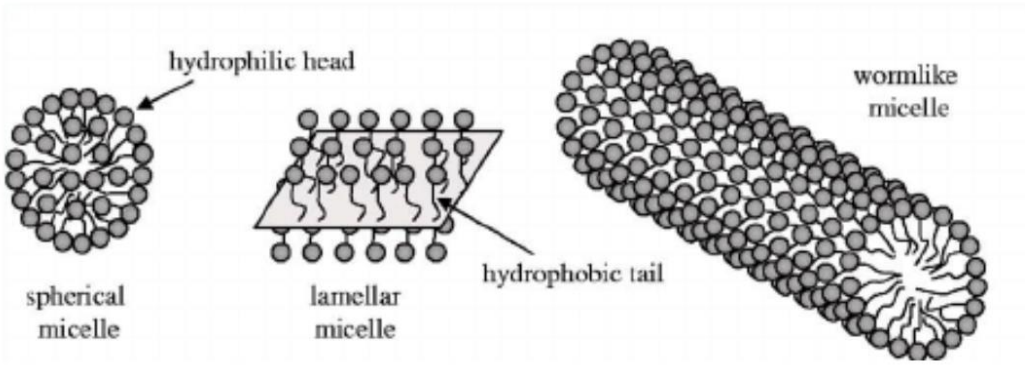

(ii)

Figure 1.1: Spherical micelle, cylindrical and lamellar micelles (ii), with simplified diagram of surfactant molecule (i),

Spreading wetting.

The spreading can be described using the spreading coefficient $S_{L/S}$.; it is the "driving force" of the spreading process.

$$S_{L/S} = \gamma_{SA} - (\gamma_{SL} + \gamma_{LA}) \tag{1.1}$$

Where γ_{SA} is the interfacial free energy per unit area of the substrate/liquid saturated air surface/interface. γ_{SL} is the interfacial free energy per unit area of the liquid/substrate interface. γ_{LA} is the surface tension of the liquid.

If $S_{L/S}$ is positive spreading, can occur spontaneously, while if $S_{L/S}$ is negative, no spreading can happen spontaneously. Young (1805) and Dupre (1869) were the first to think that the force balances at the three phase contact line, and the measurement of the contact angle is a way of measuring the wetting. They assumed that the three phases intersect at a line.

$$\cos\theta = \frac{\gamma_{SA} - \gamma_{SL}}{\gamma_{LA}} \tag{1.2}$$

This approach by Young-Dupre is a mechanistic explanation of wetting, three types of wetting occur for different values of the contact angle. When θ_{eq}<<90º gives a good liquid wetting solid, θ_{eq}>>90º gives a non-liquid wetting solid and $\theta_{eq} \cong$90º gives a partial wetting solid.

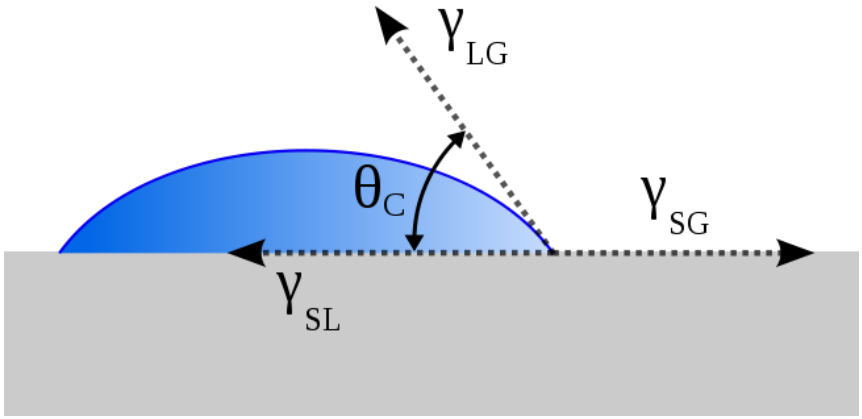

Figure 1.2: The contact angle (θ_c).

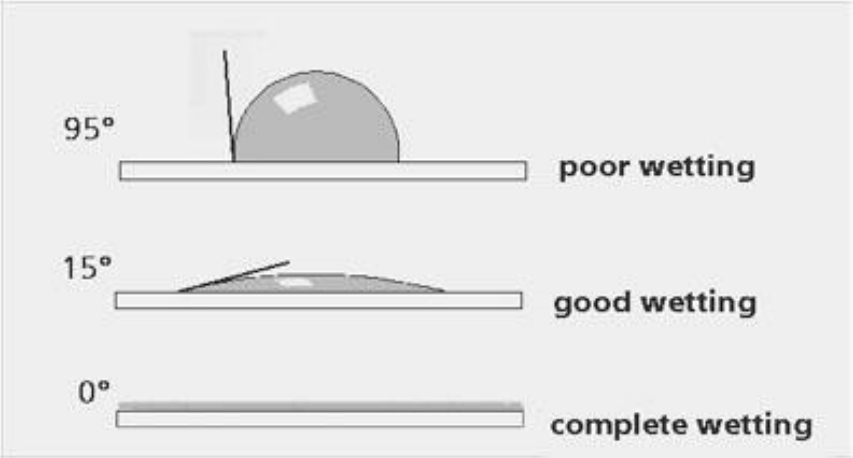

Figure 1.3: Diagram of drop with defined parameters (top) & how the contact angle varies for different final wettings (bottom).

The most straight forward way of measuring the contact angle is visually with a goniometer. Indeed this is the method which this work will use. A drop is extruded by a syringe/delivery tube vertically onto the substrate surface. A high resolution high speed camera captures the image as a video or photo, which is then analysed using image analysis software (in my case MATLAB image processing toolbox). Advantages of this technique include the ability to deposit multiple droplets in various places on the sample, (and its simple nature).

The Marangoni effect.

The Marangoni effect is the mass transfer along an interface between two fluids caused by a surface tension gradient. A liquid with a high surface tension pulls more strongly on the liquid surrounding it then a low surface tension. The liquid flows away from regions of low surface tension because of the gradient in surface tension. The surface tension gradient can be caused by temperature gradient or concentration gradient.

1.5: Aims and objectives.

As discussed above, the main aim of this work is to compare two model aqueous solutions of surfactants which have a similar chemical structure, but different superspreading properties; whilst this may seem an obvious approach, most of the existing literature either use superspreading surfactants only (that is, without a comparative sample), or use comparative surfactants of very different chemical natures. Specific objectives are:

- To investigate whether there exist micelle structures at the contact line of a drop of a superspreader solution as opposed to the non superspreading solution.

- To investigate whether the superspreading process evolves through a sequence of different stages, where the process is driven by different physical mechanisms.
- To test Ruckenstein's hypothesis (3) that the contact line of superspreading drop contains micelle bilayers which aid superspreading.

The above objectives were pursued through the following tasks:

- Macroscopic drop spreading measurements (base diameter and contact angle) were carried out on droplets of superspreading Evonik S240 (0.1%) (aq) and non-superspreading Evonik S233 (0.1%) (aq) on substrates of different wettability (polypropylene (pp), parafilm (pf), polycarbonate plastic sheet (pcp)).
- Reflection Anisotropy Spectroscopy (RAS) was used for the first time to investigate the possible formation of micelle structures at the contact line during drop spreading and/or evaporation of Evonik S240 (0.1%) (aq) and non-superspreading Evonik S233 (0.1%) (aq) and water.
- Grazing Incidence Small Angle X-ray Scattering (GISAXS) was used for the first time to look for evidence that there was a micelle bilayer as proposed by Ruckenstein (3) at the contact line of the drop of S240 (0.1%) (aq), and to estimate the thickness of the bilayer.

1.6: Outline of thesis.

- Chapter 1 states the main aims and objectives of the work and introduces some key concepts.
- Chapter 2 is the literature review.
- Chapter 3 presents drop diameter versus time graphs and contact angle versus time graphs, and also plots the drop diameter versus time graphs on a log scale which reveals for some substrate/surfactant solutions there is more then one spreading regime.
- Chapter 4 looks for evidence for micelles at the contact line of the S240 (0.1%) (aq) using RAS. RAS is also use in "dipping" experiments which reveal one and two step processes in RAS.
- Chapter 5 finds evidence, using GISAXS, that the S240 (0.1%) (aq) solution might have micelle bilayer structures (as proposed by Ruckenstein (3)) which aid superspreading
- Chapter 6 contains the conclusions.

Chapter two – Literature Review.

2.1: Introduction

The mechanism of superspreading is poorly understood to date even though the phenomenon was discovered in the 1960s. Superspreading was first witnessed with trisiloxane surfactants. Their chemical structure can be noted as $M(D'E_nP_nOH)M$, where M represents the trimethylsiloxy group $(CH_3)_3SiO_{1/2}$-, D stands for the $–O_{1/2}Si(CH_3)(R)O_{1/2}$ where R is a polyether group attached to the Silicon. R can consist of either poly(ethylene oxide) only (R= - $(CH_2)_3$-O-$(CH_2$-CH_2-O-$)_n$R' or short E_n.or can be obtained from a mixture of ethylene oxide and propylene oxide (R=-$(CH_2)_3$-O-$(CH_2$-CH_2-O-$)_n$-$(CH_2$-$CH(CH_3)$-O-$)_m$R' or in shortened terms E_nP_m.

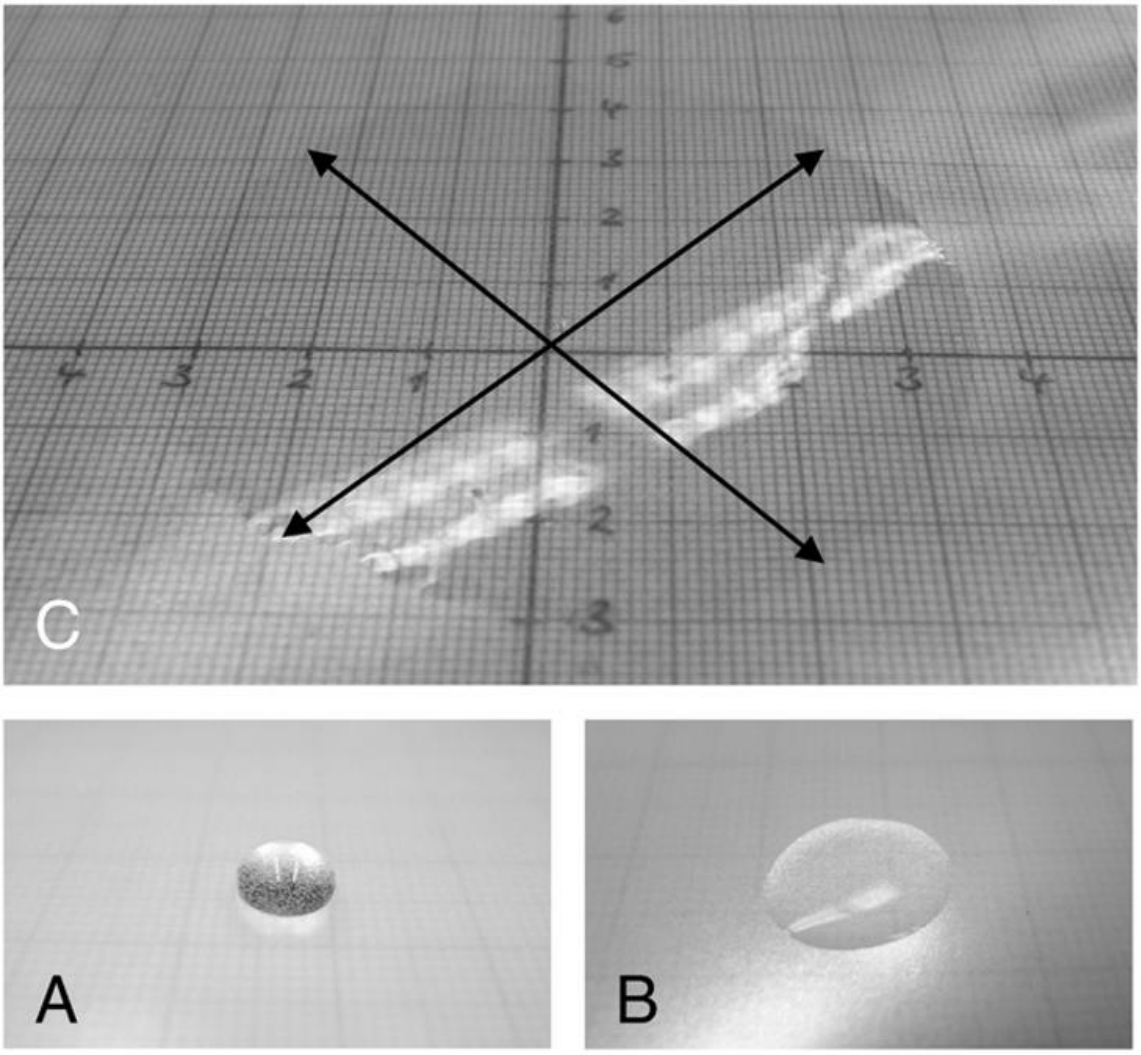

Figure 2.1: "Photos taken 1 minute after placing a 50µL droplet onto a polypropylene film A) water; B) non superspreading trisiloxane surfactant (M(D'E10P2OH)M): 15mm diameter; C) supersreading trisiloxane surfactant (M(D'E6P3OH)M): 70 mm diameter". Taken from (1)

For simplicity trisiloxane surfactants are described by the notation M(D'E_nP_nOH)M. Most work on superspreaders has focussed on SILWET® L-77 which is M(D'$E_{7.5}$OMe)M.

Figure 2.1. shows the large difference in behaviour of water, surfactant and superspreading surfactant on a hydrophobic polypropylene surface. Water stays as a small bead of liquid, the ordinary surfactant spreads a little but remains as a large bead, while the superspreader rapidly enlarges in size.

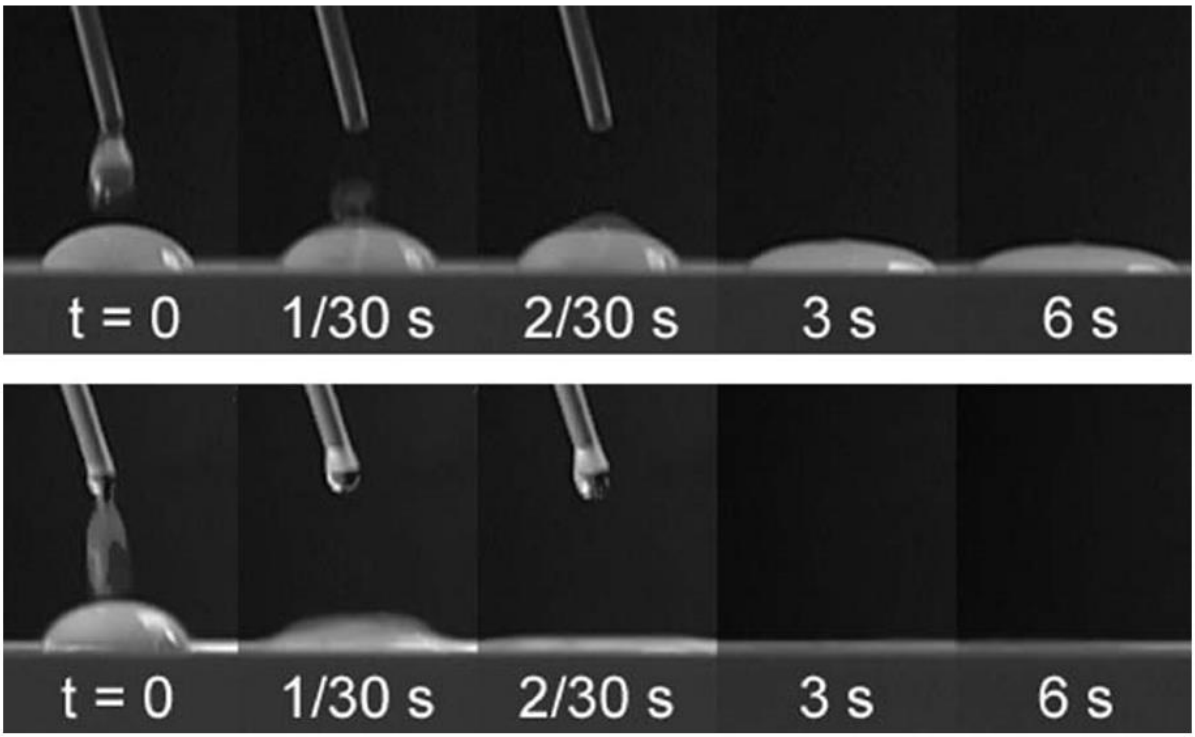

Figure 2.2: "(Top) A small quantity of alkyl polyethoxylated/alcohol solution is added to a sessile water drop on a solid substrate of moderate hydrophobicity. The aqueous surfactant solution is $C_{12}E_8$at seven times the critical aggregation concentration (CAC) and $C_{12}E_0$ at 21 times the solubility limit. The initial base diameter of the drop is approximately 1cm. (Bottom) A trisiloxane solution is added to a sessile water drop". Taken from (8)

Figure 2.2 shows the spreading rate of a drop of solution of polyethoxylated/alcohol solution added to a water drop, and the spreading of a superspreader trisiloxane solution.

In his review, Venzmer (1) highlights the following points.

1. When a drop of aqueous surfactant solution is put on a hydrophobic substrate, surfactant molecules adsorb to the liquid/solid interface.

2. The contact angle decreases as the spreading takes place which makes other surfactant molecules adsorb at the just formed liquid/gas and liquid/solid interfaces, (at or near the drop edge which is moving). This is the three phase contact line.
3. For spreading to carry on a positive spreading coefficient (S) is needed (see Eq. 1.1).

Where γ_{SA} is the solid/gas interfacial tension, γ_{SL} is the solid/liquid interfacial tension, and γ_{LA} is the liquid/gas interfacial tension. For the spreading coefficient to stay positive, then the rate of surfactant adsorption at the outer edge needs to be greater than the diluting effect caused by area expansion. It is possible surfactant diffusion might be the superspreading rate determining step.

At the leading edge of the spreading drop, if the surface tension is bigger than at the centre of the drop, then the gradient this creates will cause a tangential stress in the surface and a surface traction on the closely surrounding liquid. This is known as Marangoni flow, (as explained in chapter 1).

For superspreading to occur *(S > 0),* there needs to be a good way of transporting surfactant molecules to the new interfaces at the spreading edge of the drop. For *S* to be positive, the contact angle at the advancing edge needs to be zero. This can only happen if the rate of surfactant adsorption onto the new interfaces is greater than the diluting effect due to area expansion.

All superspreading trisiloxane surfactants have the common property to form bilayer aggregates like vesicles, lamellar phases or the L_3-phase. This is different to more hydrophilic trisiloxane surfactants with a polyether group which form spherical micelles but don't superspread, (9,10)

2.2: What the maximum in superspreader concentration versus radial rate of spreading tells us about superspreading.

The review by Nikolov et al (11) considers two main candidate mechanisms for the fast spreading rate over hydrophobic surfaces. One is that spreading is driven by the contact angle dynamics caused by the reduction in the surface tension and/or the interfacial tension of the substrate/solution. This leads to a smaller contact angle when spreading occurs and the value of the spreading coefficient $S \geq 0$. The other second mechanism is Marangoni flow, which

takes place over the stretching surface of the spreading drop. But there is a problem; neither of these two concepts explains why the rate of spreading vs. the degree of surface wettability flattens out for higher concentrations at a maximum value. See figure 2.3 which shows the relationship between radial rate of spreading and superspreader concentration on a polystyrene surface. In it the radial rate of spreading and the spread area (figure 2.4) vs. the concentration had clear maxima at a concentration of 0.1 wt% when a Silwet L-77 surfactant was used.

Superspreading experiments with a higher rate of spreading showed a circular bump forming along the droplet-spreading periphery at the end of the spreading, and this bump later broke into regular-sized droplets or "fingers". This observation was carried out while looking at the spreading of a droplet from Silwet L-77 aqueous solution with a concentration of 0.1ml. (13). The formation of this bump, the faster spreading at low concentrations, the appearance of a maximum in the spreading rate vs. concentration and the constant dynamic contact angle during the faster rate of spreading is best explained by the Marangoni effect. For the Marangoni effect to be the key factor in the superspreading process, then in the initial stages of spreading the expansion of interfacial area should be greater near the contact line then the apex. In turn there is a larger depletion of surfactant from the interfacial region near the edge of the drop than the region near the apex. This creates a radial surface tension gradient which makes the drop spread radially outward.

Trisiloxane surfactants have a strange concentration dependence at higher concentrations of superspreader solution. The spreading rate and final spreading area are largest at 0.1wt%, they then decrease at higher concentrations, (12). This agrees with the Marangoni mechanism as the surface tension gradient will be largest at an intermediate concentration (13).

It is only possible to get a maximum in final spreading area vs. concentration when there are ambient conditions. At 100% humidity the maximum spreading area of the superspreading droplet is proportional to the amount of surfactant (14) and (12). The only limiting factor in the maximum area reached is the dimension of the substrate surface, or the ability to produce a small enough drop.

The initial spreading rate increases with surfactant concentration up to 0.1 wt% but then stays at the same value for even higher concentrations. Which supports the theory that two opposing effects are involved (14). The initial period of spreading can be explained if the time required

for diffusion to the newly formed interfaces decreases with increasing concentration. Above a

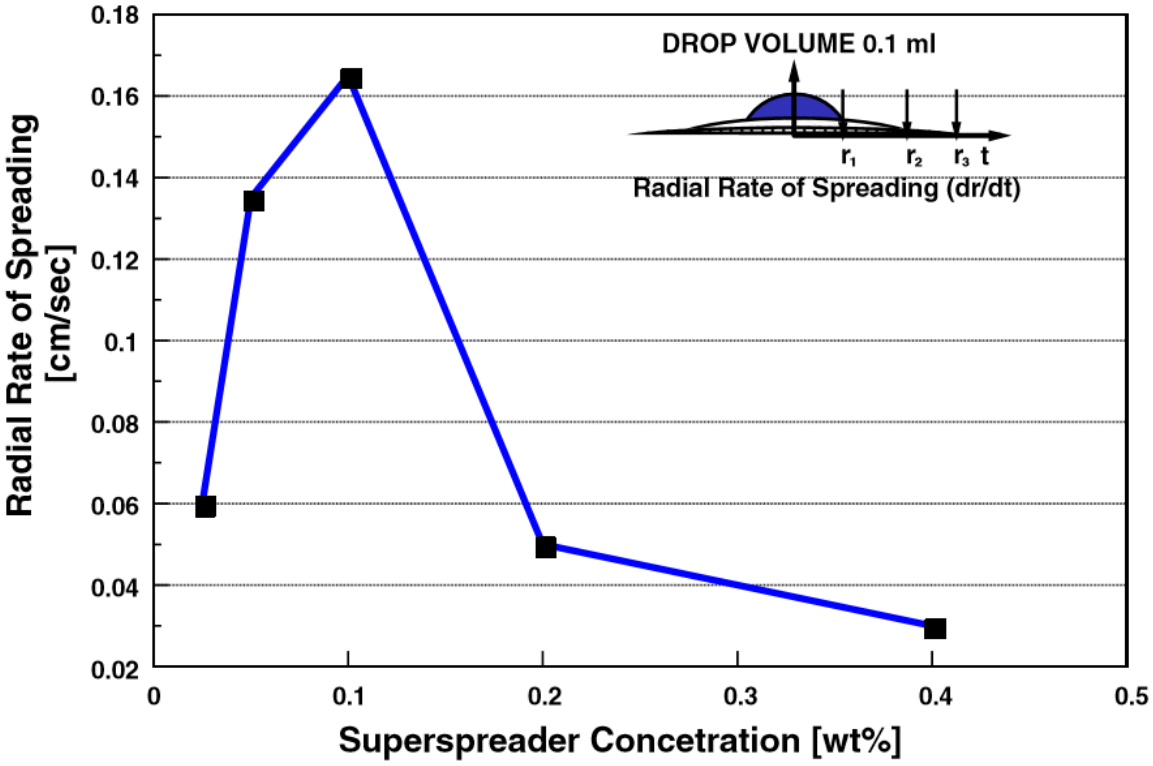

Figure 2.3: "Radial rate of spreading of a 30 µl drop of a superspreader aqueous solution on a polystyrene surface as a function of the concentration". Taken from (11)

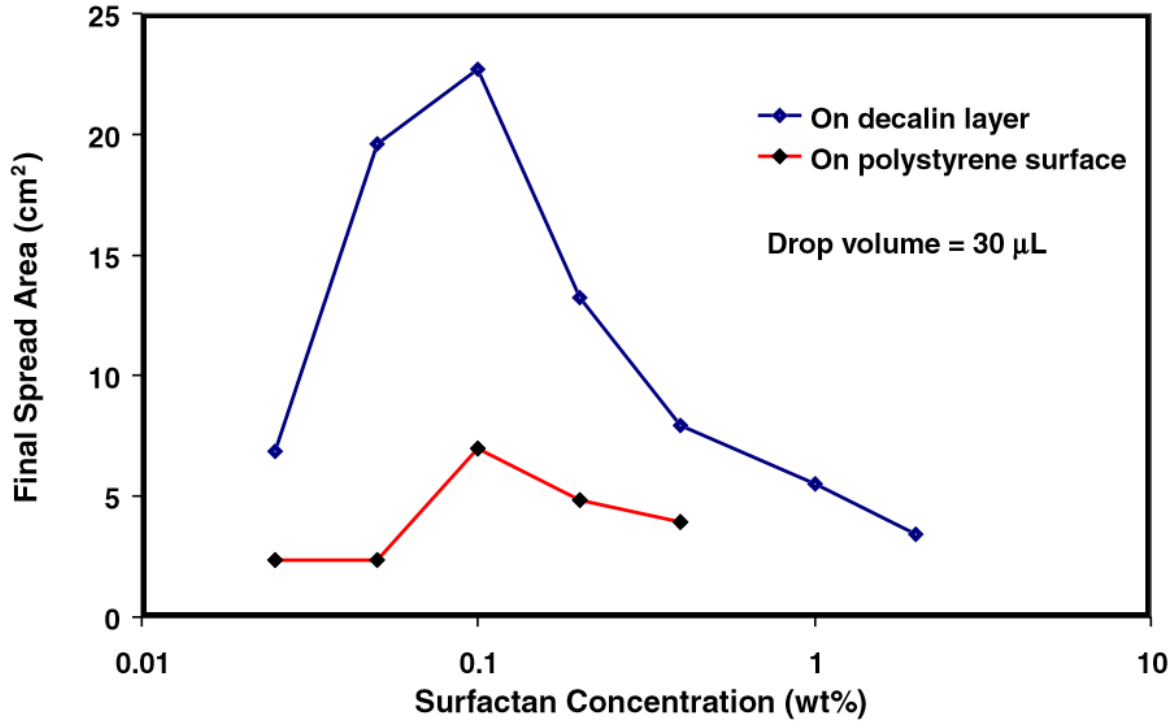

Figure 2.4: "Final spreading area vs. concentration of the aqueous solution of the superspreader Silwet L-77 on the decalin layer and on the polystyrene surface. The initial drop volume was 20 µl, taken from (11)

certain limit, another mechanism could be the rate determining step, such as the rearrangement of the molecules at the leading edge.

Figure 2.3 and 2.4 shows the reason why we chose to start our experiments with a superspreading surfactant concentration of 0.1%, it is here that the optimum rate of spreading and area of spreading occurs.

2.3: Characteristics of Superspreading.

In his overview, Hill (15) looked at the characteristics of superspreading, and in particular four features of superspreading. The first being the spreading area linearly increases with time. The second being that the time taken for the linear part and the limiting area of spreading are proportional to surfactant concentration. The third feature is there are maxima in graphs of spreading rate vs. surfactant concentration and the substrate surface energy. The fourth feature is a solution with micelles spread more slowly than a solution with a vesicle-forming surfactant. Hill (15) felt that surfactant transport and microstructure were controlling the rate of spreading.

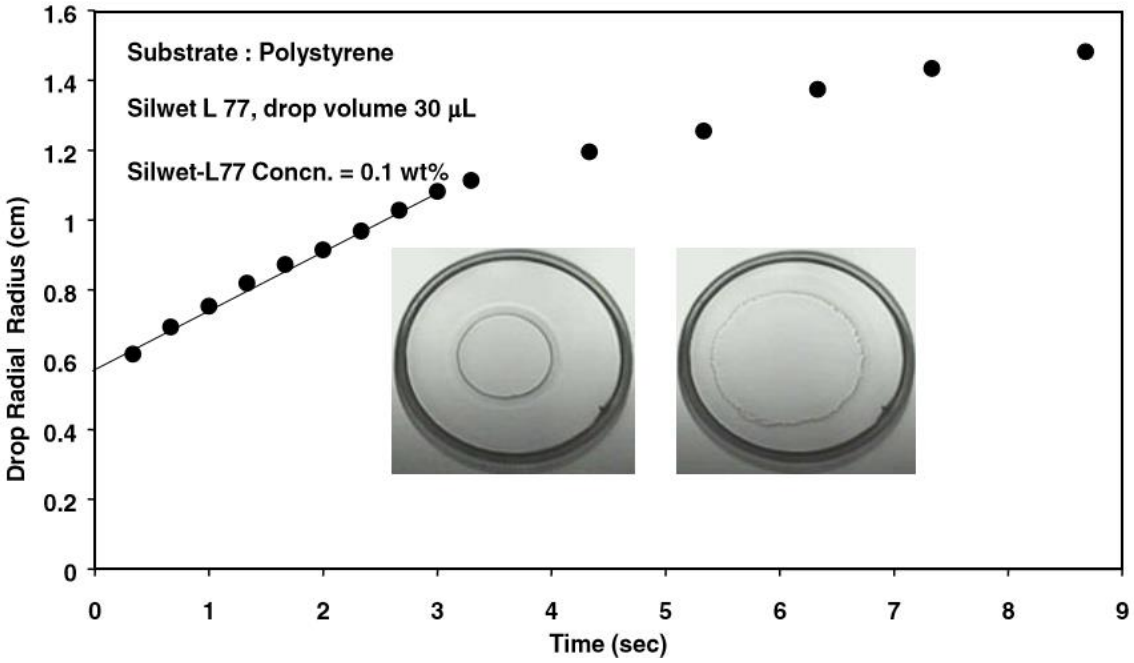

Figure 2.5: "Droplet radial radius expansion vs. time. Photos depict the formation of a bump at the spreading front (A) and then, (B) the bump breaks up". Taken from Nikolov et al (11).

Figure 2.5 shows the superspreading relationship of Silwet L77 0.1% (aq) on Polystyrene with time. The results are broadly similar to the relation of S240 0.1% (aq) with time. Figure 2.6

shows the spreading of the Silwet L77 0.1% (aq) is very different depending on the substrate surface, we found similar results for polypropylene, parafilm and polycarbonate plastic sheet.

Nikolov feels that the Marangoni flow is the best reason for explaining the initial faster spreading rate; he bases this on the following observations:

1. The faster rate of spreading at low concentrations.
2. The appearance of a maximum in the spreading rate vs. concentration.
3. During the faster rate of spreading the constant contact angle.
4. The formation of a bump following the faster rate of spreading and then its break into "fingers".

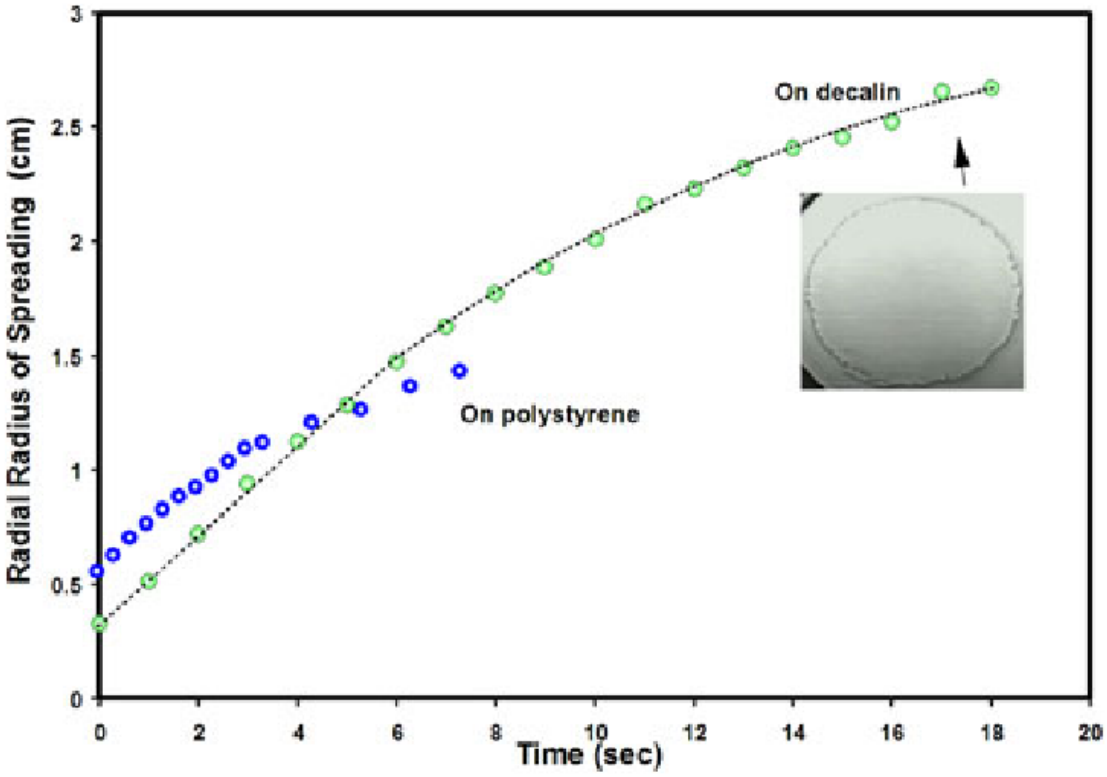

Figure 2.6: "Radial radius of spreading vs. time of a superspreader aqueous solution with a drop of size of 20 µl, 0.1wt%, Silwet L -77 on a polystyrene surface and on the decalin layer. The micrograph depicts the breakup of the bump". Taken from Nikolov et al (11)

2.4: Overview of proposed theories to explain superspreading.

In superspreading there has to be a way of transporting surfactant molecules to the newly formed interfaces near to the spreading edge of the drop. For the spreading coefficient to remain positive, the contact angle at the advancing contact line has to be zero. This is only the

case when the rate of surfactant adsorption onto the new interfaces at the spreading front exceeds the diluting effect due to area expansion. It is therefore necessary to investigate what the surface characteristics of the surfactants are.

Ananthapadmanabhan et al (2) published the first paper on superspreading. They thought that it was caused by:

1. The property of the trisiloxane surfactants to lower the surface tension at the liquid/air interface to very low values.
2. The large affinity of the surfactants for low energy substrates.
3. The very quick adsorption kinetics at the solid/liquid and liquid/air interfaces.
4. Special physical structure of the trisiloxane group leading to a beneficial molecular orientation at the spreading edge.

Ritacco et al (18) thought that the following mechanisms could cause superspreading:

1. The spreading coefficient (discussed later in this section), $S = \gamma_{sg} - \gamma_{sl} - \gamma_{lg}$, stays positive because there is a fast adsorption of surfactant molecules at the solution-air and liquid-solid interface as the circumference of the drop spreads. To keep the surfactant concentration at the liquid-air-solid contact line the flux from bulk to the interfaces needs to be quicker than the rate the perimeter expands.
2. Force due to surface tension gradients or Marangoni forces. The highest point or vertex of the drop is not depleted continuously by the adsorption of surfactant molecules and may have a higher surfactant concentration causing its surface tension to be smaller than at the perimeter. This creates a rate of flow of fluid that pulls liquid from the apex to the perimeter. This difference in surface tension between the apex and the perimeter is maintained by surfactant molecules adsorbing continuously and quick enough to the air-liquid interface.

In his work Ruckenstein (3) proposes that the superspreading of dilute aqueous solutions of siloxane surfactants over a hydrophobic surface is driven by:

1. The spreading at their leading edges of the drop as bilayers of surfactant.
2. The suction of water in the hydrophilic environment between the two layers.
3. The displacement of the surfactant and water by a Marangoni effect increased by the formation of bilayers.

Rapid spreading of water with aqueous solutions of siloxane surfactants with a trisiloxane hydrophobic group and an oligo (oxyethylene) hydrophilic group (containing 7-8 EO units), was observed by (2) on hydrophobic substrates. Reviews discussing the reasons for superspreading have been partly successful (1), (11), (15), (19), and (20). The main mechanism proposed was the Marangoni effect, but this cannot explain why the rate of spreading vs. the degree of surface wettability has a maximum.

A common property of superspreading trisiloxane surfactants is there ability to form bi-layer aggregates such as vesicles, lamellar phases or sponge phase (two continuous water phases separated by a surfactant bi-layer. The scientific community do not agree whether the correlation between phase behaviour and spreading ability is essential or just a coincidence. A reason why the phase behaviour is so important is it could have an effect on the structure of the adsorbed surfactant layer at the solid/liquid interface.

Marangoni flow was considered to be a key component of superspreading. In it the initial stages involve the expansion of interfacial area which is higher near the contact line than near the apex. In turn this causes a bigger depletion of surfactant from the interfacial region at the edge of the drop then the apex region. This creates a radial surface tension making the drop spread radially outwards

Ruckenstein put forward the idea that superspreading occurs as the surfactant used spreads from the drop over the substrate as bi-layers, which creates channels through which water is quickly moving. The Marangoni effect is also involved. The following mechanism for superspreading is proposed by Ruckenstein. The trisiloxane hydrophobic group and the hydrophobic surface are attracted to each other; this causes the spreading of the surfactant at the leading edge of the drop on that substrate surface. The hydrophobic group on the trisiloxane molecule comes into contact with air during this process. If a second layer of surfactant moves from the drop with the hydrophobic group exposed to air and the hydrophilic group exposed to the hydrophilic group of the first layer, then the free energy of the system can be decreased.

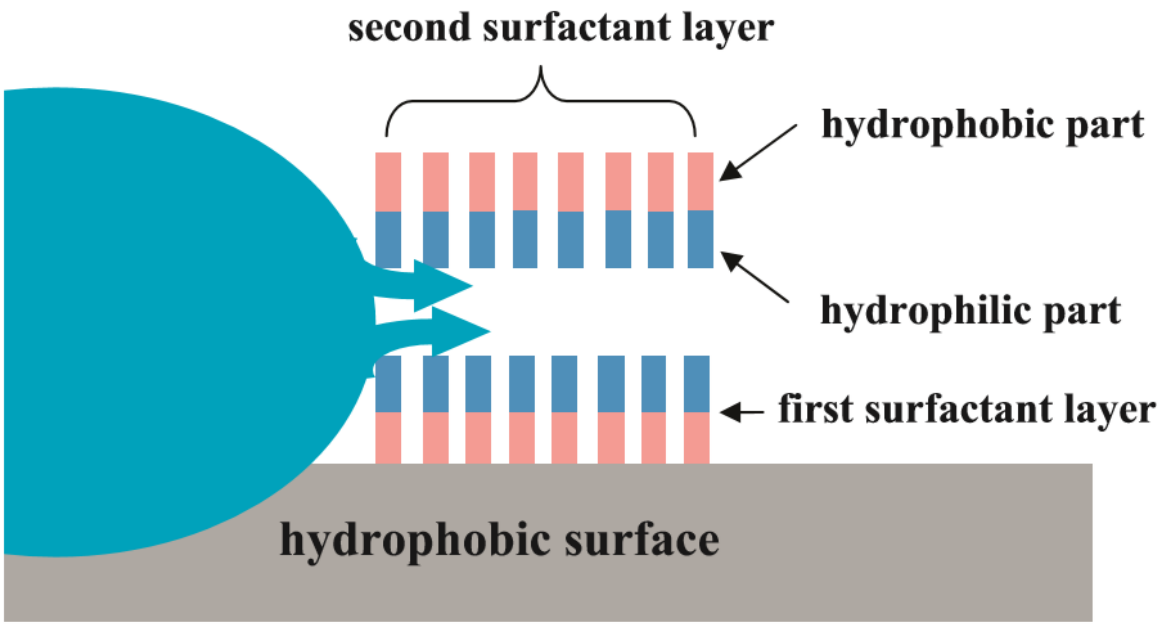

Figure 2.7: "Schematic presentation of superspreading mechanism". Taken from Ruckenstein et al (3)

The spreading of the drop is accelerated by the continuous formation of bi-layers at the contact line. The hydrophilic environment created by the hydrophilic groups of the two layers sucks in water. The second surfactant layer becomes a constituent of the liquid-air interface. The first layer adsorbed on the substrate can't move as much due to the attraction between the hydrophobic group and the hydrophobic surface. At the air-liquid and solid-liquid interfaces surfactant is adsorbed which means there is a decrease in the bulk concentration of surfactant in the direction of spreading. This causes the air-liquid surface tension to get bigger in the same direction, and the surface tension gradient to create a shear stress which helps the spreading of the bilayer and the water inside its hydrophilic environment.

For a long time it was thought that the presence of a water film at the leading edge of the spreading drop could aid superspreading. Work investigating this was undertaken by (16) In this work, a quartz crystal microbalance was used to monitor condensation of water ahead of the three phase contact line and was detected, especially on rougher surfaces. Churaev et al (17) looked at solutions of M(D'$E_{7.5}$OMe)M as they "climbed" up an angled plate. In this work a precursor film could be clearly seen and what is more the precursor film fitted well to the theoretical drop profile they predicted.

The ability of trisiloxane-ethoxylate surfactants to superspread on hydrophobic substrates is put down to their molecular structure, aggregation into solution, adsorption, wetting and surface tension properties (11). Ananthapadmanabhan et al (2) drew attention to the role of molecular structure and the role of solution aggregation and turbidity (21), While Svitova et al (22) recorded the Critical Bulk Aggregation (CAC). Zhu et al (23) and (16) looked at the effect of the precursor film on spreading. Svitova et al looked at the critical surface tension of wetting. Stoebe et al (21) and (8) recorded the specific adsorption on a solid. A model for the wetting film disjoining pressure gradient was created by Churaev et al (17), (21), (24) and (11) all thought the Marangoni effect had a profound influence on superspreading. Zhu et al (23) thought that the Marangoni flow is located at the precursor film. Furthermore, Nikolov et al (13) and (24) stated that spreading is driven by the Marangoni flow at the stretching droplet surface.

In (25) it is proposed that combined effects of different factors may explain the superspreading phenomenon. Figure 2.8 shows a possible superspreading mechansism on hydrophobic and hydrophilic substrates. When the concentration of surfactant molecules is higher then the CWC some surfactant molecules position themselves at the liquid/vapour interface of the drop. Other surfactant molecules assemble into spherical micelles. In these micelles the hydrophobic section is inside the core and the hydrophilic section is orientated to the water interface. As the drop contacts with the substrate the way that the surfactant molecule is adsorbed is different for hydrophobic and hydrophilic substrates. In figure 2.8 (a) the hydrophobic part of the surfactant molecule is adsorbed on the surface of the hydrophobic substrate from the vapour/liquid interface to the contact line. This is different to the hydrophilic substrate where the hydrophilic section of the surfactant molecule adsorbs onto it. When the surfactant molecule is adsorbed onto the substrate there is a significant lowering of interface tension and this leads to a decrease in initial contact angles. After which the drop spreads on the substrate, and a molecularly tin precursor water film is created and spreads in capillary rise geometry from the drop at the vapour/solid interface, it then spreading at the droplets edge. This happens because there is competition between the balance of the attractive interactions with other fluid molecules and the gain in entropy. At the boundary of the drop in the front of the film fluid particles move over the raised part of the uneven surface away from the drop to move ahead. The roughness of the substrate effects the potential barrier which the fluid particles must overcome. This means the shape of the precursor film is affected by the two kinds of substrate, for the low energy hydrophobic surface in figure 2.8 (b) there is a molecularly thin precursor

film, for the high energy hydrophilic surface there is a terraced shaped precursor water film (figure 2.8 (d)). When the precursor film is created surfactants can be instantly adsorbed onto the precursor film form the Solid/liquid and liquid/vapour interface as proposed by Karapetasas (26) and backed up by Theodorakis with molecular dynamics simulations. This causes the local surface concentration of the surfactant to reduce causing a higher surface tension at the perimeter then the apex. In turn this creates a surface tension gradient (shown by an arrow) between the precursor film and droplet surface. This gradient produces the Marangoni effect in the direction of the precursor film. Further information on the Marangoni effect can be found in (27), (13), (11), (28). The Marangoni effect makes the central part of the drop surface move outwards, which then spreads onto the substrate until the surface tension gradient reduces. The precursor film forms more easily on a hydrophilic surface of a substrate then a hydrophobic one. As the drop spreads the solid/liquid and liquid/vapour interfaces increase in area and the surfactant is depleted due to adsorption from micelles to the area undergoing expansion. The Marangoni effect can continue as long as the micelles can provide the surfactant molecules.

2.5: Molecular Dynamic simulations.

Considering that the phase behaviour and the related structure of the adsorbed surfactant layer on the substrate are essential factors in superspreading then simulation of these parameters should be very revealing. The problem though is that superspreading is a macroscopic process with a flow of surfactants over very small distances (~mm) and this is incompatible with molecular dynamic simulations.

Molecular dynamic simulations were carried out (29) in an attempt to study the effect of surfactant structure on spreading. Two simple structures were modelled, one T-shaped and one linear. The T shaped surfactants encouraged spreading of the drop forming a bilayer structure.

Further work on this area was done using molecular dynamics simulations using all-atom fields (8). The trisiloxane surfactant M(D'E_4OH)M and the fatty alcohol ethoxylate $C_{12}E_4$ where compared in terms of spreading properties. The simulation found the trisiloxane caused no spreading when in an aqueous drop on graphite substrate, but the organic surfactant did. Thus the simulation failed. It is thought that this is because the droplet or time interval was too short or some of the parameters for Silicon might not be suitable.

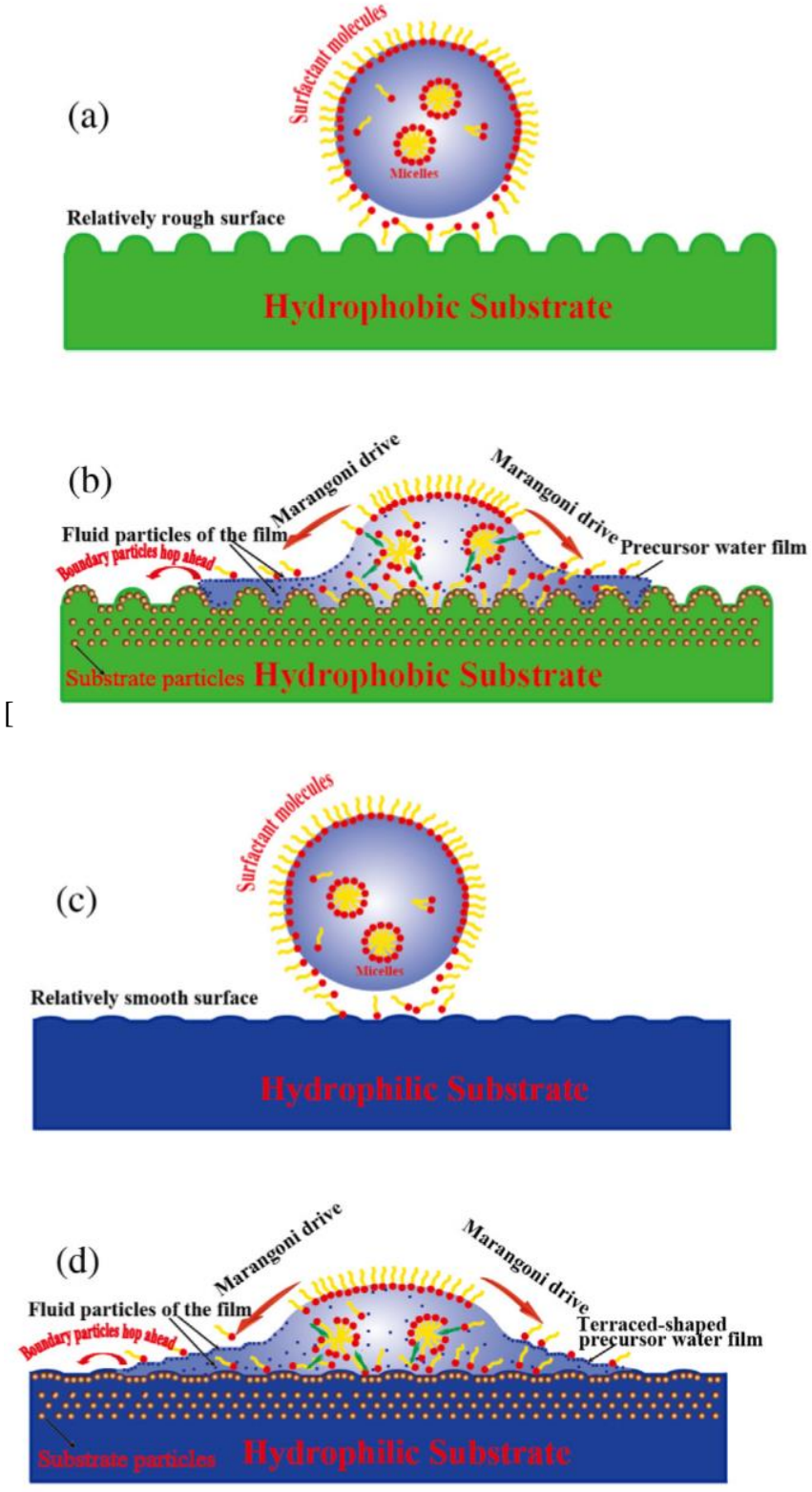

[

Figure 2.8: Schematic representation of a possible spreading mechanism on hydrophobic substrate (a-b) vs. hydrophilic substrate (c and d), taken from (31)

In his work Halverson (8) studied how the contact angle varies with time theoretically through a model.

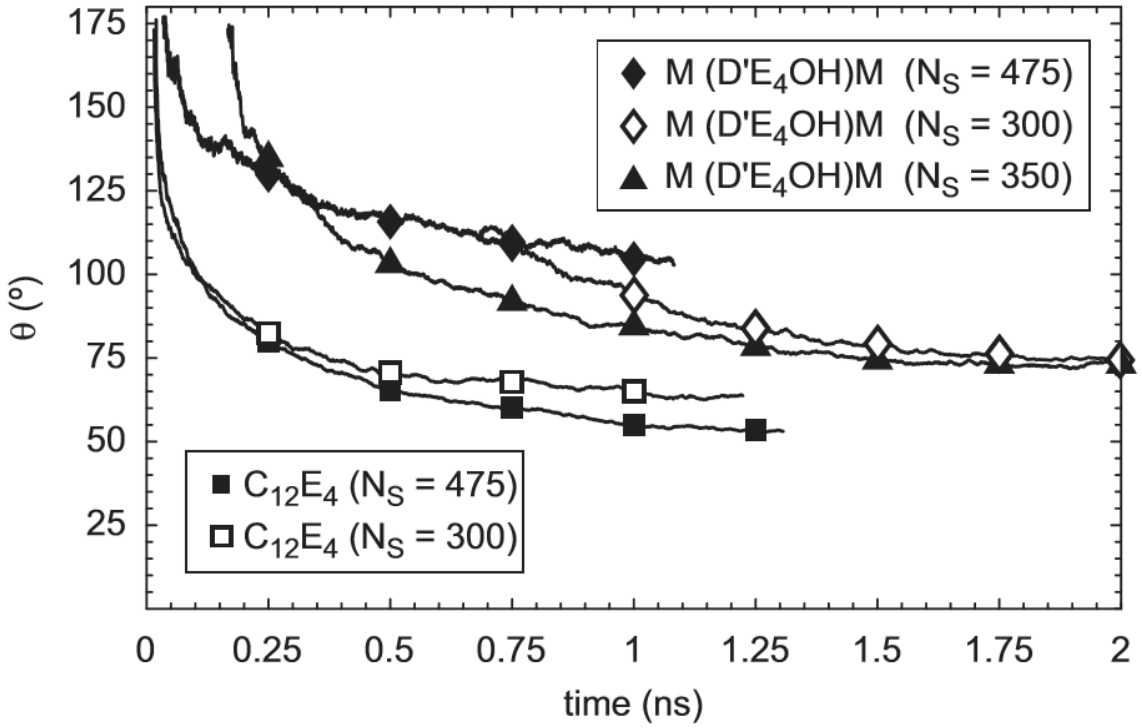

Figure 2.9: "Contact angle versus time for five surfactant-laden droplets on graphite. The number of water molecules was 9997 in all cases". (8)

Two separate programs were used in Halverson et al (8) to simulate spreading drops. For spherical drop modelling a constant number of, molecules, system volume and temperature was used in a self-written program. The simulations were run on DataStar at the San Diego Supercomputer Centre. The other program was written to simulate cylindrical drops. The advantage of cylindrical shape drops compared to spherical drops is for the former more solvent particles can be simulated for the same surface concentration of surfactant and CPU time. As for the spherical drops a number of the following was kept constant, molecules, system volume and temperature for the cylindrical drops, (30)

Halverson et al (8) performed a study of the wetting of hydrophobic substrates by drops of aqueous superspreaders and alkyl polyethoxylate surfactant solutions. Simple wetting theory

built on the Young equation described the properties of $C_{12}E_4$ systems very well, whereas trisiloxane showed a different theoretical behaviour. When the initial surface concentrations are higher than the maximum packing concentration the $M(D'E_4OH)M/H_2O$, $MDM'E_4OH/H_2O$ drops do not spread significantly. The $M(D'E_4OH)M/H_2O$ drop showed increased spreading when the surface concentration was below the maximum packing concentration,

The model in Halverson et al (8) failed because the trisiloxane drops failed to spread. This might be because the drop was too small, or the time intervals studied were too short. However Halverson expected that the simulations of drop dynamics would be possible as other work has 10,000-100000 atoms evolving over nanoseconds. Also the polyethoxylate simulations have similar length and time scales and they agree with experiment very well. It might be that the strength of the interactions used in the trisiloxane case was wrong.

2.6: The future direction of research into superspreading.

Venzmer believes that "it seems hard to believe there is only one single major cause for superspreading". Under different experimental conditions different factors have varying dominance. These factors include; the Marangoni effect, the existence of a precursor film at high humidity, and the disintegration of surfactant aggregates at the leading edge. It is not well understood why some trisiloxane surfactants with a similar structure to trisiloxane superspreaders don't superspread themselves.

Venzmer says further work is needed to understand the link between dynamic surface tension and the type of surfactant aggregates of trisiloxane surfactants. Also the effect of temperature needs to be studied especially on non-ionic surfactants. But if this is done care needs to be taken over the effect of evaporation at the leading edge. More information is needed about dry spreading and wet spreading. Also it would be useful to know if there is a precursor film, and its role in superspreading. Hydrodynamic effects could be significant especially the presence of various types of bi-layer aggregates. It is not known how the electrostatic forces from ionic surfactants effects spreading. Venzmer also says "new experimental methods are needed to allow a closer look into the processes at the leading edge". My work hopes to meet this need by using RAS and GISAXS.

Figure 2.10 shows non superspreaders in figure A, micelles form but there is no rapid spreading. Figure B illustrates how the surfactant is thought to form a bilayer which then spreads outwards.

The two main simple mechanisms used to partially explain the superspreading phenomenon are the spreading is driven by the contact angle with a spreading coefficient of $S \geq 0$ and by spreading caused by the surface tension gradient (Marangoni flow). However there is not yet been a proven definitive single mechanism driving superspreading agreed upon by the scientific community.

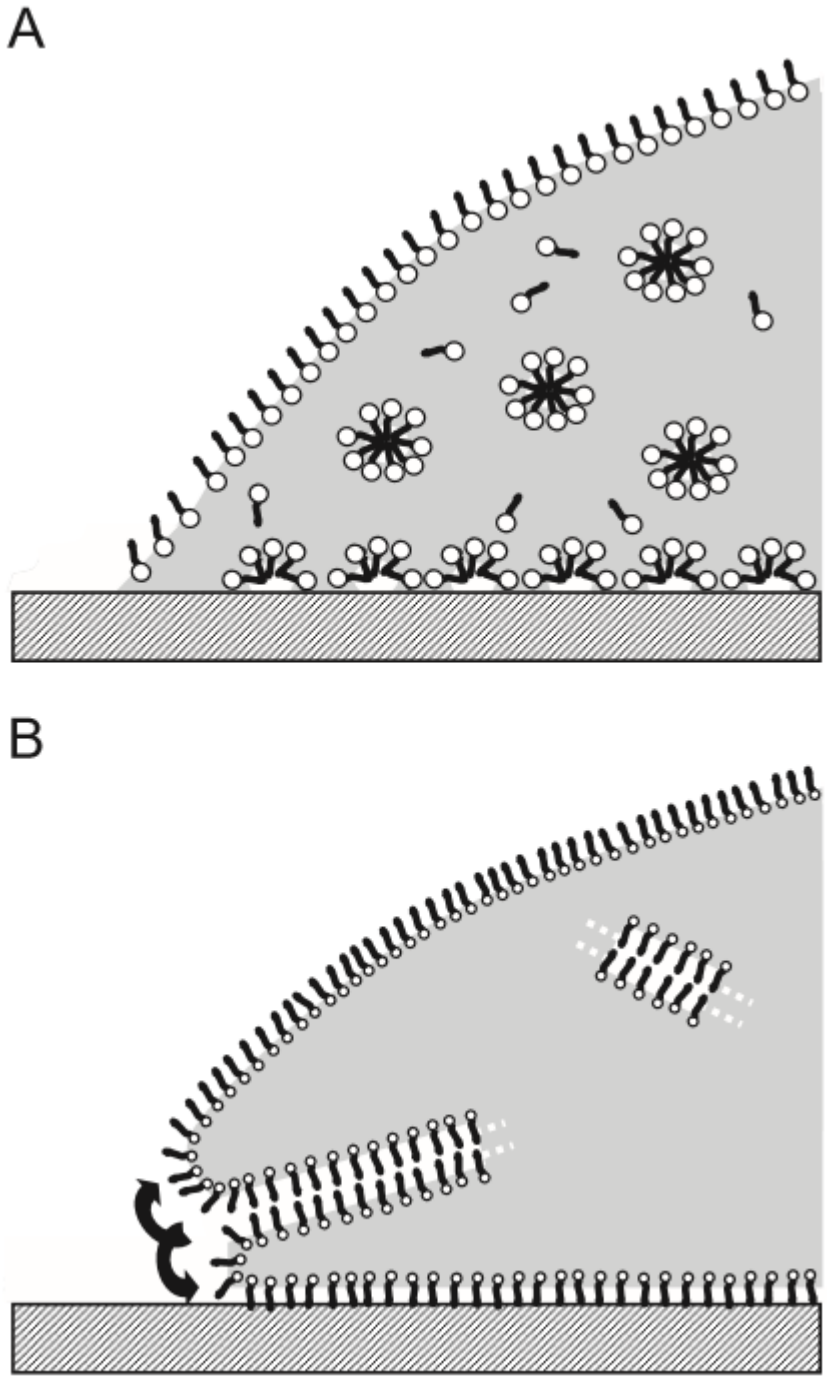

Figure 2.10: "Suggested situation at the leading edge of a droplet of an aqueous surfactant solution on a hydrophobic substrate: A) non superspreading micelle-forming surfactant: suboptimal reduction of the interfacial tension solid/water; B) superspreading bilayer-forming surfactant: best reduction of interfacial tension solid/water and efficient transport of surfactant to the leading edge especially in case of an L_3-phase". Taken from Venzmer et al (1)

Chapter 3: Macroscopic phenomenology.

3.1: Aims and Objectives of chapter 3.

This chapter aims to investigate how the drop diameter and contact angle of a spreading drop of trisiloxane superspreading surfactant and a non superspreading surfactant of similar chemical structure behaves with time. Exponential and power law function will be fitted to the drop diameter and contact angle versus time data for the two cases of superspreading and non-superspreading surfactant. Both exponential and power-law fits have been reported in the literature, and this is indeed justified since both can be solutions of the Laplace problem with suitable boundary conditions. Thus, if it was possible to establish that one of the two is a better fit to experimental data, one might be able to narrow down the range of possible boundary conditions at the drop edge during spreading.

The graphs will be analysed to look for particular evidence of the nature of the superspreading mechanism. Then the drop dimeter versus time and contact angle versus time data will be plotted on log log scales (log of drop diameter versus log time, and log of contact angle versus log time). This will show if there is evidence of different stages of spreading and is similar to the approach of (32) and (33). This will highlight if different physical mechanisms drive spreading.

3.2: Details of experimental equipment and preperations made.

A micro-syringe connected to a capillary tube of gauge 20 and diameter 0.603 mm was used to deposit drops onto the polypropylene (pp), parafilm (pf) or polycarbonate substrates (pcp) which were perfectly horizontal after being checked with a spirit level. Drops were released from a small height of 2cm to minimize inertial effects. A powerful white LED backlight with diffuser was used as a light source to stop over heating of the drop. The spreading drop was videoed by a high-speed Sanyo CCD camera which was operating at 50 frames per second. The software used was a standard frame grabber and video interface which was unbranded and a standard Windows plugin. The experiments were performed at ambient temperature and humidity. At first a control experiment was performed with distilled water on the pp, pf and pcp substrates to determine the hydrophobicity of the substrates. The superspreading surfactant used was the Evonik S240, and the non superspreading surfactant was Evonik S233. The concentration used was (0.1%) the water used to make the aqueous solutions was distilled de-ionised water (Barnstead Easypure).

3.3: Method used to perform drop diameter versus time, and drop contact angle versus time experiments.

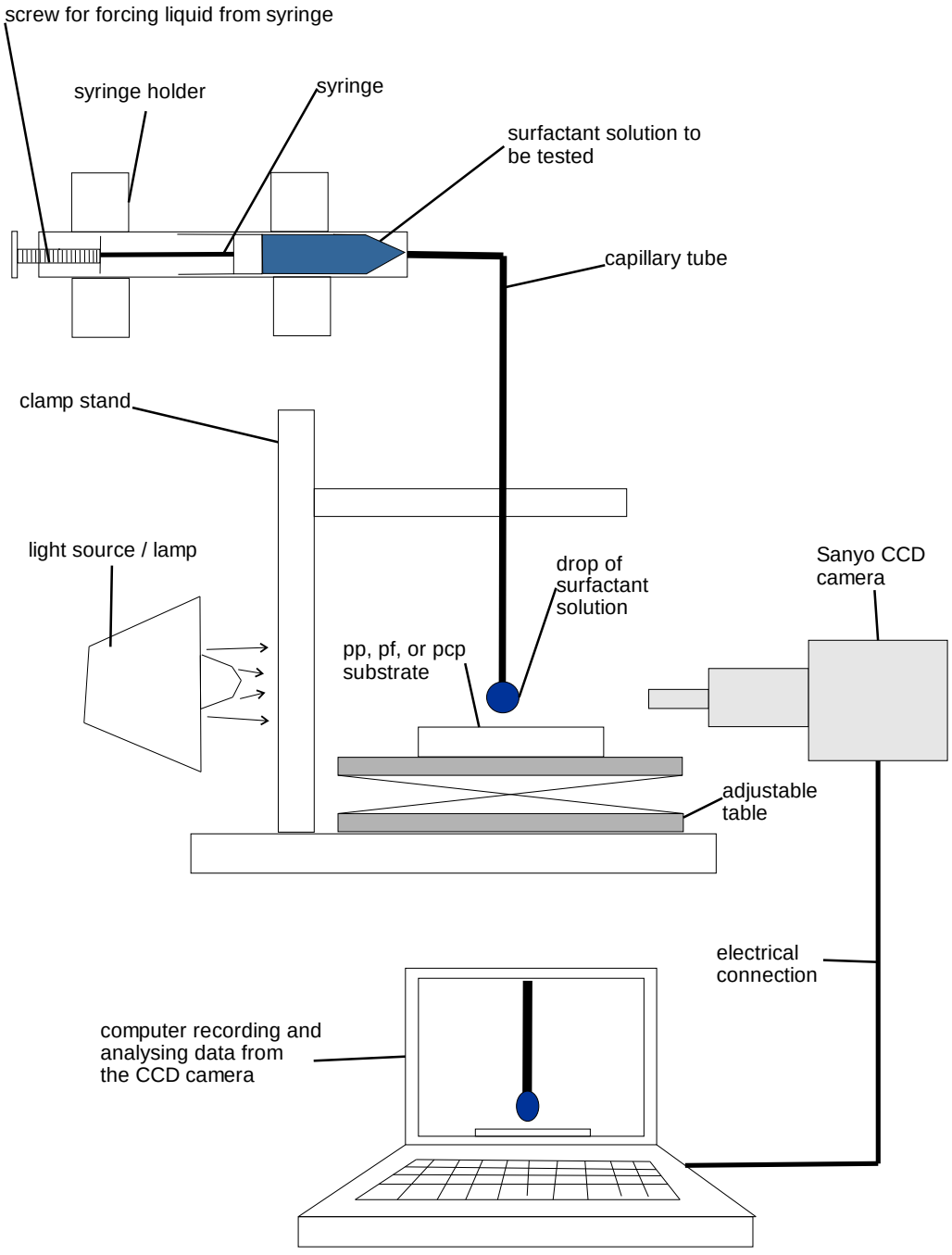

Figure 3.1: Schematic diagram of the experimental set up for the drop diameter versus time and contact angle versus time spreading drop experiments.

Using the micro-syringe deposit a drop of the surfactant onto the substrate. In the drop diameter versus time and contact angle versus time experiments a drop of S240 (0.1%) (aq) and S233 (0.1%) (aq) were put on a pp, pf and pcp substrates. Record the drop using the high speed camera until the drop has stopped spreading or its contact angle is zero.

3.4 Analysis method used to interpret the results of the drop diameter versus time, and drop contact angle versus time experiments.

1. To choose the correct frame of the image of the spreading drop required manually moving through the frames in order and this had an error of 0.1s on the time of the drop image.
2. The next stage was to calculate the mean drop diameter using equation (3.1).

$$\bar{x} = \frac{\sum x_i}{N} \tag{3.1}$$

Where $\bar{x}$ is the mean value of x, and N is the number of x readings and x_1, x_2, x_3, x_4…..x_N are the N values of x, (taken from (34). In this work, N had a value of 5 for the mean drop diameter and a value of N of 10 for the mean contact angle because for the mean contact angle both sides (2) of 5 drops were averaged.

3. The error on the mean reading of drop diameter for each particular time and contact angle versus time was calculated using the standard error on the mean shown in equation (3.3) taken from (34). "The error on a single reading is given by a spread of a distribution. The standard error on a single reading (σ_{n-1}) is:

$$\sigma_{n-1} = \sqrt{\frac{\sum\left(x_i - \bar{x}\right)^2}{N-1}} \tag{3.2}$$

Multiple readings reduce the error on the mean by the factor $\frac{1}{\sqrt{N}}$

The standard error on the mean (Δx) is:

$$\Delta x = \sqrt{\frac{\sum\left(x_i - \bar{x}\right)^2}{N(N-1)}} = \frac{\sigma_{n-1}}{\sqrt{N}} \tag{3.3}$$

4. The drop diameter versus time and contact angle versus time data for the spreading drops of S240 (0.1%) (aq) and S233 (0.1%) (aq) can be fitted to simple power law and exponential functions using the curve fitting application in Matlab software. The power law is widely used to fit this type of data in the literature, and (35) fits it with

an exponential function. For the drop diameter (d) versus time (t) data the power function is:

$$d(t) = a \cdot (t^b) + c \tag{3.4}$$

Where a is a factor and b is the power exponent number and c is the intercept. For the drop diameter data the exponential function is:

$$d(t) = a \cdot \exp(-bt) + c \tag{3.5}$$

Where a is a factor, b is the spreading exponent and c is the intercept. For the contact angle (C_A) versus time (t) data the power function used to fit it is shown in equation (3.6).

$$C_A = a \cdot (t^b) + c \tag{3.6}$$

Where a is a factor, b is the spreading exponent and c is the intercept. The exponential function used to fit the contact angle versus time data is shown in equation (3.7).

$$C_A = a \cdot \exp(-bt) + c \tag{3.7}$$

Where a is a factor, b is the spreading exponent and c is the intercept.

When fitting the drop diameter versus time and contact angle versus time graphs in the Matlab curve fitting application the statistical variables "SSE, R-square, degrees of freedom adjusted R square, and Root mean squared error" are quoted. These variables are calculated automatically by Matlab and are briefly explained in the following pages. They provide useful statistical information about the quality of the theoretical fits.

The difference in capillary pressure across the interface between two fluids at equilibrium like water and air due to surface tension is called the capillary pressure. It is described in a nonlinear partial differential equation called the Young Laplace equation.

$$\Delta p = -\gamma \nabla \cdot \hat{n} = 2\gamma H = \gamma\left(\frac{1}{R_1} + \frac{1}{R_2}\right) = \frac{2\gamma \cos\theta}{a} \tag{3.8}$$

Where Δp is the pressure difference across the fluid interface, $\hat{n}$ is the unit normal pointing out of the surface, γ is the surface tension, H is the mean curvature, and R_1 and R_2 are the principle radii of curvature, a is the radius of the circular shape of the drop The curvature of the interface and the specific interfacial free energy of the interface are related to the pressure difference between the inside and outside of a liquid drop, this is known as "capillarity".

"capillarity".

The fit to the drop diameter versus time data can be fitted by both an exponential and more commonly a power law function such as Tanner's law. This is because the power function and exponential function are two solutions to the Young Laplace partial differential equation. Power functions have been the standard way to fit drop diameter versus time data, while exponential functions have just started being used by (35).

In (36) the spreading motion is explained in terms of surface tension and viscous forces. In (36) Navier-Stokes equations are used as a starting point to explain slow viscous flow in two dimensions. During spreading viscous dissipation caused by friction and resistance oppose the enlarging of the spreading drop.

$$\frac{\partial P}{\partial x} = \mu\left(\frac{\partial^2 u}{\partial x^2} + \frac{\partial^2 u}{\partial y^2}\right) \tag{3.9}$$

$$\frac{\partial P}{\partial y} = \mu\left(\frac{\partial^2 v}{\partial x^2} + \frac{\partial^2 v}{\partial y^2}\right) \tag{3.10}$$

Where the velocity components at x and y are u and v, Pressure is (P), oil viscosity is (μ) and surface tension is (σ) (36)

Tanner's law was developed to fit pioneering work into spreading drops on completely wettable solids.

Tanner's law is given by the equation below where γ is the surface tension, η is the liquid viscocity, $B^{1/10} = 1.186$, V is the volume and n = 1/10.

$$R(t) = \left[\frac{10\gamma}{9B\eta}\left(\frac{4V}{\pi}\right)^3\right]^{1/10} \propto t^n \tag{3.11}$$

$$r(t) \propto t^n$$

When a liquid drop is put on a solid substrate it is expected to spread until it attains equilibrium. This may involve the drop spreading over the solid or remain as a spherical cap. The net horizontal force produced by the out of balance interfacial tensions at the triple phase contact line drives the drop to spread in the direction of equilibrium.

$$F = \gamma_S - \gamma_{SL} - \gamma_L \cos\theta \tag{1.2}$$

The friction at the triple phase contact line, the viscous dissipation within the drop and the inertia of the drop oppose the wetting process.

In (35) it states “the overall evolution of the drop radius during the wetting process was found to be successfully described by using the equation:

$$r(t) = r_{\infty} - a\exp(-t/\tau) \tag{3.13}$$

Reference (35) also said “the exponential function was also found to be a satisfactory model for evolution of the contact angle of the trisiloxane drops on hydrophobic surfaces:

$$\theta(t) = \theta_{\infty} + b\exp(-t/\tau) \tag{3.7}$$

An exponential function was chosen to fit the drop radius and contact angle versus time data based on the shape of the graph. A sharp increase of the drop radius and decrease of the contact angle were noticed in the initial wetting stage, then a relatively moderate increase in the radius of the drop, then an exponential relaxation at the finish of the wetting process.

3.5: Goodness of fit Statistics used in Matlab curve fitting application.

Sum of Squares due to error (SSE).

This statistical variable measures the total deviation of the response values from the fit to the response values. The SSE is the sum of residuals squared. Where the residuals are the difference between the fit values and the experimental values.

$$SSE = \sum_{i=1}^{n} w_i \cdot (y_i - f_i)^2 \tag{3.16}$$

Where y_i is the experimental point and f_i is the predicted value from the fit and w_i is the weighting applied to each data point (usually 1).

A value of SSE nearer to 0 indicates that the model has a smaller random component and the fit is more use for analysis.

R-Square.

R-square measures how much the fit is able to explain the variation of the data. It is the square of the correlation between response values and predicted response values. Another name for

it is the square of the multiple correlation coefficient and the coefficient of multiple determination.

$$R-square = 1 - \frac{\sum_{i=1}^{n} w_i \cdot (y_i - f_i)^2}{\sum_{i=1}^{n} w_i \cdot (y_i - \bar{y})^2} = 1 - \frac{SSE}{SST} \tag{3.17}$$

Where y_i is the experimental data, $\bar{y}$ is the mean of the experimental data, f_i is the predicted value from the fit and w_i is the weighting applied to each point (usually 1). SST is the "total sum of squares".

The value of R-square varies between 0 and 1, with a value nearer to 1 meaning a greater proportion of variance is accounted for by the theoretical model. A value of 0.62 would indicate the fit explains 62% of the total variation in the data about the average.

As the number of coefficients in the model increases R-square will increase also even though the fit may not get any better, to get round this it is better to use the "Degrees of Freedom adjusted R-square".

Degrees of Freedom Adjusted R-Square.

The R-square statistic is used and is adjusted based on the residual degrees of freedom where the residual degrees of freedom is defined as the number of response values n minus the number of fitted coefficients m estimated from the response values.

v = n-m

v is the number of independent pieces of information involving n data points that are needed to work out the sum of squares. The adjusted R-square statistic is usually the best indicator of the fit quality when comparing two models that are nested. In other words a series of models which adds adddtional coefficients to the previous model.

$$adj.R-square = 1 - \frac{SSE(n-1)}{SST(v)} \tag{3.18}$$

Where $adj.R-square \leq 1$

A value of adjusted R-square nearer to 1 is a higher quality fit.

Root Mean Squared Error.

Other names for this variable are the "fit standard error" and the "standard error of the regression". The Root mean Squared Error is an estimate of the standard deviation of the random part in the data.

$$RMSE = s = (MSE)^{1/2} \tag{3.19}$$

Where MSE is the mean square error of the residual mean square

$$MSE = \frac{SSE}{v} \tag{3.20}$$

A value of MSE nearer to 0 indicates that the model has a smaller random component and the fit is more use for analysis.

3.6: Method used to construct a log – drop diameter and log time spreading drop graphs and fit.

The approach of (32), (33) was adopted to see if plotting the drop diameter and the time on log scales might reveal whether the spreading of the S240 (0.1%) (aq) and S233 (0.1%) (aq) was a 1 step or 2 step process. There is a fundamental difference between (32) and (33) and this work in that in (32) and (33) the drop of surfactant was deposited onto a thin aqueous layer, however it is the opinion of the author that this approach of using log scales is still valid for this work.

A simple power law such as the one in equation (3) was fitted to the experimental data in the following way:

1. First the column of experimental data is produced in EXCEL.
2. Then a column of the log of the experimental data is calculated.
3. A trial column of the power law is calculated.
4. A column of the log of the power law is calculated
5. The sum of the residuals squared is calculated (i.e. the SSE in equation 3.8 with a w equal to 1). Where the residuals are the log of experimental data minus the log of the power function data. (It doesn't matter if the log of the experimental data is subtracted from the log of the power function data as the residuals are squared eliminating any negative differences in the residuals).No error bars were plotted for the log -log graphs because they lose their meaning on this particular scale.

6. To perform the fit "What if Analysis" was used with the "SOLVER" in Excel. For equation (3.4):

$$d(t) = a \cdot (t^b) + c \tag{3.4}$$

Where a is a factor and b is the power exponent number and c is the intercept. And with the SSE being shown in equation 3.20:

$$SSE = \sum_{i=1}^{n} (y_i - f_i)^2$$
$$SSE = \sum_{i=1}^{n} \left[(\log(h_i) - (\log(d_i) \right]^2 \tag{3.21}$$

Where y_i is the log experimental point and f_i is the predicted log value from the fit. With h being the experimental data and d being the drop diameter from the power law. The variables a, b and c were allowed to vary in the SOLVER with the constraint $b \leq 1$. The value of the SSE was made to be minimised as small as possible by the SOLVER, i.e. $SSE \geq 0$.

7. The log experimental data and log power function fit were plotted onto a graph in Excel and it was clear how to choose initial values of a, b and c by looking in real time at how well the fit correlated with the data. Once given initial values of a, b and c the SOLVER iterated to a solution by minimising the SSE. (I used the GRG Nonlinear solving method).

3.7: Hydrophobicity of pp, pf and pcp substrates.

In Wang's thesis (37) a drop of water was deposited onto the pp, pf and pcp substrates to determine the hydrophobicity of the substrate as in (35) it is thought the hydrophobicity could effect the spreading exponent – with the higher the hydrophobicity the lower the exponent. The greater the hydrophobicity the larger the equilibrium contact angle (θ_{eq}).

Table 3.1: Static water contact angle and surface tension properties of some common substrates, showing hydrophobicity for pp, pf and pcp substrates. . Taken from (37)

Substrate	static water contact angle (degrees)
Polypropylene (pp)	97
Parafilm (pf)	105
Polycarbonate (pcp)	86
Polystyrene (ps)	73
Polymethylmethacrylate (PMMA)	72
Polydimethylsiloxane (PDMS)	104
Hydrophobized glass	107

3.8: Drop diameter versus time data and graphs for superspreading Evonik S240 (0.1%) (aq), and the chemically similar non-superspreading S233 (0.1%) (aq) on pp, pf and pcp substrates.

As discussed in section 3.4, a drop of S240 (0.1%) (aq) and S233 (0.1%) (aq) were deposited onto a pp, pf and pcp substrate. As shown in equations 3.4 and 3.5 a simple power law function and simple exponential function were fitted to the drop diameter data with the results being displayed in tables 3.2 and 3.3.

Table 3.2: Drop diameter power law fits for drops of Evonik S240 (0.1%) (aq) and Evonik S233 (0.1%) (aq) spreading on a pp, pf and pcp substrates

Sol (aq)	Substrate	a	b	c	SSE	R-square	Adj. R-square	RMSE
S240 (0.1%)	pp	1.457	0.3834	3.733	0.07573	0.9905	0.9886	0.08702
S233 (0.1%)	pp	0.7118	0.2615	3.495	0.005249	0.9988	0.9987	0.01581
S240 (0.1%)	pf	1.693	0.3316	3.684	0.0443	0.9948	0.9938	0.06656
S233 (0.1%)	pf	0.4158	0.2507	3.902	0.006927	0.9906	0.9887	0.02632
S240 (0.1%)	pcp	2.952	0.4737	3.656	0.08265	0.9909	0.9864	0.1437
S233 (0.1%)	pcp	1.598	0.3494	3.394	0.114	0.9875	0.9852	0.1018

Statistically all the fits have a SSE close to zero indicating a small random component with the fit being more useful for analysis. The S233 (0.1%) (aq) pcp has the largest SSE and second highest RMSE. The S240 (0.1%) (aq) pcp has the highest RMSE. All the fits have an R square close to 1 meaning a good proportion of variance is accounted for by the theoretical model. The S233 (0.1%) (aq) pp has the highest R-square with 99.88% of the fit explaining the total variation in the data about the average. With all the fits having a Adjusted R-square very close to 1 it is safe to say that the fits are of high quality.

Looking at the adjusted R-square for the exponential fits in table 3.2 the values are not as close to 1 as for the adjusted R-square for the power fits in table 3.2. This means the fits are not of as high quality. Three of the fits (S240 (0.1%) (aq) pp, S233 (0.1%) (aq), and S240 (0.1%) (aq)) have much larger SSE values then the SSE values for the power fits is table 3.2, which indicates a lower quality fit as the best fits have near zero SSE values. The S233 (0.1%) (aq)

pp fit has a low R-square with 92.85% of the fit explaining the total variation in the data about the average.

Table 3.3: Drop diameter exponential law fits for drops of Evonik S240 (0.1%) (aq) and Evonik S233 (0.1%) (aq) spreading on a pp, pf and pcp substrates

Sol (aq)	Substrate	a	b	c	SSE	R-square	Adj. R-square	RMSE
S240 (0.1%)	Pp	-2.654	0.5762	6.552	0.1123	0.9859	0.983	0.106
S233 (0.1%)	Pp	-1.507	0.1019	5.334	0.3113	0.9285	0.9217	0.1217
S240 (0.1%)	Pf	-2.732	0.7131	6.594	0.1727	0.9798	0.9758	0.1314
S233 (0.1%)	Pf	-0.8203	0.2652	4.76	0.01363	0.9815	0.9778	0.03692
S240 (0.1%)	Pcp	-3.647	1.784	7.332	0.00812	0.9991	0.9987	0.04505
S233 (0.1%)	Pcp	-2.758	0.6444	6.302	0.09843	0.9892	0.9872	0.09459

Looking at figure 3.2 it is clear that the S240 (0.1%) (aq) drop spreads more rapidly and to a larger final diameter then the S233 (0.1%) (aq) at 6.5mm in 6 seconds compared to 5.4 mm in 38 seconds. Both the exponential and power functions fit the S240 (0.1%) (aq) data well but in the S233 (0.1%) (aq) pp data the exponential fit clearly does not correlate well with the experimental data between 0 and 8 seconds. Hence the low adjusted R-square at 0.9217.

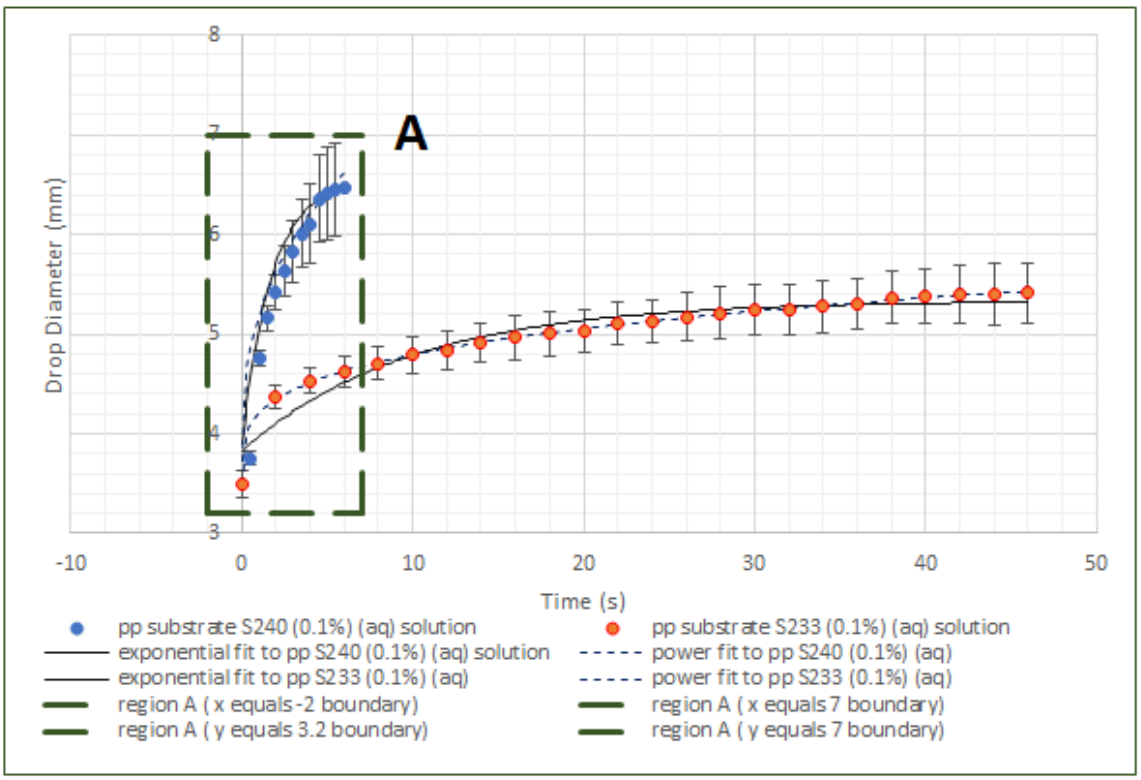

Figure 3.2 (i): Comparing the drop diameter for a spreading drop of S240 (0.1%) (aq) and S233 (0.1%) (aq) on a pp substrate versus time. Region A is labelled in the above figure and shown below.

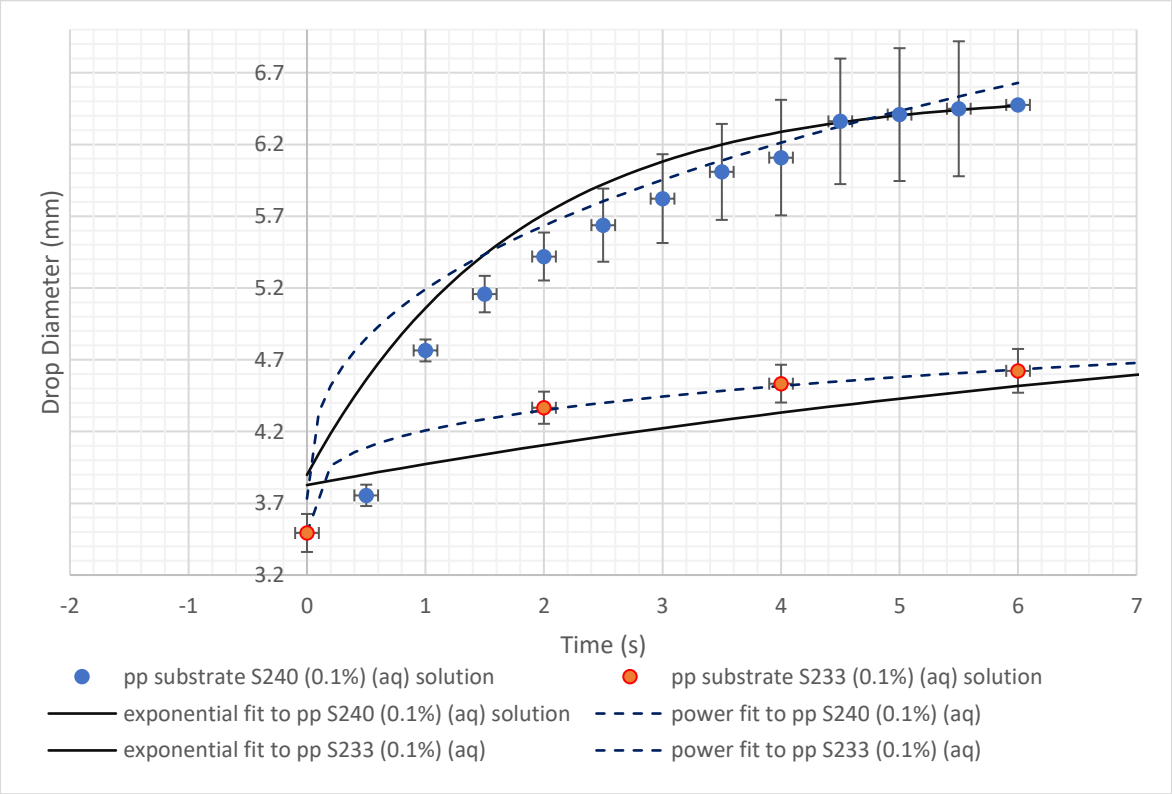

Figure3.2 (ii); Enlarged region A.

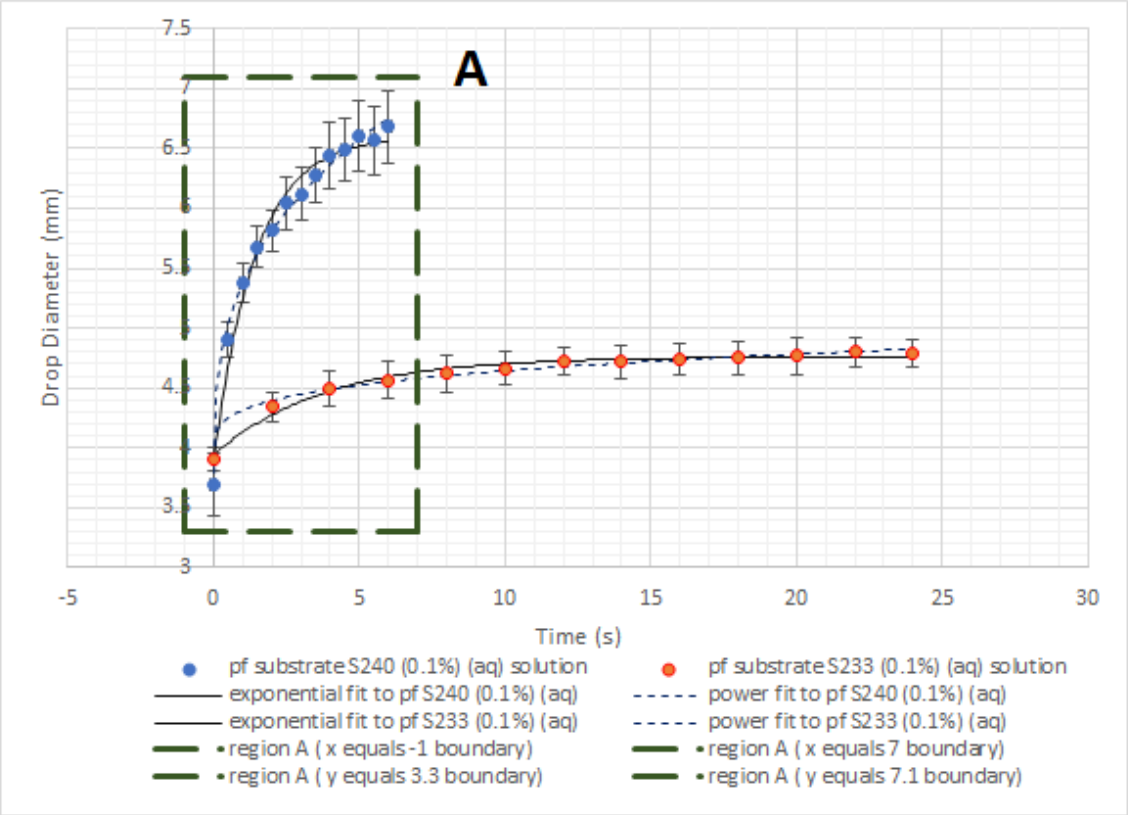

Figure 3.3 (i): Comparing the drop diameter for a spreading drop of S240 (0.1%) (aq) and S233 (0.1%) (aq) on a pf substrate versus time. Region A is labelled in the above figure and shown below.

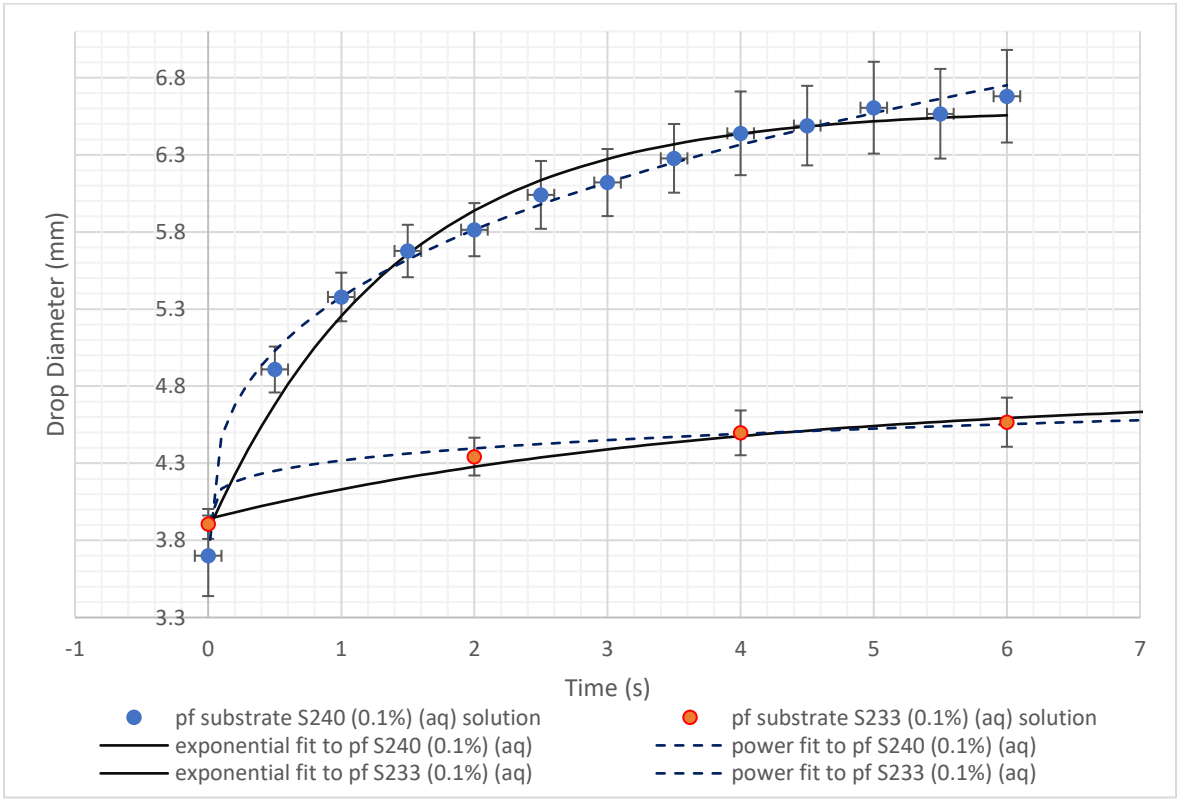

Figure 3.3 (ii): Region A

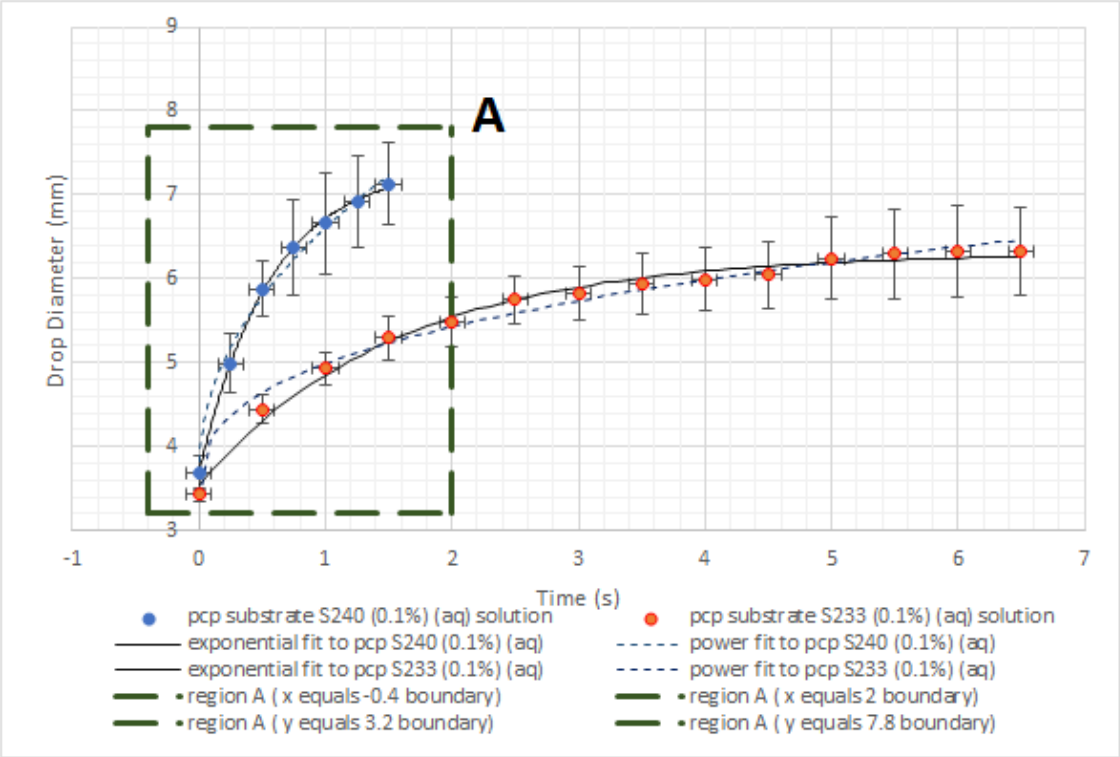

Figure 3.4 (i): Comparing the drop diameter for a spreading drop of S240 (0.1%) (aq) and S233 (0.1%) (aq) on a pcp substrate versus time. Region A is labelled in the above figure and shown below.

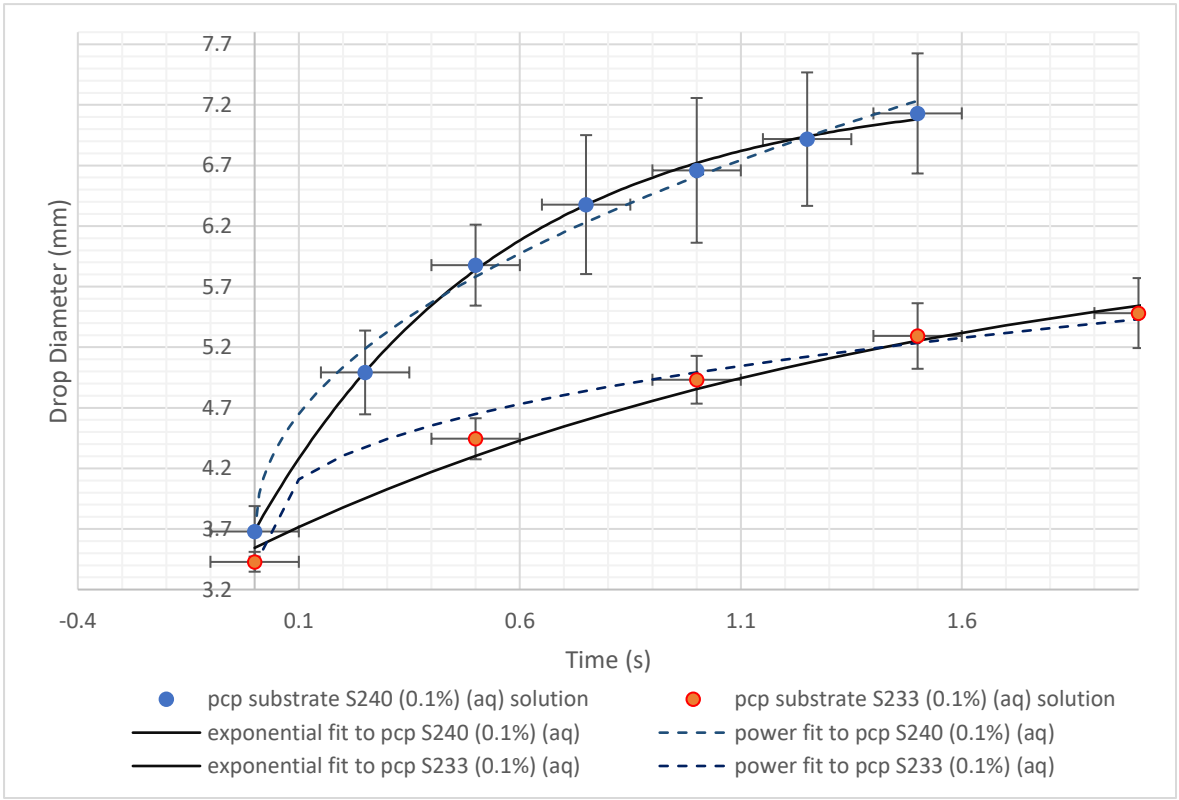

Figure 3.4 (ii): Region A.

Looking at figure 3.3 the S240 (0.1%) (aq) pf drop spreads more rapidly and to a larger final diameter then the S233 (0.1%) (aq) pf drop art 6.7 mm in 6 seconds compared to 4.8 mm in 15 seconds. The power and exponential functions fit the pp S240 (0.1%) (aq) data well. For the S233 (0.1%) (aq) the power function fits the data better then the exponential function between 0 and 2 seconds. This is shown in the adjusted R-square with the power function having a value of 0.9987 compared to the exponential fit having a value of 0.9778, and a value closest to 1 being a higher quality fit.

In figure 3.4 the spreading of both the S240 (0.1%) (aq) and S233 (0.1%) (aq) is remarkably rapid, with the S233 (0.1%) (aq) behaving comparably to the superspreading S240 (0.1%) (aq) drop on pp and pf substrates. The S240 (0.1%) (aq) drop spreads more rapidly and to a greater final diameter then the S233 (0.1%) (aq) drop at 7.2mm in 1.5 seconds compared with 6.4mm in 6 seconds. Both the power and exponential functions fit the S240 (0.1%) (aq) data well but for the S233 (0.1%) (aq) between 0 and 1 second both the power and exponential functions do not correlate with the data point at 0.5 seconds.

Figure 3.5 reveals that the pcp substrate is by far the most rapid substrate for superspreading and achieves the largest final drop diameter compared to the pp and pf substrates at 7. 2 mm in 1.5 seconds. The pp and pf substrates are remarkably similar reaching a final drop diameter of around 6.6 mm in around 5.5 seconds.

Looking at figure 3.6 it is clear the relative relations of the S240 (0.1%) (aq) drop's behaviour on the pp, pf and pcp substrates is very similar to the S233 (0.1%) (aq) substrates, but just over a larger time scale. For the S233 (0.1%) (aq) drop on pp and pf this being around 40 seconds compared to 6 seconds with a drop of S240 (0.1%) (aq) on the same substrates. The drop of S233 (0.1%) (aq) on a pcp substrate is more rapid then a similar drop on a pp or pf substrate at 6.4mm in 6 seconds. The drop of S233 (0.1%) (aq) on a pp and pf substrate are pretty similar to each other in terms of behaviour but the pf has a smaller final drop diameter of 4.8 mm compared to the pp substrate which is 5.4 mm.

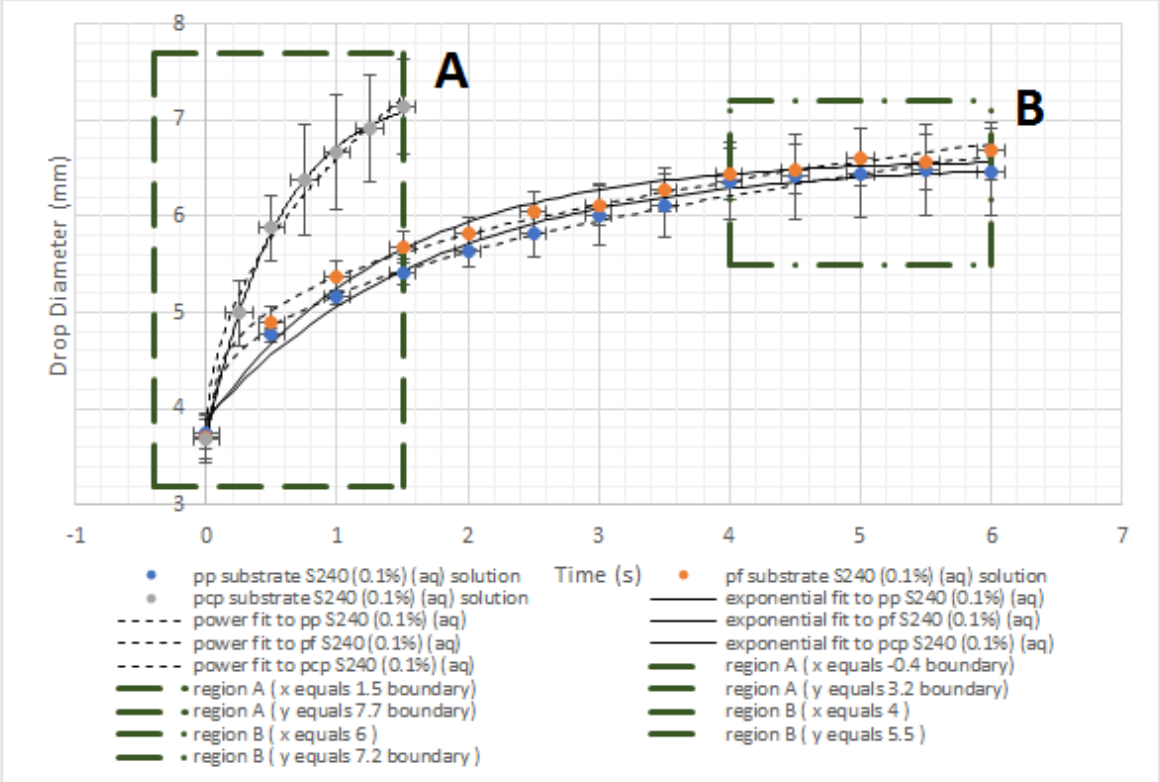

Figure 3.5 (i): Comparing the drop diameter for a spreading drop of S240 (0.1%) (aq) on a pp, pf and pcp substrate versus time. Region A and B is labelled in the above figure and shown below.

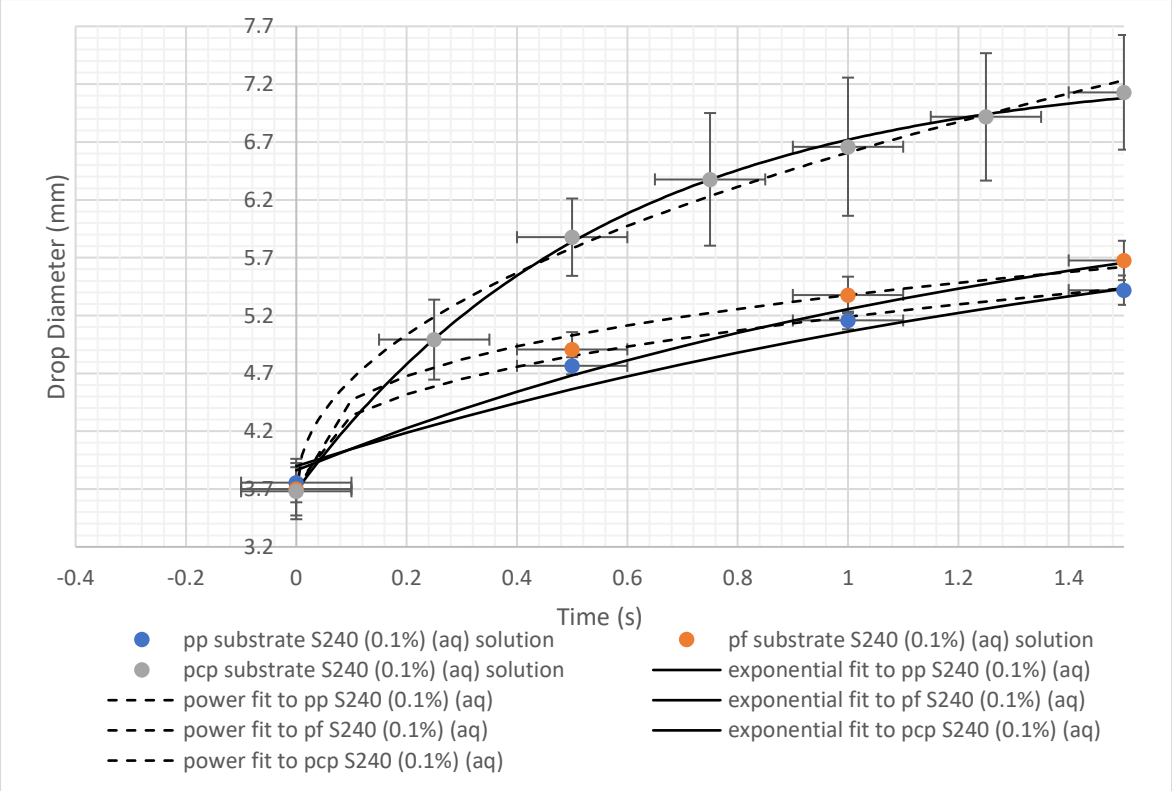

Figure 3.5 (ii): Region A.

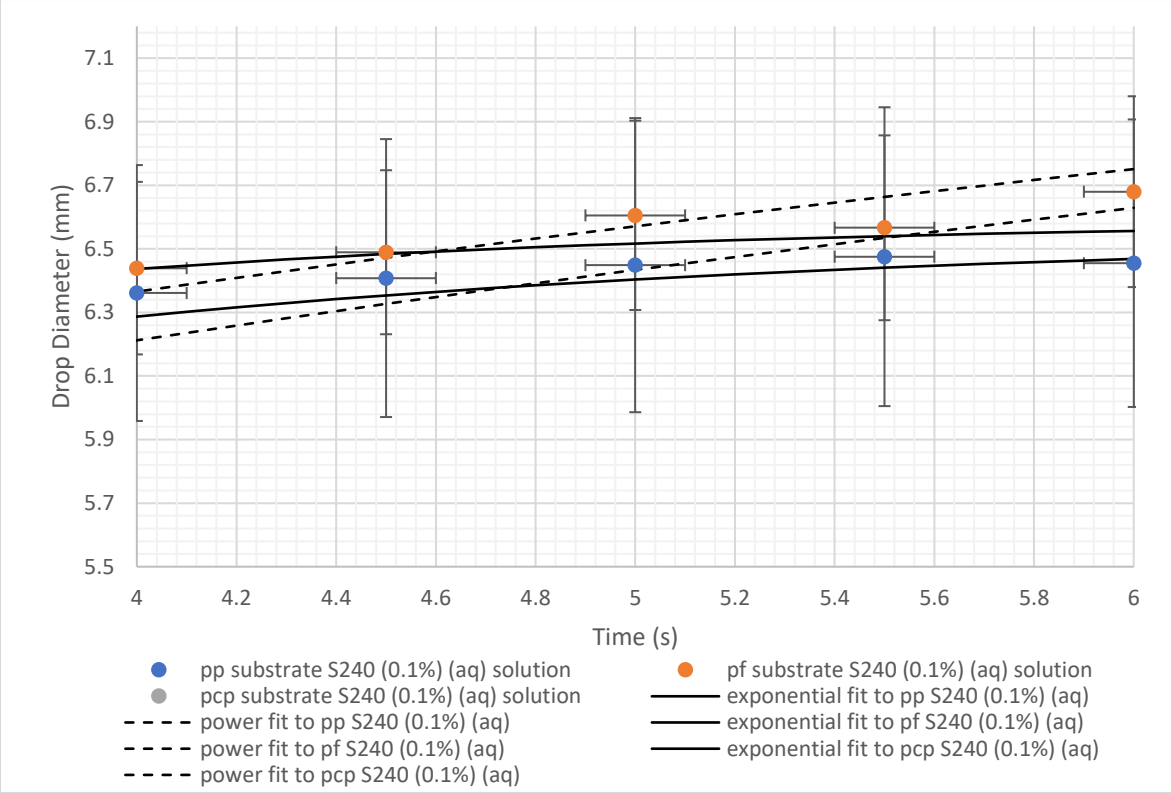

Figure 3.5 (iii): Region B

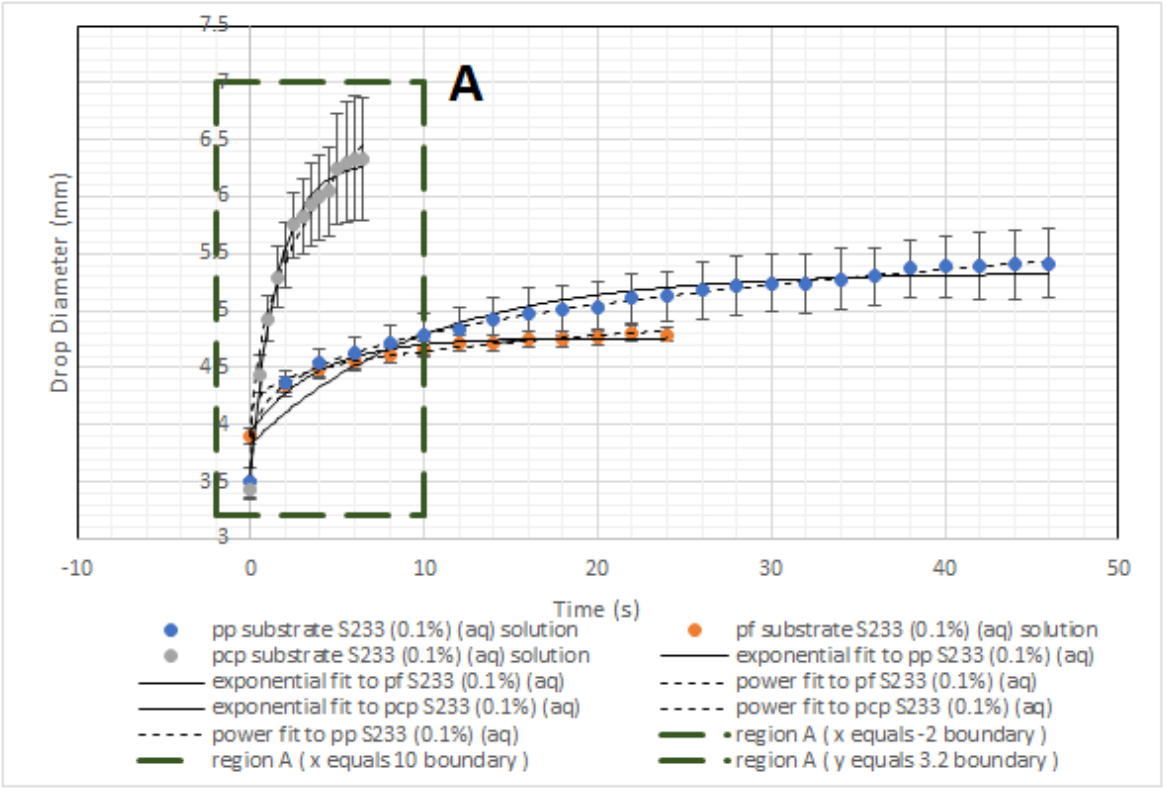

Figure 3.6 (i): Comparing the drop diameter for a spreading drop of S233 (0.1%) (aq) on a pp, pf and pcp substrate versus time. Region A is labelled in the above figure and shown below.

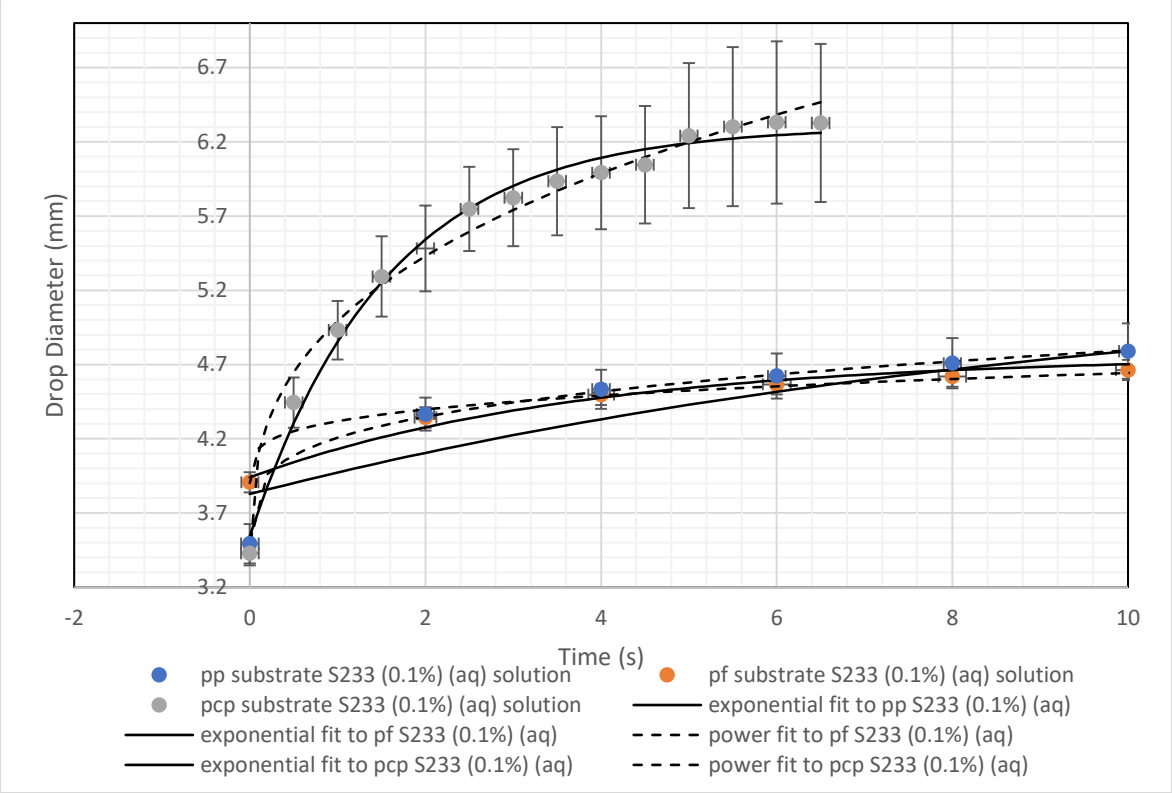

Figure 3.6 (ii): Region A.

3.9: Contact Angle versus time data and graphs for superspreading Evonik S240 (0.1%) (aq), the chemically similar non-superspreading S233 (0.1%) (aq) on pp, pf and pcp substrates.

As discussed in section 3.4 a drop of S240 (0.1%) (aq) and S233 (0.1%) (aq) were deposited onto a pp, pf and pcp substrate. As shown in equations 3.6 and 3.7 a simple power law function and simple exponential function were fitted to the contact angle data with the results being displayed in tables 3.4 and 3.5.

All the power law contact angle fits in table 3.4 with the exception of the S233 (0.1%) (aq) pcp have good quality fits with adjusted R square values close to 1 at around 0.98 – 0.995 with the adjusted R square for S233 (0.1%) (aq) pcp being 0.9419. However, the SSE values are very large compared to the drop dimeter fits shown in tables 3.2 with values significantly larger then zero. This indicates that the power law (and exponential function discussed next) do not correlate as well as the drop diameter versus time data when fitted to the contact angle data versus time data. This is a reason why later in the chapter there is no log contact angle versus log time data.

Table 3.4: Contact angle power law fits for drops of Evonik S240 (0.1%) (aq) and Evonik S233 (0.1%) (aq) spreading on a pp, pf and pcp substrates

Sol (aq)	Substrate	a	b	c	SSE	R-square	Adj. R-square	RMSE
S240 (0.1%)	Pp	-22.51	0.2122	33.45	8.027	0.9899	0.987	1.071
S233 (0.1%)	Pp	-9.079	0.2087	31.71	1.984	0.9958	0.9954	0.3074
S240 (0.1%)	Pf	-16.34	0.2125	28.93	4.181	0.9925	0.9912	0.5902
S233 (0.1%)	Pf	-11.61	0.1421	33.84	4.425	0.9846	0.9815	0.6652
S240 (0.1%)	Pcp	-21.28	0.2129	26.68	1.983	0.9944	0.9907	0.813
S233 (0.1%)	Pcp	-9.126	0.3512	21.7	7.884	0.9564	0.9419	1.146

In table 3.5 the adjusted R-square with the exception of S233 (0.1%) pp have pleasing values. But the S233 (0.1%) pp is a very poor fit with an adjusted R-square of 0.9417, (a good fit is close to 1), and a huge SSE of 25.3 (a value of close to 0 is a good SSE fit). Also the SSE of S240 (0.1%) (aq) pp at 7.708, S233 (0.1%) (aq) pp at 25.3, S240 (0.1%) (aq) pf at 8.723, and S233 (0.1%) (aq) pf at 6.55 are all significantly bigger then the SSE fit values shown for the exponential law drop diameter fits shown in table 3.3.

Figure 3.7 shows the contact angle versus time data for the S240 (0.1%) (aq) and S233 (0.1%) (aq) drop spreading on a pp substrate. The final contact angle for the S240 (0.1%) (aq) is 2 ½ degrees in 5 seconds which is much more rapid with a smaller final contact angle then the S233 (0.1%) (aq) which reaches 12 degrees in 40 seconds. Visually it is clear that for the S233 (0.1%) (aq) data both the power and exponential functions do not fit the data well between 0 and 3 seconds

Figure 3.8 shows the contact angle versus time data for the S240 (0.1%) (aq) and S233 (0.1%) (aq) drop spreading on a pf substrate. The final contact angle for the S240 (0.1%) (aq) is 5 degrees in 6 ½ seconds which is much more rapid with a smaller final contact angle then the S233 (0.1%) (aq) which reaches 16 degrees in 20 seconds. The exponential function fitted to the S233 (0.1%) (aq) pf data is a very poor fit between 0 and 4 seconds with very poor correlation between fit and experiment. The exponential function is a very poor fit to the S240 (0.1%) (aq) pf data at the data point at ½ seconds.

Table 3.5: Contact angle exponential law fits for drops of Evonik S240 (0.1%) (aq) and Evonik S233 (0.1%) (aq) spreading on a pp, pf and pcp substrates

Sol (aq)	Substrate	a	b	c	SSE	R-square	Adj. R-square	RMSE
S240 (0.1%)	pp	29.03	1.451	3.92	7.708	0.9903	0.9875	1.049
S233 (0.1%)	pp	16.85	0.1535	12.74	25.3	0.9467	0.9417	1.098
S240 (0.1%)	pf	22.04	1.098	6.088	8.723	0.9843	0.9817	0.8526
S233 (0.1%)	pf	16.97	0.4622	16.65	6.55	0.9772	0.9727	0.8093
S240 (0.1%)	pcp	21.56	5.05	5.086	0.9779	0.9972	0.9954	0.5709
S233 (0.1%)	pcp	14.24	1.134	7.579	0.791	0.9956	0.9942	0.3631

Figure 3.9 shows the contact angle versus time data for the S240 (0.1%) (aq) and S233 (0.1%) (aq) drop spreading on a pcp substrate. The final contact angle for the S240 (0.1%) (aq) is 4 degrees in 1 ¼ seconds which is much more rapid with a smaller final contact angle then the S233 (0.1%) (aq) which reaches 8 degrees in 2 ½ seconds. Here the time taken for

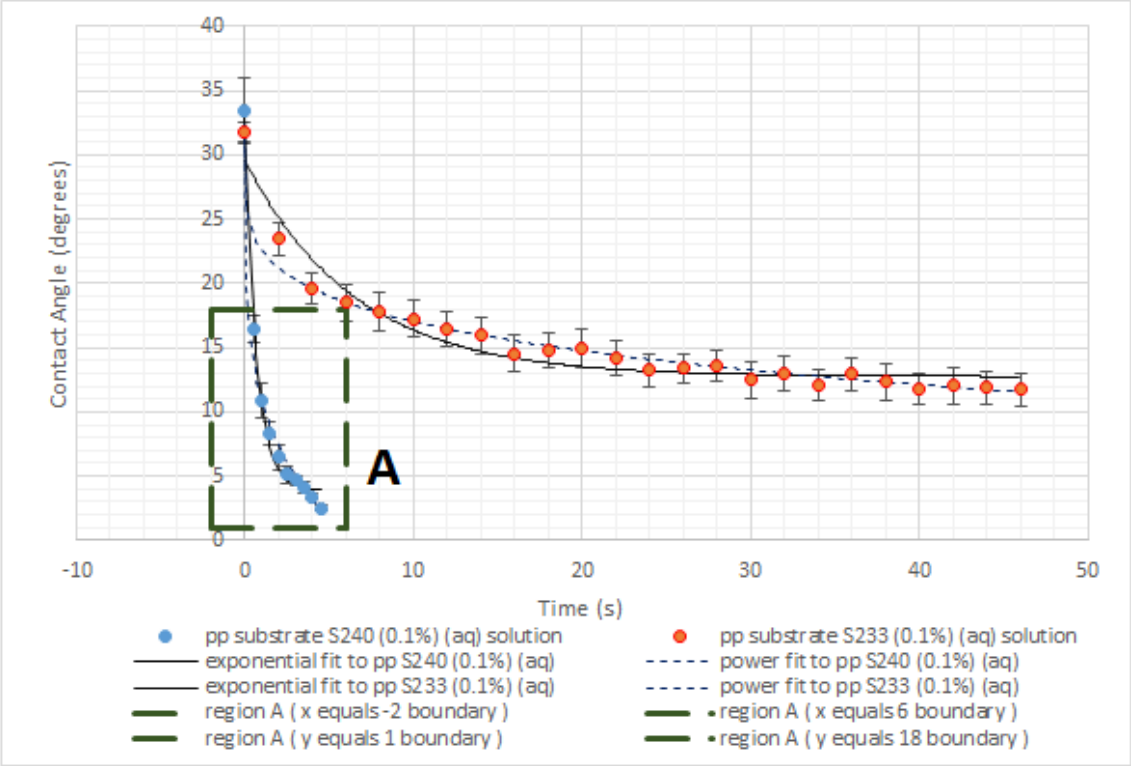

Figure 3.7 (i): Comparing the contact angle for a spreading drop of S240 (0.1%) (aq) and S233 (0.1%) (aq) on a pp substrate versus time. Region A is labelled in the above figure and shown below.

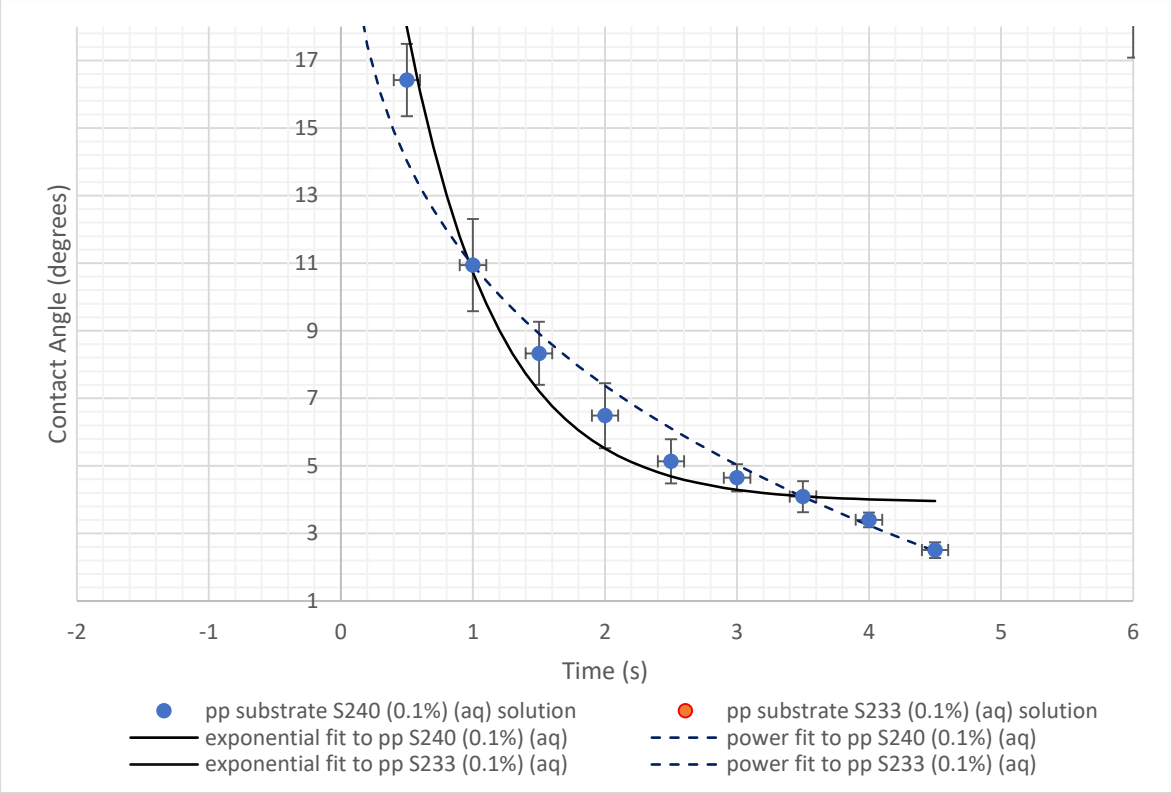

Figure 3.7 (ii): Region A

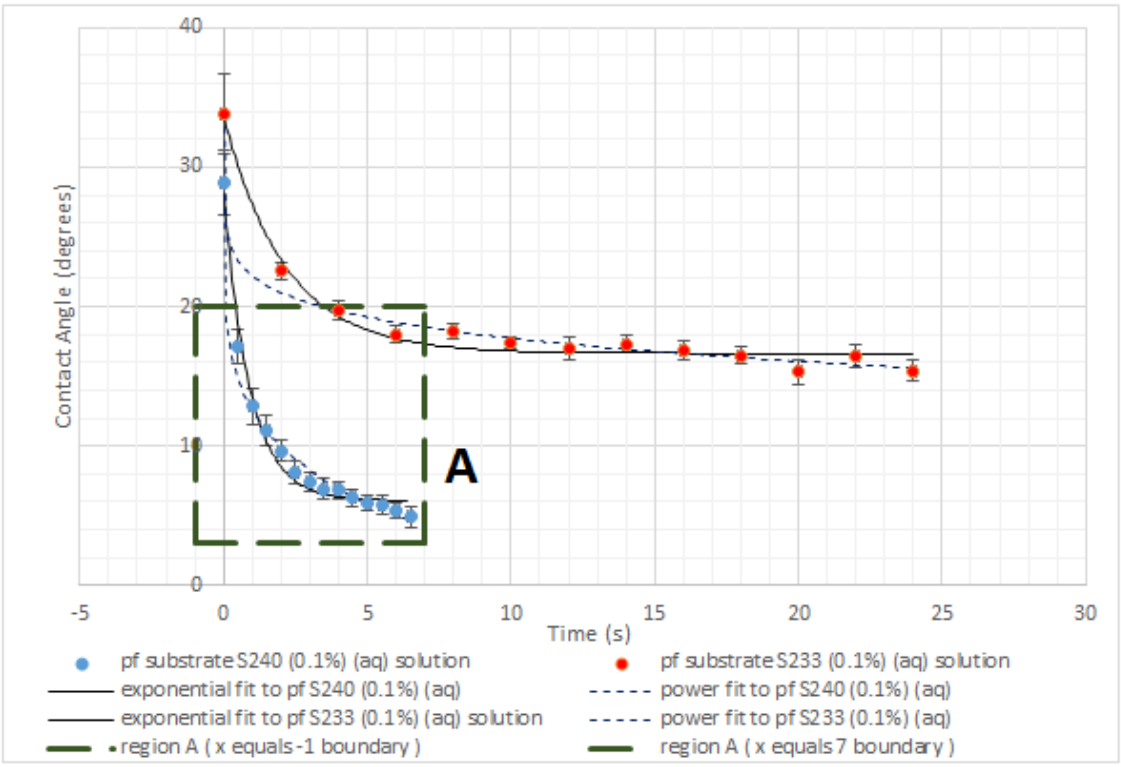

Figure 3.8 (i): Comparing the contact angle for a spreading drop of S240 (0.1%) (aq) and S233 (0.1%) (aq) on a pf substrate versus time. Region A is labelled in the above figure and shown below.

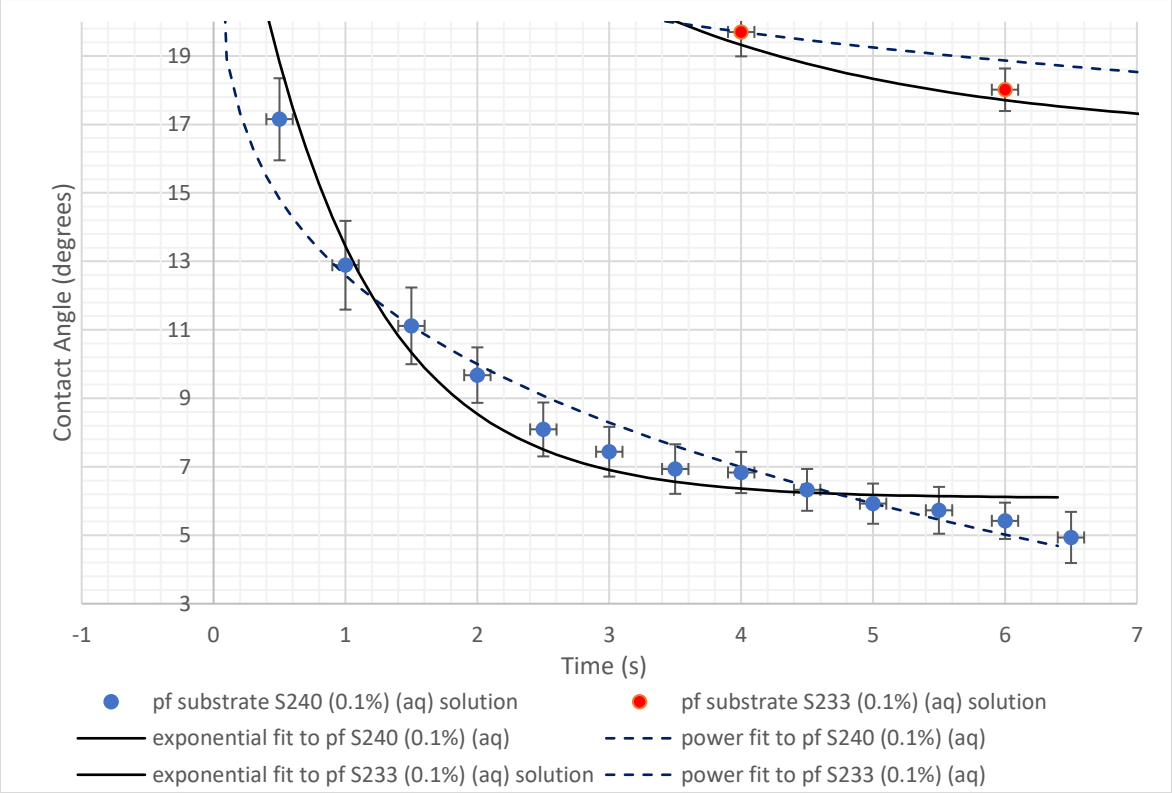

Figure 3.8 (ii): Region A

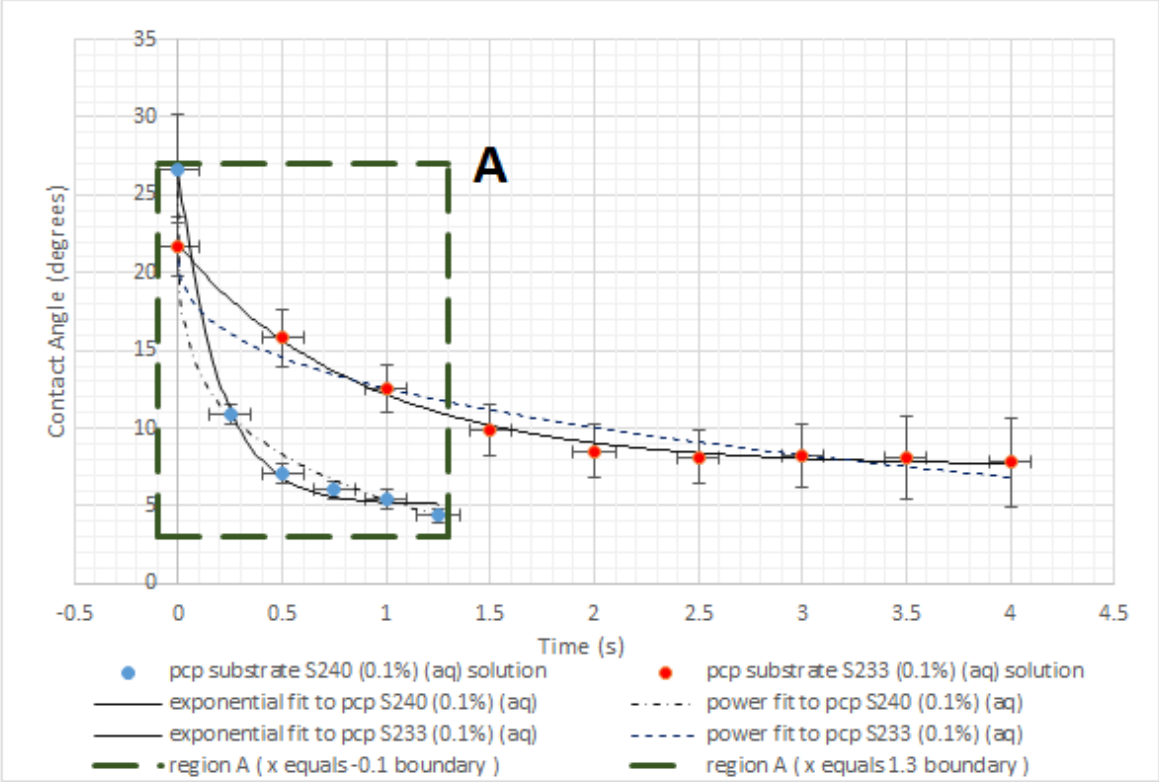

Figure 3.9 (i): Comparing the contact angle for a spreading drop of S240 (0.1%) (aq) and S233 (0.1%) (aq) on a pcp substrate versus time. Region A is labelled in the above figure

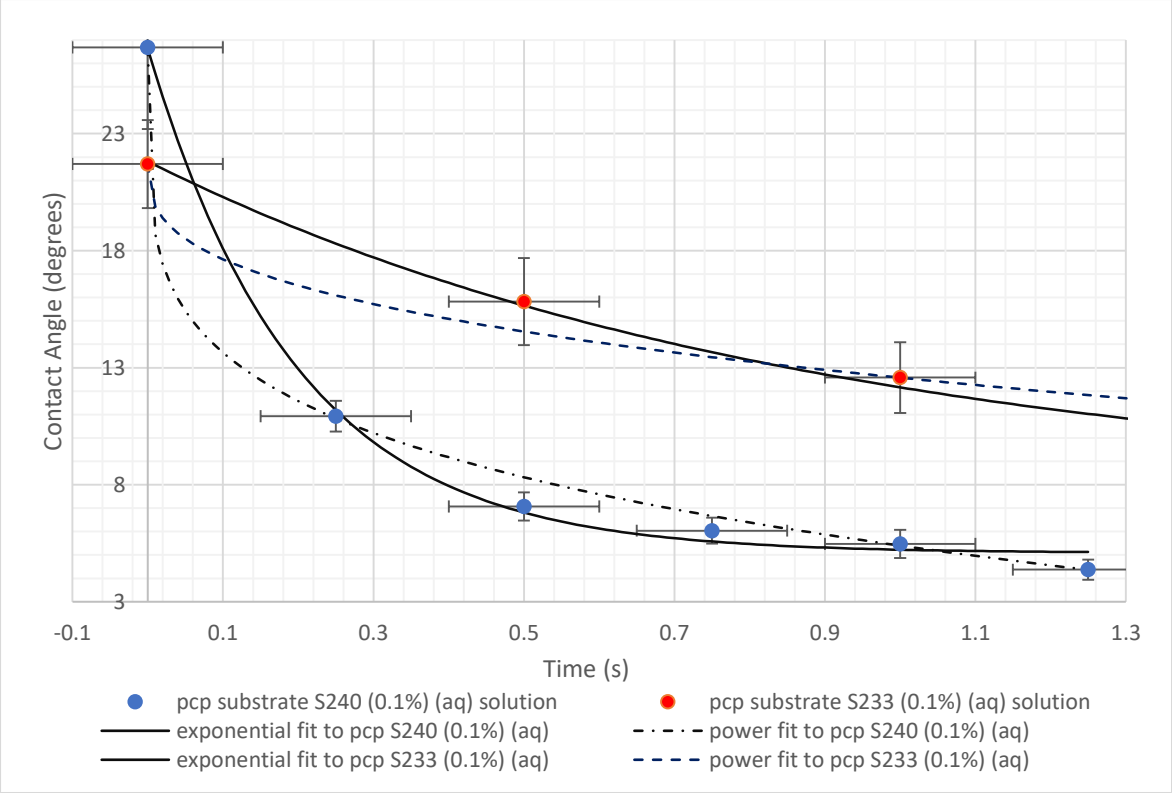

Figure 3.9 (ii): Region A

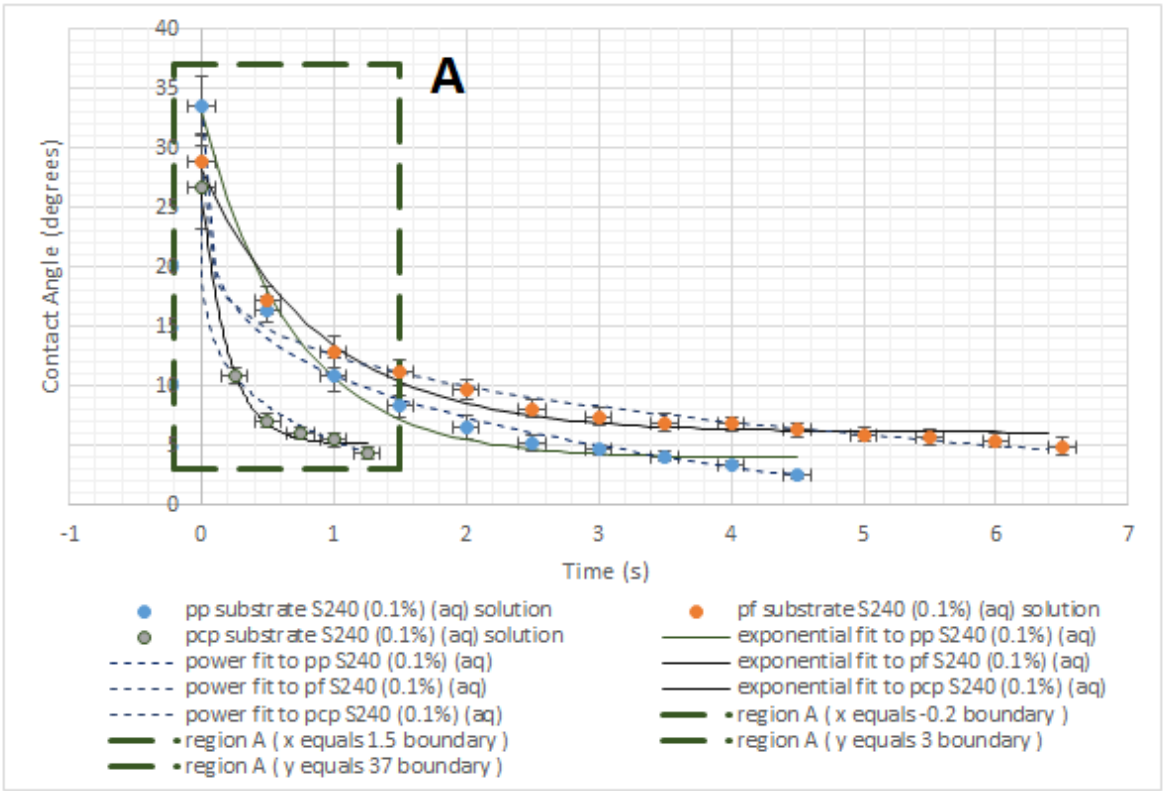

Figure 3.10 (i): Comparing the contact angle for a spreading drop of S240 (0.1%) (aq) on a pp, pf and pcp substrate versus time. Region A is labelled in the above figure and shown below.

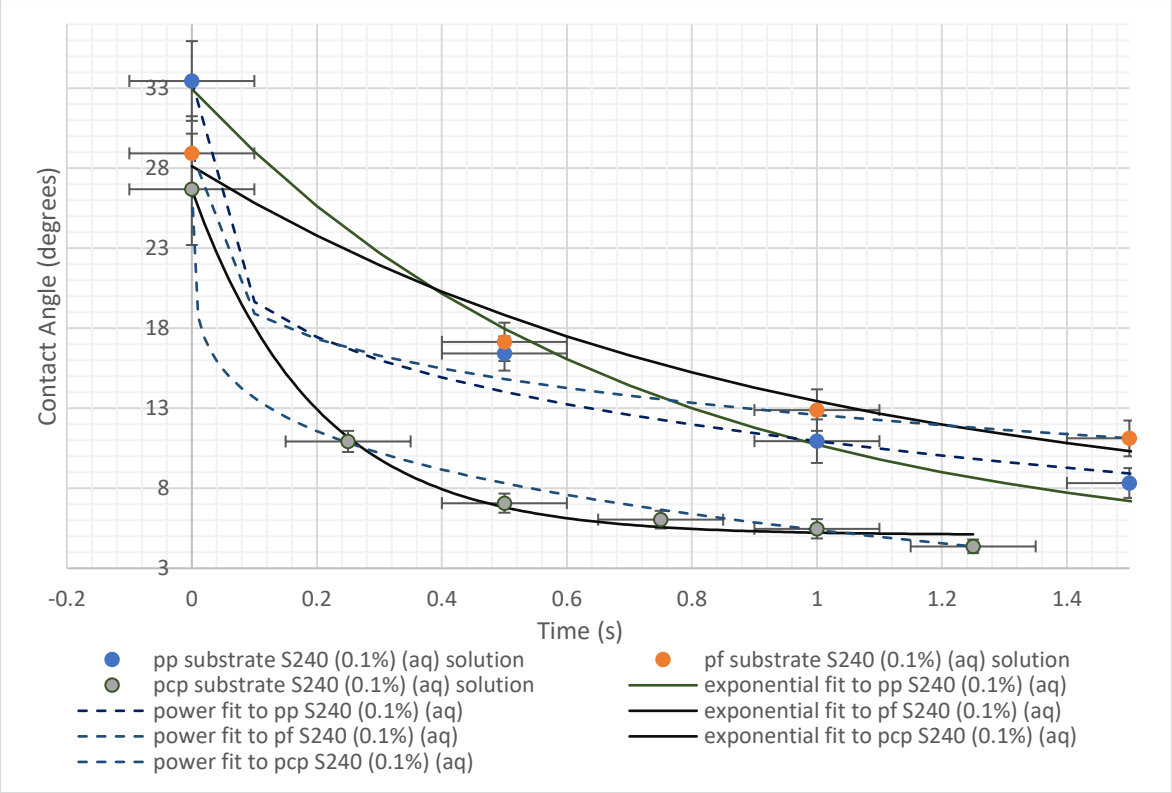

Figure 3.10 (ii): Region A.

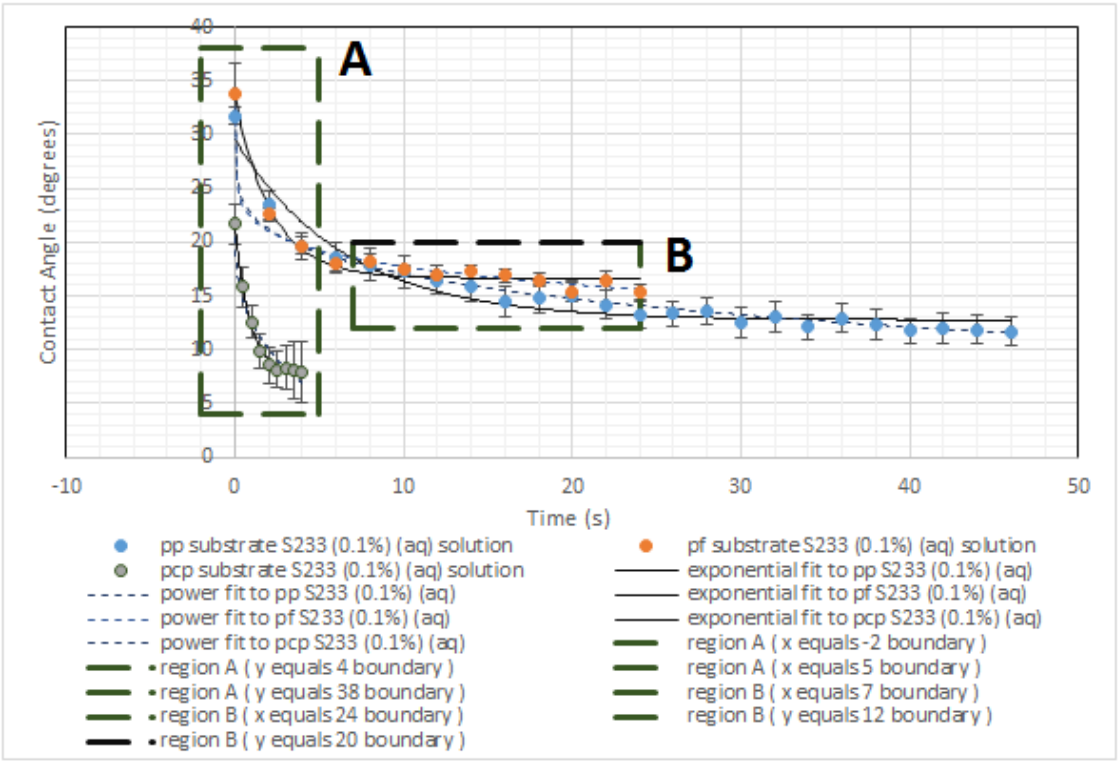

Figure 3.11 (i): Comparing the contact angle for a spreading drop of S233 (0.1%) (aq) on a pp, pf and pcp substrate versus time. Region A and B is labelled in the above figure and shown below.

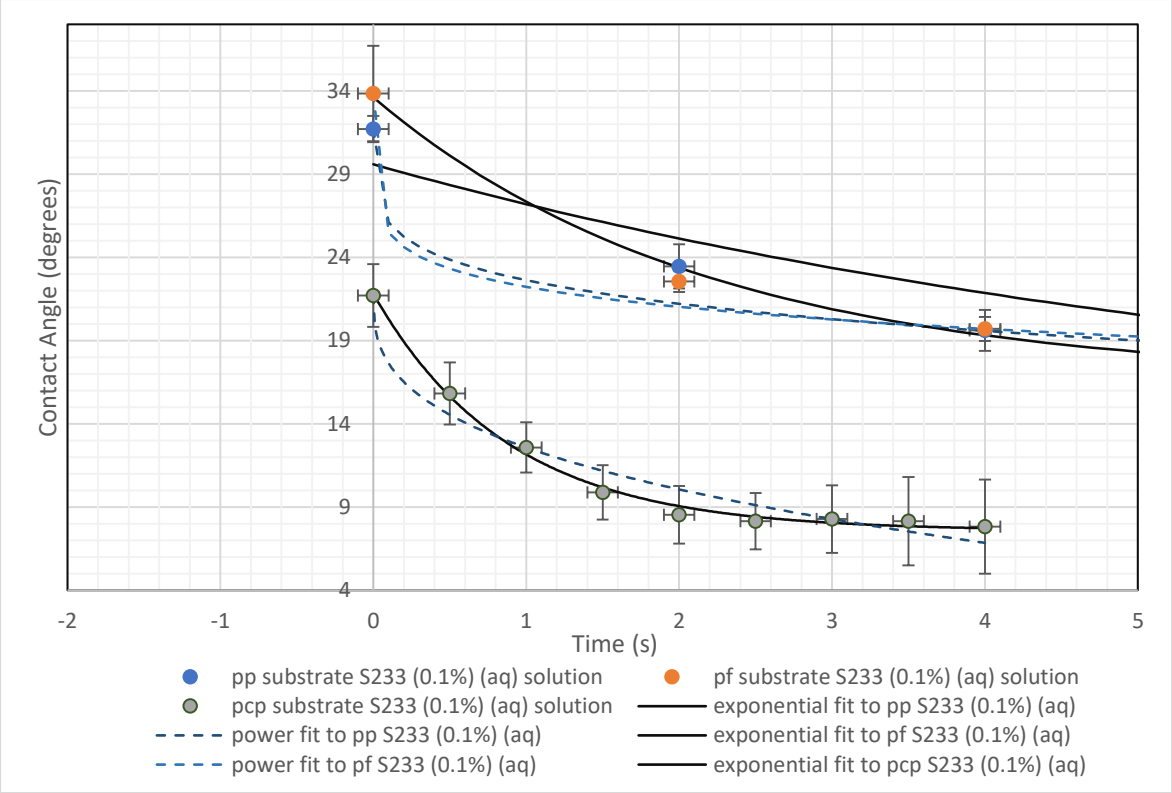

Figure 3.11 (ii): Region A

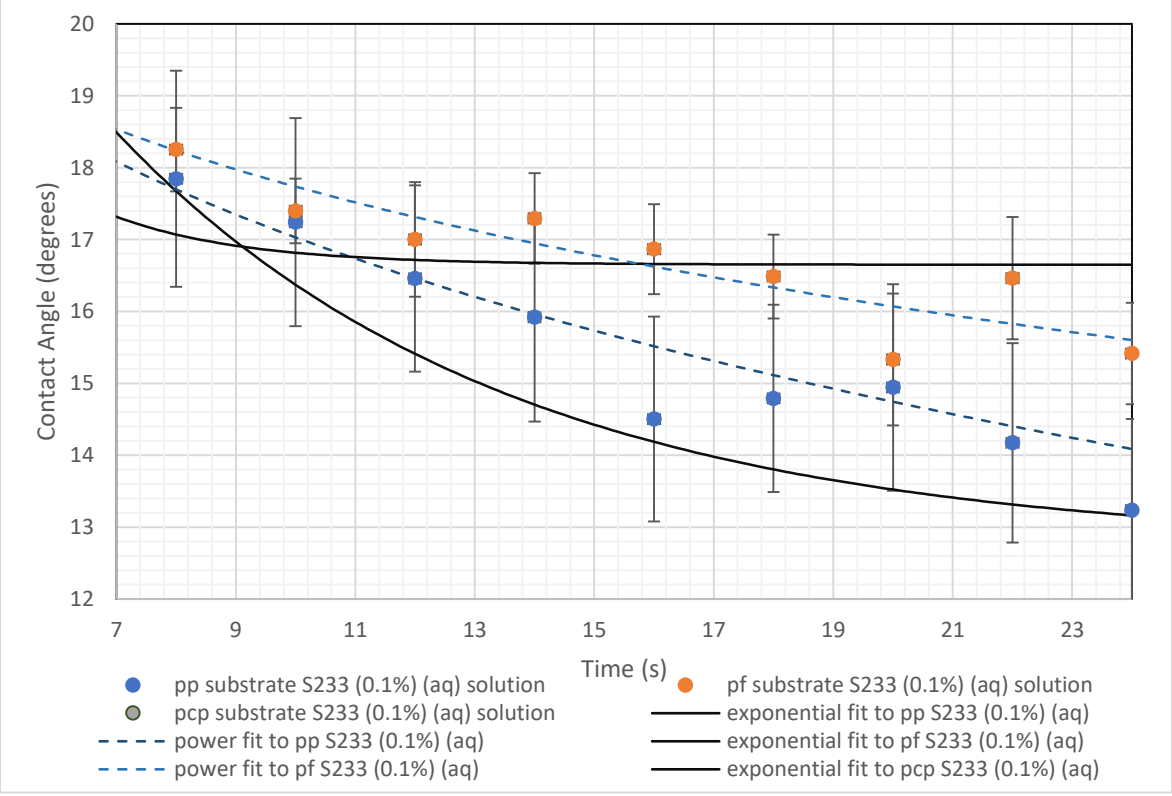

Figure 3.11 (iii): Region B.

the S233 (0.1%) (aq) drop spreading on a pcp substrate is comparable to the superspreading S240 (0.1%) (aq) drop spreading on a pp and pf substrates. A possible reason why the S240

(0.1%) (aq) and S233 (0.1%) (aq) drop spread so quickly on the pcp substrate is that the pcp had a plastic covering film which when removed prior to experiment may have charged up the pcp film electrostatically encouraging quicker spreading. It is well known that charging up a surface can increase spreading. Another interesting difference between the contact angle versus time data for the pcp compared to the pp and pf data is that the exponential function fits both the S240 (0.1%) (aq) and S233 (0.1%) (aq) data better then the power law function which is vice versa for the contact angle versus time data for the pp and pf substrates.

In figure 3.10 drops of S240 (0.1%) (aq) spread on pp, pf and pcp substrates. The pp data reaches the smallest final contact angle, (compared to pcp and pf), of 2 ½ degrees in 4.5 seconds. The pcp data and pf data reach a final contact angle of around 5 degrees in 1.25 and 6 seconds respectively. The time taken to reach the final contact angle is the shortest at 1.25 seconds for the pcp substrate, then 4.5 seconds for the pp, and 6 seconds for the pf substrate.

In figure 3.11 drops of S233 (0.1%) (aq) spread on pp, pf and pcp substrates. The pcp data reaches the smallest final contact angle of 8 degrees in the shortest time of 4 seconds. The pp data is the third quickest in terms of time taken to reach its final contact angle and second in terms of the size of final contact angle at 12 degrees in 46 seconds. The pf reaches a final contact angle of 15 ½ degrees in 20 seconds.

3.10: **Comparing the power law and exponential fits to the drop diameter versus time and drop contact angle versus time data in terms of which is superior and long and short term behaviour.**

The Young equation describes the relation between surface tensions and the contact angle of a spreading drop:

$$\gamma_{SG} - \gamma_{SL} - \gamma_{LG} \cos\theta_C = 0 \tag{1.2}$$

The Young LaPlace equation describes how the pressure difference across the fluid interface is related to the surface tension and curvature of the drop.

$$\Delta p = -\gamma \nabla \cdot \hat{n} = 2\gamma H = \gamma\left(\frac{1}{R_1} + \frac{1}{R_2}\right) = \frac{2\gamma\cos\theta}{a} \tag{3.8}$$

Where Δp is the pressure difference across the fluid interface, $\hat{n}$ is the unit normal pointing out of the surface, γ is the surface tension, H is the mean curvature, and R_1 and R_2 are the principle radii of curvature, a is the radius of the circular shape of the drop.

As a S240 (0.1%) (aq) or S233 (0.1%) (aq) drop spreads with time there are 3 main stages, the first stage being a rapid linear increase in drop diameter, the second a flattening out of the line of best fit curve, and the final third stage being a horizontal relation with the drop reaching its equilibrium size or completely wetting with zero degree contact angle. These stages are created by the driving force of the capillary force and resisted by the following factors; the friction at the triple phase contact line, the viscous dissipation within the drop and the inertia of the drop oppose the wetting process. In the first stage the driving force is much greater then the resistive forces hence a rapid increase with time for the drop diameter. In the second stage the resistive forces grow bigger as the time increases so the rate the drop diameter grows gets progressively less. In the third stage the resistive forces and the driving capillary forces reach equilibrium leading to no further increase in drop diameter. Also note that the drop diameter can only get so big as once the contact angle reaches zero the drop cannot physically get any bigger.

For the figure showing the drop diameter versus time data for the S240 (0.1%) (aq) and S233 (0.1%) (aq) on a pp substrate the exponential function for the S233 data misses the first 4 data points while the power law function passes through them all. For the S240 data both the exponential function and power law function miss the first 4 points (i.e. outside the error bars). The R-square for the power law functions fits for the S240 (0.1%) (aq) data and S233 (0.1%) (aq) data are 0.9905 and 0.99886. The R-square for the exponential function for the fits for the S240 (0.1%) (aq) data and S233 (0.1%) (aq) data are 0.9859 and 0.9285. The value of R square is significantly lower for the exponential function for the S233 (0.1%) (aq) data then the other fits, with only 92.85% of the fit explaining the total variation in the data about the average. The adjusted R square for the power law functions fits for the S240 (0.1%) (aq) data and S233 (0.1%) (aq) data are 0.9886 and 0.9987 indicating a good and almost identical quality of fit. While for the the adjusted R-square for the exponential function for the fits to the S240 (0.1%) (aq) data and S233 (0.1%) (aq) data are 0.983 and 0.9217. It is clear that the best fit for the S233 data is the power law function for short term behaviour, while the fit to the S240 (0.1%) data for short term behaviour is very similar but slightly better for the exponential function. The long term behaviour of the exponential and power law functions correlates better between fitting function and data points with the fits being very similar in terms of fitting quality. The

exponential and power law function fits vary for short term behaviour for S240 (0.1%) (aq) and S233 (0.1%) (aq) on a pp substrate but the long term behaviour is very similar as the curves in the line of best fit flatten out. Overall the power law function fits the S240 (0.1%) (aq) and S233 (0.1%) (aq) data better then the exponential function for a pp substrate.

For the figure showing the enlarged region A from the graph of S240 (0.1%) (aq) and S233 (0.1%) (aq) drops on a pf substrate, it is clear the power law function fits both curves the best for short term behaviour. However the exponential function fits the data reasonably well also only missing the range of the error bars of one data point (at 0.5s).

Sol (aq)	Substrate	Type of fit	R-square	Adj R square
S240 (0.1%)	pp	power	0.9905	0.9886
S240 (0.1%)	pp	exponential	0.9859	0.983
S233 (0.1%)	pp	power	0.9988	0.9987
S233 (0.1%)	pp	exponential	0.9285	0.9217
S240 (0.1%)	pf	power	0.9948	0.9938
S240 (0.1%)	pf	exponential	0.9798	0.9758
S233 (0.1%)	pf	power	0.9906	0.9887
S233 (0.1%)	pf	exponential	0.9815	0.9778
S240 (0.1%)	pcp	power	0.9909	0.9864
S240 (0.1%)	pcp	exponential	0.9991	0.9987
S233 (0.1%)	pcp	power	0.9875	0.9852
S233 (0.1%)	pcp	exponential	0.9892	0.9872

Table 3.6: showing the R-square and adjusted R-square for power and exponential function fits to the drop diameter versus time data from S240 (0.1%) (aq) or S233 (0.1%) (aq) drop experiments on a pp, pf and pcp substrate.

For the long term behaviour of the two curves the S240 (0.1%) (aq) curve reaches its final size more rapidly then the S233 (0.1%) (aq) data at 6 s. In terms of the quality of the fits the

power law fit to the S240 (0.1%) (aq) and S233 (0.1%) (aq) data has an R square of 0.9948 and 0.9906, with an adjusted R-square of 0.9938 and 0.9887 respectively. The quality of the exponential fits on the other hand are of lower quality with the R square of the S240 (0.1%) (aq) and S233 (0.1%) (aq) data being 0.9798 and 0.9815, with an adjusted R-square of 0.9758 and 0.9778. For the power law function fit to the S240 (0.1%) (aq) and S233 (0.1%)

(aq) data on a pf substrate it fits the data marginally better then the exponential function fit with better correlation between points and the fitted function line.

For the figure showing the enlarged region A of the graph of an S240 (0.1%) (aq) and S233 (0.1%) (aq) drop spreading on a pcp substrate visually the S240 (0.1%) (aq) data is fitted slightly better by the power law function then the exponential one. Both the power function and exponential function do not fit the S233 (0.1%) (aq) data to the same degree of quality as the S240 (0.1%) (aq) data, with both functions not going through the data point at 0.5s. This is seen for the power function fits in the R-square of the S240 (0.1%) (aq) data at 0.9909 and an R-square of the S233 (0.1%) (aq) data at 0.9875. With an adjusted R-square of 0.9864 for the S240 (0.1%) (aq) data and a adjusted R-square of 0.9852 for the S233 (0.1%) (aq) data. The exponential function fits to the same data yields an R-square of 0.9991 and adjusted R-square of 0.9987 for the S240 (0.1%) (aq) data. The exponential fit to the S233 (0.1%) (aq) data has an R-square of 0.9892 and a adjusted R-square of 0.9872. For the pcp substrate the power law function is very marginally surpassed by the exponential function when fitting the S240 (0.1%) (aq) and S233 (0.1%) (aq) data. However this very slight difference is not significant enough to say that the exponential function fits the data better then the power law function. Instead the exponential function and power law function are considered equally as good at fitting the S240 (0.1%) (aq) and S233 (0.1%) (aq) data on a pcp substrate.

For the figure showing the expanded region A for the graph showing the contact angle versus time data for the S240 (0.1%) (aq) and S233 (0.1%) (aq) drop on a pp substrate, it is clear for the S240 data that the power fit is superior to the exponential fit. Visually this can be seen in the way the exponential fit flattens of starting at around 2 seconds. However mathematically both the power and exponential fits have almost identical R squares (0.9899 for power fit to S240 (0.1%) (aq) data, 0.9903 for exponential fit to S240 (0.1%) (aq)) meaning both graphs explain around 99% total variation in the data about the average. The adjusted R square for both the power and exponential fits are very similar at around 0.99. This contradiction might

be just that the points which do not correlate well to the exponential function might have their distance from the exponential function exaggerated by zooming in so closely.

Looking at the figure for the S233 (0.1%) (aq) on a pp substrate the power and exponential functions fitting the data do not behave well for short term behaviour between 0 and 6 seconds. The power function fit only misses 1 data point at 2 seconds, while the exponential function fit misses data points at 2 and 4 seconds. Looking at the long term behaviour after 10 seconds the power fit appears to more closely match the data then the exponential fit.

Table 3.7: showing the R-square and adjusted R-square for power and exponential function fits to the contact angle versus time data from S240 (0.1%) (aq) or S233 (0.1%) (aq) drop experiments on a pp, pf and pcp substrate

Sol (aq)	Substrate	Type of fit	R-square	Adj R square
S240 (0.1%)	pp	power	0.9899	0.987
S240 (0.1%)	pp	exponential	0.9903	0.9875
S233 (0.1%)	pp	power	0.9958	0.9954
S233 (0.1%)	pp	exponential	0.9467	0.9417
S240 (0.1%)	pf	power	0.9925	0.9912
S240 (0.1%)	pf	exponential	0.9843	0.9817
S233 (0.1%)	pf	power	0.9846	0.9815
S233 (0.1%)	pf	exponential	0.9772	0.9727
S240 (0.1%)	pcp	power	0.9944	0.9907
S240 (0.1%)	pcp	exponential	0.9972	0.9954
S233 (0.1%)	pcp	power	0.9564	0.9419
S233 (0.1%)	pcp	exponential	0.9956	0.9942

.

Statistically the previous comments are backed up by the adjusted R-squares with the better power fit being closer then the exponential function to a value of 1 at 0.9954 compared with 0.9417. The R square for the exponential fit to the S233 (0.1%) (aq) data also shows a low total variation in the data about the average with a value of 94.67%.

For the figure showing the fits to the contact angle versus time graphs for a S240 (0.1%) (aq) drop spreading on a pf substrate the power fit visually fits the data better then the exponential function fit. The exponential fit flattens of to quickly at 3 seconds and misses the error range of the points at 0.5, 6 and 6.5 seconds, while the power function goes through all data points except the one at 0.5 seconds. The power function is a higher quality fit then the exponential

function with an adjusted R-square nearer to 1 at 0.9912 compared with 0.9817. The power function also explains 99.25% of the total variation in the data about the average compared to 98.43% for the exponential fit.

For the contact angle versus time graphs for a the S233 (0.1%) (aq) drop spreading on a pf substrate the power fit does not correlate well with data points for short term behaviour with it completely missing the point at 2 seconds. The longer term behaviour for the power function when fitting the S233 (0.1%) (aq) data is much better then the short term behaviour with most points fairly close to the power function fit. For the exponential function fit the short term fitting behaviour is of high quality and is much better then the power function. At longer term behaviour the exponential fit misses the error range of the data points at 6, 20 and 24 seconds. Mathematically the poor quality of the short term behaviour for the power function between 0 and 2 seconds does not seem to significantly affect the quality of the fit with an adjusted R square of 0.9815. Surprisingly the exponential function fit has a lower adjusted R square of 0.9727 meaning the quality of the power fit is superior to the exponential fit. The power fit explains a greater amount of the total variation in the data about the average at 98.46% compared with the exponential function at 97.72%.

Looking at the figure showing the contact angle versus time data for a S240 (0.1%) (aq) and S233 (0.1%) (aq) drop spreading on a pcp substrate, visually the power and exponential function fits to the S240 (0.1%) (aq), and S233 (0.1%) (aq) data are both of high quality. In terms of the short term behaviour the power function for the S240 (0.1%) (aq) data does not go through the error range of the points at 0.5 seconds. The exponential function for the S240 (0.1%) (aq) data has a point at 1.26 s which is narrowly outside the exponential function. In terms of the long and short term behaviour for the S233 (0.1%) (aq) data the exponential

function visually fits the data better then the power law function. Looking at the S240 (0.1%) (aq) data the exponential function fits the data marginally better then the power law with the exponential function not passing through 1 data point's error range compared with 2 point's error range for the power function.

Statistically the adjusted R square is closer to 1 for the exponential function fit for the S240 (0.1%) (aq) data on a pcp substrate at 0.9954 then the power function fit to the same data at 0.9907. This means the exponential fit has higher accuracy. For the exponential function fit the R square was 99.72% meaning that 99.72% of the fit explains the total variation in the data about the average, this is compared with the power function fit which has an R square of 99.44%. Looking at the S233 (0.1%) (aq) data on a pcp substrate the adjusted R square suggests that the exponential fit is far more accurate then the power law function with values of 0.9942 compared with 0.9419. The R square explains 99.56% for the exponential function fit of the total variation in the data about the average, compared with 95.64% for the power function fit.

Summary of comparison of exponential and power function fits to S240 (0.1%) (aq) and S233 (0.1%) (aq) data for drop diameter versus time and contact angle versus time for pp, pf and pcp substrates

Solution (aq)	Substrate	Most accurate fit	difference Adj R square	Marginal/significent
S240 (0.1%)	pp	power	0.0056	marginal
S233 (0.1%)	pp	power	0.077	significant
S240 (0.1%)	pf	power	0.018	significant
S233 (0.1%)	pf	power	0.0109	significant
S240 (0.1%)	pcp	exponential	0.0123	significant
S233 (0.1%)	pcp	exponential	0.002	marginal

Table 3.8: comparing the accuracy of drop diameter versus time fits to S240 (0.1%) (aq) and S233 (0.1%) (aq) spreading drops on pp, pf and pcp substrates when using power and exponential functions

In the table, the most accurate fit is considered to be the one with the closest Adjusted R-square to a value of 1. The difference in the adjusted R square value is simple the largest adjusted R square minus the smaller adjusted R square. I have based the significance of the difference of the two fits on the magnitude of the difference between the two adjusted R squares.With the exception of the pcp substrate, power functions fitted the drop diameter versus time data better

than the exponential functions. Even the S233 (0.1%) (aq) data was only marginally better fitted by an exponential function then a power function

Solution (aq)	Substrate	Most accurate fit	difference Adj R square	Marginal/significent
S240 (0.1%)	pp	exponential	0.0005	marginal
S233 (0.1%)	pp	power	0.0537	significant
S240 (0.1%)	pf	power	0.0095	significant
S233 (0.1%)	pf	power	0.0088	significant
S240 (0.1%)	pcp	exponential	0.0047	marginal
S233 (0.1%)	pcp	exponential	0.0523	significant

Table 3.9: comparing the accuracy of contact angle versus time fits to S240 (0.1%) (aq) and S233 (0.1%) (aq) spreading drops on pp, pf and pcp substrates when using power and exponential functions

For the contact angle versus time graphs most fits were better fitted by exponential functions then power law functions, only the pf substrate was better fitted by a power function.

3.11: Literature on log drop radius versus log time for a spreading trisiloxane surfactant on a hydrophilic substrate.

In their work (32), a thin layer of water of thickness 0.32 mm was deposited evenly across the surface of a Petri dish and a high precision 5 µl Hamilton syringe was used to inject 1.5 or 3 µl droplets of surfactant onto this layer. Talcum powder was used to trace the motion of the liquid front under the influence of the surfactants, and the time evolution of the radius of this spreading front R(t) was monitored, then plotted on a log-log scale axis.In all the work in (32) it was found that the spreading process can separated into two stages, a rapid first stage and a second slower stage.In Figure 3.12 the highly soluble trisiloxane T9 has the highest spreading exponent and the lowest soliuble trisiloxane T_3 has the lowest spreading exponent.

Trisiloxane	Molecular weight g/mol	spreading exponent	
		1st stage	2nd stage
T_3	426.86	0.44 +/- 0.03	0.11 +/- 0.01
T_4	470.92	0.52 +/- 0.01	0.12 +/- 0.02
T_5	514.98	0.53 +/- 0.01	0.10 +/- 0.01
T_6	559.04	0.63 +/- 0.02	0.12 +/- 0.01
T_7	603.1	0.73 +/- 0.05	0.20 +/- 0.01
T_8	647.16	0.76 +/- 0.02	0.12 +/- 0.01
T_9	691.22	0.80 +/- 0.01	0.13 +/- 0.01

Table 3.10: First and Second stage exponents for trisiloxanes taken from (32)

A selection of non superspreading poly(ethylene glycol) monododecyl ether surfactants with 4, 5 and 6 ethoxylate groups at concentrations 20 times the CMC and are shown in figure 3.13 and table 2.

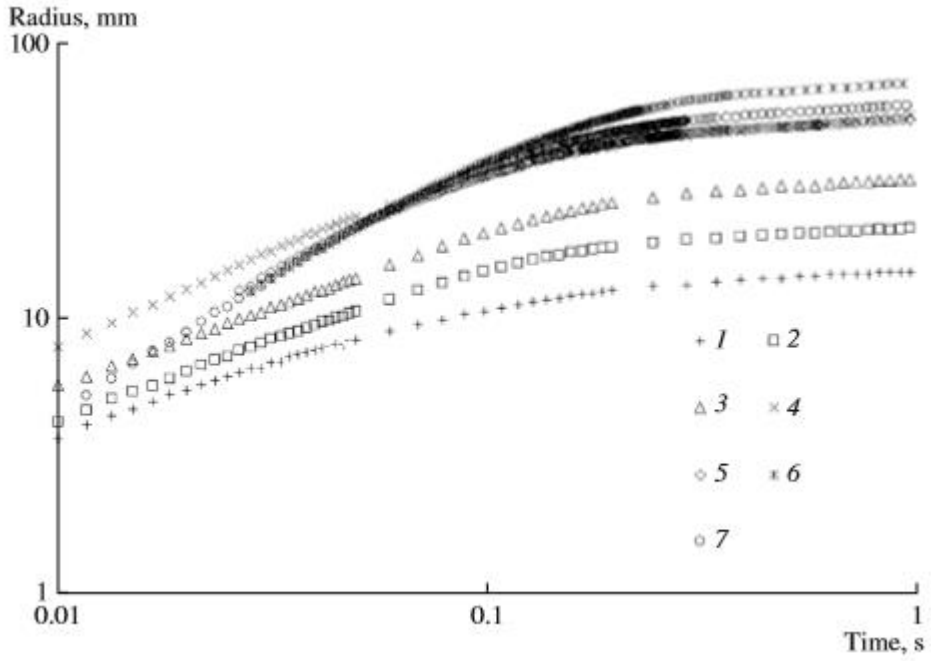

Figure 3.12: Log-log plots of spreading front against time for seven different trisiloxanes: (1) T_3, (2) T_4, (3) T_5, (4) T_6, (5) T_7, (6) T_8 and (7) T_9

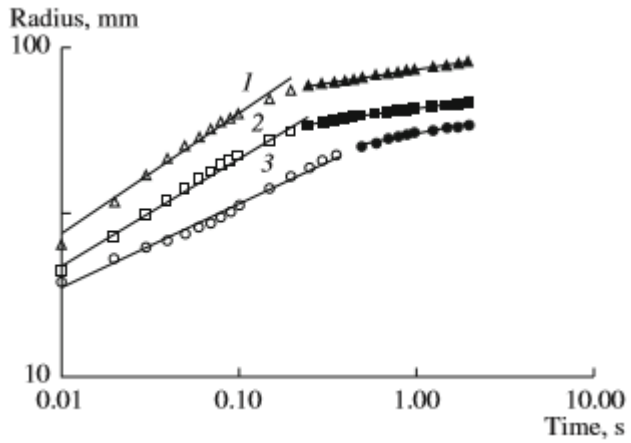

Figure 3.13: Log-log plots of spreading front against time for poly(ethylene glycol) monododecyl ether surfactants (1) $C_{12}E_6$ (2) $C_{12}E_5$ and (3) $C_{12}E_4$ taken from (32)

Surfactant	Molecular weight g/mol	CMC mM	spreading exponent	
			1st stage	2nd stage
$C_{12}E_4$	362.55	0.05	0.51 +/- 0.01	0.21 +/- 0.01
$C_{12}E_5$	406.61	0.085	0.65 +/- 0.01	0.15 +/- 0.01
$C_{12}E_6$	450.66	0.087	0.72 +/- 0.02	0.16 +/- 0.02

Table 3.11: Properties of poly(ethylene glycol) monododecyl ether surfactants. (32)

Both the trisiloxane and ethylene glycol monododecyl ether surfactants have a similar relation where the 1st stage spreading rates increase as the solubility increases. But the solubility appears to have no effect on the 2nd stage spreading rate with the exception of T_7 or $C_{12}E_4$. In (32) it is assumed the bulk properties of surfactants effect the size of the surface tension gradient driving force. For trisiloxane surfactants self assembly processes at specific temperatures and concentrations were found at temperatures and concentrations where superspreading occurred. Theoretical models were constructed on the premise that micelles disintegrate providing a continuous supply of surfactants to the contact line allowing spontaneous spreading. It follows that different types of aggregates might be important in effecting surfactant transfer to the edge.

3.12: Drop diameter on a log scale versus time on a log scale showing data and graphs for superspreading Evonik S240 (0.1%) (aq), and the chemically similar non-superspreading S233 (0.1%) (aq) on pp, pf and pcp substrates.

The drop diameter versus time data was plotted on a log scale adopting the approach of (32) and (33) who investigated the spreading of trisiloxane surfactants on thin aqueous layers. Although this work is looking at solid substrates not an aqueous layer there is no reason why the data in this work can not be looked at with a different scale to see if it reveals anything about the superspreading mechanism. In fact this scale of plot gives clear evidence for some systems that the spreading has two clear stages which are not apparent in the earlier non log plots.

In table D2 the log drop diameter versus log drop diameter fits are presented with the SSE providing an idea of the quality of fit in Excel.

All the fits have small sum squared errors or SSE (the sum of the residuals squared) indicating a good correlation between fit and data. A simple power law was used to fit the data shown in equation 3.4.

In figure 3.14 both the S240 (0.1%) (aq) and S233 (0.1%) (aq) have a 2 stage spreading mechanism, with the first stage being more rapid then the second. For the S240 (0.1%) (aq) the boundary between these two stages is 4 seconds and for the S233 (0.1%) (aq) it is 38 seconds.

In figure 3.15 the S240 (0.1%) (aq) drop spreading on a pf substrate has only one stage of spreading while the S233 (0.1%) (aq) has two very similar stages of spreading (in terms of gradient). However the 2nd stage of spreading for the S233 (0.1%) (aq) is different if only very subtly. The boundary between stages 1 and 2 for the S233 (0.1%) (aq) on pf was 12s.

In figure 3.16 the S240 (0.1%) (aq) spreading on the pcp substrate had only 1 stage of spreading, while the S233 (0.1%) (aq) had 2 very similar but separate stages. The boundary of these stages being 5s.

Sol (aq)	Substrate	region	a	b	c	SSE
S240 (0.1%)	pp	1	1.419	0.433	3.722	3.12E-05
S240 (0.1%)	pp	2	0.592	0.278	5.504	6.81E-06
S233 (0.1%)	pp	1	0.503	0.319	3.739	2.60E-05
S233 (0.1%)	pp	2	0.792	0.158	3.963	9.54E-08
S240 (0.1%)	pf	1	5.368	0.124	0	7.74E-05
S233 (0.1%)	pf	1	4.216	0.045	0	3.22E-06
S233 (0.1%)	pf	2	0.442	0.176	4.022	4.29E-06
S240 (0.1%)	pcp	1	6.651	0.197	0	1.33E-04
S233 (0.1%)	pcp	1	4.95	0.144	0	1.56E-04
S233 (0.1%)	pcp	2	1.849	0.141	3.934	4.39E-06

Table 3.12: Simple power law fits in Excel using the SOLVER for log time versus log drop diameter for the superspreading Evonik S240 (0.1%) (aq) and chemically similar Evonik S233 (0.1%) (aq) on a pp, pf and pcp substrate

Interestingly in figure 3.17 it is clear that only the pp substrate has 2 stages of spreading with the pf and pcp having only 1 clear stage of spreading. In figure 3.18 the spreading of the S233 (0.1%) (aq) drop on pp, pf and pcp substrates all have 2 stages to the spreading. With the final

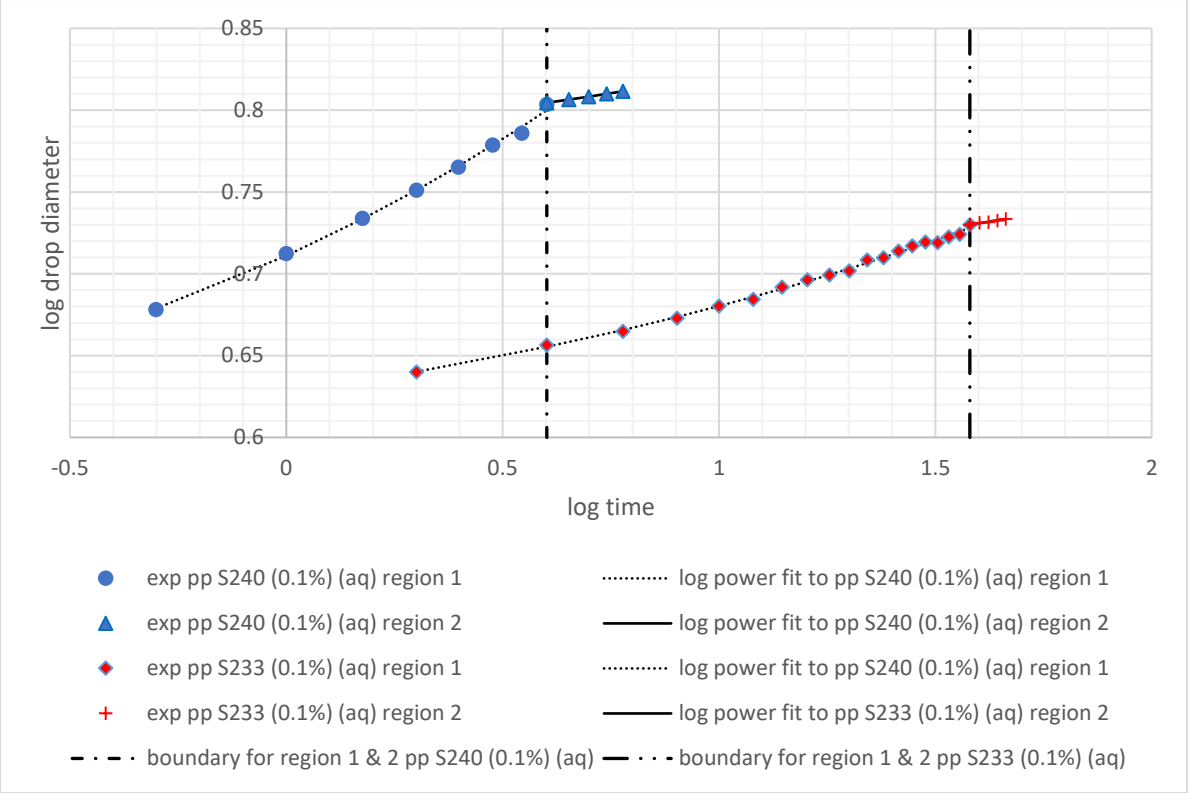

Figure 3.14: Log time versus log drop diameter for the superspreading Evonik S240 (0.1%) (aq) and chemically similar Evonik S233 (0.1%) (aq) on a pp substrate.

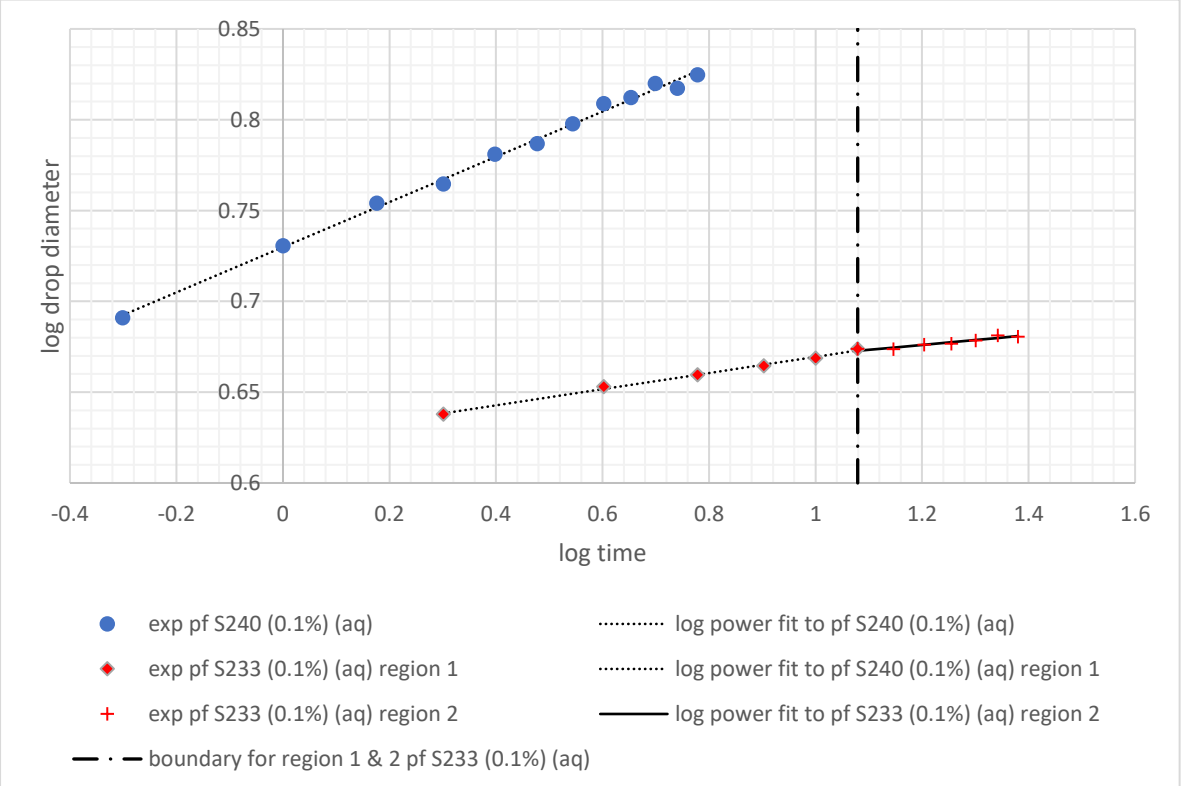

Figure 3.15: Log time versus log drop diameter for the superspreading Evonik S240 (0.1%) (aq) and chemically similar Evonik S233 (0.1%) (aq) on a pf substrate.

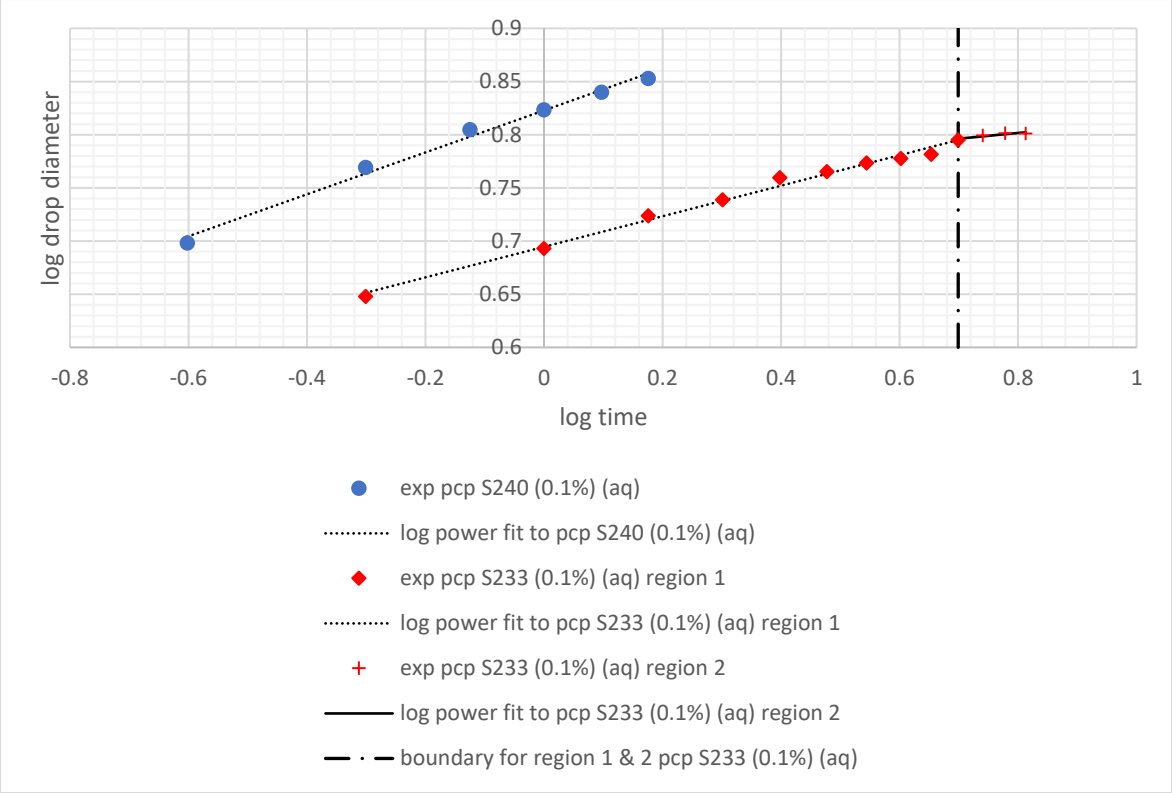

Figure 3.16: Log time versus log drop diameter for the superspreading Evonik S240 (0.1%) (aq) and chemically similar Evonik S233 (0.1%) (aq) on a pcp substrate.

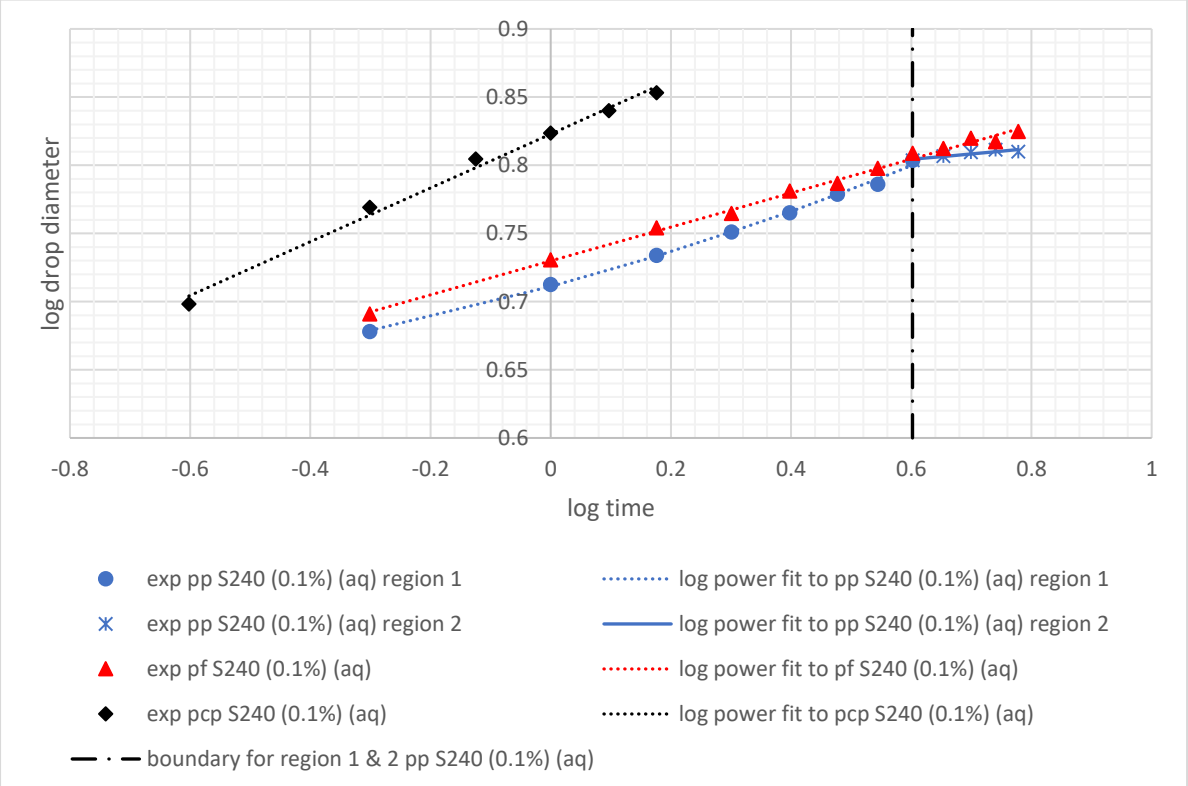

Figure 3.17: Log time versus log drop diameter for the superspreading Evonik S240 (0.1%) (aq) on a pp, pf and pcp substrate

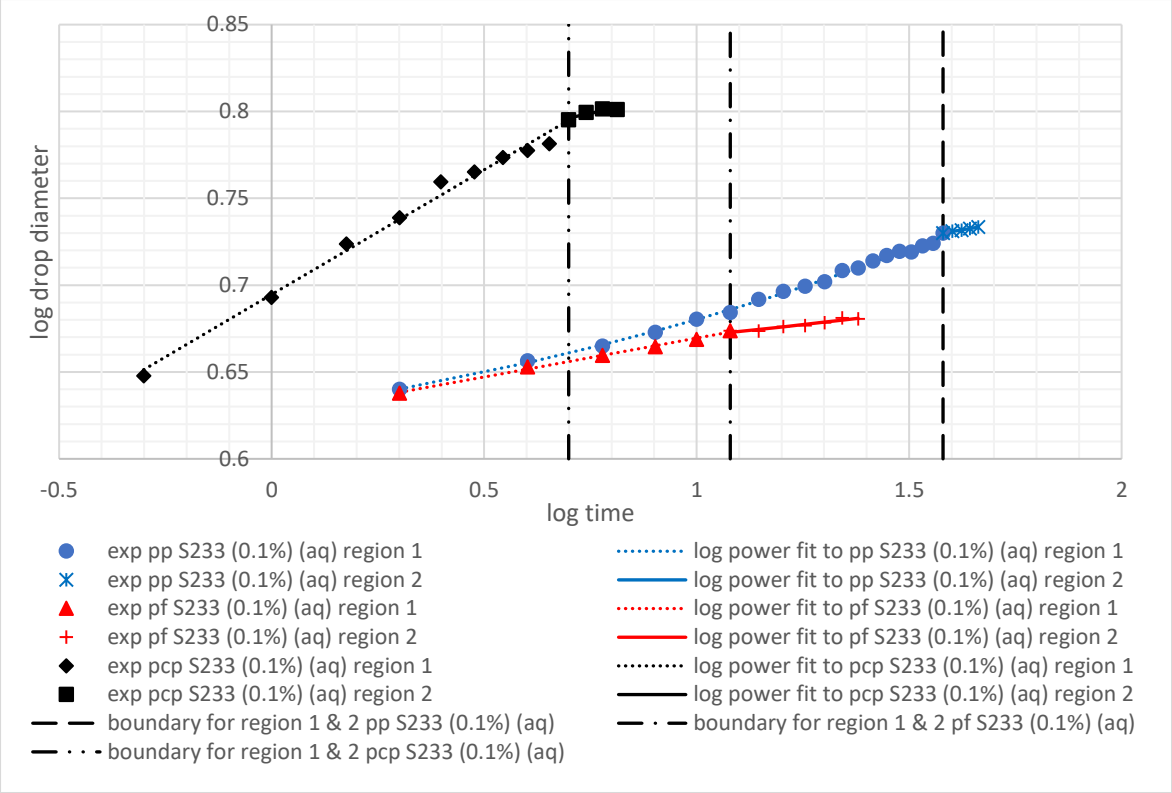

Figure 3.18: Log time versus log drop diameter for the superspreading Evonik S233 (0.1%) (aq) on a pp, pf and pcp substrate.

stage for the spreading being short in duration for the pp and pcp substrates and longer for the pf substrate.

3.13: Discussion

The drop of S240 (0.1%) (aq) and S233 (0.1%) (aq) drop on pp both exhibit 2 regimes when the diameter and time are plotted with log axis. The S233 (0.1%) (aq) drop on pf and pcp has two regimes when the diameter and time axis are plotted with a log scale. The S240 (0.1%) (aq) drop on pf and pcp both have 1 regime when the diameter and time are plotted on log scales.

The two regimes could be caused by the increasing surface area of the drop as it spreads causing a dilution of the number of surfactant molecules per unit surface area which affects the surface tension. At some point there may be no more molecules available in the bulk. Below is Young' s equation which clearly shows the Young-Laplace force is affected by the surface tension of the liquid (γ_{LG}).

$$F = \gamma_S - \gamma_{SL} - \gamma_L \cos\theta \qquad (1.2)$$

Micelles can form in the bulk of a surfactant solution when the free surface of the liquid is saturated with surfactant molecules (i.e. there is an excess of surfactant molecules that cannot go to the surface because there is no space for them). If the free surface increases (e.g. because of spreading), then there is more free space available; then some molecules belonging to micelles in the bulk may leave the micelle and migrate to the free surface. If there are a lot of molecules migrating to the surface, this may decompose several micelles.

The friction at the triple phase contact line, the viscous dissipation within the drop and the inertia of the drop oppose the wetting process.

$$\Delta p = -\gamma \nabla \cdot \hat{n} = 2\gamma H = \gamma\left(\frac{1}{R_1} + \frac{1}{R_2}\right) = \frac{2\gamma \cos\theta}{a} \tag{3.8}$$

In Laplace's equation it is clear the surface tension affects the pressure difference across the fluid interface which could cause the 2 regimes in some log diameter, log time graphs.

Where for Laplace's equation Δp is the pressure difference across the fluid interface, $\hat{n}$ is the unit normal pointing out of the surface, γ is the surface tension, H is the mean curvature, and R_1 and R_2 are the princilple radii of curvature, a is the radius of the circular shape of the drop.

Chapter 4: Microscopic analysis of the drop/substrate interface using Reflection Anisotropy Spectroscopy (RAS) and Atomic Force Microscopy (AFM).

4.1: Aims and objectives of chapter 4.

This chapter with the exception of the "dipping" experiment (4.7.3), looks at the area on the substrate where the evaporated drop's of S240 (0.1%) (aq), S233 (0.1%) (aq) and water's contact line was. It is thought in the superspreading community that micelle structures in superspreading solutions assemble at the contact line and aid the superspreading of these solutions over the substrate. It is thought that by looking for evidence of these structures at the evaporated contact line might reveal how the superspreading phenomenon occurs. This work will use Reflection Anisotropy Spectroscopy (RAS) to look for the evaporated micelle structures where the contact line was. RAS produces a non zero spectra when it detects anisotropic structures and zero signal when detecting isotropic structures. It is thought that the evaporated drop's micelles structures if still adsorbed into the substrate where the contact line was will be aligned in favoured directions hence producing a non zero RAS signal. This is while at the centre of the evaporated drop any signal should be zero as there should be no specially aligned micelles there, any structures from the bulk should not favour any one direction and should therefore have zero RAS signal. Figure 4.1 shows a graphical representation of this hypothesis.

As well as using RAS the work in this chapter also utilises Atomic Force Microscopy (AFM) to image any micelles that may be present on the polymer substrates after drop evaporation.

When looking for micelle structures adsorbed into the substrate where the contact line was there are 4 main outcomes that could occur:

1. The micellae are/are not adsorbed.
2. The micellae do/do not survive drying.
3. The micellae are/are not detectable
4. The likelihood of not finding them is low/high.

The last 3 outcomes are discussed later in the chapter while the first outcome was assumed to be positive, i.e. micellae are adsorbed at the contact line, and experiments were carried out on this basis.

4.2: Hypothesis.

It is expected that the Evonik S240 (0.1%) (aq), after evaporation, will leave micelle structures where the contact line was and none at the centre of the evaporated drop where the bulk was. The next stage of the investigation will look at the non superspreading (but chemically similar) Evonik S233 (0.1%) (aq). Since the S233 does not superspread, it might be expected that no micellae structures were assembled then left adsorbed at the evaporated contact line. But this may be an over simplification of the situation, some structures may form just not to the same degree as the S240 (0.1%) (aq) superspreading solution. However, it would be expected no RAS signal would pick up any anisotropic structures in the centre of the evaporated drop of S233 (0.1%) (aq) where the bulk was.

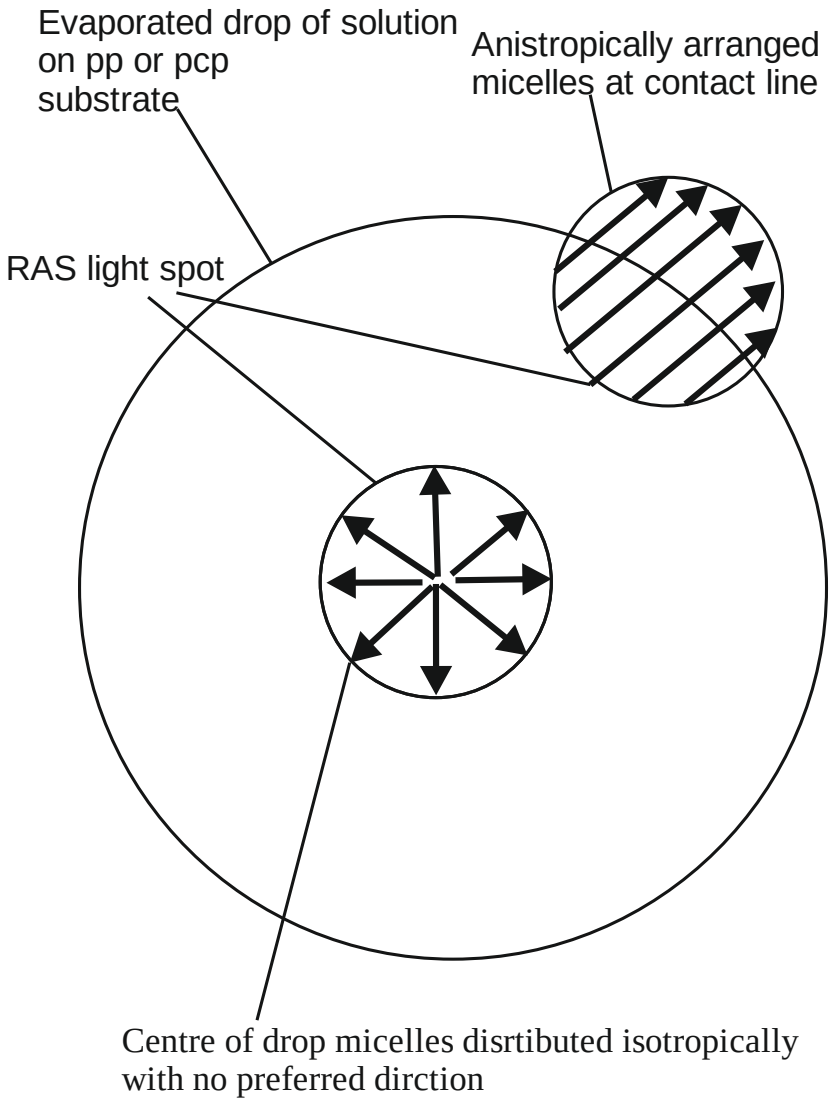

Figure 4.1: Simplified diagram of the hypothesis that the RAS signal for the evaporated drop of the superspreader solution S240 (0.1%) (aq) on a pp or pcp substrate is not the same in the centre and edge region of the evaporated drop because the adsorbed micelle orientation is different in these regions.

4.3: Background theory to the Reflection Anisotropy Spectrosopy (RAS) technique.

The RAS technique uses reflected light to yield data on the anisotropy of a surface. It is a linear optical probe which is non-destructive with visible light being used. RAS first emerged in the 1980s as a way of investigating semiconductors and has applications in electrochemistry, molecular assembly, liquid crystal device fabrication and remote stress sensing. The RAS technique can be used in ambient, high pressure and liquid environments. RAS has the advantage of being able to monitor macroscopic areas with a good rapid response.

RAS is a linear optical technique working at normal or near normal incidence. When measuring the RA light careful consideration is given to taking the measurements at or within 5 degrees of the surface normal. Within this range s and p-polarisations of the light upon reflection from the surface are equal, this makes the RA spectrometer surface sensitive.

However understanding RAS theoretically from first principles is extremely difficult and involves the complex dielectric function of both the surface region and the bulk. But an advantage of RAS is that as long as the environment is an optically transparent medium then any environment can be used – including accessing surfaces under liquids.

To perform the measurement polarized light at normal or near normal incidence is shone onto the sample surface (see figure 4.2). The light is shone such that the direction of the incident plane of polarization as at 45 degrees to the x and y axis, enabling both axes to be evenly illuminated by the incident radiation. If the structures of the surface along the x and y direction are different the Fresnel reflection coefficents along the two directions will also be different. As a result the x and y components of the polarization vector of the reflected light are also unequal. This makes the reflected light elliptically polarized. In RAS the x and y component of the polarization vector of the reflected light is Fourier analysed. Samples with zero anisotropy on the surface reflect linearly polarized light.

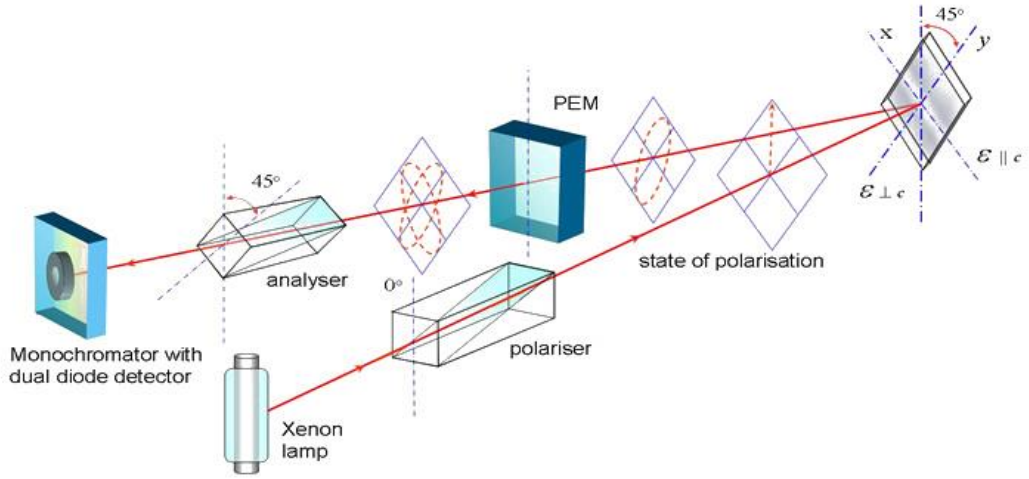

Figure 4.2: Schematic layout of RAS Setup (38)

The photoelastic modulator or PEM has optical properties which enable it to modulate the plane of polarization of transmitted light. The PEM affects the phase of light passing through the instrument. The PEM is classed as a dynamic wave plate, were a wave plate is an optical device that changes the polarization state of a light wave passing through it. Wave plates are made from birefringent material (such as quartz), for which the index of refraction is different for different orientations of light passing through it. As the light passes through the PEM one linear polarization perpendicular to the modulation axis is unaffected by the PEM but light polarized along the modulation axis undergoes a retardation in different directions causing a modulation in the polarization of the light.

Using an analyser prism the signal can be transformed into an intensity modulated waveform. Only elliptically polarized light is affected by this modulation while linearly polarized light goes along either the fast or slow axis of the PEM. Modulation extracts the harmonics that carry the real and imaginary data allowing a good analysis.

Definition of RAS:

"RAS measures the difference in reflectance (Δr) of normal incidence plane-polarised light between two orthogonal directions in the surface plane (x, y) normalized to the mean reflectance (r)". (39)

$$\frac{\Delta r}{r} = \frac{r_x - r_y}{\left[\frac{r_x + r_y}{2}\right]} = \frac{2(r_x - r_y)}{r_x + r_y} \tag{4.1}$$

Where $\Delta r / r$ is the measured complex reflectance anisotropy and r_x and r_y are the complex Fresnel reflection coefficents in the x and y directions of the surface plane.

4.4: Background theory to the Atomic Force Microscopy (AFM) technique.

In the AFM setup shown in figure 4.3 from (40) a sharp tip is in close proximity to the surface, there is a force between them. The tip is scanned across the surface; the deflection is monitored by a reflected laser beam which is detected by an array of photodiodes. The AFM is said to act like a record player.

The probe is fixed at the apex of a flexible Si or Si_3N_4 cantilever. Either the sample surface or cantilever is mounted on a piezocrystal. This allows the probe to be moved relative to the surface. When the cantilever is deflected, it is monitored by the change in the path of the laser beam as it is reflected from the top surface of the cantilever.

The cantilever on the kit used in this work was V-shaped (but the tips can be rectangular shaped). The part of the cantilever that comes into contact with the sample surface is usually in the shape of a square based pyramid or cylindrical cone. Tips are usually made from Silicon Nitride or Silicon, with the upper surface coated with reflective gold or aluminium.

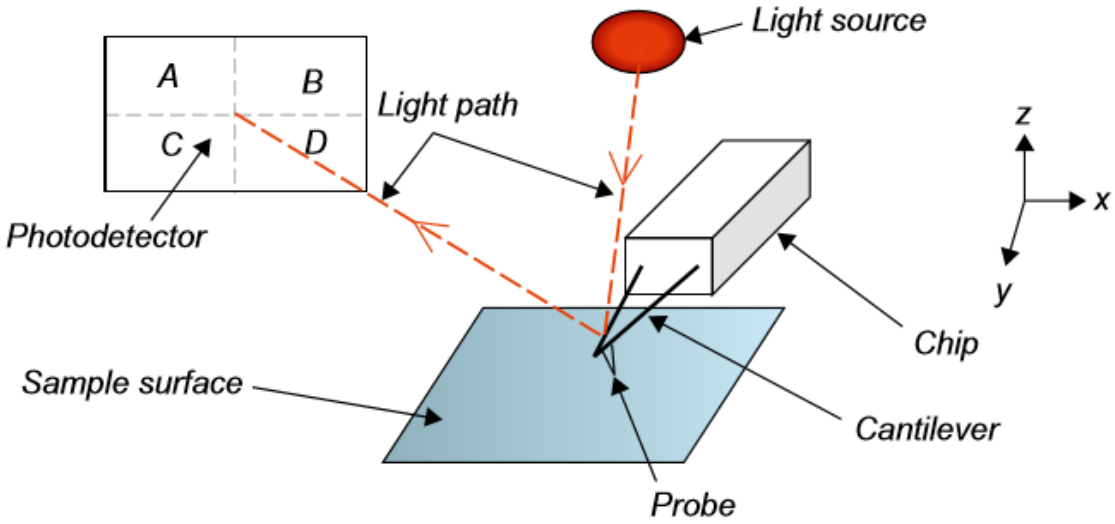

Figure 4.3: Basic AFM set up (40)

The AFM was used in "contact mode imaging". In this mode of operation the probe remains in contact with the sample at all times. It is the simplest type of mode of operation.

A piezocrystal is used to bring the probe into and out of contact with the surface of the sample being investigated. The cantilever chip or the surface is mounted on to the piezocrystal. A

laser beam is reflected from the top of the cantilever into a position sensitive photo detector. As the cantilever is moved or deflected the position of the laser light in the photo detector changes position, which enables changes in the deflection of the cantilver to be monitored.

The most typical type of photodetector is a quadrant photodiode divided into four parts (see figure 4.4). The deflection signal is found by the difference in signal detected from the A + B versus C + D quadrants. Comparing A + C versus B + D quadrants signal allows lateral or torsional bending of the lever to be found. When the probe is in contact with the surface it can be scanned over the surface to get relative height information of topographic features of the sample surface.

The AFM works on the same order of size as the micelles we hope to find, i.e. down to 1 Angstrom, (where 1 micelle is of the order of 1 nm or 10 Angstroms). By using AFM it may be possible to "see" the micelles adsorbed on the substrate in the region of the contact line of the evaporated superspreader solution. However this is not trivial and is fraught with difficulty due to the problem locating exactly where the correct region is to analyse.

4.5: Details of experimental equipment used.

A microsyringe with a needle diameter of 2mm was used to deposit drops onto the polypropylene (pp), parafilm (pf) or polycarbonate (pcp) substrates which were mounted on a glass microscope slide and were checked to be horizontal with a spirit level. Drops were released from a small height to minimize inertial effects. The experiments were performed at ambient temperature and humidity. Two RAS kits were employed in these studies, one being designed for vertical-oriented samples and the other being designed for experiments where the sample needs to remain horizontal – such as for fluid droplet spreading over a horizontal substrate. Apart from the sample geometry, both RAS kits were identical and of the Aspnes design, as described in detail in (39).

The software used to run the kit was homemade.

The superspreading surfactant used was the Evonik S240, and the non superspreading surfactant was Evonik S233. The concentration used was (0.1%) the water used to make the aqueous solutions was distilled.

4.6: Methods used to perform RAS experiments.

In total there were 5 approaches adopted in performing the RAS experiments. To perform RAS experiments polarised light at near normal incidence, (less then 5 degrees) is shone onto the sample surface so the direction of the incident plane of polarisation is at 45 degrees to the x and y axis. Which enables both axes to be evenly illuiminated. If the structures along the x and y axes are different the Fresnel coefficients along the two axes will also be different. This causes the x and y components of the polarisation vector of the reflected light to be unequal leading to elliptically polarised light. The polarisation of the reflected light is analysed to yield the anisotropy of the system according to equation 4.1.

Method 1 for initial experiments

The first RAS experiment undertaken was looking at the RAS signal from a Silicon wafer which is used as a mirror under the substrate in the later experiments because it has a zero RAS signal and so does not affect the signal received for other substrates. The next RAS experiment we carried out was on a PP substrate (on top of a reflective Si wafer). We took RAS data as we rotated the substrate through 90 degrees

Method 2 for 2nd group of experiments.

A different RAS kit was used to the one used in the first group of experiments. This kit was identical to the others used, but had a smaller light spot (~ 1 mm diameter) chosen to increase any signal caused by adsorbed micelles on the contact line of an evaporated drop of surfactant solution. This is because the larger spot might average out the surface signal because the area being investigated includes areas not on the contact line of the evaporated drop.

The following notation is used polypropylene (pp), parafilm (pf), polycarbonate plastic sheet (pcp). S240 (aq) and S233 (aq) refer to the surfactant solutions in water, both solutions had a concentration of 0.1%. with the S240 (0.1%) (aq) being a superspreader.

RAS spectra were taken after the drop of surfactant solution had evaporated, they were taken on the contact line and centre of the drop. I had marked in pen the circumference/contact line of the evaporated drop being careful not to get ink on the areas to be investigated.

Please note we couldn't get a signal from the pf substrate because we think the surface was too opaque and rough causing specular reflection.

Method 3 for 3rd group of experiments.

The pp and pcp substrates were placed on a glass microscope slide, with a black absorbing surface put underneath to eliminate reflections from the bottom surface of the slide. The reflection from the pf substrate was too weak to get a RAS spectra.

Method 4 for 4th experiment.

A piece of Polycarbonate plastic (pcp) substrate was used with a mirror behind to amplify the intensity of the reflected beam.

Distilled water, S240 (0.1%) (aq) superspreader and S233 (0.1%) (aq) was sprayed onto the vertical pcp substrate & mirror combination. The RAS signal was taken at an energy of 3eV (wavelength of 4.13×10^{-7}m) and monitored with time

Method 5 for 5th group of experiments involving RAS vs. time – the "dipping experiment".

Originally it was decided when undertaking the "dipping" experiment that I would put the substrate into the foam holder (connected to a height gauge), and put the substrate at the correct height with the RAS light spot at a suitable position. I would then record the exact height of the substrate. Then lower the height gauge holding the substrate into a small beaker of the solution to be tested. Then put the substrate connected to the height gauge back at the earlier recorded level, and wait for the contact line to reach the RAS spot and record a spectra.

However there were a number of problems which meant it was necessary to modify the method. The contact line was very difficult to see with the solution and the pcp both being transparent.

Also the substrate could not be moved once optimised for the RAS experiment. The slightest movement of even a few mm knocks the light spot out of the correct optical path which it must travel through to the detector.

Obviously, not being able to see the contact line makes the experiment less elegant, but the results can be still seen with any difference in the time taken to reach the contact line being possible corrected by shifting the x axis.

Figure	Method number used.
4.9	5
4.10	1
4.11	3
4.12	1
4.13	3
4.14	2
4.15	3
4.16	3
4.17	3
4.18	3
4.19	3
4.20	3
4.21	3
4.22	5
4.23	5

Table 4.1: The method used for each RAS figure in this chapter.

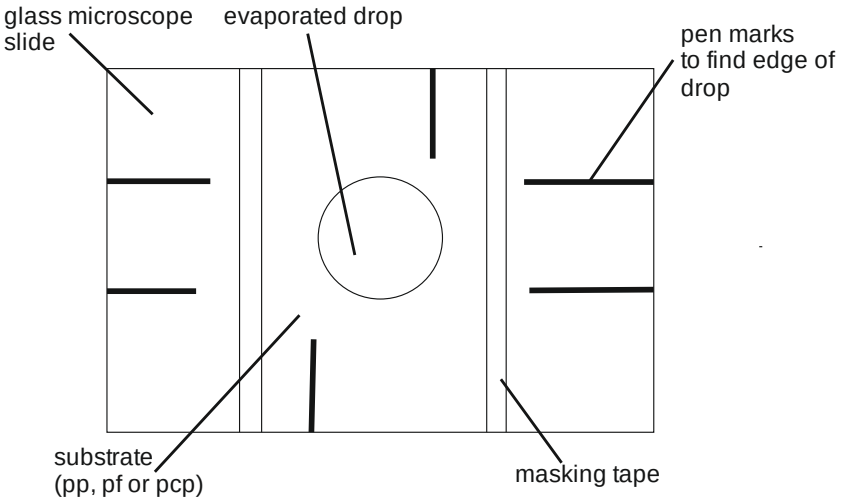

Figure 4.4: Schematic diagram of how the evaporated drop was prepared for the AFM and RAS techniques.

RAS experiments were performed looking at the contact line of S233 (0.1%) (aq), S240 (0.1%) (aq) and water after the substrate (pp or pcp) was dipped into these solutions. Below is the method by which I took results.

1. Fill a small beaker with the solution to be tested.
2. Cut a thin long rectangle of substrate (eg pcp) with the width being the correct dimension to fit in the foam holder on the height gauge.
3. Put the rectangular substrate next to the beaker and mark on it the depth of the solution.

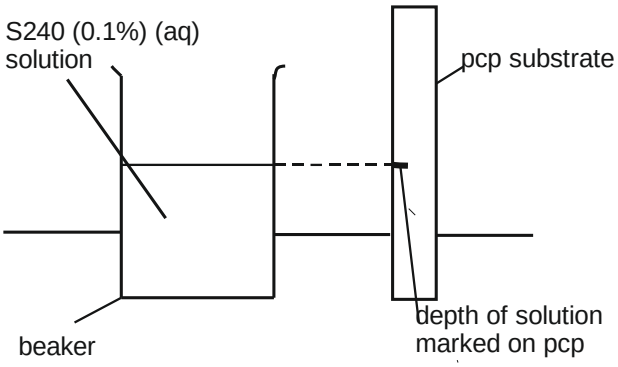

Figure 4.5: Diagram showing the depth of solution marked on the substrate.

4. Next put the substrate back into the foam holder on the height gauge. Shine the RAS light spot at the height shown by the pen mark (showing the depth of the solution). Manipulate the substrate so the light spot is reflected correctly into the detector. Once the number of counts is above 0.3V leave the substrate in the foam holder, being careful not to move it again. Please note that the position and relative angle of the substrate has to be exactly aligned to give sufficient counts, even a small movement of the substrate stops the reflected light following the correct path.

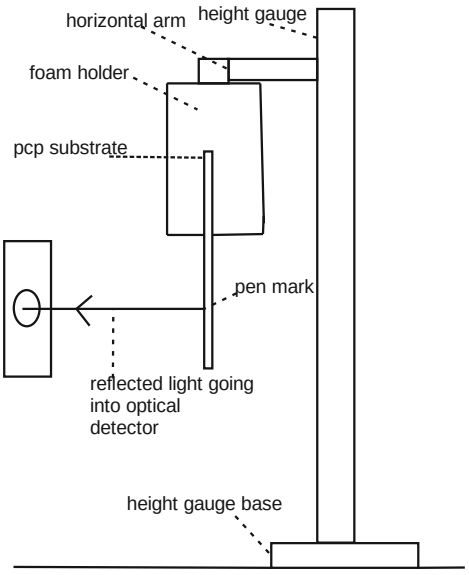

Figure 4.6: Diagram showing the substrate optimised for RAS light spot counts.

5. The next step is to lift the small beaker underneath the substrate until the bottom half of the substrate is completely submerged.

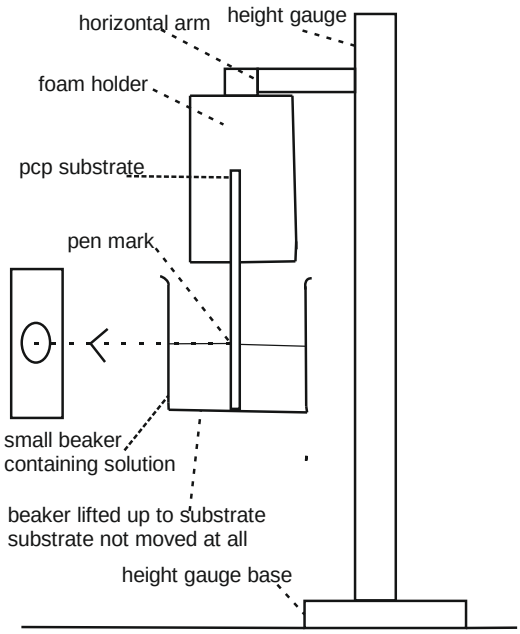

Figure 4.7: Diagram showing how the substrate is dipped in the solution to be tested.

6. The next step is to remove the small beaker and start the RAS scan.

Obviously not being able to see the contact line makes the experiment less elegant, but the results can be still seen with any difference in the time taken to reach the contact line being possible corrected by shifting the x axis.

Figure 4.8 shows the reflection anisotropy (RA) spectrometer set up and the geometry of the substrate with the y direction chosen to be vertical and aligned to the direction of fluid flow with x perpendicular . In this experiment RAS is used to search for anisotropic entities that may be aligned in a preferred direction resulting from the flow of fluid across an isotropic substrate.

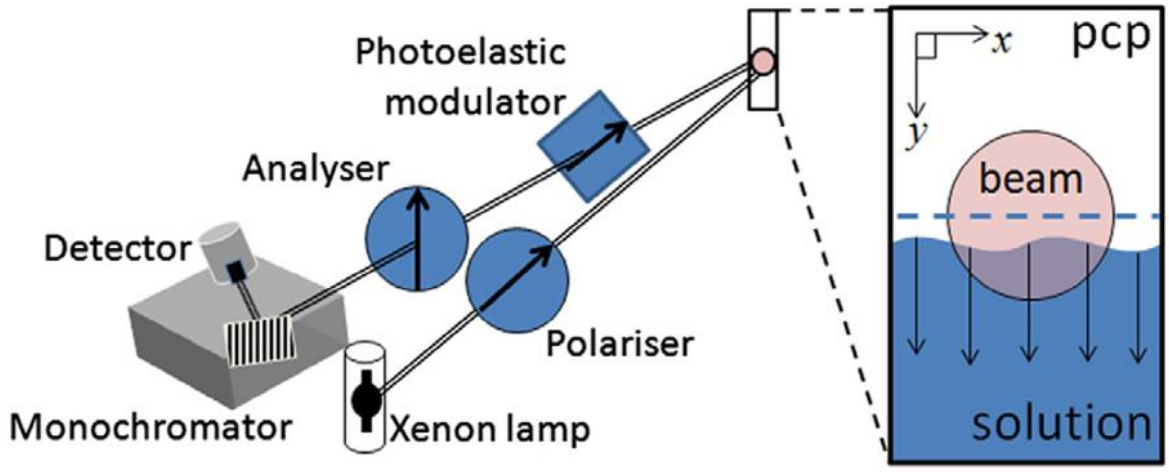

Figure 4.8: Schematic layout of the RAS setup and sample orientation. The solution is shown receding primarily due to gravity, down the pcp substrate and through the RAS beam. (41)

Fluid flow over the substrate was monitored with dynamic RA measurements set at a fixed wavelength and the anisotropy measured as a function of time. The RA signal (real part of equation 4.1), the DC signal (denominator in equation 4.1), and reflectivity were monitored at a wavelength of 414nm (3eV photon energy). Figure 4.B shows this wavelength gives an optimum RAS signal on a horizontal pcp substrate covered with a thin film of S240 (0.1%) (aq) solution.

The receding contact line of S240 (0.1%) (aq), S233 (0.1%) (aq), (both supplied by Evonik Industries Germany) and water were analysed with dynamic RA experiments. The S233 (0.1%) (aq) was chosen as it has a similar molecular structure as the superspreading S240 (0.1%) (aq) without itself being a superspreader. The pcp substrate was aligned vertical and submerged in a beaker containing the solution to a level bisecting by half the position of the RAS beam incident on the pcp substrate (see figure 4.8). The RAS beam has a diameter of 8mm and the rectangular pcp substrates had dimensions of 25mm × 60mm × 1mm. The beaker was removed downwards and as soon as it was clear of the optical path the RA time scan was started. The RA time scan analysed the solution as it moved down the pcp substrate and across the lower half of the RAS beam. The substrate was not moved so the reflected beam did not have its position and direction changed. The water used was Ultrapure (Milli – Q) including in the S240 and S233 solutions.

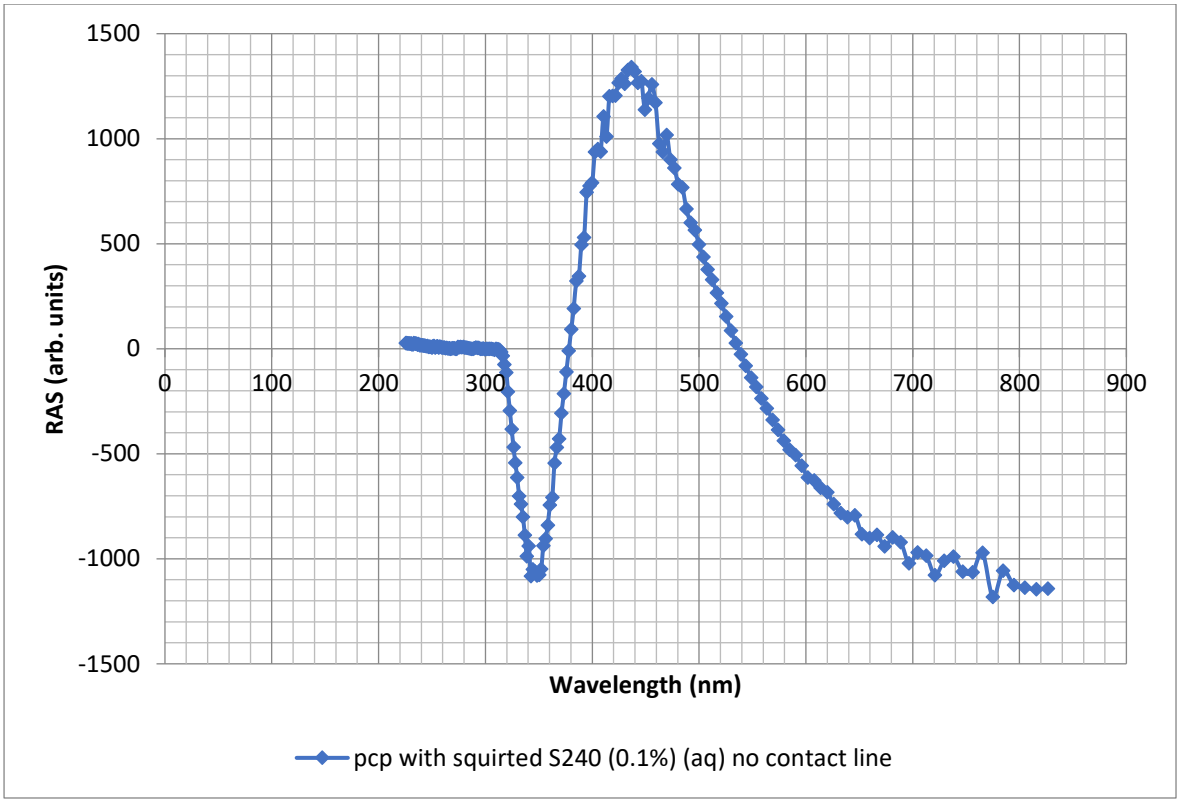

Figure 4.9: Light (photon) wavelength versus RAS scan for S240 (0.1%) (aq) squirted onto a vertical pcp substrate.

4.7: RAS results.

4.7.1: Preliminary RAS experiments.

A preliminary experiment was to find out what the RAS signal was for a Silicon wafer as its reflective surface was used a mirror under the different substrates in the later experiments to boost counts recorded. There is no significant RAS signal and as expected the surface is isotropic meaning it will not alter or contribute to the signal from other substrates when placed underneath them as a mirror.

The second preliminary experiment was to check that there was no signal from the glass microscope slides on which the substrates pp and pcp were mounted, (evaporated drops of S240 (0.1%) (aq) , S233 (0.1%) (aq) and water where placed on these pp and pcp substrates). As can be seen from figure 4.11 there was a flat horizontal RAS signal meaning the glass surface was isotropic and would not contribute to the RAS from the pp and pcp substrates.

In figure 4.12 RAS data was taken as the pp substrate (on top of a silicon wafer) was rotated through 90 degrees. There is a RAS signal which increases with rotation, with the scans being symmetric about the flat line.

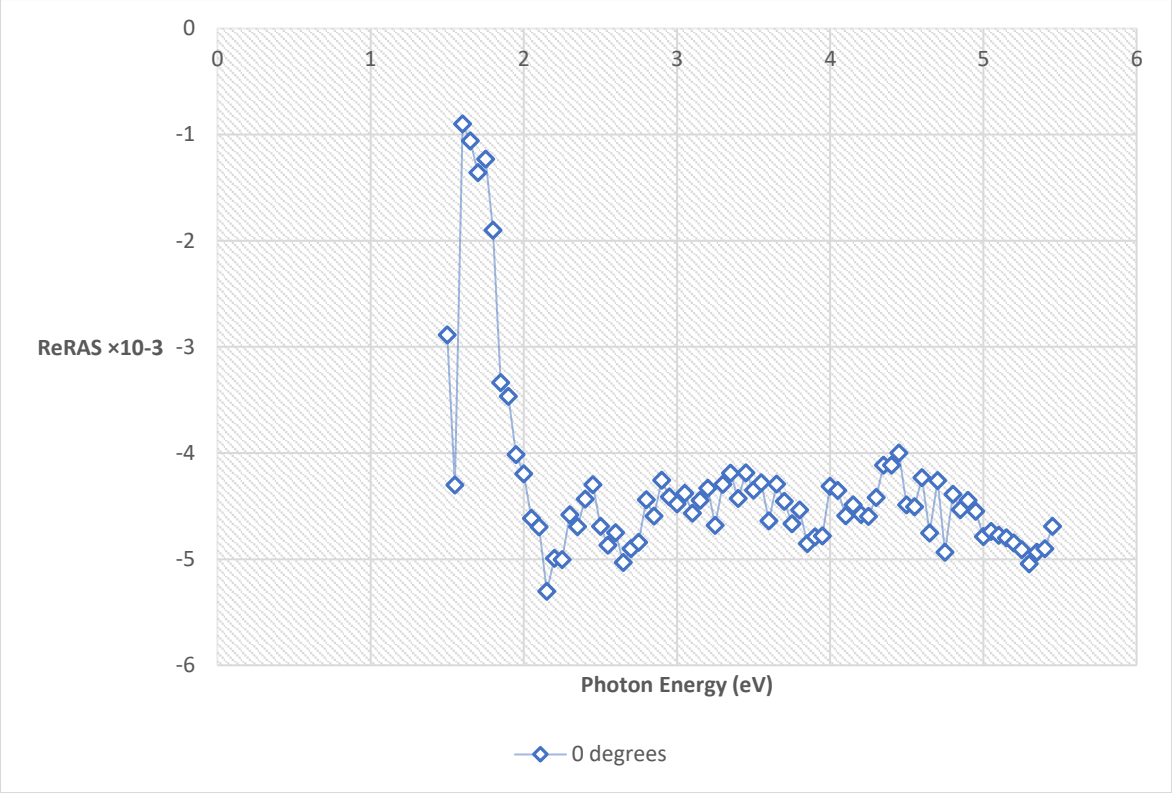

Figure 4.10: RAS spectra of Si surface".

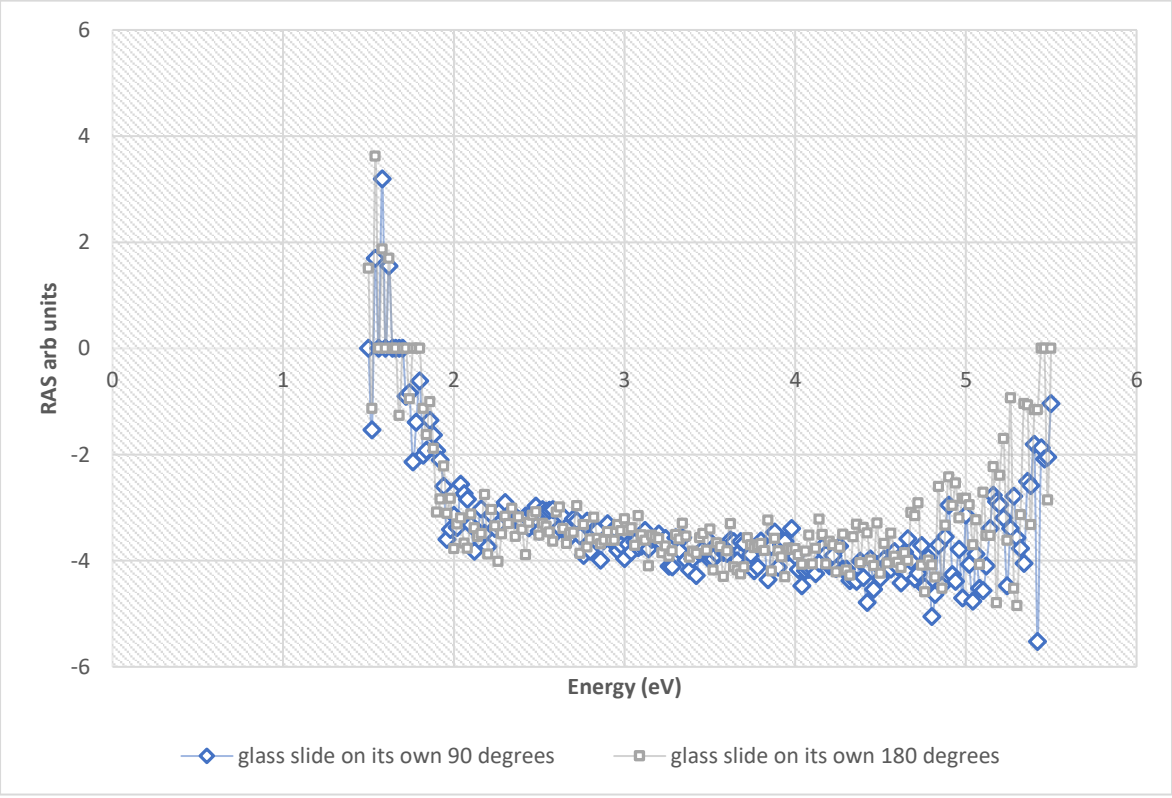

Figure 4.11: RAS scans of Borosilicate glass in two orthogonal directions.(M3)

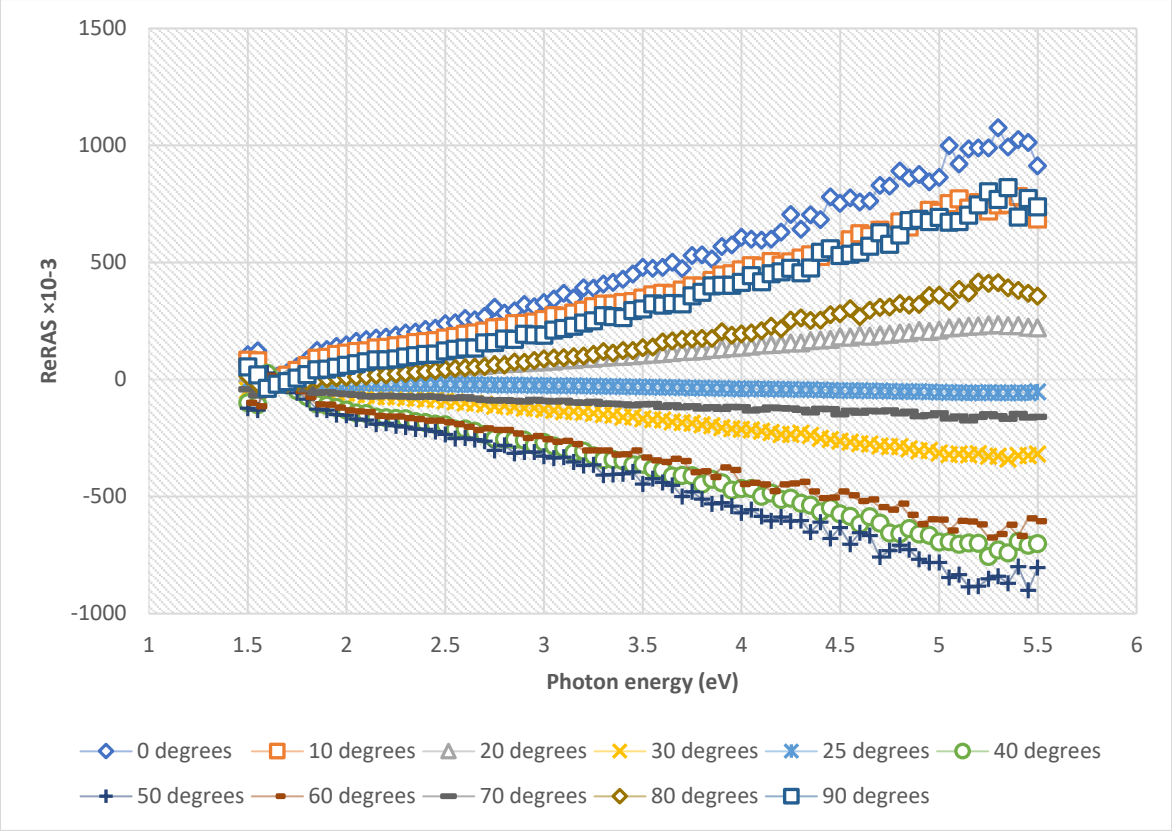

Figure 4.12: RAS experiments of pp substrate rotated through 90 degrees (M1).

The next preliminary experiment was using figure 4.12 to plot the RAS values for each angle at a fixed energy of 5eV. To do this figure 4.11 was used with equation 4.2.

$$f(x) = a \cdot \sin(bx + c) \tag{4.2}$$

The values of the fit parameters are shown in table 4.1:

parameter	numerical value
a	823
b	3.698
c	1.577
SSE	9398
R-square	0.9973
Adj. R-square	0.9966
RMSE	34.27

Table 4.2: Fit parameters to values of RAS at different angles at a fixed energy of 5eV

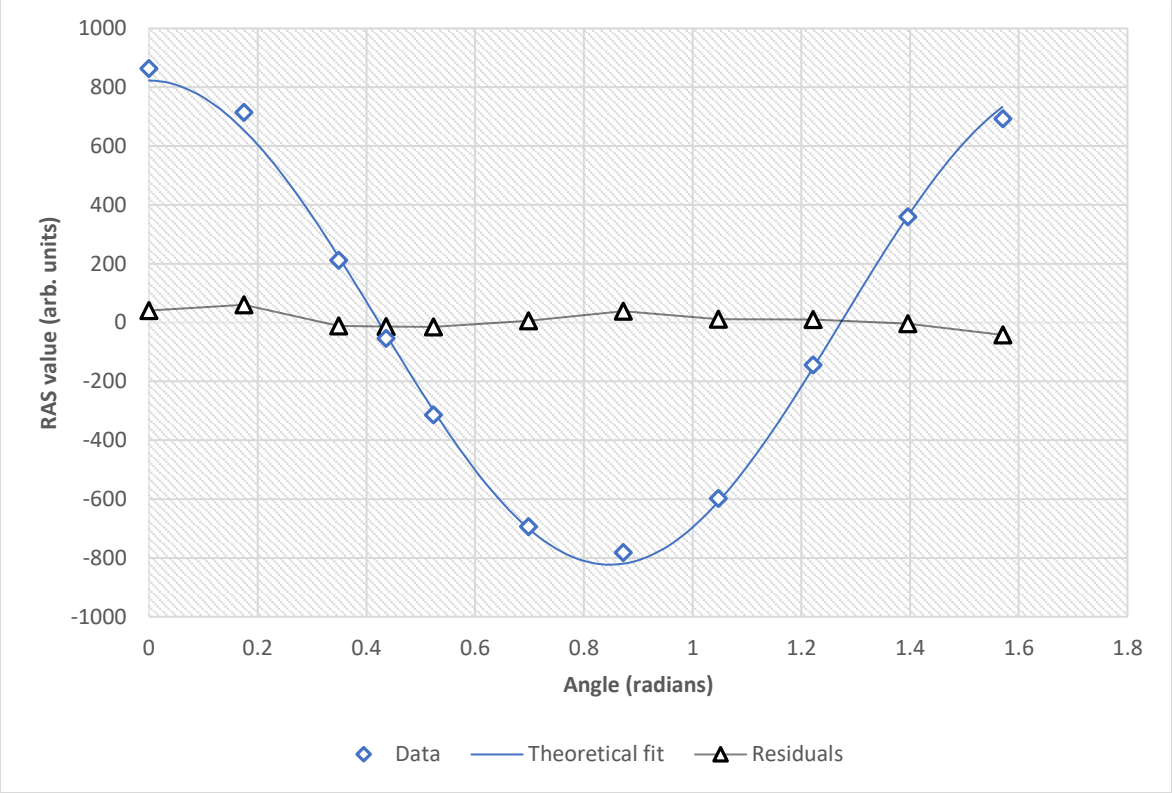

Figure 4.13: RAS values for different angles (0-90 degrees or 0-1.57 radians) at an energy of 5eV for a pp substrate on its own.

The parameter labelled c is a small phase shift included due to the difficulty in exactly determining zero degrees rotation in the experiment at 1.577 radians or 90.36 degrees, this means the data is aligned to 0.36 degrees. The value of b is near the value of 4, this sin(4θ) relationship has been seen before in polymers and indicates the signal is coming from the bulk of the pp substrate more so then the surface.

The adjusted R – square indicates a good fit being close to 1 at 0.9966. The R square tells us that the fit explains 99.73% of the total variation in the data about the average.

4.7.2: Main RAS experiments.

Figure 4.14 shows the RAS spectra for a pp substrate with no evaporated drop, (of S240 (0.1%) (aq), S233 (0.1%) (aq) or water), on it. From figure 4.15 we can assume that this is the bulk RAS signal from the pp substrate.

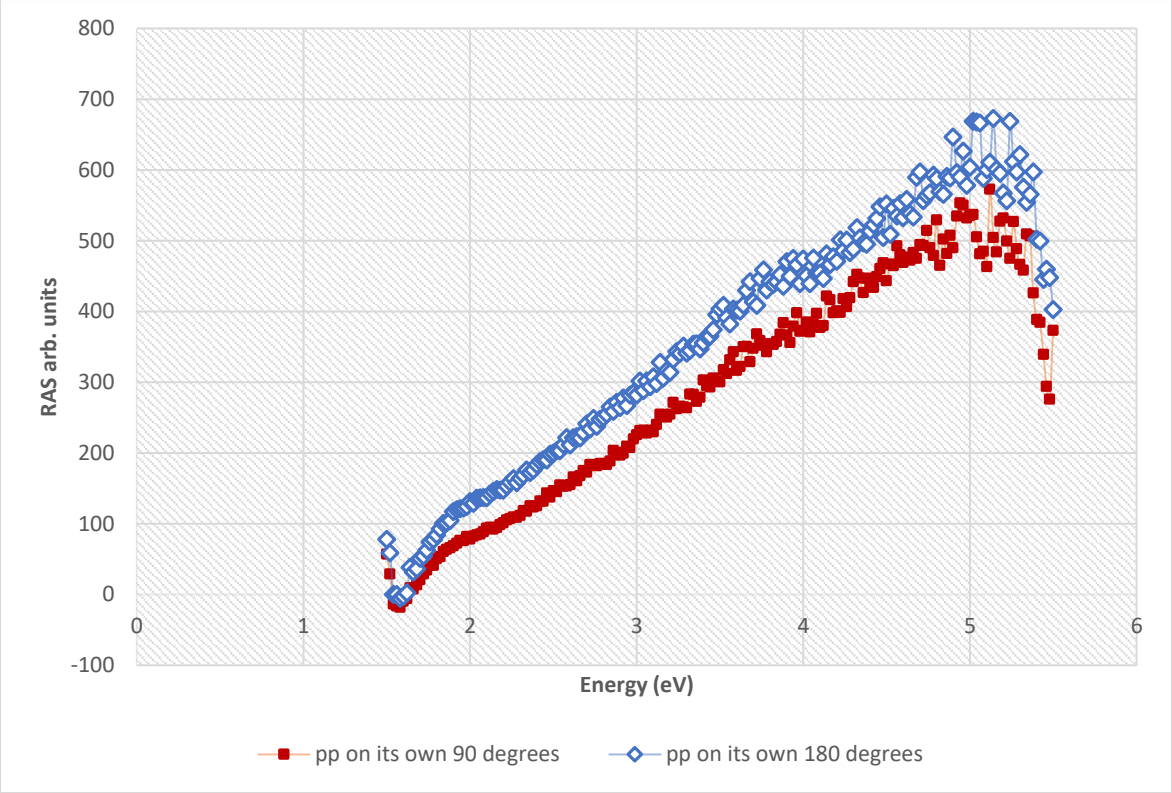

Figure 4.14: RAS scans of pp substrate in two perpendicular directions

Figure 4.15 shows the RAS spectra for a pcp substrate with no evaporated drops on it. There is a clear trough and peak feature which may indicate anisotropy of the surface.

Figure 4.16 shows that regions where the edge and centre of the evaporated drops of S240 (0.1%) (aq) on a pp substrate and the pp on its own (figure 4.15) both have the same spectra shape. This indicates that the evaporated drop has no effect on the RAS spectra for the pp substrate which means that there is no anisotropy from micelle structures at the contact line.

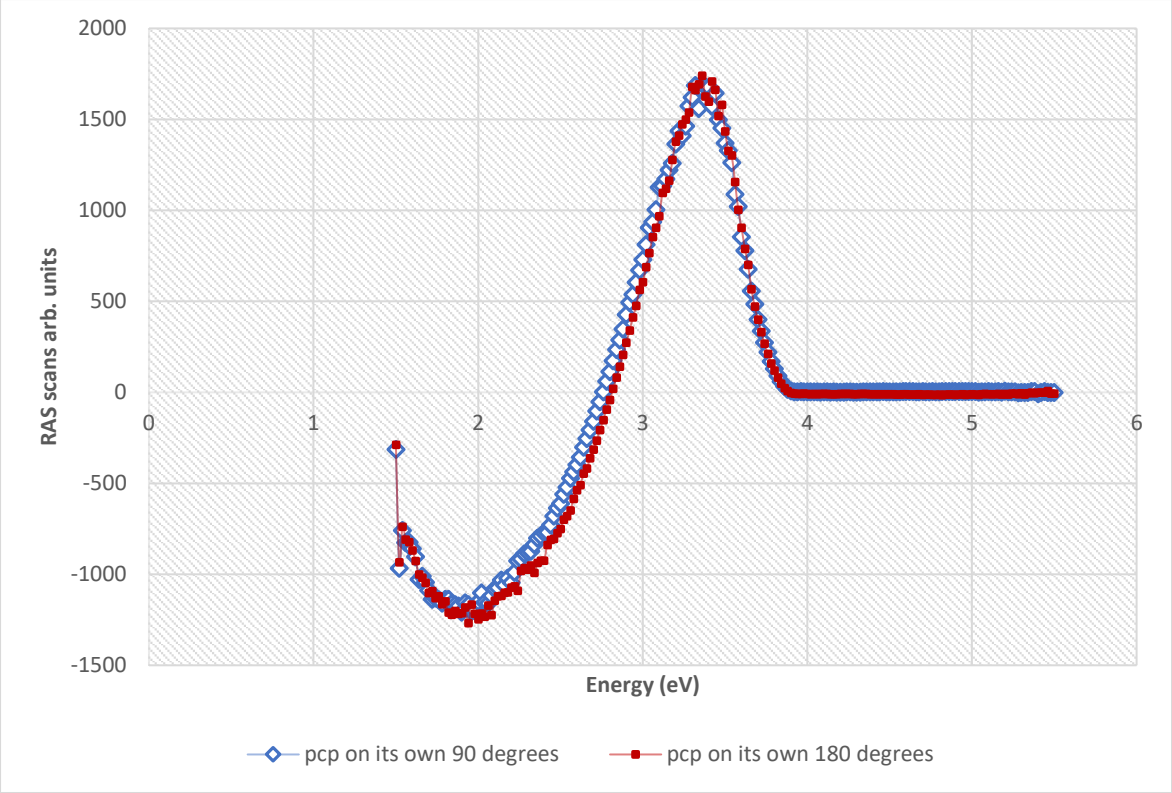

Figure 4.15: RAS scans of pcp substrate in two orthogonal directions.

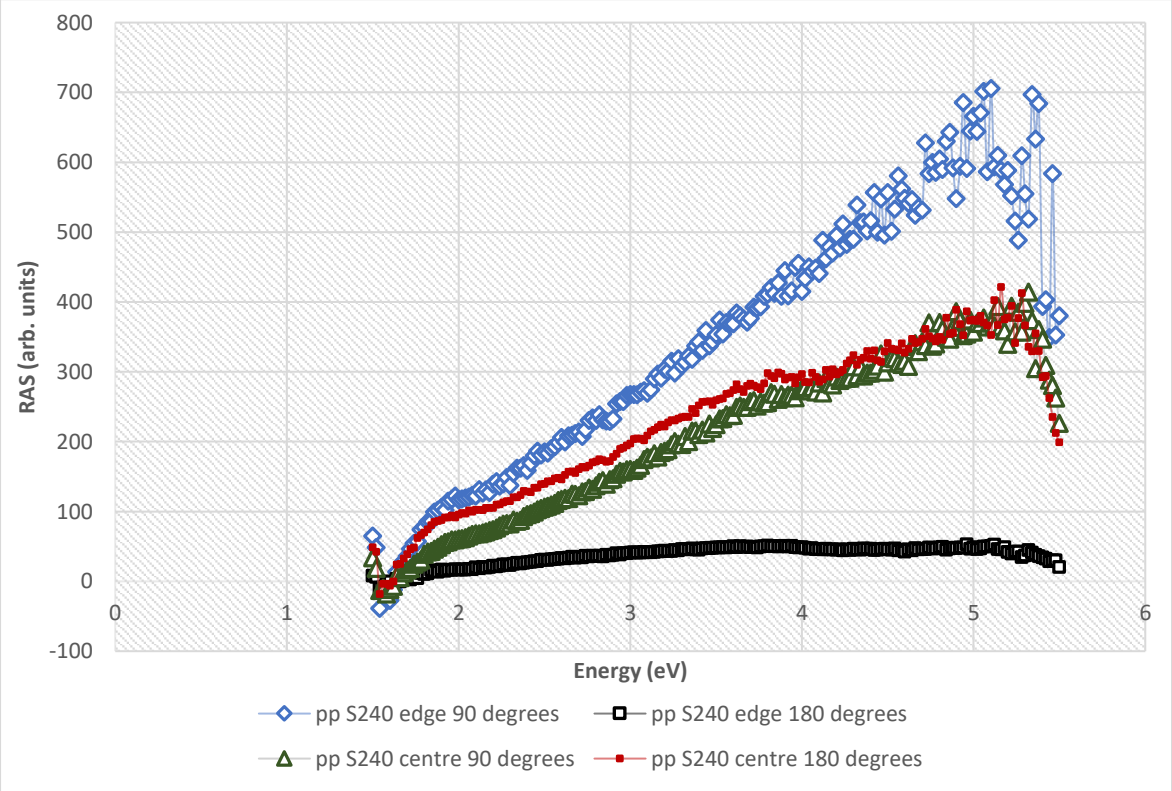

Figure 4.16: RAS scans of evaporated drop of S240 (0.1%) (aq) when the substrate is pp and it is taken at two perpendicular angles.

Also there is no difference between the edge and centre of the evaporated drop of S240 (0.1%) (aq). We expected the S240 (0.1%) (aq) evaporated drop contact line region, (labelled as the "edge"), to have anisotropy caused by micelle structures aiding superspreading while the bulk region of the evaporated drop was expected to be isotopic with randomly orientated/aligned surfactant molecule structures. Reasons for this were proposed in the aims and objectives section and are the following:

1. The micellae are/are not adsorbed.
2. The micellae do/do not survive drying.
3. The micellae are/are not detectable
4. The likelihood of not finding them is low/high

In figure 4.17 the same scenario occurs the pcp substrate scan (figure 4.17), the edge of the evaporated drop of S240 (0.1%) (aq), and the centre of the evaporated drop of S240 (0.1%) (aq) all have identical RAS spectra. This means there is no micelle characteristic anisotropic RAS signal from the RAS spectra for the "edge" of the drop of S240 (0.1%) (aq), with the edge of the evaporated drop having the same RAS spectra as the pcp substrate and the centre of the evaporated drop of S240 (0.1%) (aq).

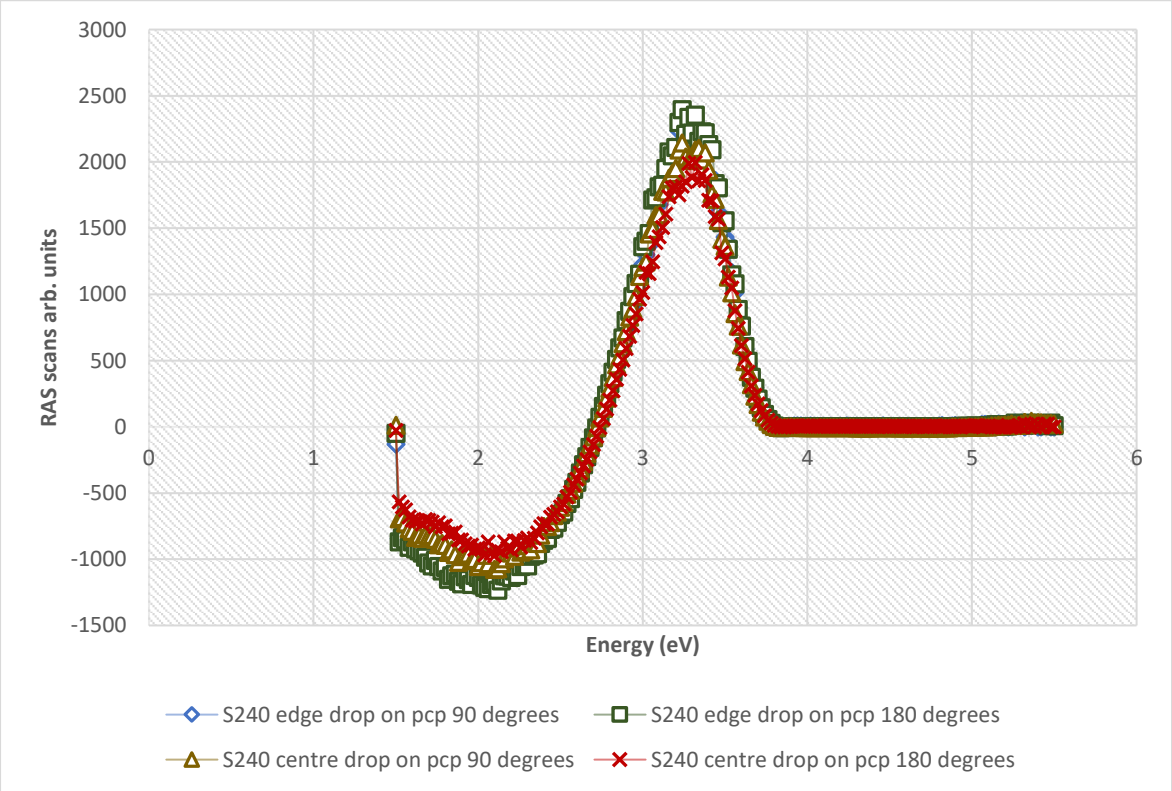

Figure 4.17: RAS scans of the centre and edge of an evaporated drop of S240 (0.1%) (aq) on a pcp substrate.

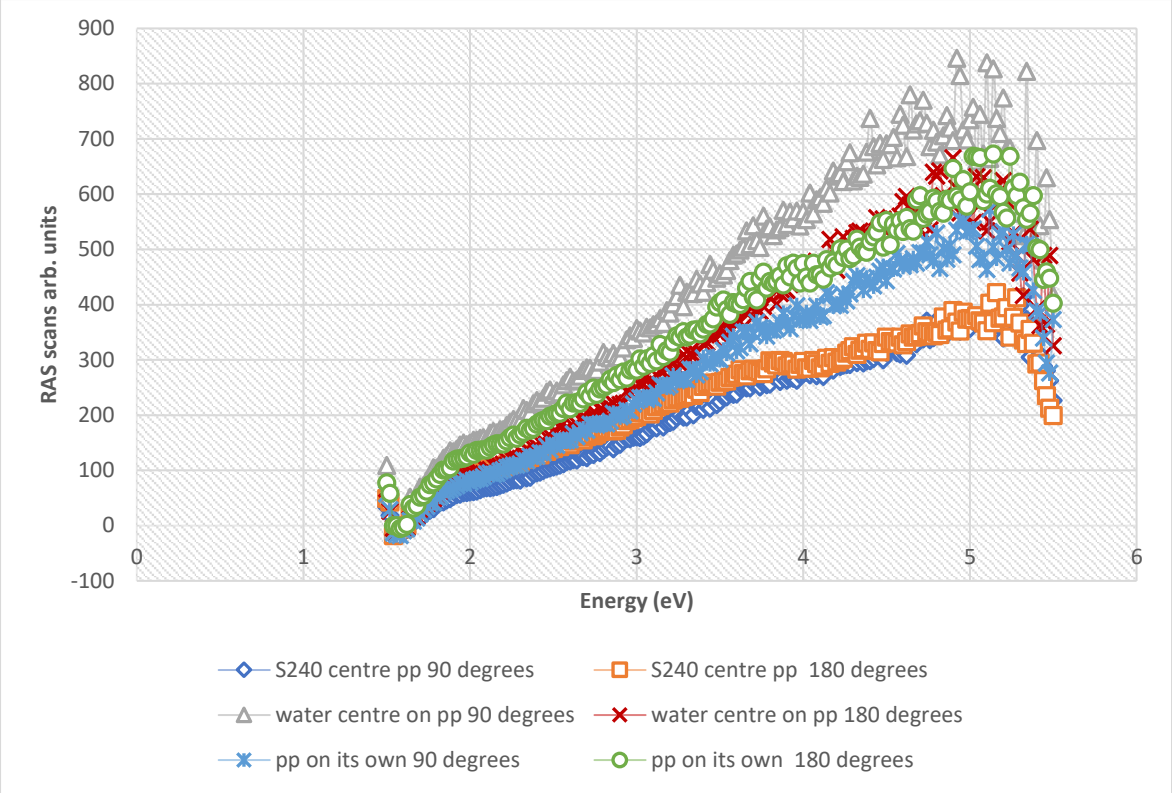

Figure 4.18: RAS scans of the centre of an evaporated drop of S240 (0.1%) (aq) on a pp substrate compared with the centre of water drop on a pp substrate and a pp substrate, in two orthogonal directions. (M3).

Figure 4.18 shows that the RAS scans for the centre of the evaporated drop of S240 (0.1%) (aq) (and from figure 4.16 the edge of the evaporated drop of S240 (0.1%) (aq)), the centre of the evaporated drop of water and the pp substrate by itself all have the same RAS spectra. This indicates that most of the signal is coming from the bulk of the substrate which backs up figure 4.13. The scans show that the centre of the S240 (0.1%) (aq), (and from figure 4.18 the edge of the evaporated drop of S240 (0.1%) (aq)), the centre of the evaporated drop of water and the signal from the pp substrate on its own all have the same degree of surface anisotropy. However since there are not too many features on these RAS scans it can be concluded that the surfaces are fairly isotropic with randomly orientated surface structures. The edge of the evaporated drop of S233 (0.1%) (aq) also has exactly the same RAS spectra (see appendix) which also backs up these conclusions.

In figure 4.19 the RAS scans from the pcp substrate by itself and the scan for the centre of the evaporated drop of S240 (0.1%) (aq) have the same spectra indicating that the signal is coming from the bulk for the scan for the centre of the evaporated drop of S240 (0.1%) (aq). Interestingly the centre of the evaporated drop of water has a diffrerent RAS scan with a peak between 2.6 and 2.7 eV and a trough between 3.1 to 3.2 eV. It is not clear why this is as it

would not be expected for the water to from anisotropic structures in the bulk. The RAS scan for the edge of the evaporated drop of S233 (0.1%) (aq), (see appendix), has a similar peak to the S240 "centre" at around 3.2 eV all though other RAS scans for the edge of the water and pcp substrate by itself are similar but not the same as figure 4.20.

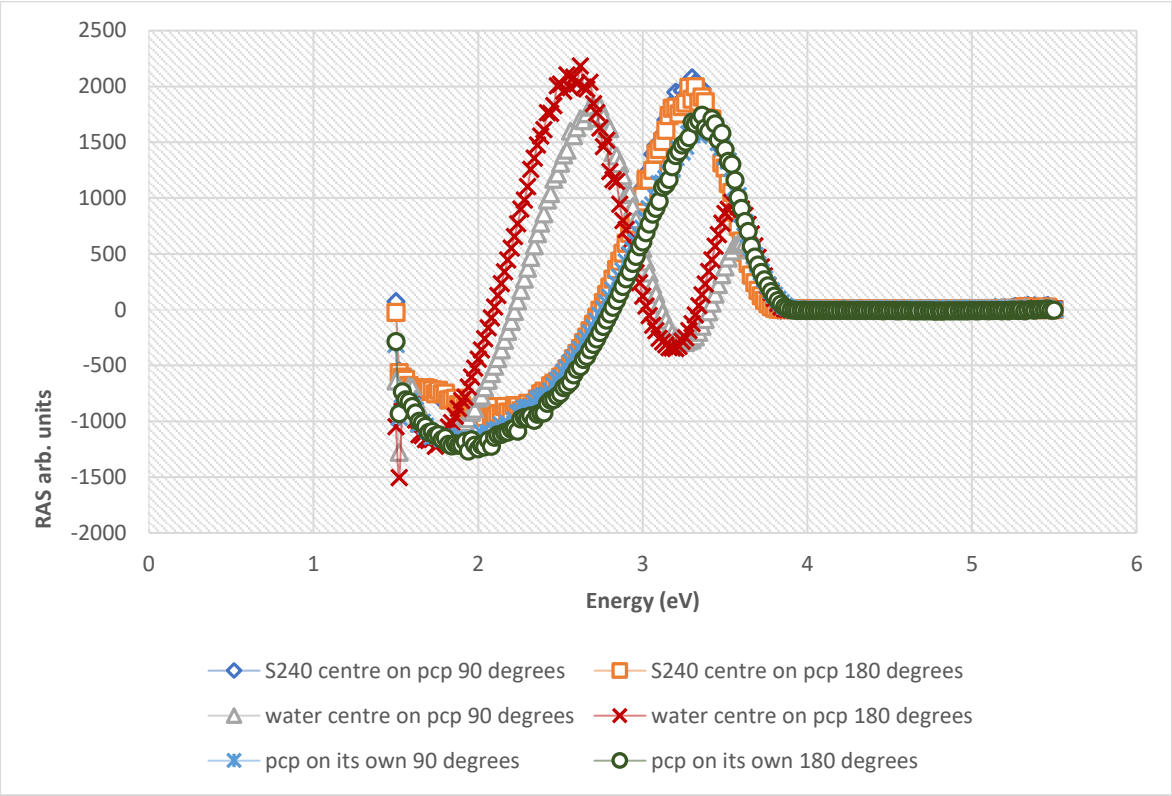

Figure 4.19: RAS scans of the centre of evaporated drops of S240 (0.1%) (aq) on a pcp substrate, and the centre of an evaporated drop of water on pcp and pcp.

Figure 4.20 shows the RAS scans for the edge of the evaporated drops of S240 (0.1%) (aq) on a pp and pcp substrate. In the appendix is the RAS scan for the centre of the evaporated drops of S233 (0.1%) (aq) on pp and pcp substrate. Note that the RAS scans for the centre of the evaporated drops of S233 (0.1%) (aq) on pp and pcp have the same spectra as figure 4.20 indicating the same signal from the bulk. (We know the RAS signal is coming from the bulk for both the pp and pcp substrates as figures 4.15 and 4.16 have identical spectra to those in figure 4.20). The two RAS spectra in figure 4.20 are very different in shape with the pcp spectra displaying a trough and peak while the pp spectra is a diagonal line with a peak at around 5eV. This may indicate that the pcp signal has greater anisotropy then the pp signal as it has more prominent features.

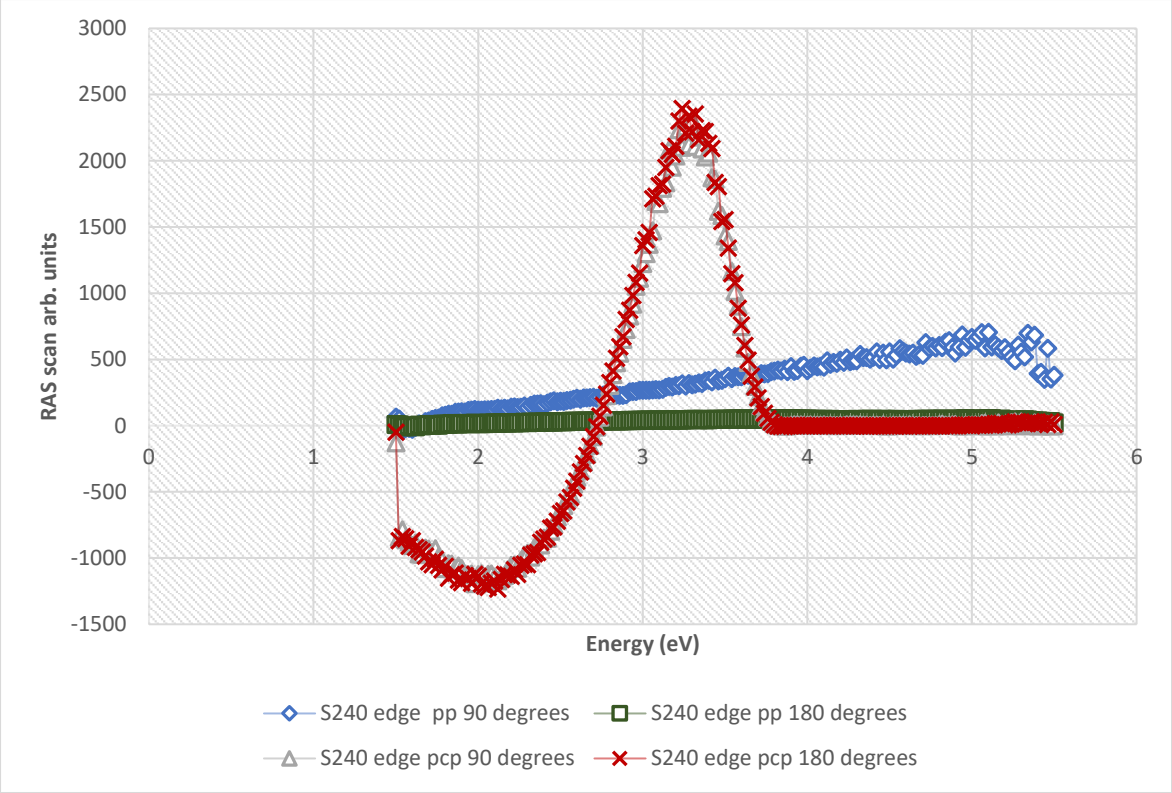

Figure 4.20: RAS scans of the edge of an evaporated drop of S240 (0.1%) (aq) on a pp and pcp substrate.

Figure 4.21 shows the RAS scans for the edge of the evaporated drops of S233 (0.1%) (aq) on a pp and pcp substrate. The figure showing the RAS scan for the centre of the evaporated drops of S233 (0.1%) (aq) on a pp and pcp substrate are shown in the appendix. Once again the edge and centre of the evaporated drops of S233 (0.1%) (aq) have the same RAS spectra. Also apart from an extra trough at 3.6eV for the pcp signal, the scans are the same as those in figure 4.20.. This leads to the conclusion that whether the RAS spot is shone on the edge region or central region of the evaporated drop makes no difference to the RAS signal. Also there is evidence that there are some differences (trough at 3.6eV) between the signal of S240 (0.1%) (aq) and S233 (0.1%) (aq) on a pcp substrate.

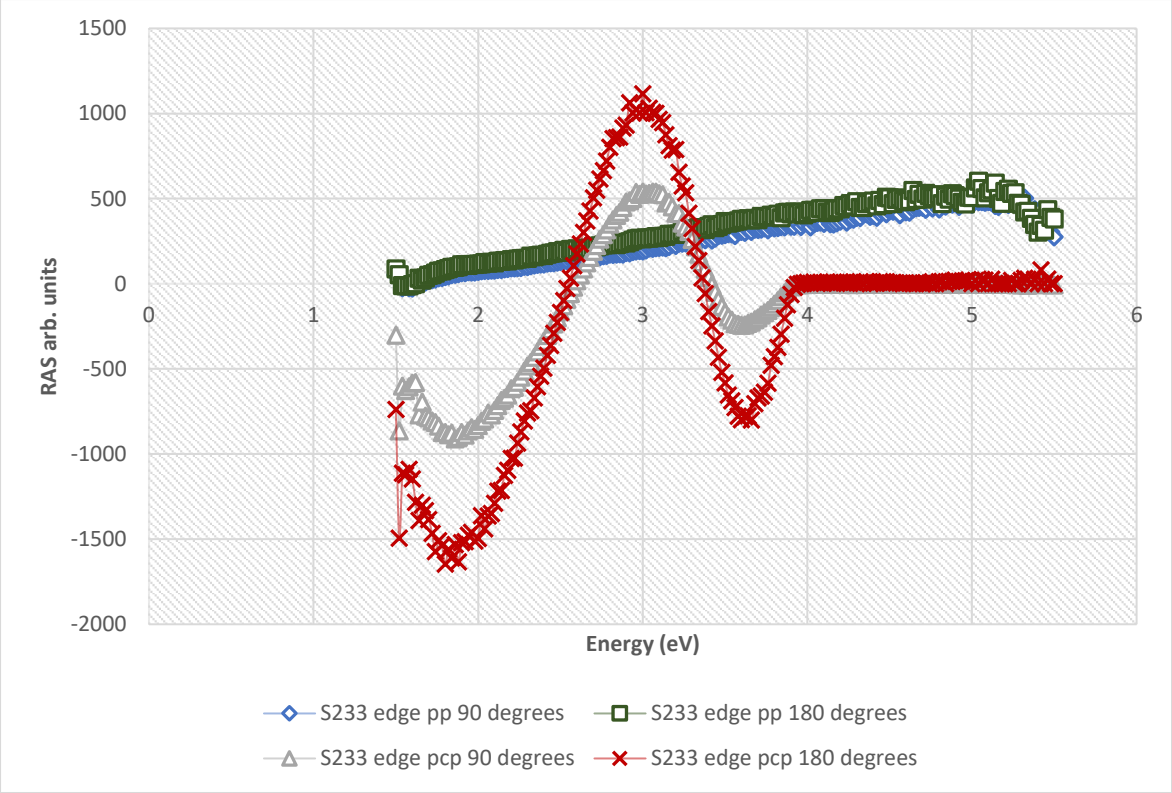

Figure 4.21: RAS scans of the edge of an evaporated drop of S233 (0.1%) (aq) on a pp and pcp substrate.

4.7.3: The "Dipping" RAS experiments.

The aim of this experiment is to investigate whether the superspreading S240 (0.1%) (aq) encourage the creation of ordered macromolecular structures (e.g. micelles or bi-layers) which could help explain how superspreading works.

Two experiments are shown in figure 4.22 with both looking at RA and DC spectra. There was some variation in the apearence in time when features appeared in these scans. But overall there were two main types of property to the DC scans with either one or two step change in the DC signal (see figure 4.22).

A two-step process is displayed in the upper graphs of figure 4.22 with the DC signal increasing at 40 and 80 seconds. The rate of change of reflectivity is practically the same (i.e. the gradient) at these times. The two-step behaviour could be due to the presence of a "bulk" film receeding first followed by a thinner "interfacial" film. The lower curves of figure 4.22 i.e. the second experiment show in the RA and DC signal a steady slow change in the spectra. It is not known why there are two types of behaviour, further experiments are required

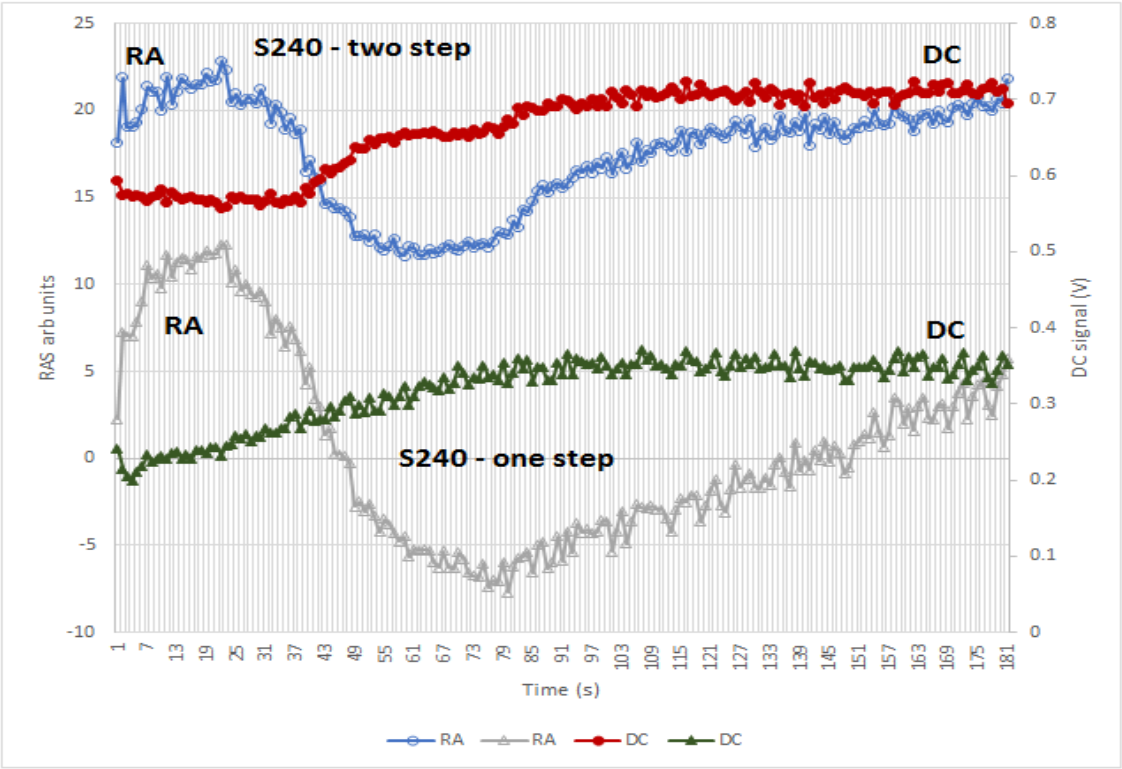

Figure 4.22: RA signal (open symbols) and DC signal (filled symbol) at 414 nm versus time for the moving contact line of S240 (0.1%) (aq) on a pcp substrate. Results of two experiments are shown (circles and triangles) depicting a two step and one step process, shifted in the y axis for clarity.

to investigate why this is the case. It would also be necessary to control all the different parameters such as the removal speed of the beaker and the exact electrostatic charge on the pcp substrate.

In figure 4.22 both RA curves show first a small increase followed by a decrease to a minimum and a recovery towards its starting value. If we presume there is no change orthogonal to the flow (i.e. r_x) then in the direction of the flow (r_y), there would be a reduction initially in the first 20 seconds, then an increase to a maximum followed by reduction back towards its starting value. The maximum anisotropy of the two-step behaviour is between the first and second step changes in the DC signal. This could be explained by the possibility that the anisotropic thin surface layer exists on the substrate during this time period. The biggest anisotropy signal for the one-step results could be due to a temporal anisotropic surface layer. It is possible this layer might be lost by evaporation.

Figure 4.23 shows the dipping experiments for S233 (0.1%) (aq) and water. The S233 solution has a flat horizontal RA and DC spectra which support the theory that there is no anisotropy at the contact line of the descending S233 film or elsewhere.

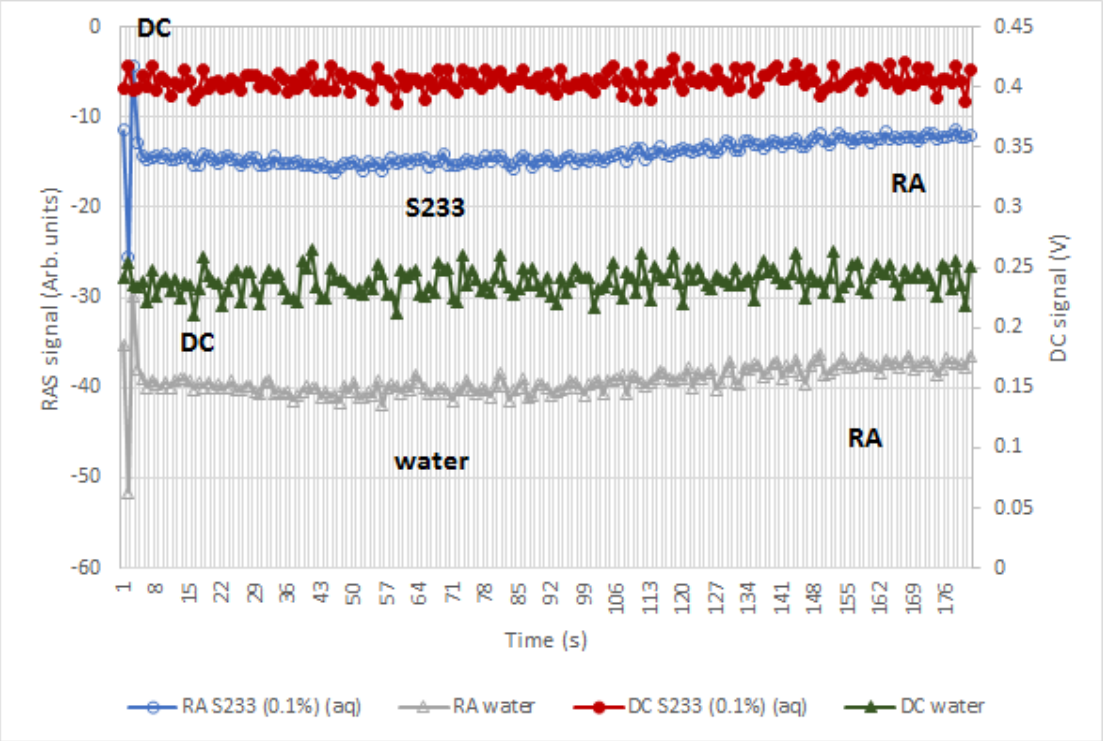

Figure 4.23: RA signal (open symbols) and DC signal (filled symbols) at 414nm versus time for water (triangles) and S233 (0.1%) (aq) (circles). Scans are shifted in y axis for clarity.

The RA signal versus time spectra for water are flat and without peaks or features which means the water film is isotropic. The reflectivity scans (DC scans) for the descending S233 (0.1%) (aq) and water films are flat and featureless indicating the light is reflected in a uniform way as the film moves down the substrate under gravity.

4.8: AFM results

The characteristic lines on the pcp substrate seen in part A of figures 4.24, 4.25 and 4.26 are thought to be caused by the manufacturing process which may involve mechanical rolling. On metal surfaces similar lines can be seen, which are caused by polishing. Part D the topological image of water on a pp substrate is shown in figure 4.24. It has characteristic “donut” shapes, which are not as clearly defined in figures 4.25 and figure 4.26. The pp substrate has the most features compared to the pf and pcp substrate as can be seen in the differentiated image of part

C figure 4.24, 4.25 and 4.26. The pf substrate is the most featureless and smooth as can be seen in part E of figure 4.24, 4.25 and 4.26.

Figure 4.24 part A, figure 4.25 part A and figure 4.26 part A show no discernible difference between the solutions of water, S240 0.1% (aq) and S233 0.1% (aq) on a pcp substrate and the surface structure in the region of the evaporated contact line. No structures are present which could be surface aggregates of micelles.

Figure 4.24 part C had very large features not seen on figure 4.25 part C, figure 4.27 part C had the same sort of features as figure 4.24 part C but not as well defined. This may be simply local variation on the surface. No adsorbed micelles can be seen for any pp surfaces not matter what the solution whether it be water, S240 0.1% (aq) or S233 0.1% (aq).

Figure part 4.24 part E, figure 4.25 part E and figure 4.26 part E show there is no difference in terms of surface structure for different evaporated drops of water , S240 0.1% (aq), or S233 0.1% (aq) on a pf substrate. Again no micelles were seen absorbed onto the surface of the pf substrate.

The pf followed by the pcp then the pp appears to be the order of increasing surface roughness..

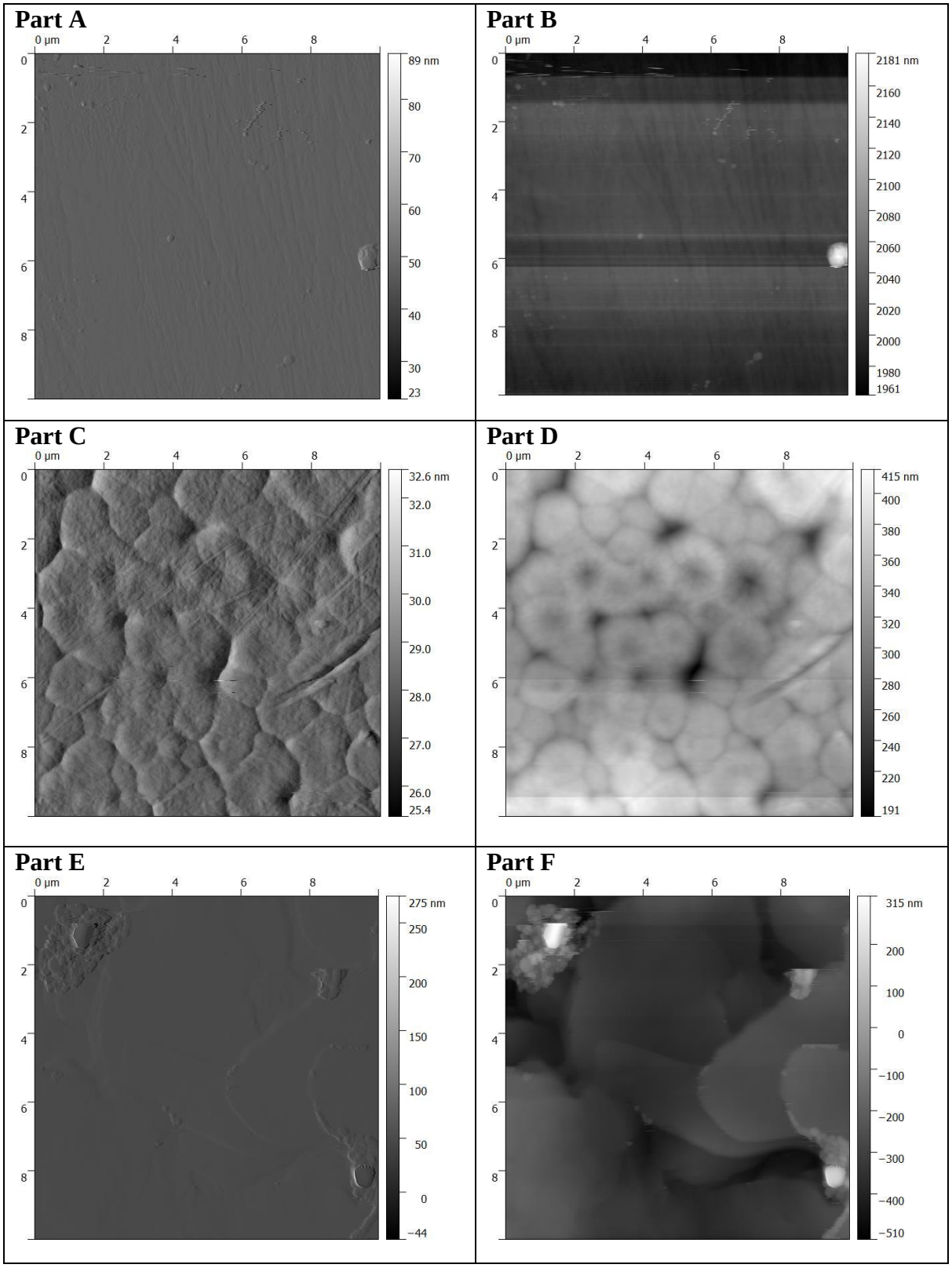

Figure 4.24: AFM images for substrates of pcp (part A), pp (part C), pf (part E), and topological images for substrates of pcp (part B), pp (part D), and pf (part F), all with an evaporated drop of water in the region of the contact line.

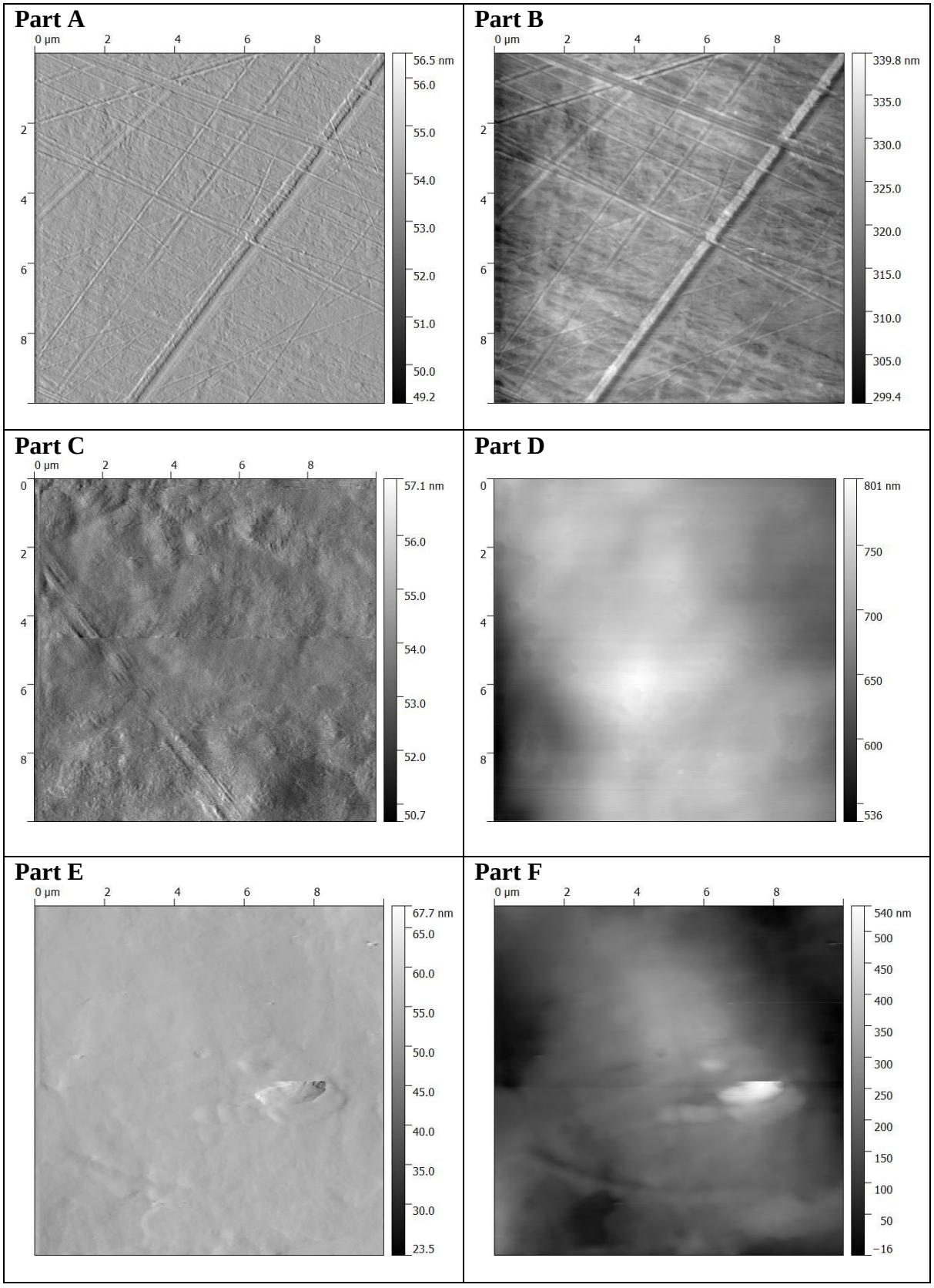

Figure 4.25: AFM images for substrates of pcp (part A), pp (part C), pf (part E), and topological images for substrates of pcp (part B), pp (part D), and pf (part F), all with an evaporated drop of S240 0.1% (aq) superspreading trisiloxane surfactant in the region of the contact line.

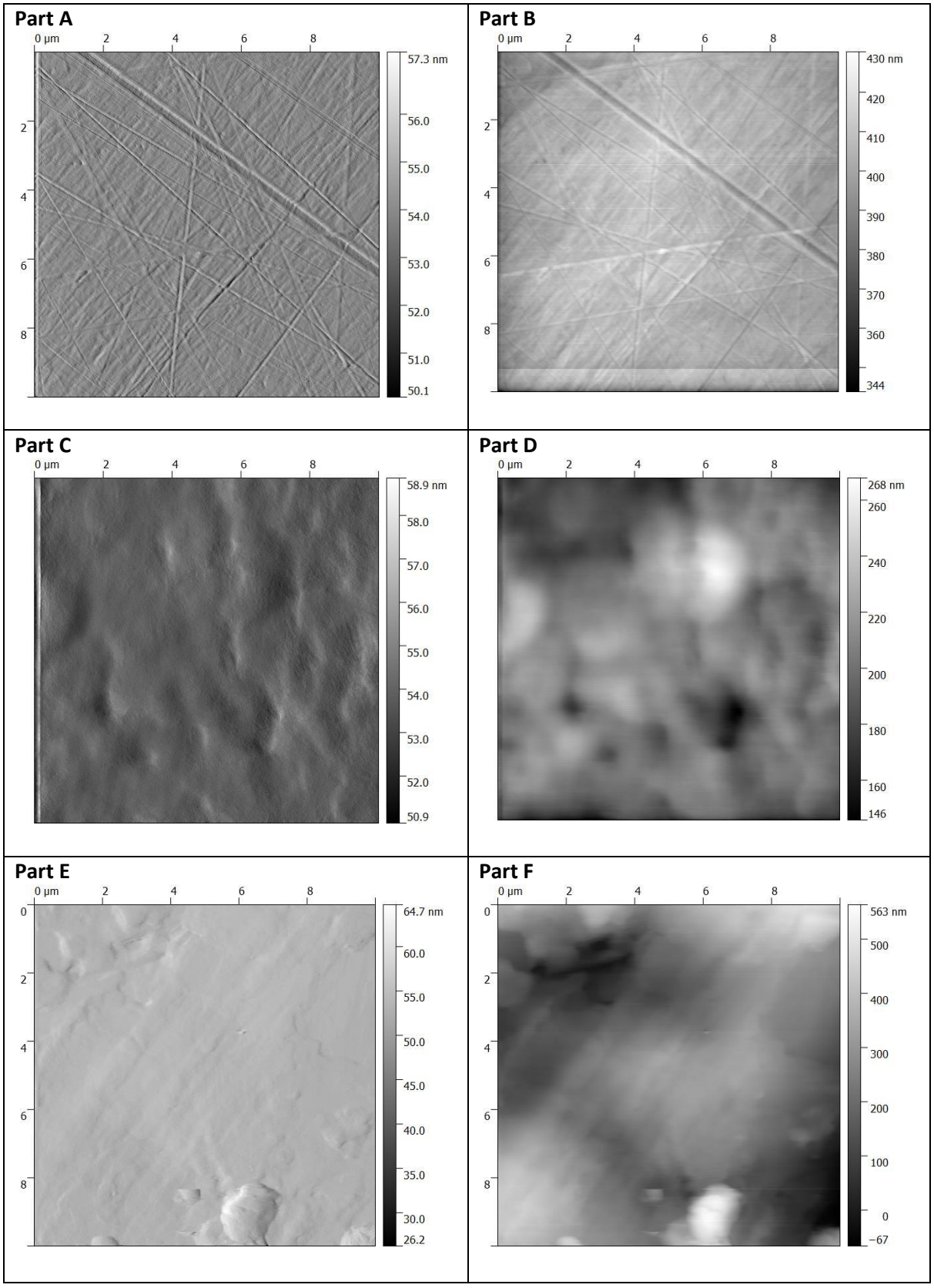

Figure 4.26: AFM images for substrates of pcp (part A), pp (part C), pf (part E), and topological images for substrates of pcp (part B), pp (part D), and pf (part F), all with an evaporated drop of S233 0.1% (aq) non superspreading trisiloxane surfactant in the region of the contact line.

4.9: Conclusions drawn from chapter 4.

The plot of the RAS value versus angle of pp substrate rotation at an energy of 5eV (figure 4.14) indicates most of the RAS signal is coming from the bulk with a characteristic sin(4θ) relation. The centre and edge of the evaporated drop of S240 (0.1%) (aq) on a pp substrate have the same signal as the pp on its own and each other. This relation is also true for the S240 (0.1%) (aq) evaporated drop on a pcp substrate with the centre and edge of the evaporated drop having the same spectra to each other and the pcp on its own. The centre of the evaporated drop of the S240 (0.1%) (aq), the water and pp substrate all have the same RAS spectra and they share this spectra with the edge of the evaporated drop of S233 (0.1%) (aq). The pcp substrate has different RAS spectra for an evaporated drop of water and the shared spectra for the centre of the evaporated drop of S240 (0.1%) (aq) and the pcp on its own. The RAS scans for the edge and centre of an evaporated drop of S233 (0.1%) (aq) on pp and pcp are the same.

In the "dipping" experiment results support the theory that descending films of S240 (0.1%) (aq) contain anisotropic structures and/or a preferred directional alignment of structures in the solution. In comparison the S233 (0.1%) (aq) and water descending films had featureless RA time scans which means the behaviour was isotropic. The "dipping" experiment supports the idea that anisotropic RA signals are related to superspreading. But the work is limited in that it is not possible to say if the anisotropy is at the contact line or to a specific structure e.g. micelles or bi-layers.

In conclusion the AFM has limitations in terms of the ability to detect any adsorbed micelles at the evaporated contact line. This means it is not intended to continue using this technique any further. The limitations of AFM include the difficulty in finding the very small area of interest, and the inability to check large areas in one scan, with images being from a highly localised small area. If there were adsorbed micelles at the contact line it would be very easy to miss them completely.

AFM is not a suitable technique to investigate superspreading, while the RAS does have potential, but at present it has a limitation in the time resolution, which is not sufficiently fast to follow the process in real time.

4.10: Summary of the findings of chapter 4:

- The RAS signal is coming from the bulk of the substrate
- The RAS scans for the centre/edge of the S240 (0.1%) (aq), S233 (0.1%) (aq), water and substrate are identical. There is no evidence that there are structures such as bi-layers when the horizontal substrate RAS experiments were carried out. Possible reasons why no micelle structures located at the contact line of the evaporated drop of S240 (0.1%) (aq) or S233 (0.1%) (aq) were detected are as follows:
- The micellae are not adsorbed;
- The micellae do not survive drying;
- The micellae are not detectable;
- The likelihood of not finding them is low;
- The "dipping" experiment supports the theory that the descending film of S240 (0.1%) (aq) has anisotropy (in terms of alignment and structures) while the S233 (0.1%) (aq) do not.
- The AFM images had a very low probability of finding evidence for micelle structures due to the small size of micelles and the large area to be analysed.
- It was not possible to monitor in real time the contact line as it spread with the RAS technique as the moving contact line was transparent (difficult to see) and was very fast moving.

Chapter 5 – GISAXS investigation into superspreading.

5.1: Aims and Objectives of chapter 5.

Ruckenstein proposed the superspreading of aqueous trisiloxane surfactant drops on hydrophilic surfaces is caused by (1) the spreading at the leading edges of the surfactant as bilayers, (2) the suction of water between the two layers due to the hydrophilic environment, and (3) the increased displacement of the water and surfactant due to the Marangoni effect caused by the formation of bilayers. In this chapter it is intended to test this hypothesis using GISAXS (Grazing Incidence Small Angle X-ray Scattering). GISAXS is a technique which can be used to reveal structures on the surface of solids and films. Primarily this will be done by looking for evidence of bi-layers of micelles at the contact line which will be achieved by looking for spots on the GISAXS images. It will also be possible to find what size these bilayers are by analysing the distance between spots, to support Ruckenstein these should be around 10nm.

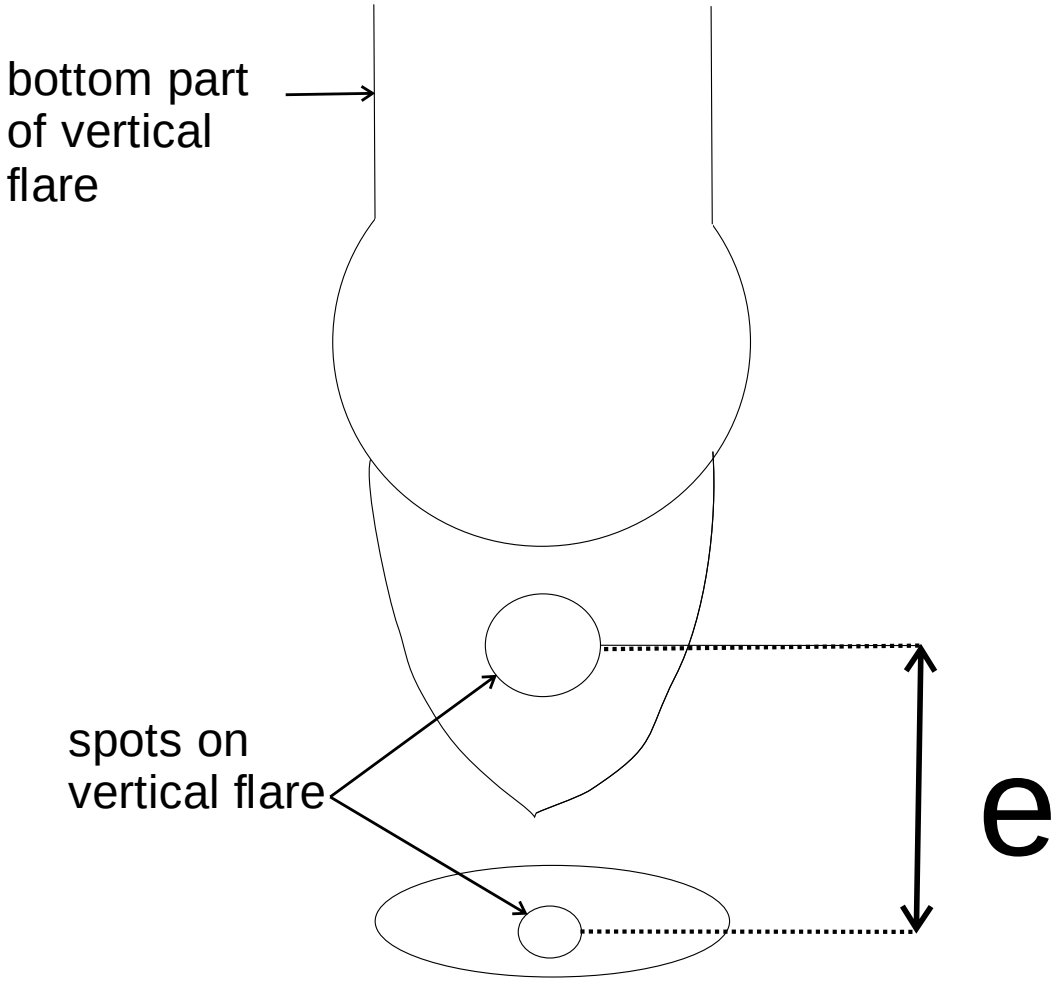

Figure 5.1: Diagram showing a GISAXS image and the dimension labelled "e" used to calculate d for run 1.30 a spreading drop of S240 (0.1%) (aq) on a pp substrate.

Figure 5.1 shows the distance "e" between the spots on the vertical flare, this dimension can be used to calculate the size/dimensions of structures on the substrate surface.

It is thought that the distance "e" is characteristic of micelle structures on the surface of the substrate in particular bilayer structures which aid superspreading. So the hypothesis is that superspreading solution, (S240 (0.1%) (aq)), would have these bilayer micelle structures which aid superspreading and therefore their characteristic spots. Meanwhile the non superspreading S233 (0.1%) (aq) would not have these micelle bilayer structures, or therefore the spots on the GISAXS image.

The micelle bilayer structures thought to be characterised by the spots on the GISAXS images is based on a model put forward by (3)

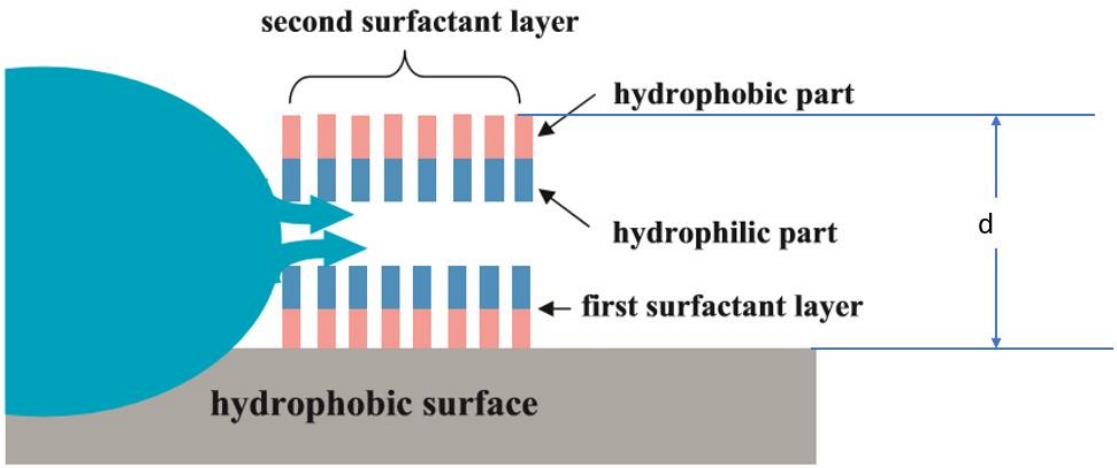

Figure 5.2: Bilayer micelles structures which aid superspreading as proposed by Ruckenstein (3)

The dimension "e" can be used to calculate the bi-layer dimension d shown in figure 5.2. (as shown in section 5.4).

5.2: Introduction to Grazing Incidence Small Angle Scattering (GISAXS).

The technique of Grazing Incidence Small Angle X-ray Scattering (GISAXS) is particularly useful when X-ray Diffraction is not suitable because of the strongly penetrating nature of X-rays which means the signal from the bulk overpowers any surface signal. In GISAXS a grazing-incidence geometry is used which takes advantage of the fact that the refractive index (n) is slightly less then unity, where $= n = 1 - \delta + i\beta$ and δ is related to the scattering properties and β the absorption properties of the material. This grazing incidence geometry causes a

critical incident angle α_c where all the incident radiation undergoes total external reflection and the X-rays only have a limited penetration depth into the sample. This provides surface sensitivity allowing systematic control of the penetration depth by altering the incident angle around the critical incident angle, allowing the structural properties of the different areas of the film on the substrate to be examined. This means with a 2-dimsional detector the out-of-plane and in-plane structural details of the crystallographic orientations relative to the substrate can be probed. GISAXS allows the determination of sample structures and inner electron density fluctuations of deposited material. GISAXS has increased in popularity due to it being able to be performed at experimental stations at synchrotrons. The technique is widely accepted as a useful tool for investigating coatings, films, and particles on surfaces. Typical length scales detectable by GISAXS are of the order of a few nanometers. GISAXS can be used to find what internal or surface morphologies of films, coatings and substrates are present.

The GISAXS experiments were undertaken at BM28 (Xmas) the UK-CRG beamline at the European Synchrotron Radiation Facility (ESRF), Grenoble, France. At the synchrotron a 844m circumference storage ring circulates electrons at an energy of 6 GeV and a current of 200 mA, the storage ring having been fed by a booster ring of 300 m circumference booster ring and a LINAC (Linear accelerator) pre-injector. The X-ray wavelength used in our beamline being 1.24 Angstroms. The sample was mounted on a six-circle Huber diffractometer and the location of the X-ray spot was found using reactive photographic film. A lead beam stop was used to stop the direct beam hitting the detector. Figure 5.3 shows a schematic of a typical synchrotron.

Figure 5.4 taken from (42) shows the working principles of the GISAXS technique. A monochromatic X-ray is incident with the surface along the wavevector k_i, which has a very small incident angle α_i with respect to the sample surface. Normal to the surface plane is the Cartesian z-axis. The x axis is parallel to the surface plane in the same direction as the incident X-ray. The y axis is perpendicular to the x axis in the plane of the surface. The x-rays are scattered along k_f in the direction $(2\theta_f, \alpha_f)$ caused by electron density fluctuations on the surface being analysed.

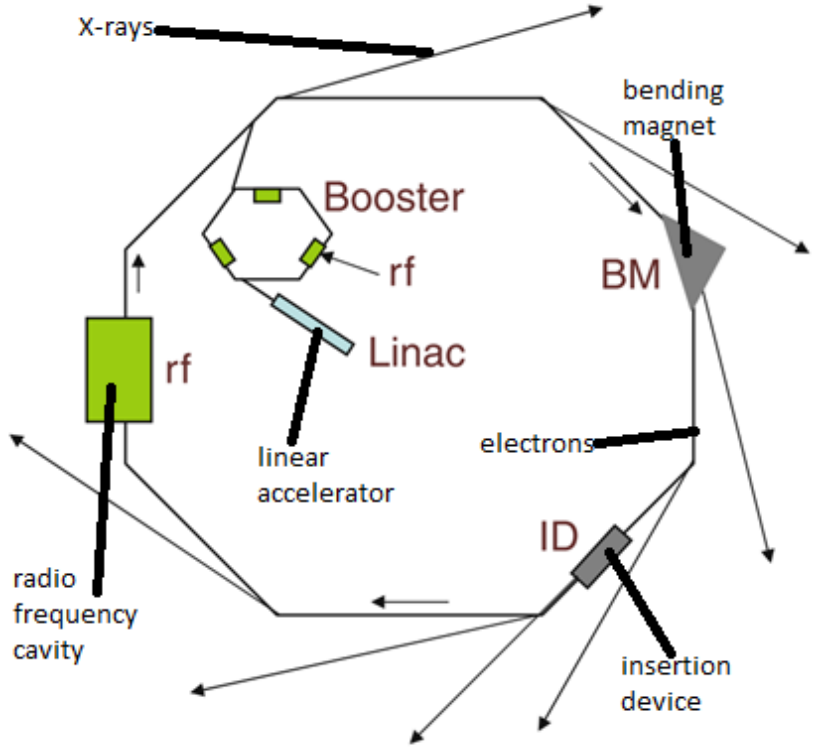

Figure 5.3: Schematic diagram of synchrotron.

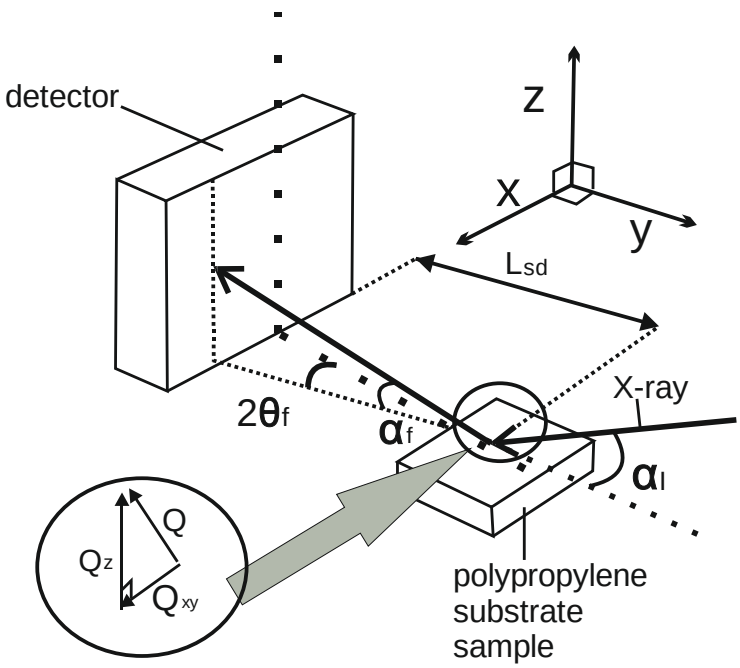

Figure 5.4: Diagram showing the geometry of GISAXS

Beam stops are needed to prevent the direct beam hitting the detector. The raw images are transformed into reciprocal space maps. (Intensity maps are a function of Q_{xy} and Q_z).
GISAXS patterns are presented as false colour maps, with scattering intensity as a log scale. The colour of each pixel shows the intensity of scattered X-rays. The counts per pixel are shown on a scale bar in the bottom left corner.

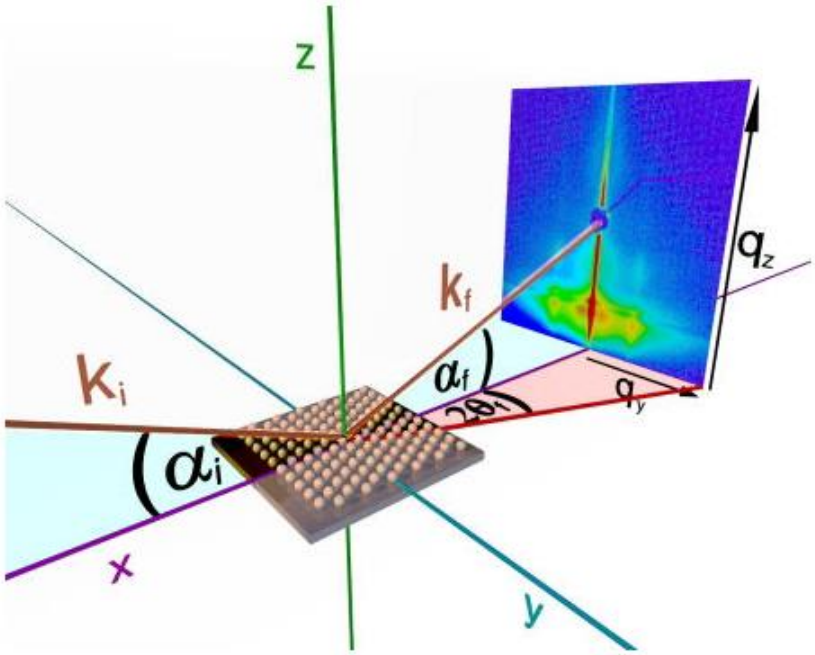

Figure 5.5: GISAXS geometry (43)

In the GISAXS technique the incident X-ray beam is incident at α_i, it is scattered by the film and is viewed on the 2D detector. Scattering features are effected by α_f and $2\theta_f$, which are used to find Q_{xy} and Q_z, the in plane and out of plane scattering vectors.

$$
\begin{aligned}
Q_{xy} &= k\sqrt{(\cos^2\alpha_i - 2(\cos\alpha_i)(\cos 2\theta_f)(\cos\alpha_f) + \cos^2\alpha_f)} \\
Q_z &= k(\sin\alpha_f + \sin\alpha_i) \\
Q &= \sqrt{(Q_{xy}^2 + Q_z^2)} \\
d &= \frac{2\pi}{Q}
\end{aligned}
\tag{5.1}
$$

Figure 5.5 shows the geometry of the GISAXS experiment, with a monochromatic X-ray beam with wavevector k_i shone on a surface with a small incident angle α_i with respect to the surface. Normal to the surface plane is the Cartesian z-axis, the x axis is parallel the beam, and the y axis perpendicular to it. After hitting the surface the X-rays are scattered along the wavevector

k_f in the direction ($2\theta_f$, α_f) by electron density fluctuations by the portion of the surface upon which the X-rays are illuminating.

Figure 5.6 shows the scattering situation of the GISAXS experiment. This situation can only be used for very small angles of α_f and small q_z because the detectorplane and the surface normal aren't completely parallel to one another. This has to be accounted for larger angles. Looking at figure 5.6 the sample horizon scattering is not observable. At the Yoneda Peak the scattering of the material has its maximum and the qz position depends on the critical angle α_c.

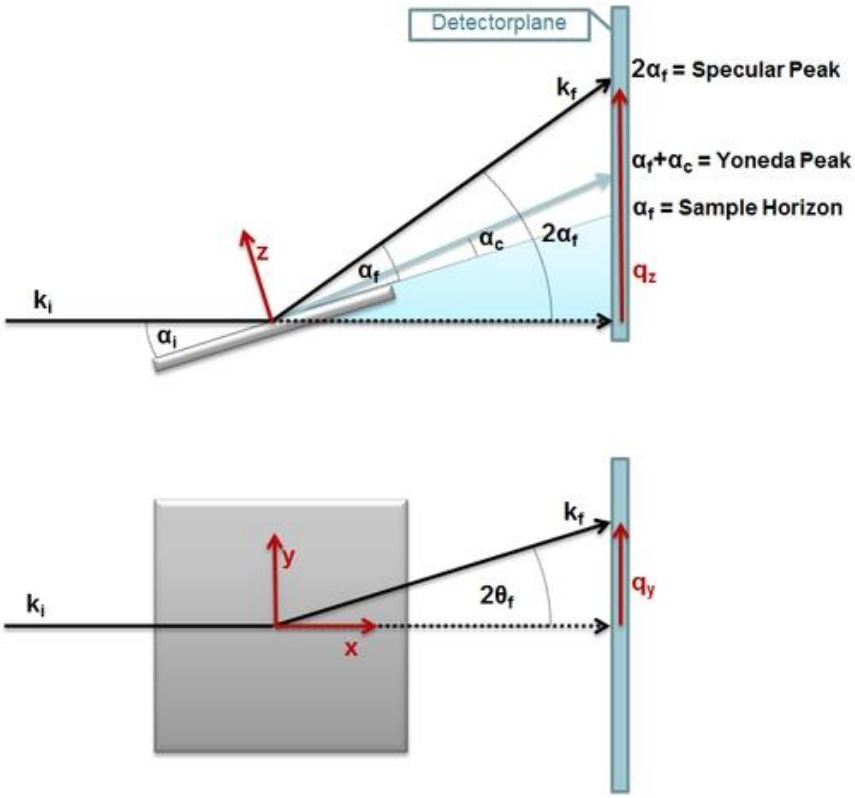

Figure 5.6: Top and side view of a GISAXS experiment taken from (43)

For a lateral electron density fluctuation on the surface the scattering intensity I(q) can be expressed by equation 5.2.

$$I(\bar{q}) = \left\langle |F|^2 \right\rangle S(q_{11}) \tag{5.2}$$

Here F is the Form Factor and S(q) is the total interference function. S(q) describes the spatial arrangement of the objects on the surface and is the Fourier transform of the island position autocorrelation function. When the simple Born approximation (BA) is applied to F, then F is the Fourier transform of the shape function of the objects defined as:

$$F(\bar{q}) = \int_V \exp(i\bar{q} \cdot \bar{r}) d^3 r \tag{5.3}$$

When reflection-refraction effects at the surface have to be considered, F is calculated with the distorted wave Born approximation (DWBA). Combining the calculated form factor within the DWBA together with the total interference function leads to equation 5.4 showing the expression for the total incoherent cross section:

$$\frac{d\sigma}{d\Omega} = \left\langle \left| F_{DWBA} \right|^2 \right\rangle S(q_{11}) \tag{5.4}$$

5.3: Discussion on GISAXS experimental method.

The outline of the method is as follows: Put the substrate where the X-ray beam spot hits the substrate holder, then perform a search of the hutch before interlocking the doors. Open the X-ray beam shutter and align the X-ray beam so it is intersecting the substrate. Dispense a drop of solution using the infra red remote control which turns the syringe pump on and off. Perform a time vs. X-ray intensity scan until the drop has evaporated while continuously taking GISAXS images. Close the shutter then unlock the hutch and prepare the next substrate.

For the GISAXS analysis two different cameras were used for the 2014 (MarCCD) and 2015 data (Pilatus) runs. The spatial resolution of the MarCCD (2014) is higher (~74 micron pixel size) compared to the Pilatus (2015) camera (172 micron pixel size). The time resolution of the Pilatus (20Hz in brochure = 0.05 sec per frame at best) is greater than the MarCCD (2014) (~1 sec per frame at best).

Figure 5.7 to figure 5.13 show digital photographs of the GISAXS equipment in the Xmas beamline in the ESRF.

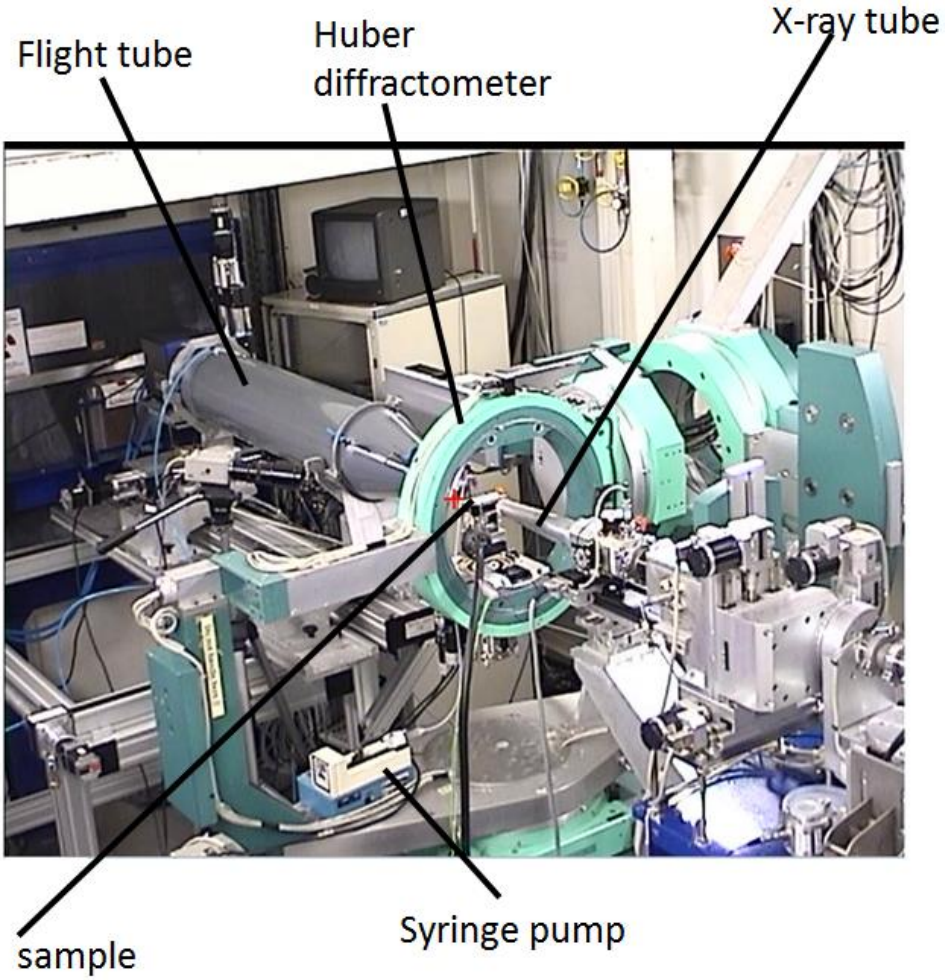

Figure 5.7: Labelled photograph of GISAXS set up from aerial camera.

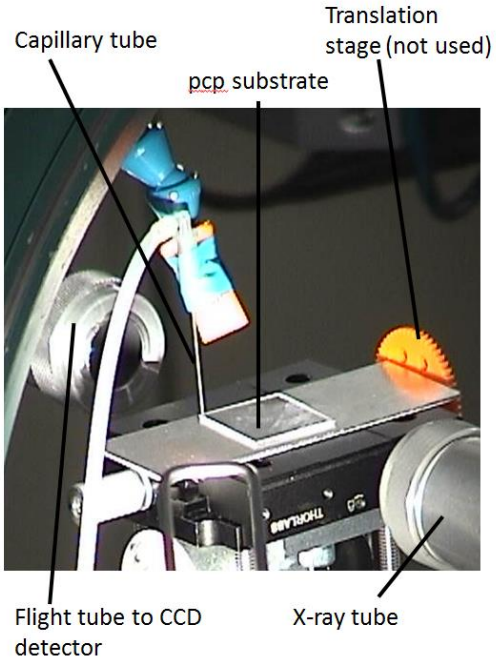

Figure 5.8: Zoomed in photograph of sample set up

Figure 5.9 : Looking toward the diffractometer in the experimental hutch for XMas beamline 28 in the ESRF, taken from (A)

Figure 5.10 : Looking down the beamline from the diffractometer in the experimental hutch for Xmas beamline 28 in the ESRF.

5.4: Method for calculating the bi-layer dimension d from the position of the spots on the vertical flare of the GISAXS images, (with worked example for run 1.27).

- The first step is to calculate the difference in pixels between the co-ordinates of the two spots on the vertical flare of the GISAXS image. The lower spot has the co-ordinates x'_{pix}, y'_{pix} and the higher spot x'_{dir}, y'_{dir}.

	x	y
lower spot image	326	327
higher spot image	328	335

$y'_{pix} - y'_{dir} = -8$ pixels, $x'_{pix} - x'_{dir} = -2$ pixels.

We now ignore the minus sign which gives us:

$y'_{pix} - y'_{dir} = 8$ pixels, $x'_{pix} - x'_{dir} = 2$ pixels.

- The next step is to change the difference in pixels to a real distance. Each pixel is equivalent to 1.72×10^{-6} m or 1.72 Microns.

$$\Delta y = (y'_{pix} - y'_{dir}) \times 1.72 \times 10^{-6} = 8 \times (1.72 \times 10^{-6}) = 1.38 \times 10^{-5} \quad \text{m}$$

$$\Delta x = (x'_{pix} - x'_{dir}) \times 1.72 \times 10^{-6} = 2 \times (1.72 \times 10^{-6}) = 3.44 \times 10^{-6} \quad \text{m}$$

- The out of plane scattering (α_{f0}) is then calculated with the sample-detector distance L_{SD} being 1.252 m:

$$\alpha_{f0} = a\tan\left(\frac{\Delta y}{\sqrt{\left(\Delta x^2 + L_{SD}{}^2\right)}}\right) = a\tan\left(\frac{1.38 \times 10^{-5}}{\sqrt{\left((3.44 \times 10^{-6})^2 + 1.252^2\right)}}\right) = 1.09904 radians$$

- The in-plane scattering angle ($2\theta_{f0}$) is then calculated:

$$2\theta_{f0} = a\tan\left(\frac{\Delta x}{L_{SD}}\right) = a\tan\left(\frac{3.44 \times 10^{-6}}{1.252}\right) = 2.75 \times 10^{-6} radians$$

- The in plane scattering angle ($2\theta_f$) is constant when the incident angle is non zero:

$$2\theta_f = 2\theta_{f0}$$

- The out of plane scattering angle (α_f) must be converted from the lab frame to the surface frame:

$$\alpha_f = \alpha_{f0} - \alpha_i \cos(2\theta_f) = 1.099 - (0.007 \times (\cos(2 \times 2.75 \times 10^{-6})) = -0.00697033 radians$$

- Once the scattering angles are determined the wavevector transfer Q components can be calculated:

$$Q_z = k\left((\sin(\alpha_f) + (\sin(\alpha_i)\right)$$
$$Q_x = k\left((\cos(\alpha_f)\cos(2\theta_f) - \cos(\alpha_i)\right)$$
$$Q_y = k(\cos(\alpha_f)\sin(2\theta_f))$$
$$Q_{xy} = \sqrt{\left(Q_x^2 + Q_y^2\right)} = k\sqrt{\left(\cos^2(\alpha_i) - 2\cos(\alpha_i)\cos(2\theta_f)\cos(\alpha_f) + \cos^2(\alpha_f)\right)}$$
$$Q = \sqrt{\left(Q_{xy}^2 + Q_z^2\right)}$$

- For simplicity I have calculated the following terms below to show in the worked example of the calculation of the Q wavevector:

$$\alpha_i = 0.4° = 0.0070 radians$$
$$E(J) = E(eV) \times 1.6 \times 10^{-19} = 10000 \times 1.6 \times 10^{-19} = 1.6 \times 10^{-15}\, J$$
$$\lambda = \frac{hc}{E} = \frac{6.63 \times 10^{-34} \times 3 \times 10^{8}}{1.6 \times 10^{-15}} = 1.24 \times 10^{-10}\, m$$
$$k = \frac{2\pi}{\lambda} = \frac{2\lambda}{1.24 \times 10^{-10}} = 50543471551$$
$$\sin(\alpha_f) = \sin(1.56) = -0.00697$$
$$\sin(\alpha_i) = \sin(0.007) = 0.006981$$
$$\cos(\alpha_f) = \cos(1.56) = 0.999976$$
$$\cos(2\theta_f) = \cos(2 \times 2.75 \times 10^{-6}) = 1$$
$$\cos(\alpha_i) = \cos(0.007) = 0.999976$$
$$\cos(\alpha_f) = \cos(1.56) = 0.999976$$
$$\sin(2\theta_f) = \sin(2 \times 2.75 \times 10^{-6}) = 5.5 \times 10^{-6}$$

- Below is the worked example of the Q wavevector.

$$Q_z = 50543471551 \times \left(-0.00697 + 0.006981\right) = 5554802345$$
$$Q_x = 50543471551 \times (0.999976 \times 1 + 0.999976) = 3874230.863$$
$$Q_y = 50543471551 \times (0.999976 \times 5.5 \times 10^{-6}) = 277740125.2$$
$$Q_{xy} = \sqrt{\left((3874230.863)^2 + (277740125.2^2\right)} = 277767145$$
$$Q = \sqrt{\left(277767145^2 + 555480234.5^2\right)} = 621057869.8$$

- The final part of the calculation is to calculate the d-spacing (bi-layer dimension d):

$$d = \frac{2\pi}{Q} = \frac{2\pi}{621057869\ .8} = 1.012 \times 10^{-8} = 10.12\, nm$$

5.5: GISAXS results – Introduction.

Figure 5.11 shows the 4 main stages that the spreading drop undergoes as it spreads through the X-ray beam in the GISAXS experiment.

Figure 5.12 shows an example of a count versus time for run 1.32. The region of interest is shown with black dashed lines, and is the area in time in which the GISAXS images shown in figure 5.13 are shown spaced equally in time. The region of interest is between regions B and C (region boundaries shown in figure 5.11). Count versus time graphs and GISAXS images for all the runs mentioned in this chapter can be found in appendix B.

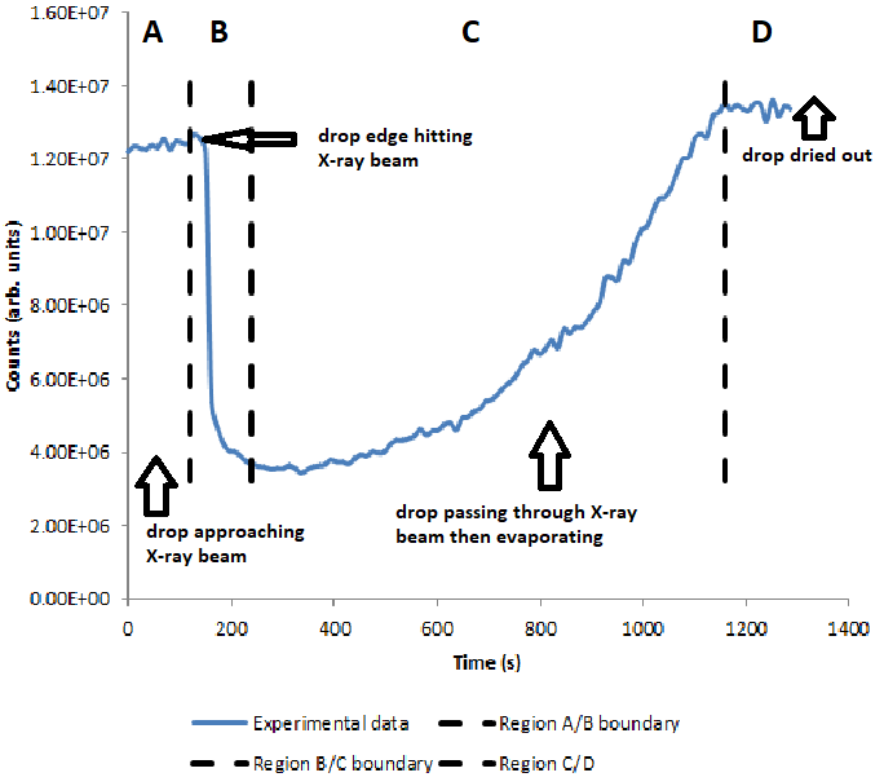

Figure 5.11: The 4 main stages the spreading drop undergoes in the GISAXS experiment.

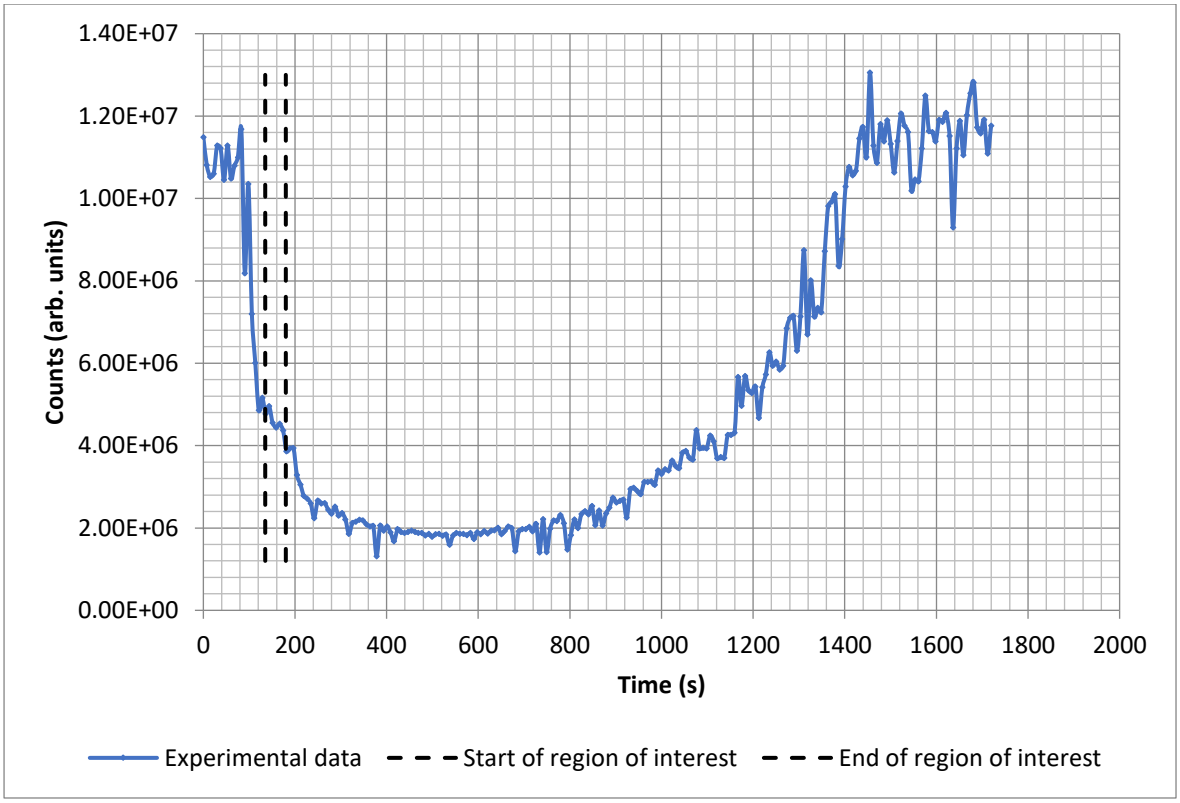

Figure 5.12: Example count versus time graph for drop of S240 (0.1%) (aq) spreading on pp substrate for run 1.32.

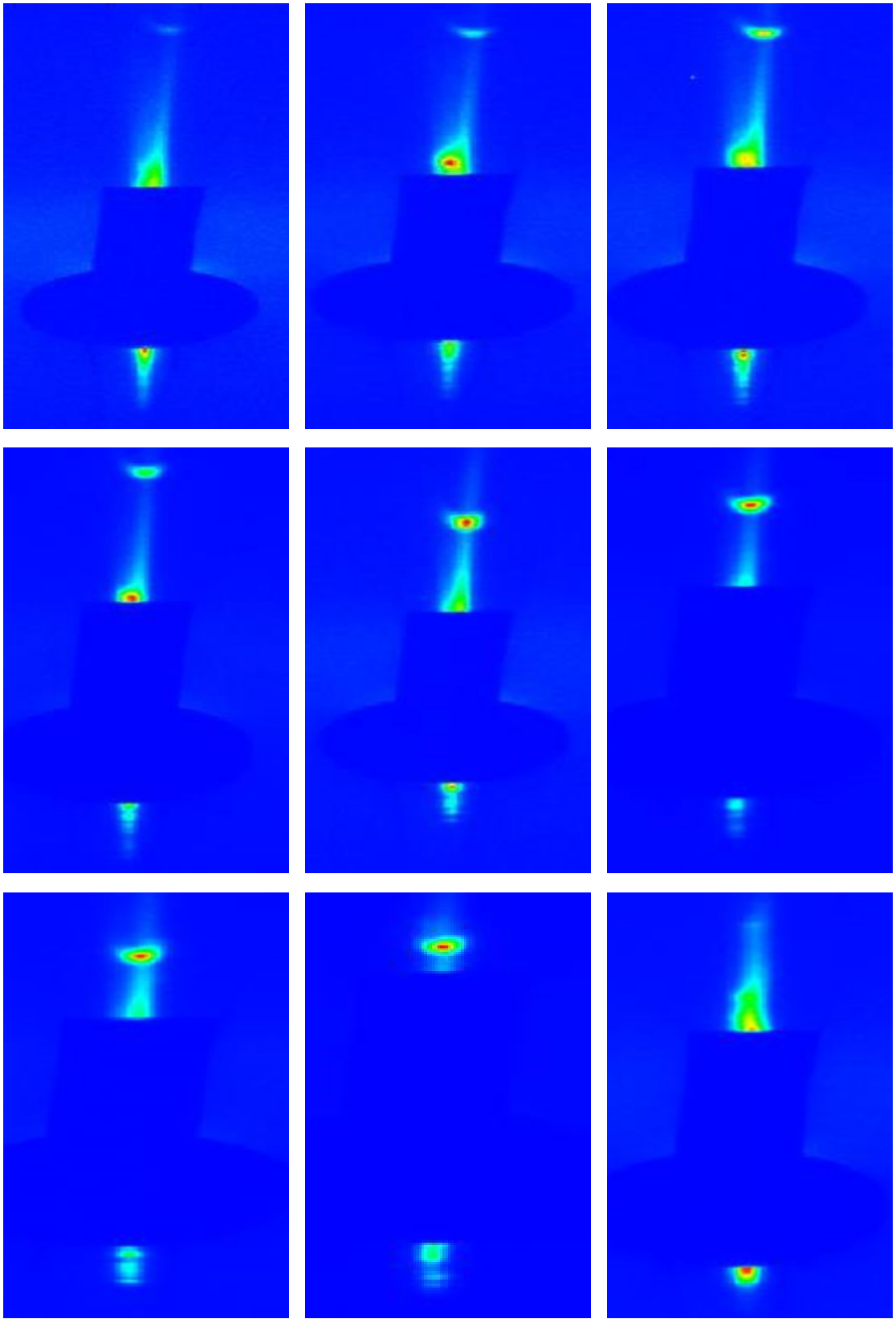

Figure 5.13: Example GISAXS images of S240 (0.1%) (aq) superspreading solution on polypropylene substrate showing periodic spots on both bottom and top vertical flare. Run 1.32.

5.6: Main GISAXS results.

In total two sets of GISAXS experiments were carried out one in summer 2014 and one in winter in 2015. For the data taken in 2014 data compared to the 2015 data different cameras were used (as discussed earlier) with different resolutions, also different shaped beamstops were used to stop over saturation of the detector.

In table 5.1 the 2014 GISAXS images were no spots were visible on the vertical flares are shown. Table 5.2 shows the 2015 negative results.

Substrate	Surfactant solution	image run
pp	S240	1.1
pp	S240	1.2
pp	S240	1.3
pp	S240	1.4
pp	S240	1.5
pp	S240	1.6
pp	S240	1.7
pp	S240	1.8
pp	S240	1.9
pp	S240	1.10
pp	S240	1.11
pp	S240	1.12
pp	S240	1.13
pp	S240	1.14
pp	S240	1.15
pcp	S240	1.16
pf	S240	1.17
pf	S240	1.18
pcp	S233	1.19
pcp	S233	1.20
pcp	S233	1.21
pcp	S233	1.22
pcp	S233	1.23
pf	S233	1.24
pf	S233	1.25
pf	S233	1.26

Table 5.1: 2014 GISAXS images with a negative result in terms of no spots being visible on the vertical flares.

Substrate	Surfactant solution	new image run
pp	S240	2.1
pp	S240	2.2
pp	S240	2.3
pp	S240	2.4
pp	S240	2.5
pp	S240	2.6
pp	S240	2.7
pp	S240	2.8
pp	S240	2.9
pcp	S240	2.1
pcp	S240	2.11
ac	S240	2.12
ac	S240	2.13
pp	S233	2.14
pp	S233	2.15
pp	S233	2.16
pp	S233	2.17
pp	S233	2.18
pp	S233	2.19
pp	S233	2.2
pcp	S233	2.21

Table 5.2: 2015 GISAXS images with a negative result in terms of spots being visible on the vertical flares.

Every third image taken of the 2014 data was analysed for evidence of spots on the vertical flares, table 5.3 shows those experimental runs with this positive result. In table 5.3 "x pix 1" is the shortened notation for the position 1 of the x pixel and so on for the other 3 columns, while "d" is the calculated bilayer dimension.

Substrate	Surfactant solution	Image run	x pix 1	y pix 1	x pix 2	y pix 2	d (nm)	Region
pp	S240 (0.1%) (aq)	1.27	326	327	328	335	10.12	B/C
pp	S240 (0.1%) (aq)	1.28	310	5.17	311	353	10.97	B
pp	S240 (0.1%) (aq)	1.29	324	342	322	352	8.4	C
pp	S240 (0.1%) (aq)	1.30	308	346	307	359	6.88	A
pp	S240 (0.1%) (aq)	1.31	312	308	316	323	5.32	A
pp	S240 (0.1%) (aq)	1.32	316	323	316	330	12.43	A
pp	S233 (0.1%) (aq)	1.33	315	329	316	334	16.8	C
pp	S233 (0.1%) (aq)	1.34	330	305	329	322	5.29	C
pp	S233 (0.1%) (aq)	1.35	314	327	314	333	15.08	C
pcp	S233 (0.1%) (aq)	1.36	313	318	314	327	9.81	B

Table 5.3: 2014 GISAXS images with a positive result in terms of spots being visible on the vertical flares.

For the 2015 GISAXS data there were a huge number of scans (much more then the 2014 data) so I only analysed experimental runs with parts of the data taken from region B (see figure 5.14). Table 5.5 shows the experimental runs with a positive result for spots on the vertical flares of the GISAXS images.

Substrate	Surfactant solution	new image run	x pix 1	y pix 1	x pix 2	y pix 2	d (nm)	Region
pp	S240 (0.1%) (aq)	2.22	243	494	244	500	14.31	B
pp	S240 (0.1%) (aq)	2.23	243	488	243	498	9.05	B
ac	S233 (0.1%) (aq)	2.24	243	527	243	529	45.24	B
ac	S233 (0.1%) (aq)	2.25	239	526	239	528	45.24	B
ac	S233 (0.1%) (aq)	2.26	239	502	237	511	9.19	B
ac	S233 (0.1%) (aq)	2.27	239	493	239	509	5.49	B

Table 5.4: 2015 GISAXS images with a positive result in terms of spots being visible on the vertical flares.

When analysing the d calculations it has been decided to include in the mean and standard deviation calculations image runs 1.29, 1.30, 1.31, 1.32, 1.33, 1.34 and 1.35 because for a lot of these runs they are just outside region B which is defined in figure 5.14.

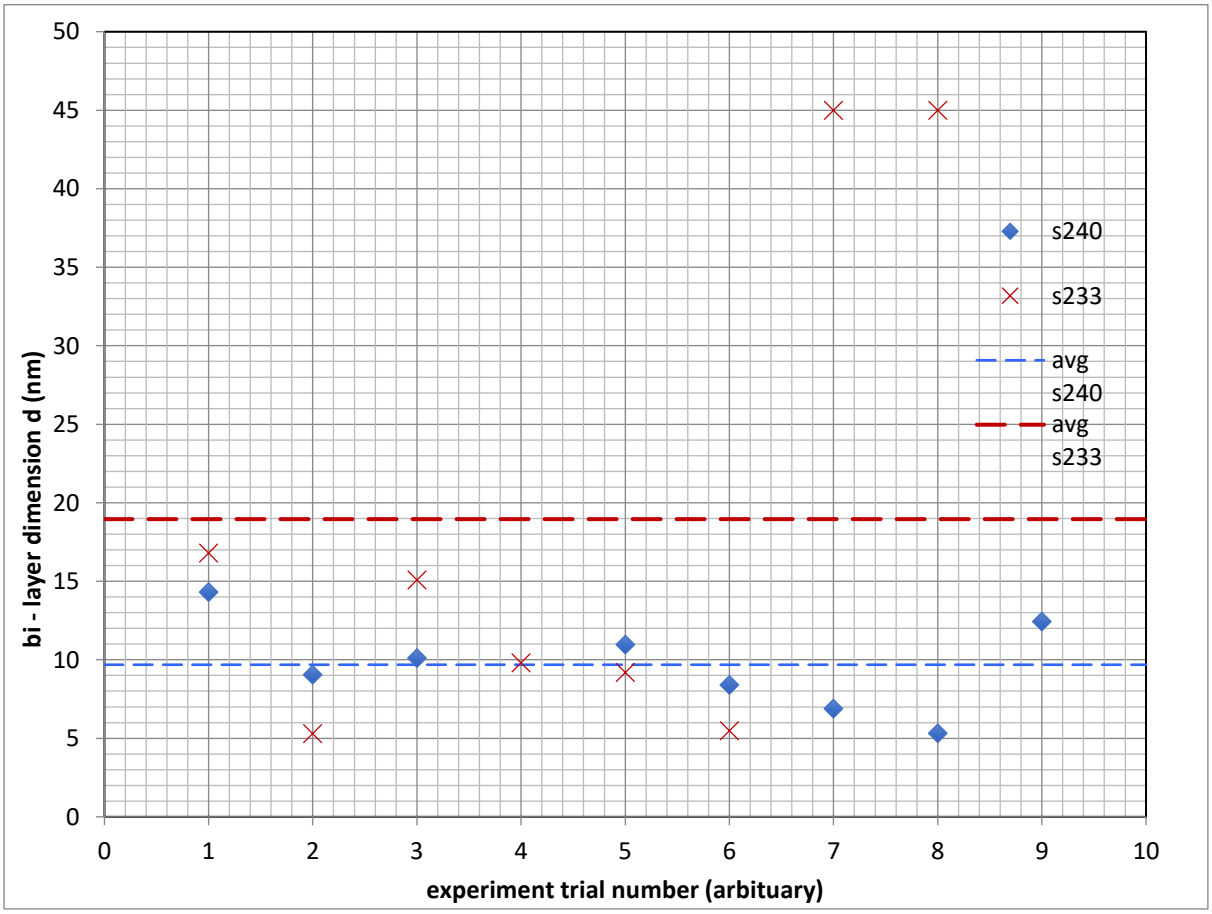

Figure 5.14: Scatter of S233 (0.1%) (aq) and S240 (0.1%) (aq) bilayer dimension d data.

Figure 5.17 shows the mean bilayer dimension and standard deviation for the S233 (0.1%) (aq) and S240 (0.1%) (aq) GISAXS data.

	S233 (0.1%) (aq)	S240 (0.1%) (aq)
mean d (nm)	18.96	9.69
standard deviation of mean d calculation (nm)	16.58	2.92

Table 5.5: Mean and Standard Deviation of the bilayer dimension d calculation for the combined 2014 and 2015 GISAXS experimental runs.

The standard deviation is calculated using equation 3.2, where σ is the standard deviation, x_i is a value of d, $\bar{x}$ is the mean d, and N is the number of values of d.

$$\sigma_{n-1} = \sqrt{\frac{\sum\left(x_i - \bar{x}\right)^2}{N-1}} \tag{3.2}$$

A low standard deviation indicates the data points are close to the mean, a higher standard devation indicates the data points are spread out over a wider range of values.

5.7: Conclusions for GISAXS data.

The data from the S240 (0.1%) (aq) experimental runs indicates the presence of molecular layering with a thickness of approximately 10 nm. On the contrary, data for the S233 (0.1%) (aq) solutions exhibit a large scatter with a standard deviation comparable to the mean value. This suggests that measurements obtained for the S233 solution are not conclusive therefore it is likely no consistent structure of layering occurs.

The 10nm thickness of the layer is bigger then the size of a water molecule at 2.75 Angstroms and a generic surfactant size of around 5nm. (Actual sizes of the S244 and S233 surfactant molecules are unavailable as they are patented). These magnitudes of water and generic surfactant molecule size compared to the layer size of 10nm is compatible with the scenario put forward by Ruckenstein. Whilst there is no direct evidence that the layer is due to surfactants, (as it could be just water molecules) , the observation that the S233 does not have a layer probably suggests the layer does contain S240 molecules.

Chapter 6 – Conclusions.

6.1: Conclusions

In chapter 3 spreading drops of superspreading S240 (0.1%) (aq) and non-superspreading S233 (0.1%) (aq) were deposited on a pp, pf and pcp substrates. Parafilm was the most hydrophobic substrate with an equilibrium contact angle of 105^{o}, followed by polypropylene at 97^{o} then polycarbontate plastic sheet at 86^{o}. As expected the more hydrophobic substrates had lower power law exponents (b) with pf, pp and pcp having values for the power law fit to the S240 (0.1%) drop of 0.3316, 0.3834, 0.4737, and the S233 (0.1%) drop of 0.2502, 0.2615, and 0.3494.

From looking at the drop diameter versus time graphs for the spreading drops of S240 (0.1%) (aq) and S233 (0.1%) (aq) on pp, pf and pcp substrates it is clear that:

- On all substrates (pp, pf and pcp) the superspreading S240 (0.1%) (aq) spreads to its final state diameter more rapidly then the S233 (0.1%) (aq) drop.
- The S240 (0.1%) (aq) drop reaches a larger final diameter size for its final state then the S233 (0.1%) (aq) drop for all substrates
- The S240 (0.1%) (aq) drop on a pcp substrate spreads to a larger final diameter faster then the pp and pf drop substrates which behave very similarly.
- The S233 (0.1%) (aq) drop on a pcp substrate spreads to a larger final diameter more rapidly then a similar drop on the pp substate, which in turn spreads at about the same rate as the pf substrate but to a larger final diameter.

The drop contact angle versus time graphs had the following observations:

- On all substrates (pp, pf and pcp) the S240 (0.1%) drop spread to a smaller contact angle in a shorter time then the S233 (0.1%) drop.
- The S240 (0.1%) (aq) drop spreads to its final contact angle more rapidly on a pcp substrate then the pp and pf substrates all though all have a similar final contact angle.
- The S233 (0.1%) (aq) drop spreads on a pcp substrate more rapidly and to a smaller final contact angle then the drop on a pp and pf substrates which behave in a similar way.

For both the drop diameter versus time and contact angle versus time graphs the drops of S240 (0.1%) (aq) and S233 (0.1%) (aq) on a pcp substrate behaved significantly differently then the pp and pf substrates whose drop of S240 (0.1%) (aq) and S233 (0.1%) (aq) behaved similarly.

The pcp substrate's S240 (0.1%) (aq) and S233 (0.1%) (aq) drop was significantly more rapid in reaching its final drop state and with the exception of the contact angle versus time graph for the S240 (0.1%) (aq) solution the final state was a larger drop dimeter and smaller contact angle then the pp and pf substrate's drops. A possible reason for this is that the pcp is manufactured with a plastic film covering the pcp surface, to perform the experiment this film had to be removed, in doing this it is likely the pcp surface was charged up with static electricity. It is known that charging a surface effects the way some drops spread on it.

The drop diameter versus time and contact angle versus time data was fitted with a simple power law and exponential fit and these two fits were then compared revealing the following:

- With the exception of the pcp substrate power functions fitted the drop diameter versus time data better then the exponential functions.
- For the contact angle versus time graphs most fits were better fitted by exponential functions then power law functions, only the pf substrate was better fitted by a power function.

Graphs were plotted for the drop dimeter versus time data this time with a log x and y axis, and simple power laws were used to fit the data. The data showed evidence of more then one regime for some S240 (0.1%) (aq) and S233 (0.1%) (aq) drops on pp, pf and pcp substrates, the results were as follows:

- The drop of S240 (0.1%) (aq) and S233 (0.1%) (aq) drop on pp both exhibit 2 regimes when the diameter and time are plotted with log axis.
- The S233 (0.1%) (aq) drop on pf and pcp has two regimes when the diameter and time axis are plotted with a log scale.
- The S240 (0.1%) (aq) drop on pf and pcp both have 1 regime when the diameter and time are plotted on log scales.

The reasons why some of the graphs had two regimes are as follows:

As the drop spreads the increasing surface area of the drop causes a dilution of the number of surfactant molecules per unit surface area which effects the surface tension. At some point there may be no more molecules available in the bulk. Young's equation shows the Young-Laplace force is affected by the surface tension of the liquid (γ_{LG}).

$$F = \gamma_S - \gamma_{SL} - \gamma_L \cos\theta \tag{1.2}$$

When the free surface of the liquid is saturated with surfactant molecules, (i.e. there is an excess of surfactant molecules that cannot go to the surface because there is no space for them), micelles can form in the bulk of the surfactant solution. If the free surface increases due to spreading then there is more space available allowing some molecules belonging to micelles in the bulk leave the micelle and migrating to the free surface. If there are a lot of molecules migrating to the surface this may decompose several micelles.

In the novel RAS experiments in chapter 4 work was carried out to try and see if there was evidence that there was a characteristic RAS spectra for an anisotropic signal from micelles adsorbed at the contact line for the superspreading S240 (0.1%) (aq) solution drop when evaporated. How ever there was no such evidence and it was concluded that the following one or more reasons why applied:

- The micellae are/are not adsorbed.
- The micellae do/do not survive drying.
- The micellae are/are not detectable
- The likelihood of not finding them is low.

It is thought that the RAS signal is coming from the bulk of the substrate. RAS scans for the centre/edge of the S240 (0.1%) (aq), S233 (0.1%) (aq), water and substrate are identical. There is no evidence that there are structures such as bi-layers when the horizontal substrate RAS experiments were carried out.

The aim of the novel "dipping" experiment is to investigate whether the superspreading S240 (0.1%) (aq) encourage the creation of ordered macromolecular structures (e.g. micelles or bi-layers) which could help explain how superspreading works. In the dipping experiments a pp or pcp substrate was placed vertically and a film of S240 (0.1%) (aq), S233 (0.1%) (aq), or water was allowed to descend under gravity on the substrate surface through a RAS light spot which analysed the light and produced a RAS spectra.

There were two main types of property to the DC scans with either one or two-step change in the DC signal. The two-step behaviour could be due to the presence of a "bulk" film receding first followed by a thinner "interfacial" film. The maximum anisotropy of the two-step behaviour is between the first and second step changes in the DC signal. This could be explained by the possibility that the anisotropic thin surface layer exists on the substrate during this time period. The biggest anisotropy signal for the one-step results could be due to a temporal anisotropic surface layer. It is possible this layer might be lost by evaporation. The

RA signal versus time spectra for water are flat and without peaks or features which means the water film is isotropic. The reflectivity scans (DC scans) for the descending S233 (0.1%) (aq) and water films are flat and featureless indicating the light is reflected in a uniform way as the film moves down the substrate under gravity.

In the "dipping" experiment results support the theory that descending films of S240 (0.1%) (aq) contain anisotropic structures and/or a preferred directional alignment of structures in the solution.

AFM scans of the pp, pcp and pf substrates for S240 (0.1%) (aq), S233 (0.1%) (aq) and water did not find evidence of micelle structures at the contact line and the 4 reasons why are noted above. The limitations of AFM for investigating superspreading are discussed in the next section.

In chapter 5 the GISAXS technique was used for the first time to see if there was experimental evidence supporting Ruckenstein's model (9) which is used to explain superspreading.

The data from the S240 (0.1%) (aq) experimental runs indicates the presence of molecular layering with a thickness of approximately 10 nm. On the contrary data for the S233 (0.1%) (aq) solutions exhibit a large scatter with a standard deviation comparable to the mean value which suggests no layering occurs. The 10nm thickness of the layer is bigger then the size of a water molecule at 2.75 Angstroms and a generic surfactant size of around 5nm. (Actual sizes of the S244 and S233 surfactant molecules are unavailable as they are a patented secret). These magnitudes of water and generic surfactant molecule size compared to the layer size of 10nm is compatible with the scenario put forward by Ruckenstein. Whilst there is no direct evidence that the layer is due to surfactants, (as it could be just water molecules) , the observation that the S233 does not have a layer probably suggests the layer does contain S240 molecules.

6.2: Limitations to this work.

- In chapter 3 it would have been useful to have a video camera mounted vertically above the spreading drop to record how the whole drop spreads. This may have shown "fingering" at the contact line which may be important in explaining superspreading.
- It was not possible to look at drops on a pf substrate with RAS as it was too opaque.
- It would have been better if the drops had been wet while being investigated as the contact line spreads. It seems likely that any micelles structures that may aid

superspreading at the contact line are destroyed when evaporated. This was a common limitation for both chapter 4 and 5.

- When using AFM it was extremely difficult to find such a small thing such as micelles structures at the contact line because the AFM looks at a highly localised area.

6.3: Future work on superspreading.

- The pcp substrate's drop was significantly more rapid when spreading in attaining the larger drop diameter and smaller contact angle, and in the shortest time, for both the S240 (0.1%) (aq) and S233 (0.1%) (aq) then the pp and pf substrates. It would seem a good approach to understanding superspreading would be to find out why. In particular it is thought static electricity might be involved because the pcp substrate had a protective plastic film which was removed before the spreading experiments took place.

- It would have been useful if when using RAS, the technique could have been used while the drop spreads while still wet, and the scan taking place at the moving contact line in real time. To do this the RAS light spot and the dynamic spreading contact line would have to move together in a synchronised way so the light spot was always focused on the spreading periphery of the drop. This would require some non-trivial computer coding and a means of moving the experimental stage holding the substrate relative to the RAS light spot. There would also have to be some dummy runs moving the light spot synchronised to the speed of the spreading drop's contact line so the stage is moved at the correct speed.
- Another problem with the previous point is that the spreading drop is transparent and so very difficult for the human eye or an image detecting camera to observe. When the surfactant solutions spread to make it visually easier to observe it could have been possible to use talcum powder in the solution.
- When using AFM it could have been possible to write a computer program that could find the small area where the micelles were thought to be all though this would be highly challenging. This computer program would have to search the surface for objects that would look like micelle structures. To do this there would have to be an interface between the machinery that moves the AFM tip and the program that is trying to find these structures. Some sort of code that can identify micelle structures from video images would also be required.

- While using the GISAXS technique it would have been informative to have a translation stage which moved the substrate so the X-ray spot was always on the contact line as the drop spreads. This is a similar problem to that discussed about the RAS technique although even more difficult because the moving stage would have to be operated remotely from outside the beam hutch. As with the RAS technique the stage would have to move synchronously with the spreading contact line of the drop. Practically this would involve dummy runs to tune the moving speed of the translation stage to the speed of the spreading contact line.
- When taking video images of the spreading drops in chapter three it would have been useful to take video images from a "birds eye view" so the spreading drop could be analysed with a different perspective. In the literature the formation of "fingers" in a spreading drop's contact line is used to support the Marangoni effect. It would have been very interesting to see if the surfactant drops broke into these fingers and what this would support in terms of different superspreading mechanisms.
- In the literature there is some discussion about the effect of humidity on superspreading it would have been interesting to investigate this further.
- It would be useful to increase the scale of the number of surfactant solutions tested, and the number of substrates tested (all though there is a limited number). It would be useful to see what the results were for the most commonly used surfactant Silwet L-77.
- It would be useful to find new substrates that allow superspreading on them, then to carefully analyse what these substrates have in common, in doing so this might reveal why they allow superspreading on them.

Appendix A

In this appendix all the RAS and reflectivity graphs not included in chapter 4 are shown. This appendix relates to the work done in chapter 4. The first 8 reflectivity graphs correspond to the RAS graphs shown in chapter 4.

Figure	Method number used.
A.1	2
A.2	3
A.3	3
A.4	3
A.5	3
A.6	3
A.7	3
A.8	3
A.9	3
A.10	3
A.11	3
A.12	3
A.13	3
A.14	3
A.15	3
A.16	3
A.17	3
A.18	3
A.19	3
A.20	3
A.21	3
A.22	3
A.23	3
A.24	3
A.25	3
A.26	3
A.27	3
A.28	3
A.29	3
A.30	3
A.31	3
A.32	3
A.33	3
A.34	3
A.35	3
A.36	3

Table A.1: Method type used in RAS figures in appendix A.

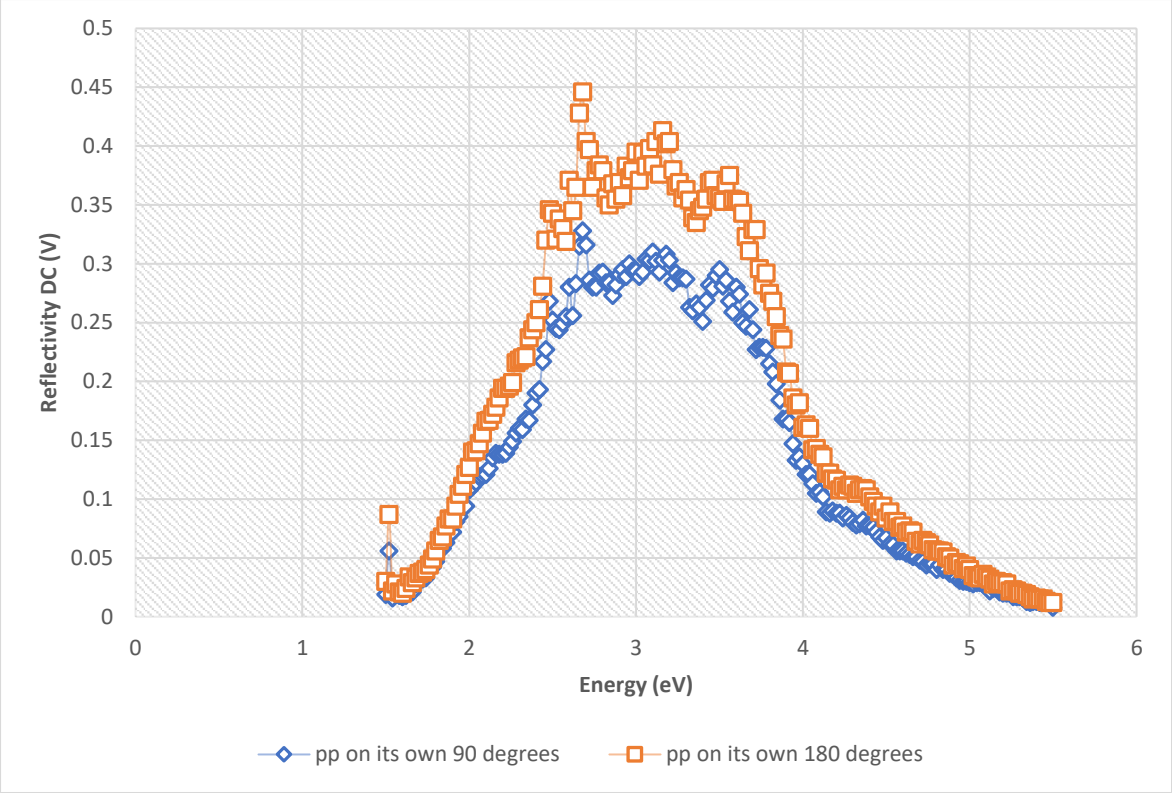

Figure A.1: Reflectivity scans of pp substrate in two perpendicular directions.

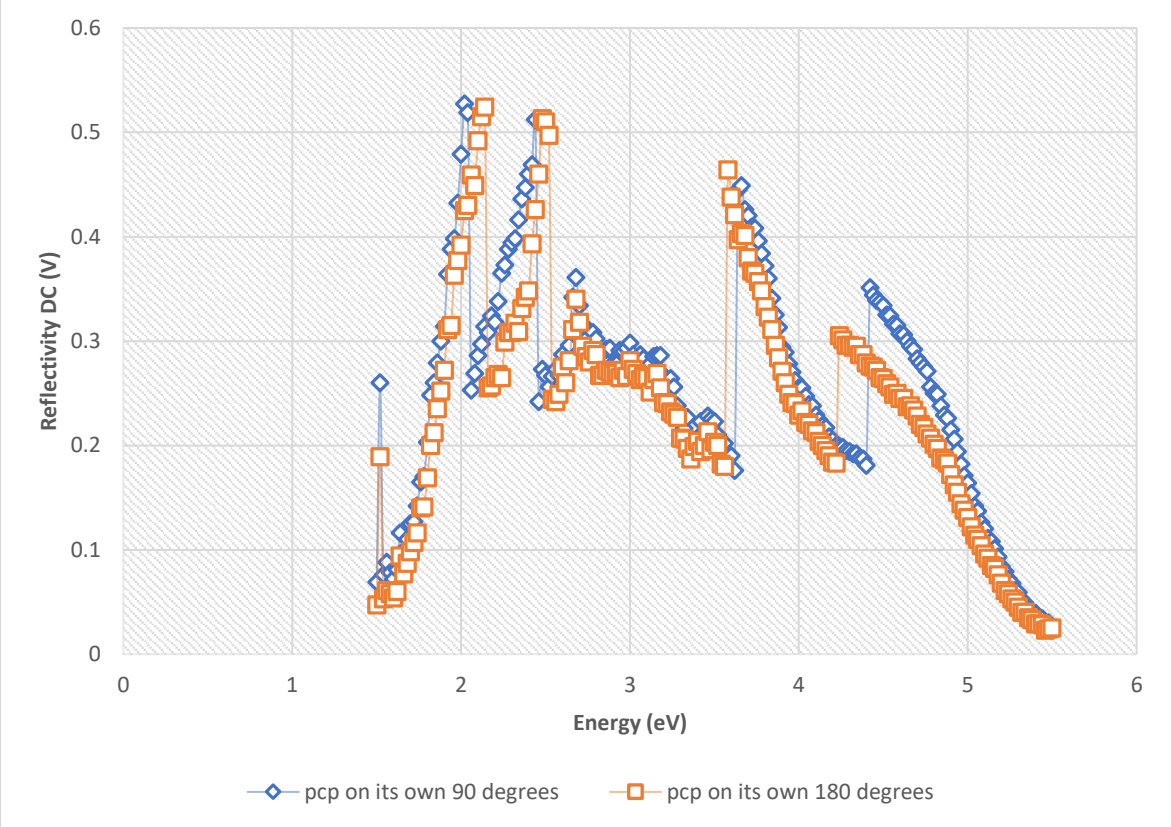

Figure A.2: Reflectivity scans of pcp substrate in two orthogonal directions

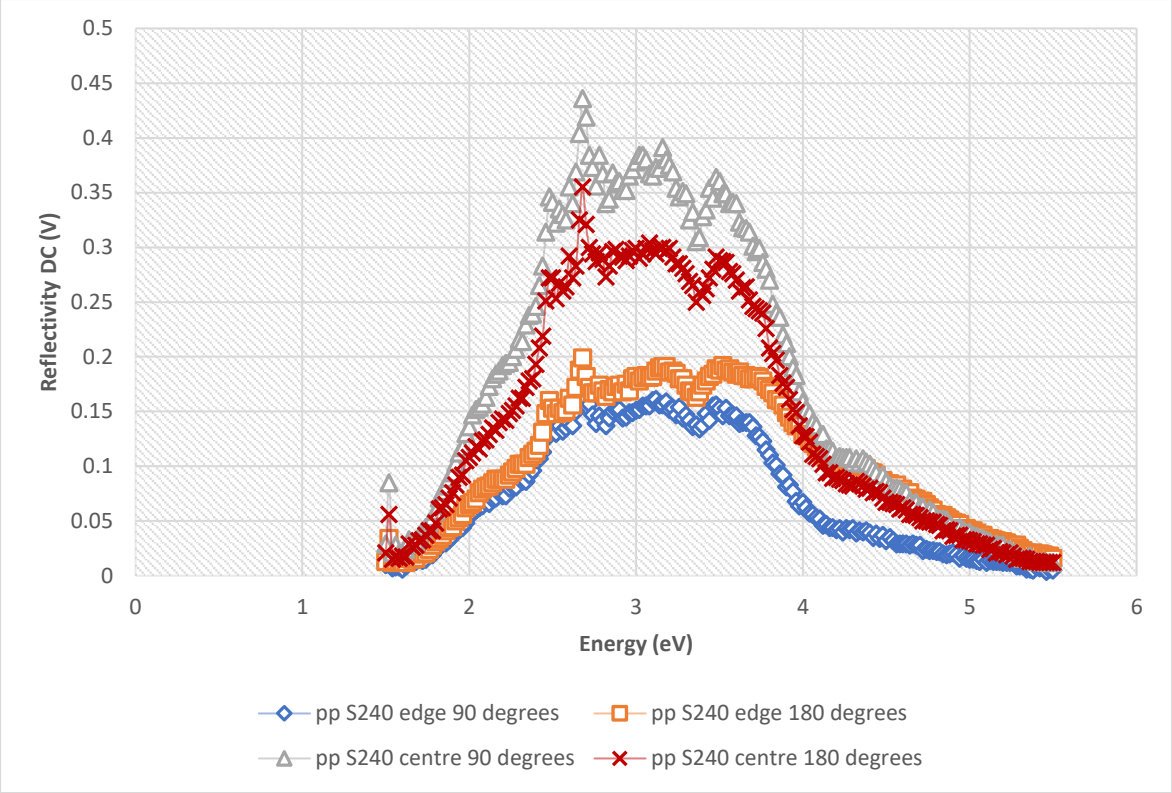

Figure A.3: Reflectivity scans of evaporated drop of S240 (0.1%) (aq) when the substrate is pp and it is taken at two perpendicular angles. (M3).

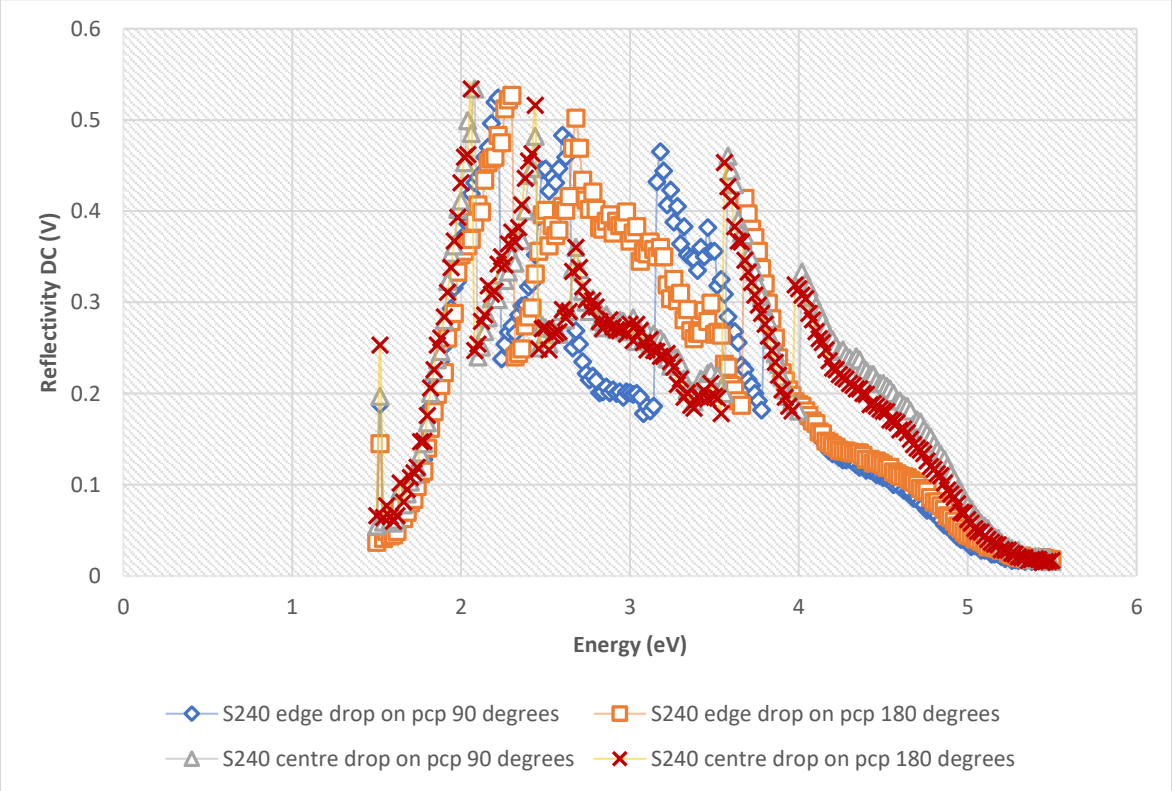

Figure A.4: Reflectivity scans of the centre and edge of an evaporated drop of S240 (0.1%) (aq) on a pcp substrate.

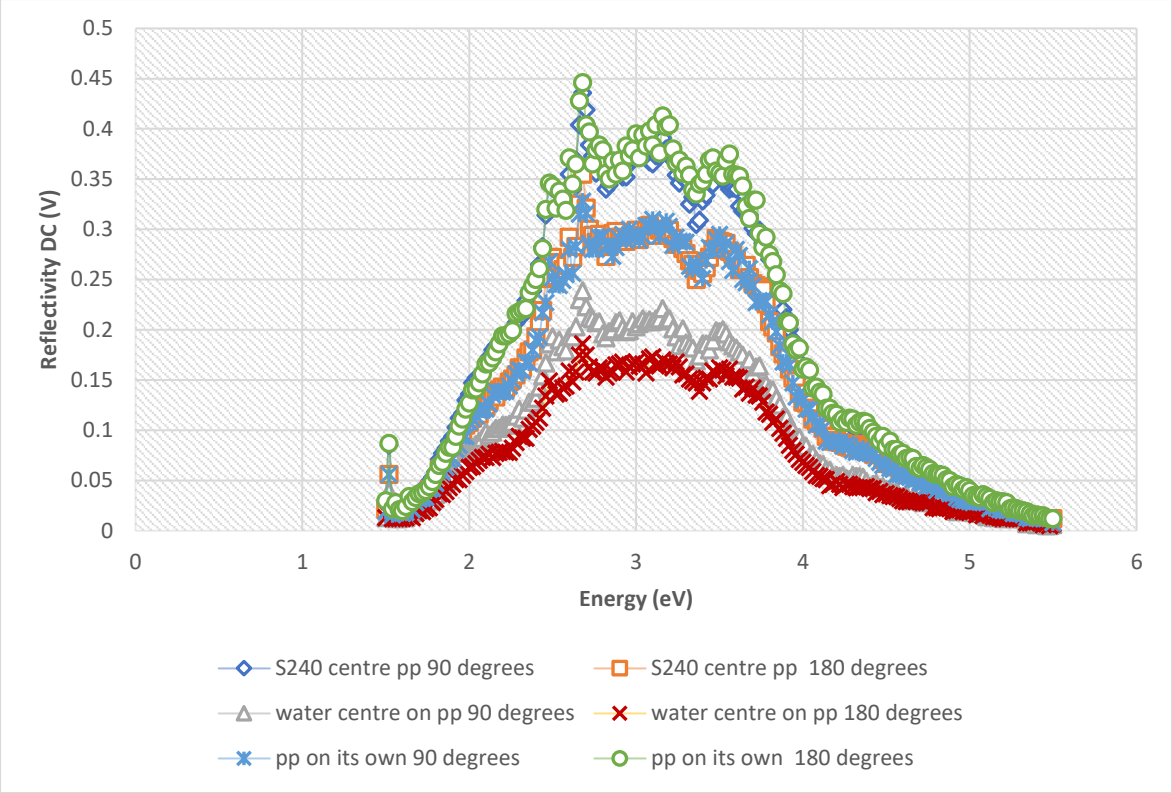

Figure A.5: Reflectivity scans of the centre of an evaporated drop of S240 (0.1%) (aq) on pp substrate compared with the centre of water drop on a pp substrate and a pp substrate, in two orthogonal directions

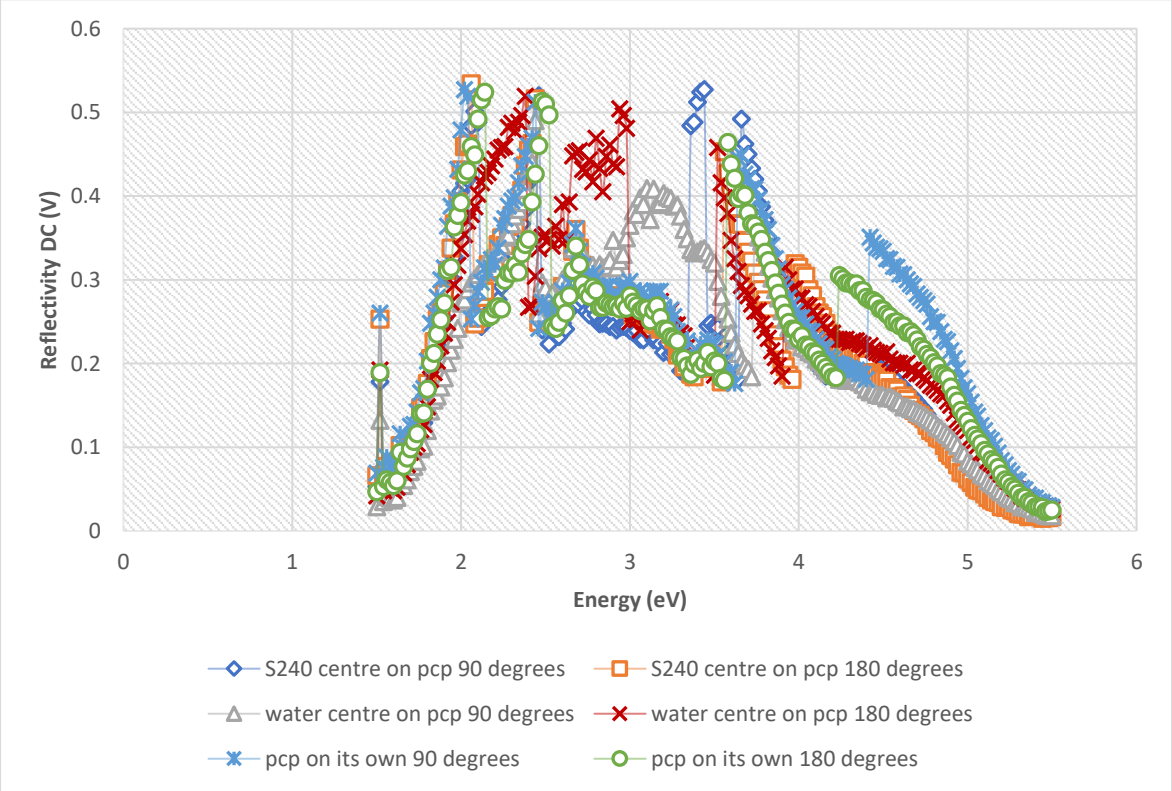

Figure A.6: Reflectivity scans of the centre of evaporated drops of S240 (0.1%) (aq) on a pcp substrate, and the centre of an evaporated drop of water on pcp, and pcp.

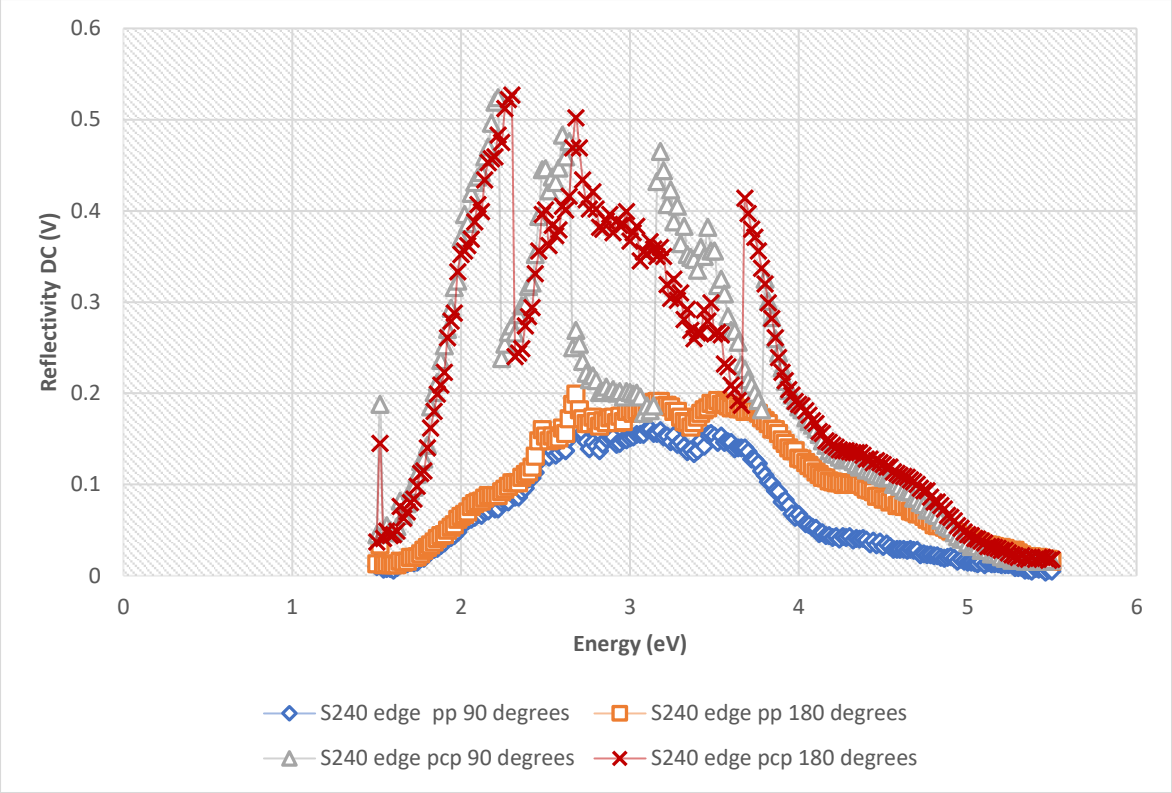

Figure A.7: Reflectivity scans of the edge of an evaporated drop of S240 (0.1%) (aq) on a pp and pcp substrate.

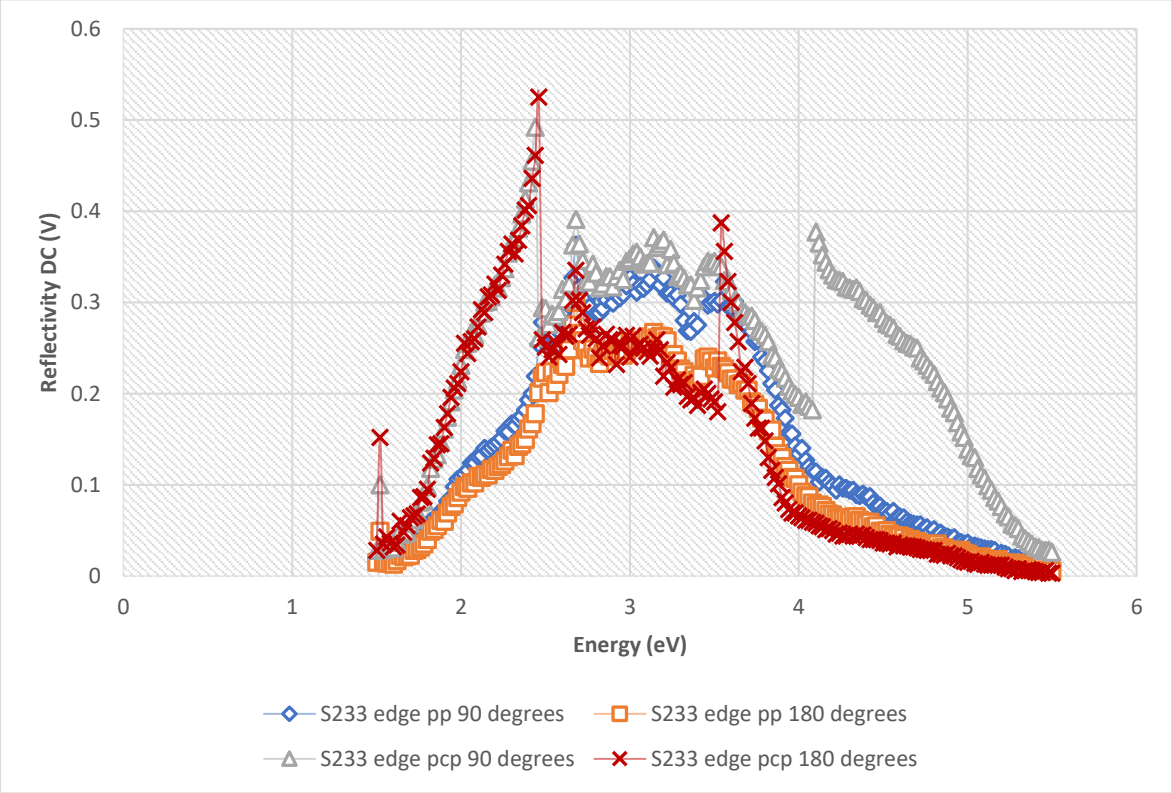

Figure A.8: Reflectivity scansof the edge of an evaporated drop of S233 (0.1%) (aq) on a pcp and pp substrate.

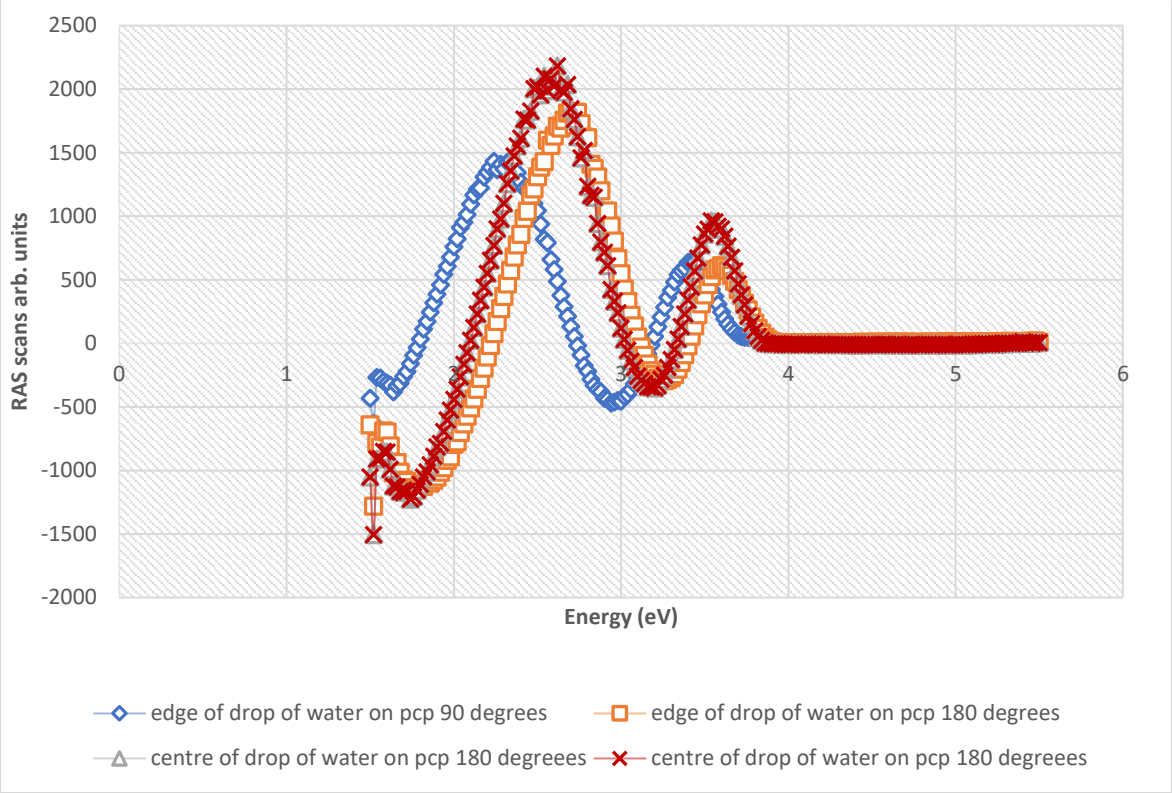

Figure A.9: RAS scans of a drop of evaporated water on a pcp substrate in two orthogonal directions.

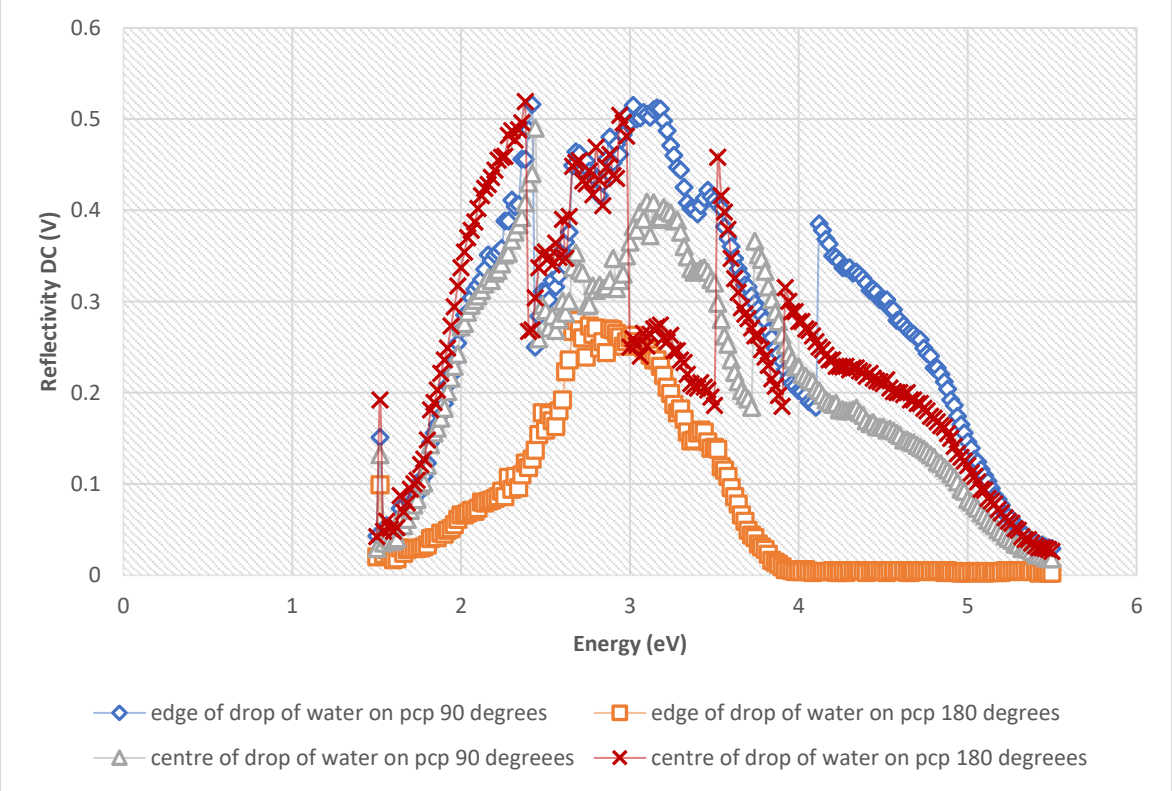

Figure A.10: Reflectivity scans of a drop of evaporated water on a pcp substrate in two orthogonal directions

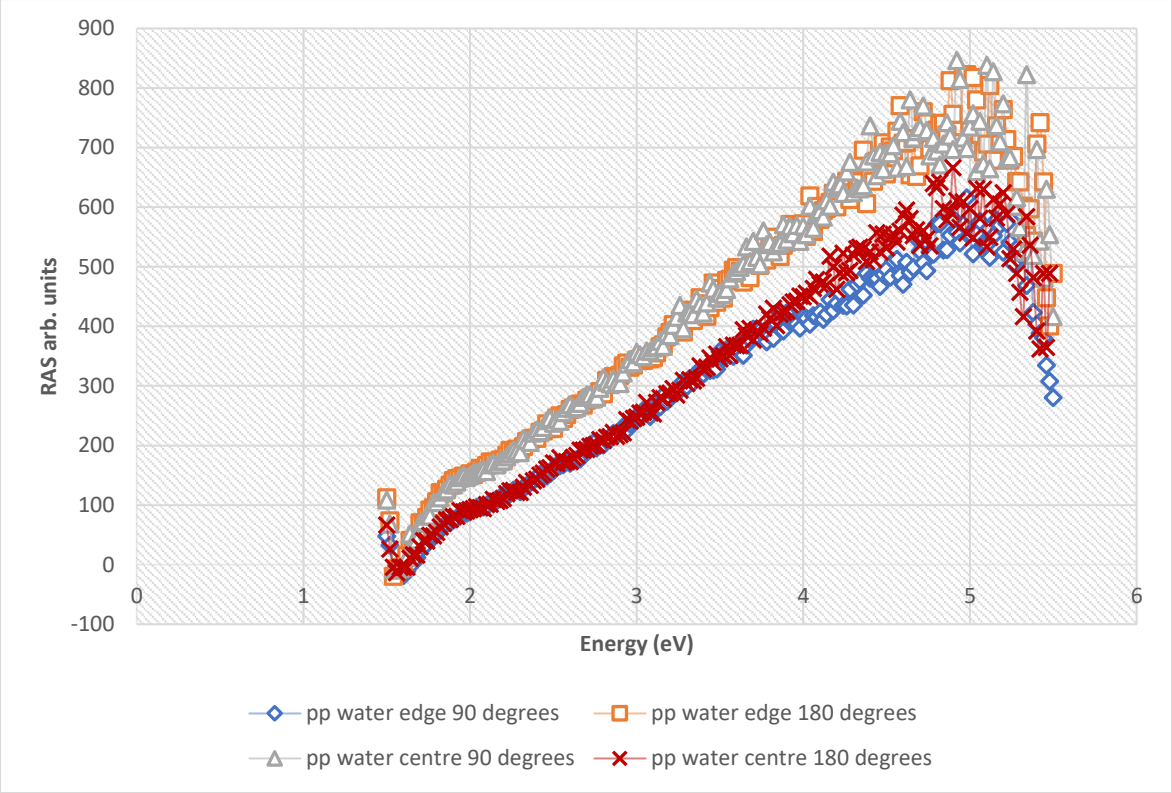

Figure A.11: RAS scans of evaporated drop of water on a pp substrate taken in two orthogonal directions.

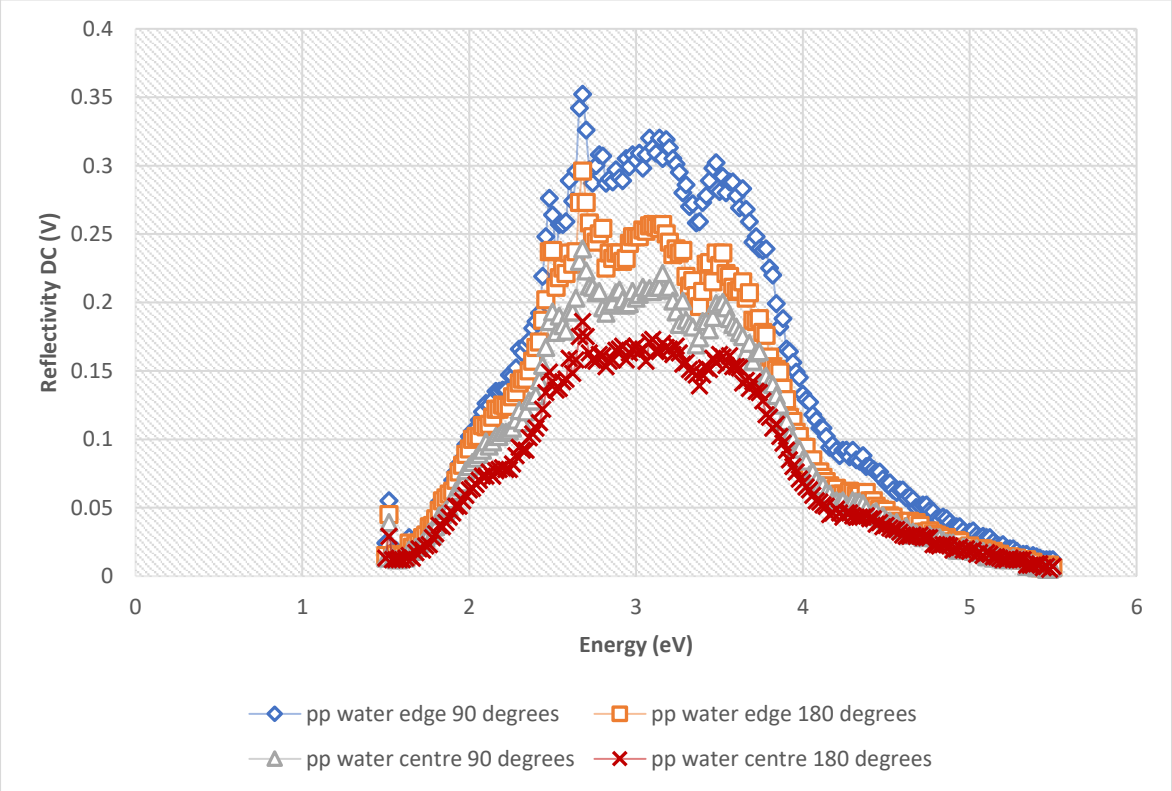

Figure A.12: Reflectivity scans of evaporated drop of water on a pp substrate taken in two orthogonal directions.

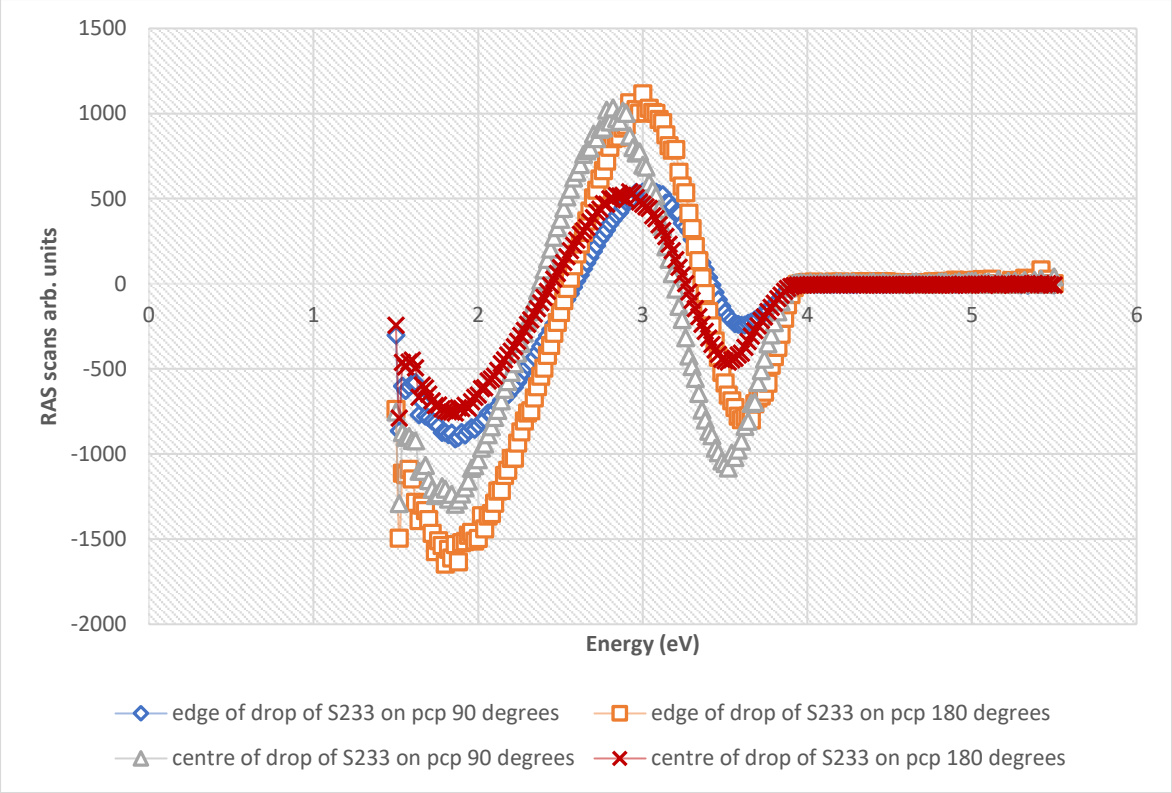

Figure A.13: RAS scans of the edge and centre of an evaporated drop of S233 (0.1%) (aq) on a pcp substrate in two orthogonal directions.

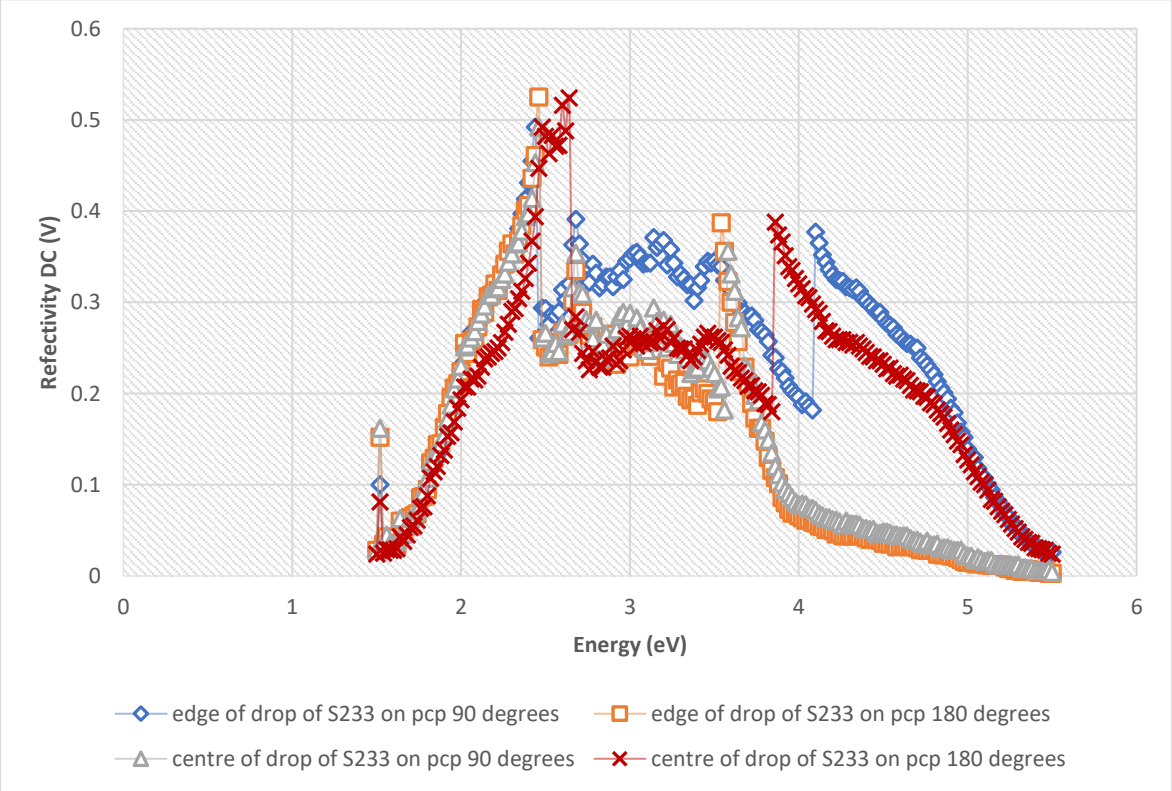

Figure A.14: Reflectivity scans for the edge and centre of an evaporated drop of S233 (0.1%) (aq) on a pcp substrate in two orthogonal directions. (M3)

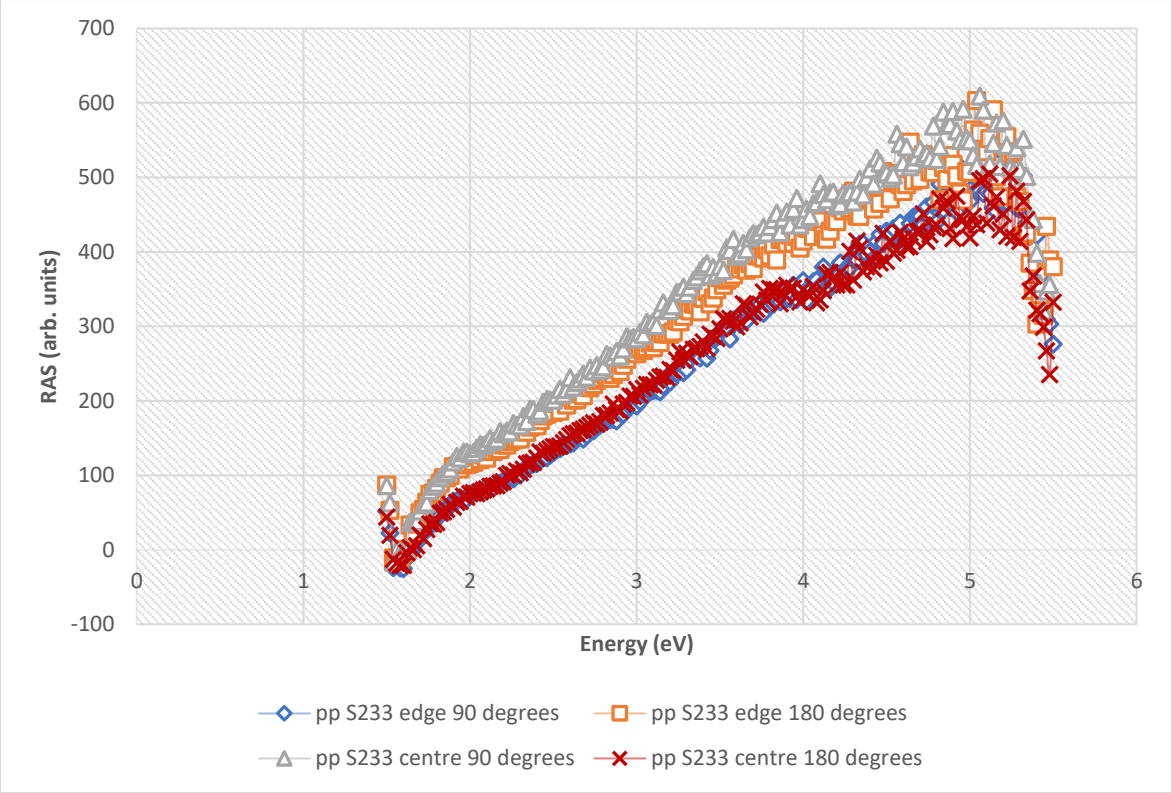

Figure A.15: RAS scans of evaporated drop of S233 (0.1%) (aq) at two perpendicular angles on a pp substrate.

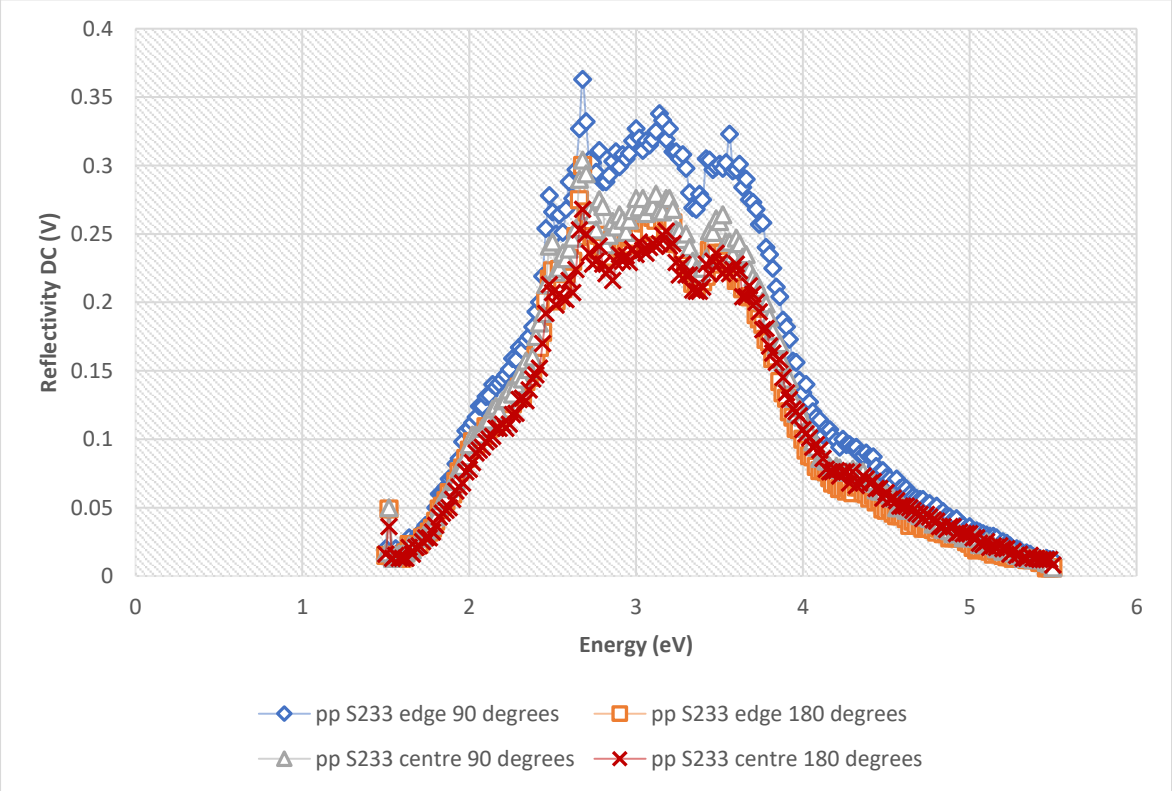

Figure A.16: Reflectivity scans of evaporated drop of S233 (0.1%) (aq) at two perpendicular angles on a pp substrate

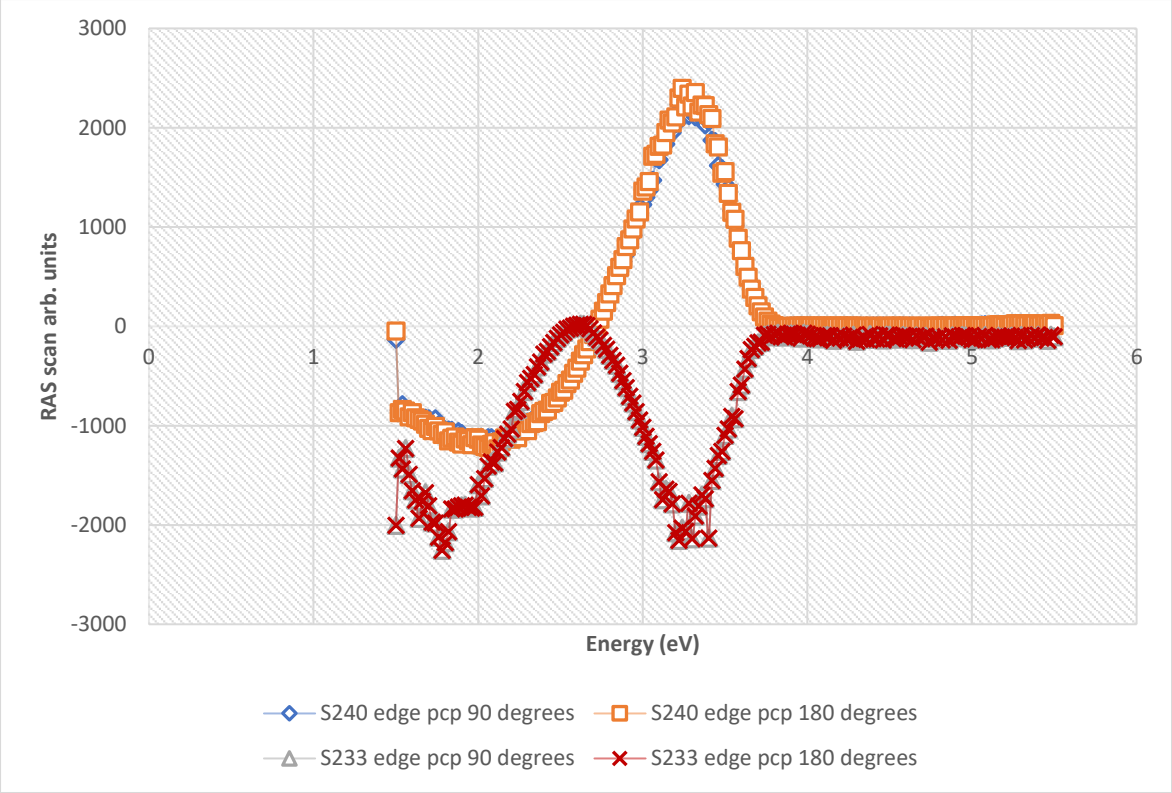

Figure A.17: RAS scans of the edge of an evaporated drop of S233 (0.1%) (aq) and a S240 (0.1%) (aq) on a pcp substrate in two orthogonal directions.

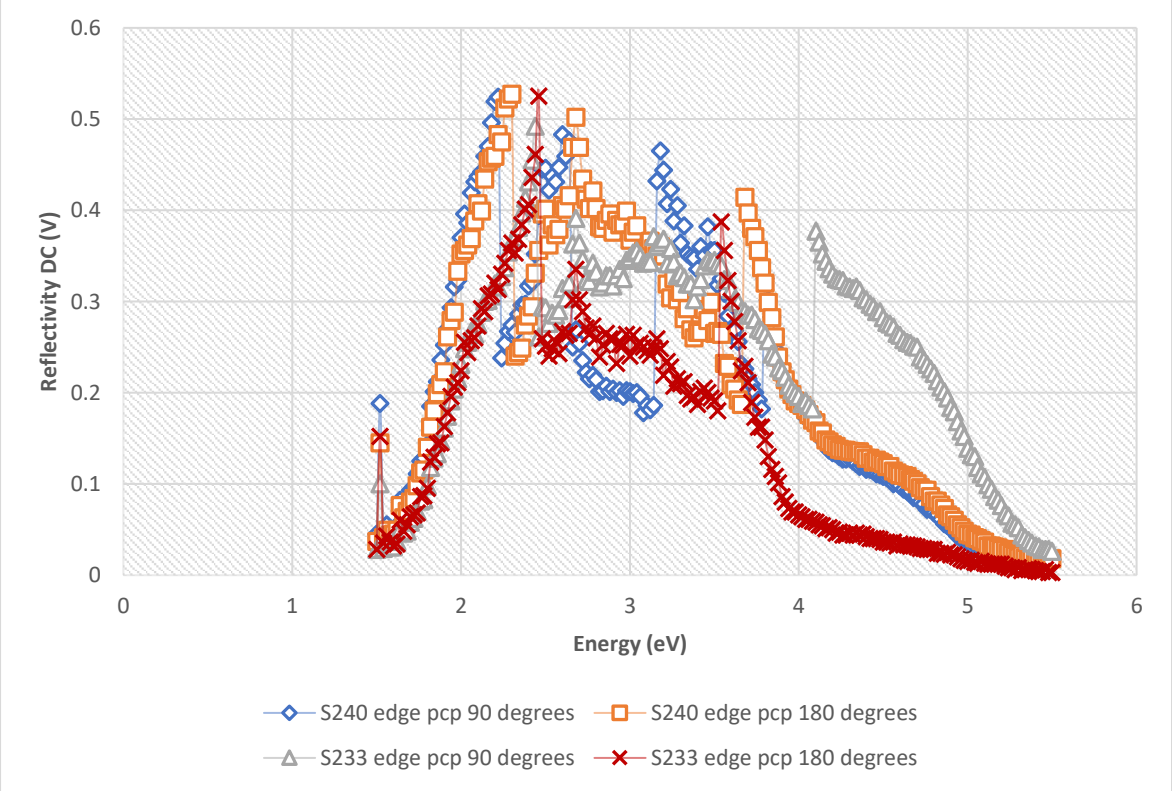

Figure A.18: Reflectivity scans of the edge of an evaporated drop of S233 (0.1%) (aq) and S240 (0.1%) (aq) on a pcp substrate in two orthogonal directions.

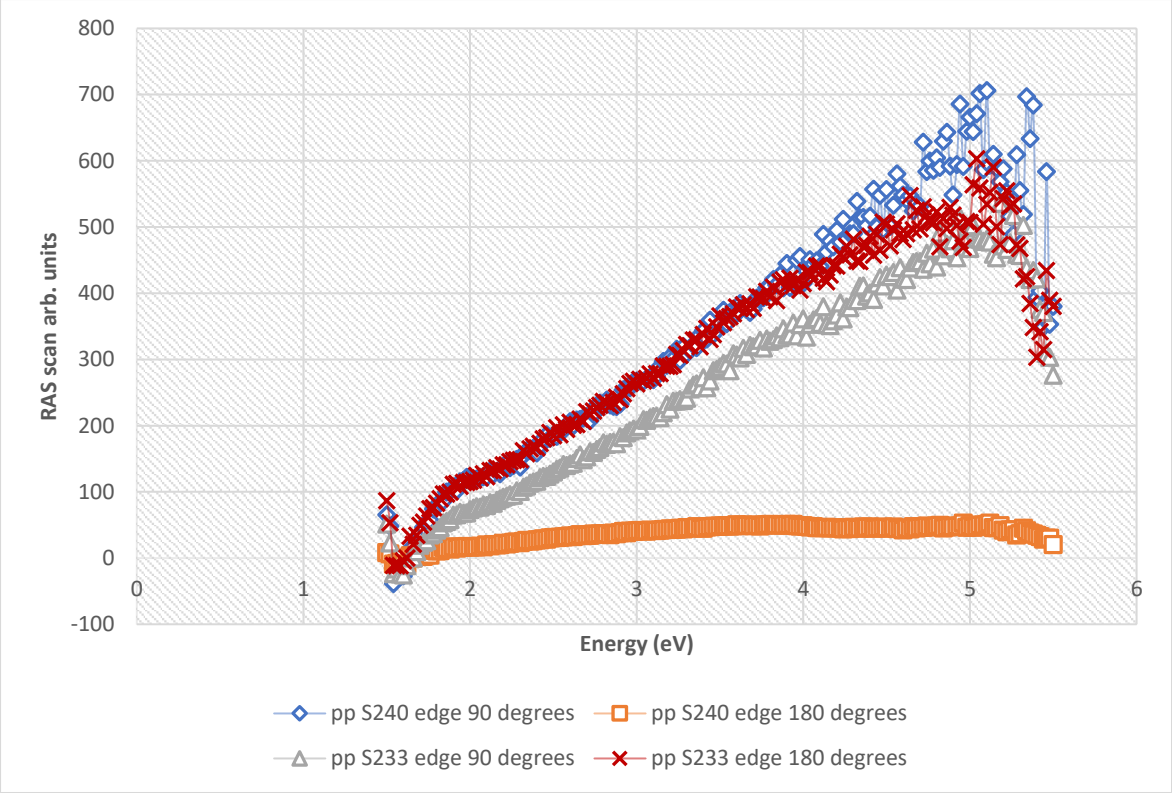

Figure A.19: Comparing reflectivity scans for the edge of evaporated drops of S233 (0.1%) (aq) and S240 (0.1%) (aq) in two orthogonal directions on a pp substrate.

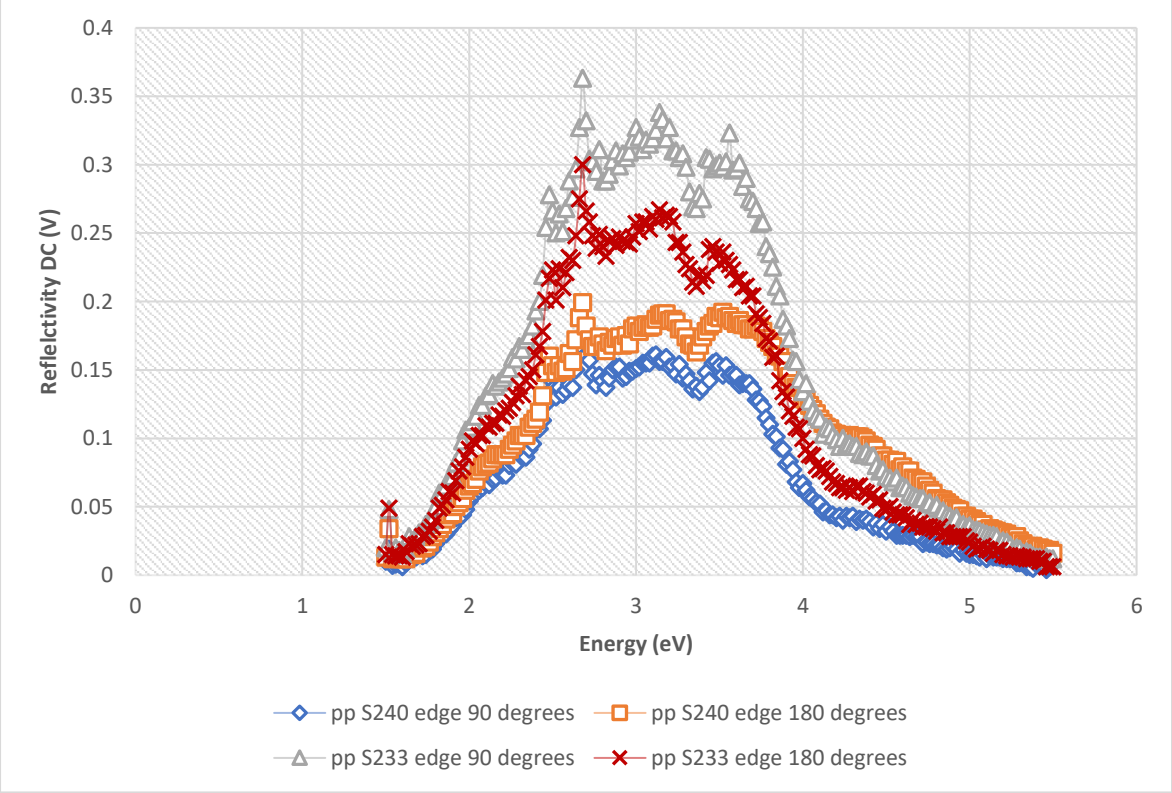

Figure A.20: Comparing reflectivity scans for the edge of evaporated drops of S233 (0.1%) (aq) and S240 (0.1%) (aq) in two orthogonal directions on a pp substrate.

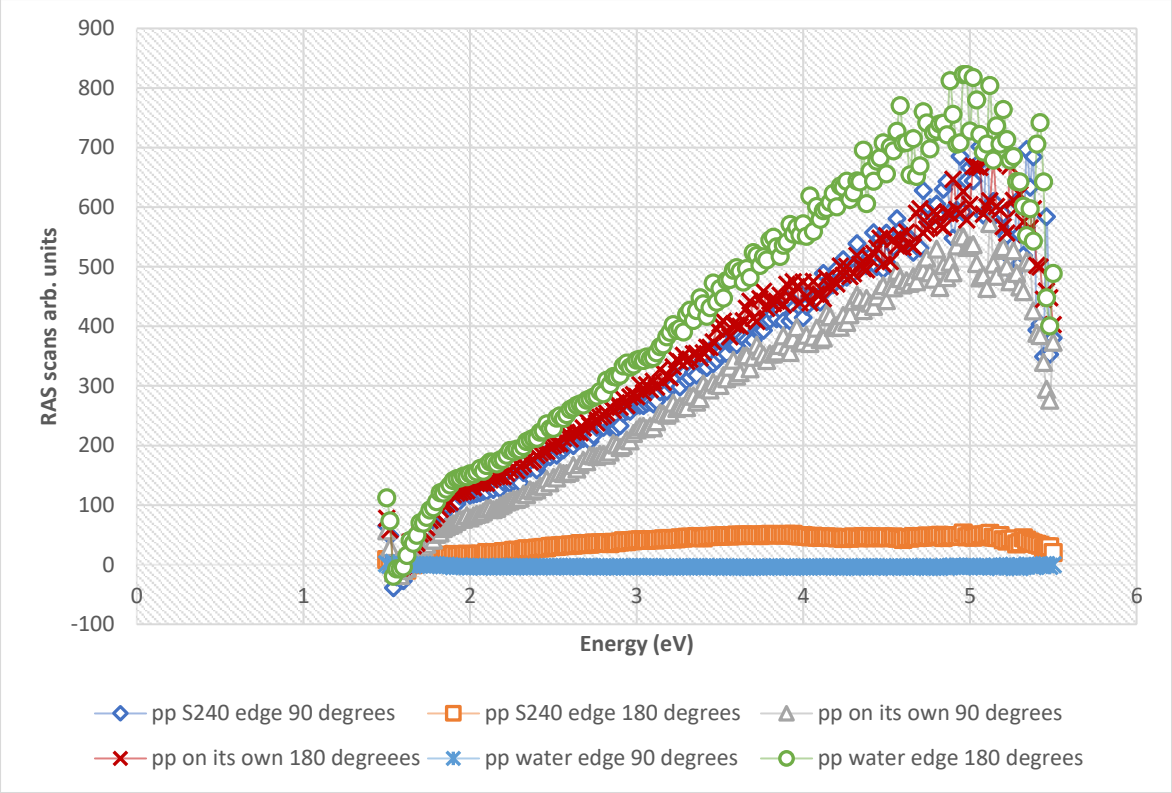

Figure A.21: Comparing RAS scans of the edge of a drop of S240 (0.1%) (aq) on a pp substrate with an evaporated drop of water on pp, and just a pp substrate.

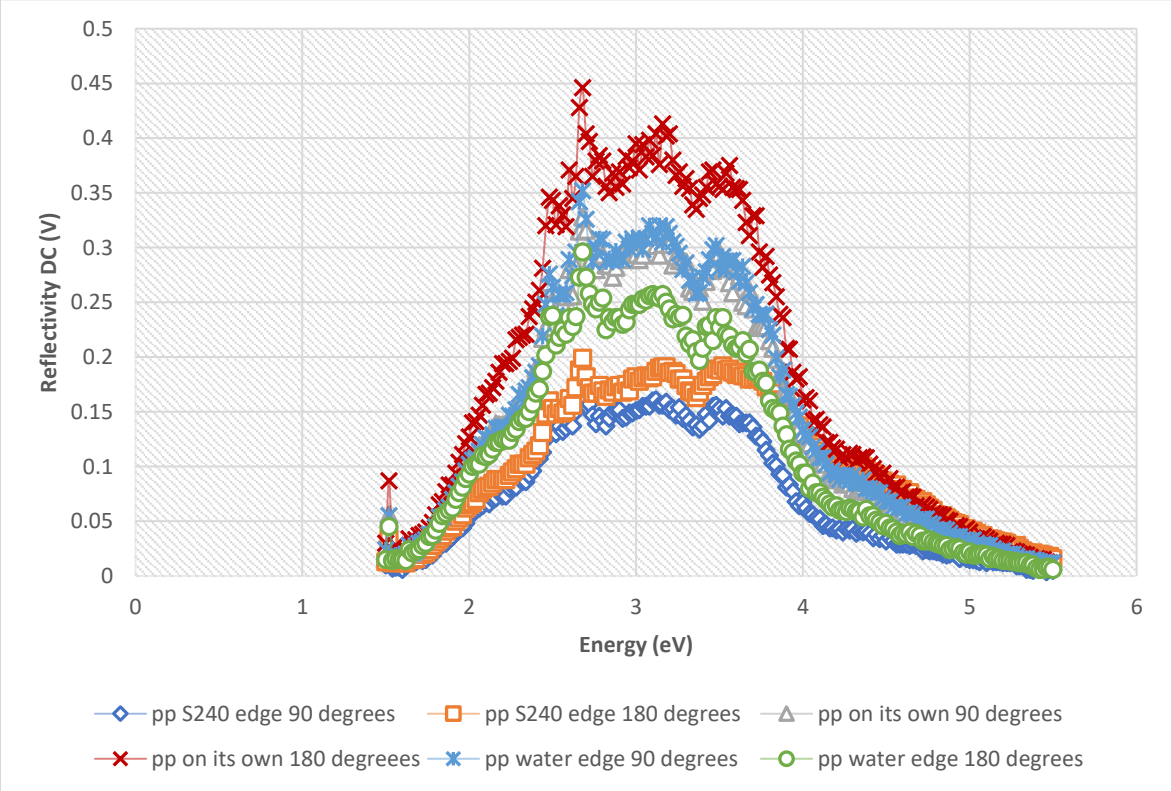

Figure A.22: Comparing reflectivity scans of the edge of a drop drop of S240 (0.1%) (aq) on a pp substrate with an evaporated drop of water on pp, and just pp

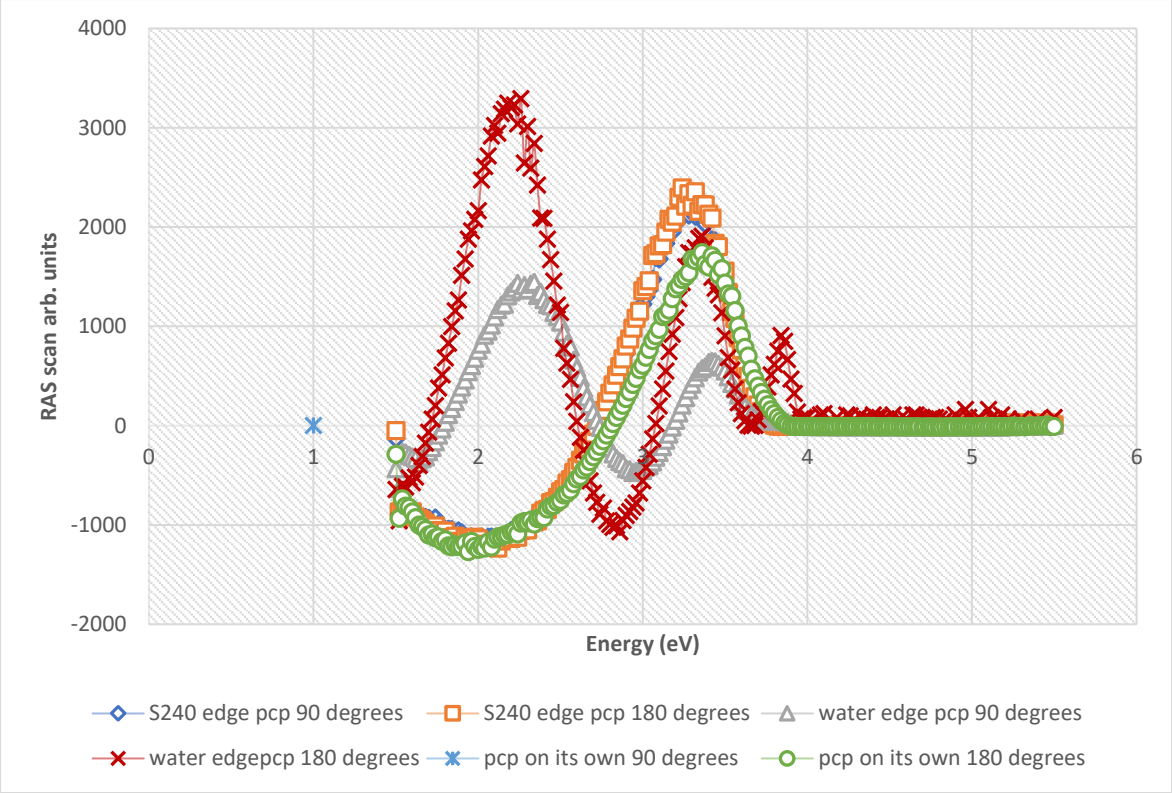

Figure A.23: RAS scans of the edge of a drop of S240 (0.1%) (aq), the edge of a water drop on a pcp substrate, and a pcp substrate on its own.

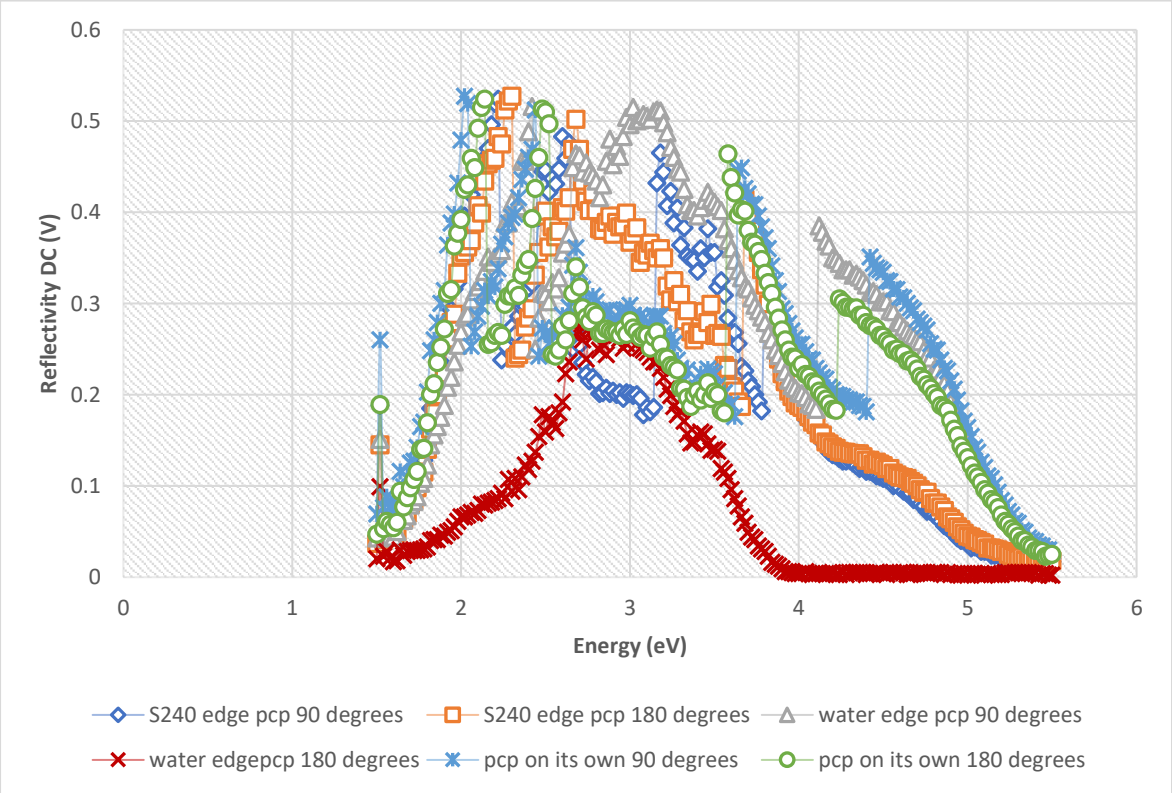

Figure A.24: Reflectivity scans of the edge of a drop of S240 (0.1%) (aq), the edge of a water drop on a pcp substrate on its own.

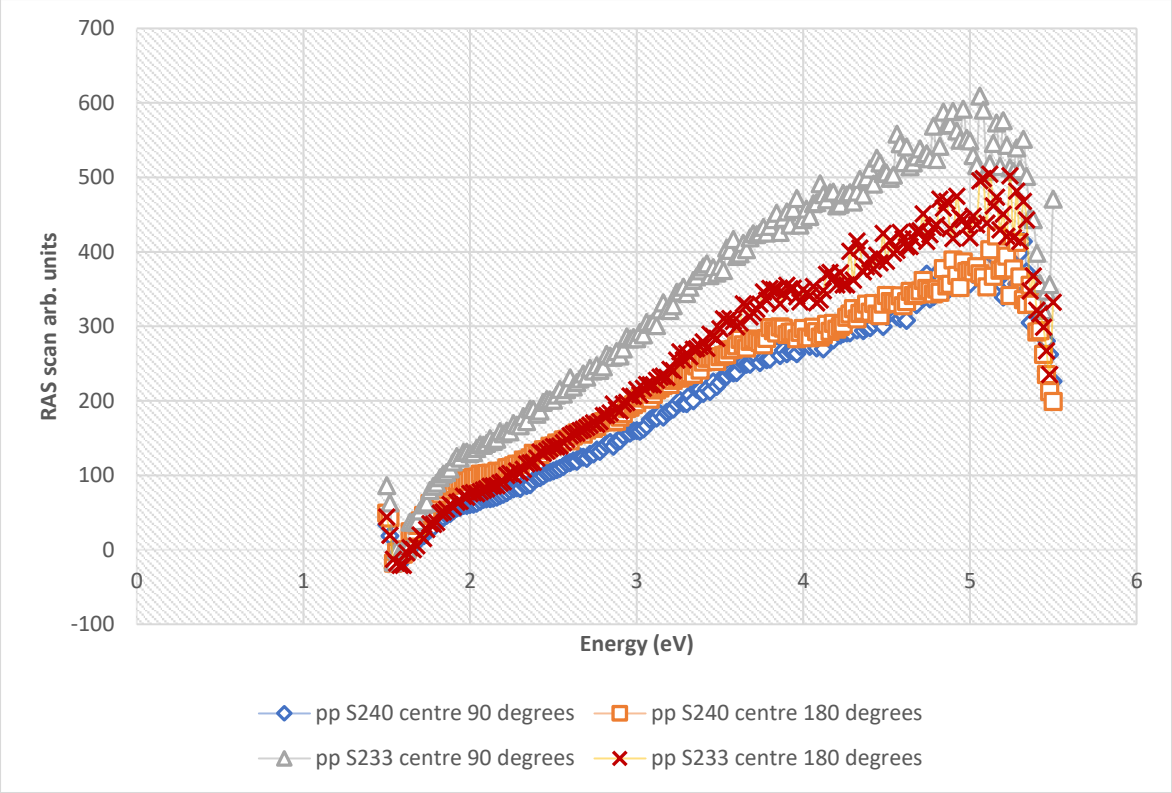

Figure A.25: RAS scans of the centre of evaporated drops of S240 (0.1%) (aq) and S233 (0.1%) (aq) on a pp substrate in two orthogonal directions.

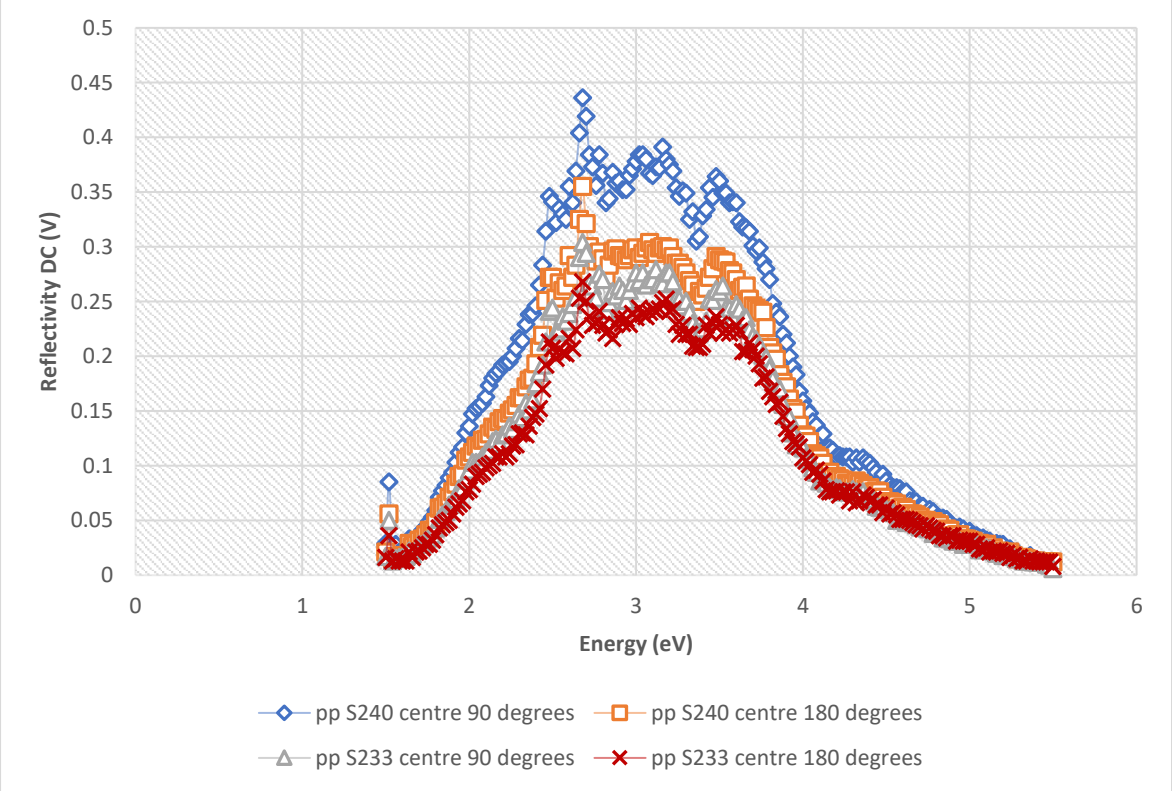

Figure A.26: Reflectivity scans of the centre of evaporated drops of S240 (0.1%) (aq) and S233 (0.1%) (aq) on a pp substrate in two orthogonal directions.

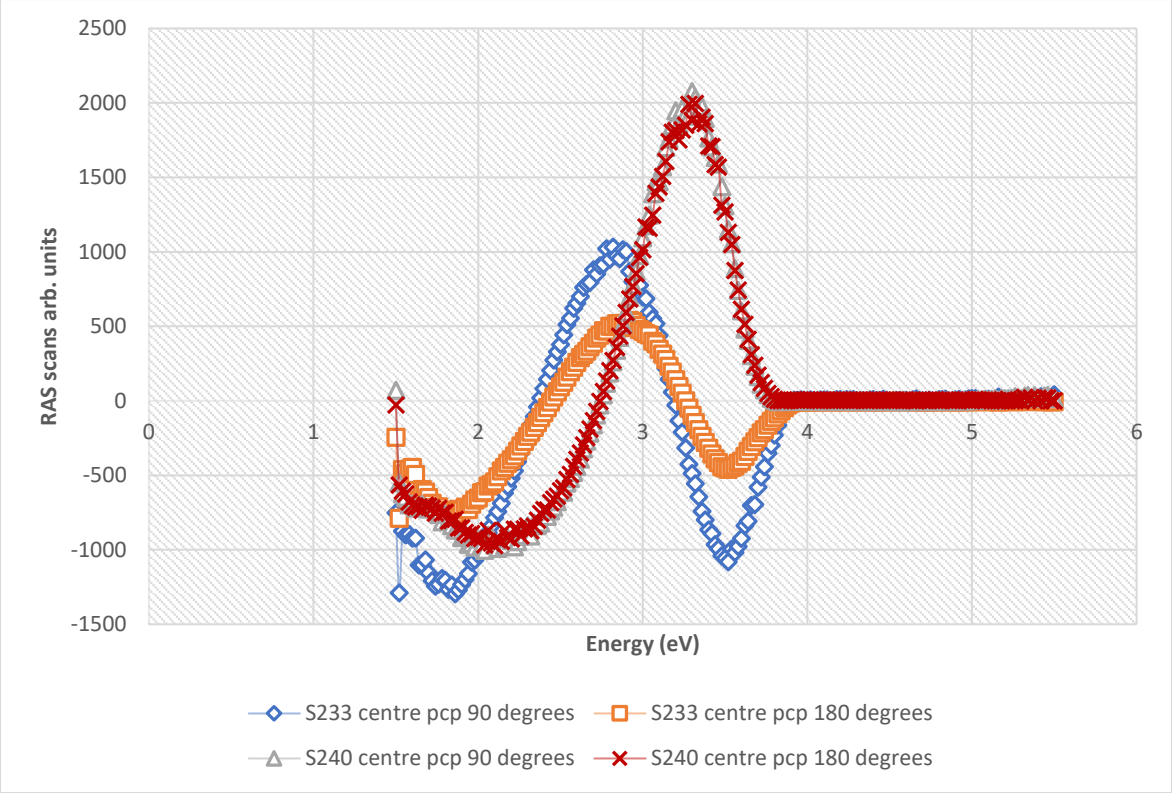

Figure A.27: RAS scans of the centre of an evaporated drop of S240 (0.1%) (aq) and S233 (0.1%) (aq) on a pcp substrate in two orthogonal directions.

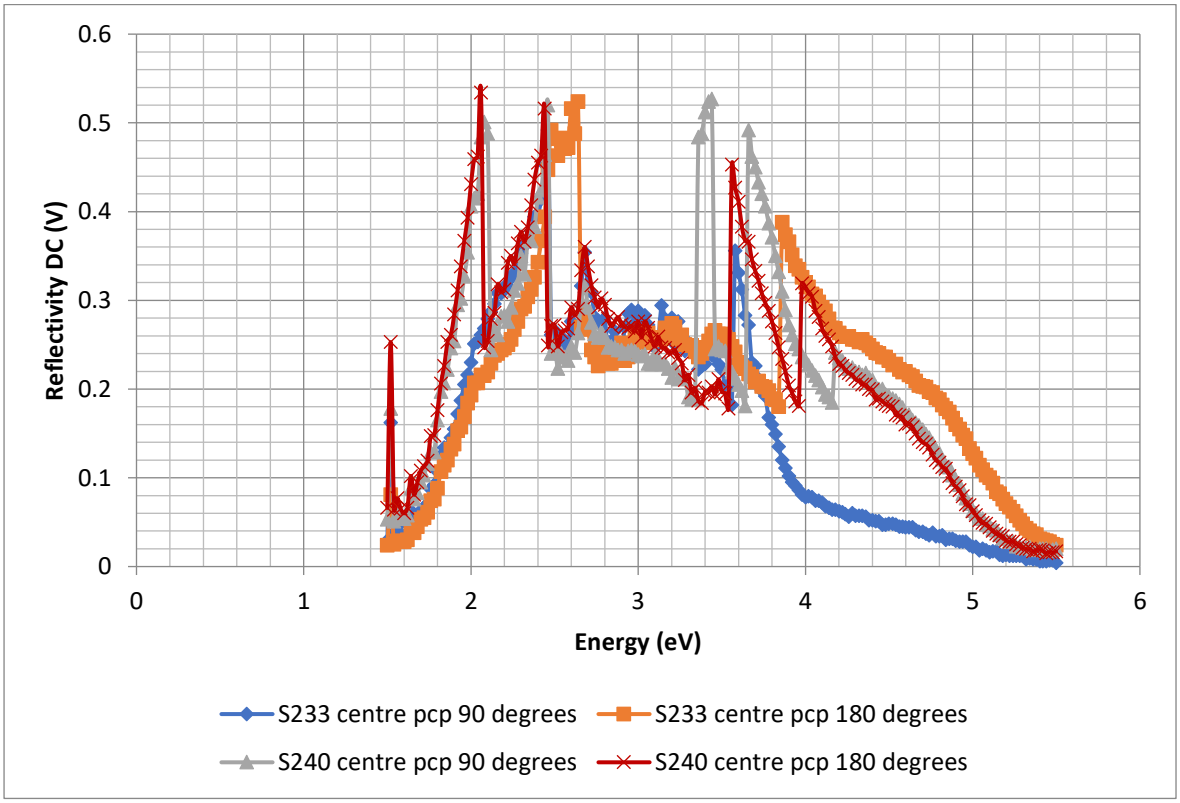

Figure A.28: Reflectivity scans of the centre of an evaporated drop of S240 (0.1%) (aq) and S233 (0.1%) (aq) on a pcp substrate on two orthogonal directions

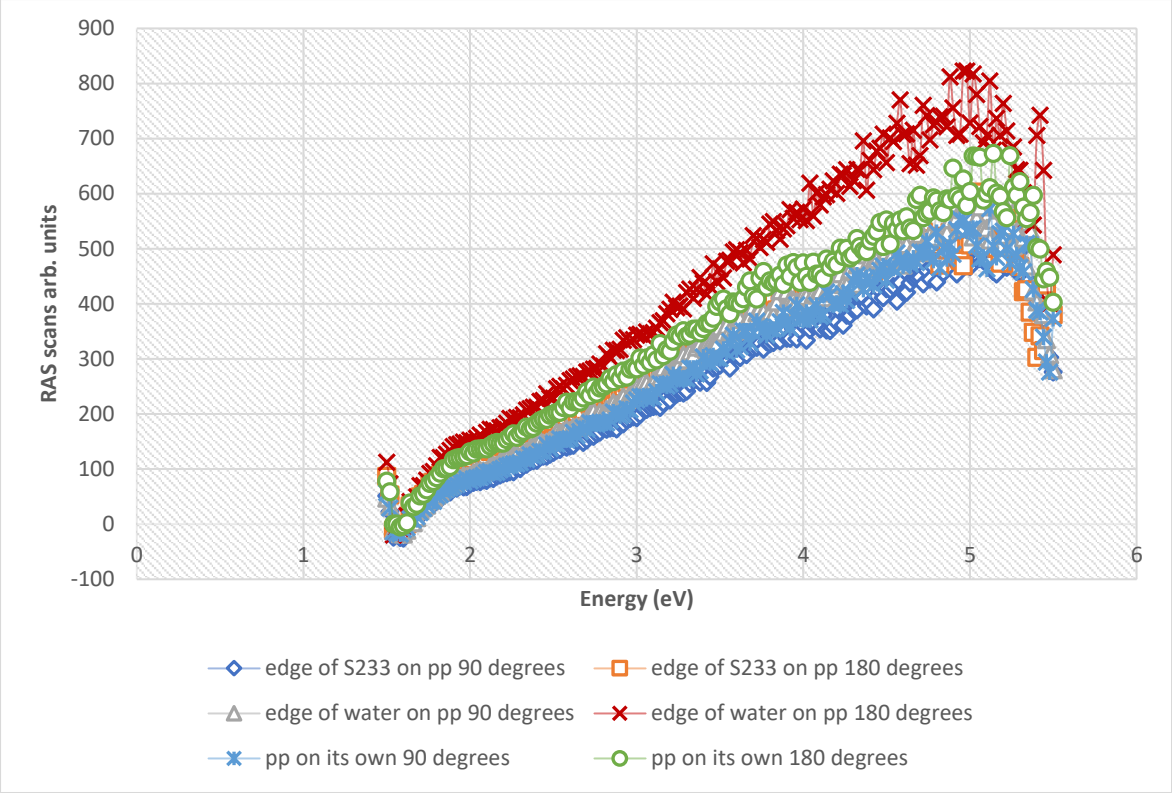

Figure A.29: RAS scans of the edge of evaporated drops of S233 (0.1%) (aq), and water compared with a RAS scan of just a pp substrate.

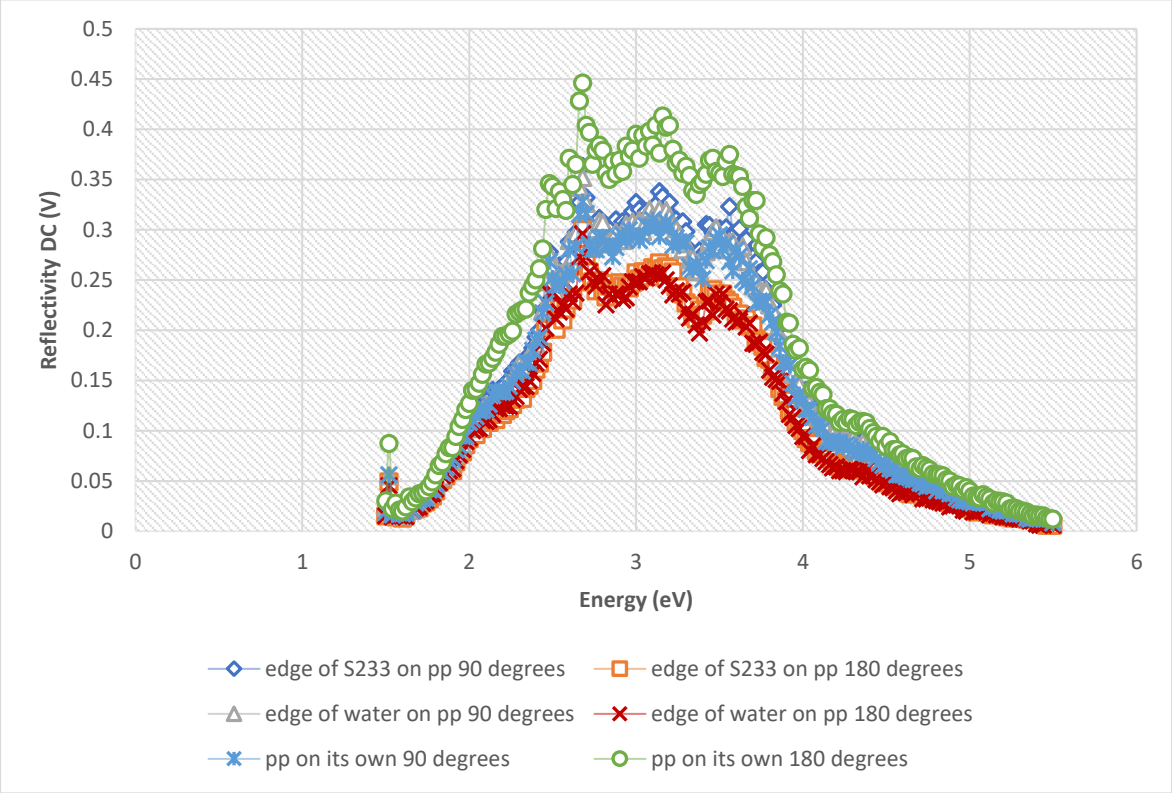

Figure A.30: Reflectivity scans of the edge of evaporated drops of S233 (0.1%) (aq) and water compared with a scan of just a pp substrate.

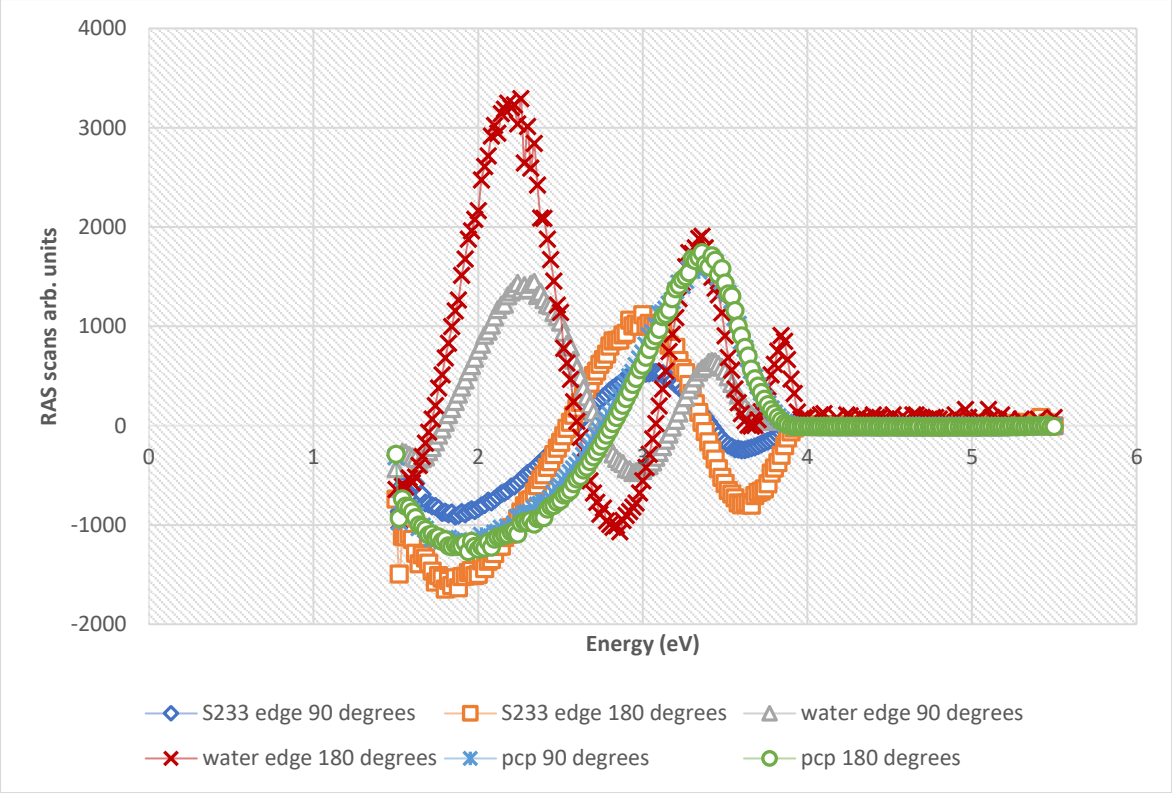

Figure A.31: RAS scans of the edge of an evaporated drop of S233 (0.1%) (aq) on a pcp substrate and the edge of an evaporated drop of water on a pcp substrate, and pcp.

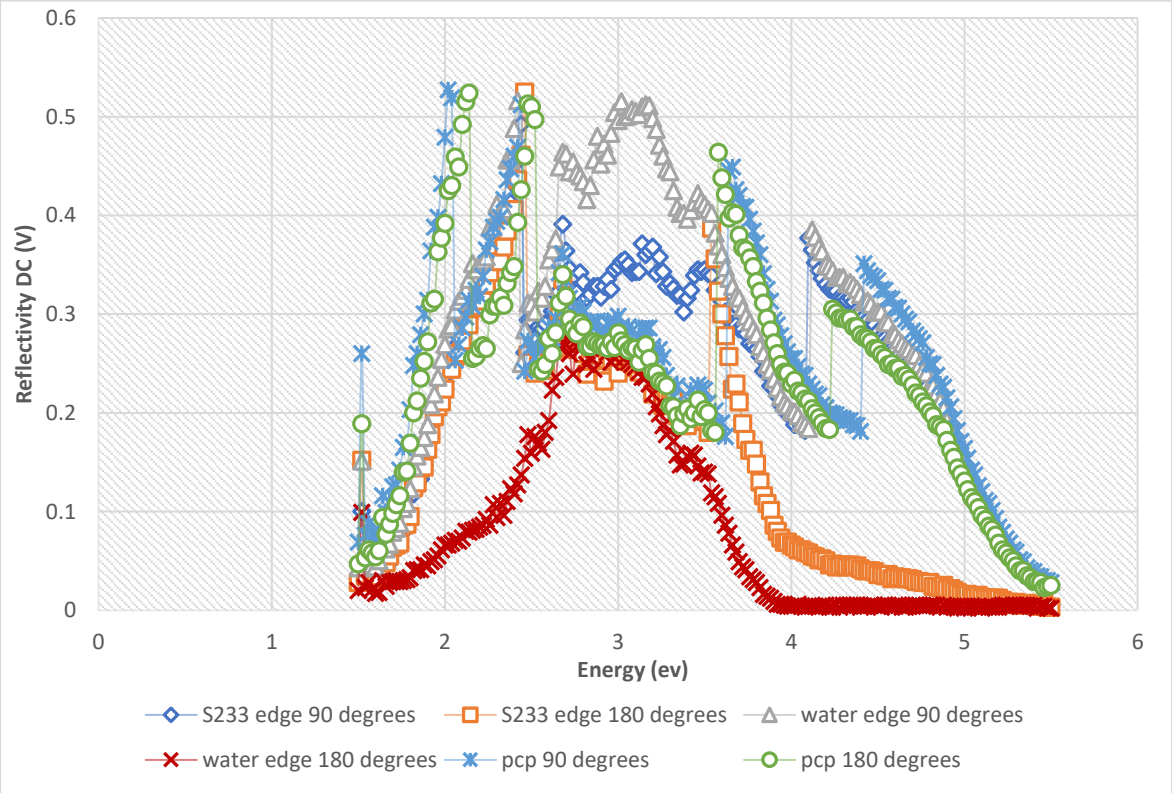

Figure A.32: Reflectivity scans of the edge of an evaporated drop of S233 (0.1%) (aq) on a pcp substrate and the edge of an evaporated drop of water on a pcp subnstrate, and a pcp substrate in two orthogonal directions. (M3).

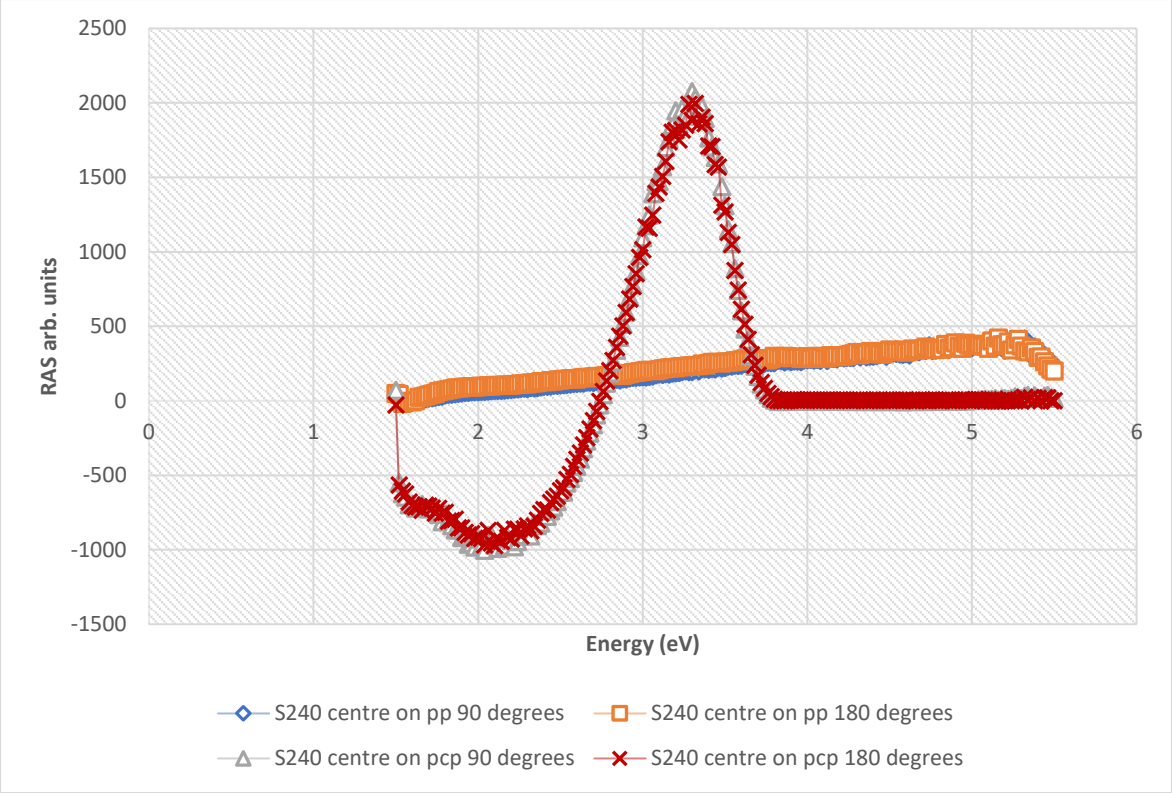

Figure A.33: RAS scans of the centre of evaporated drops of S240 (0.1%) (aq) on a pcp and pp substrate in two orthogonal directions.

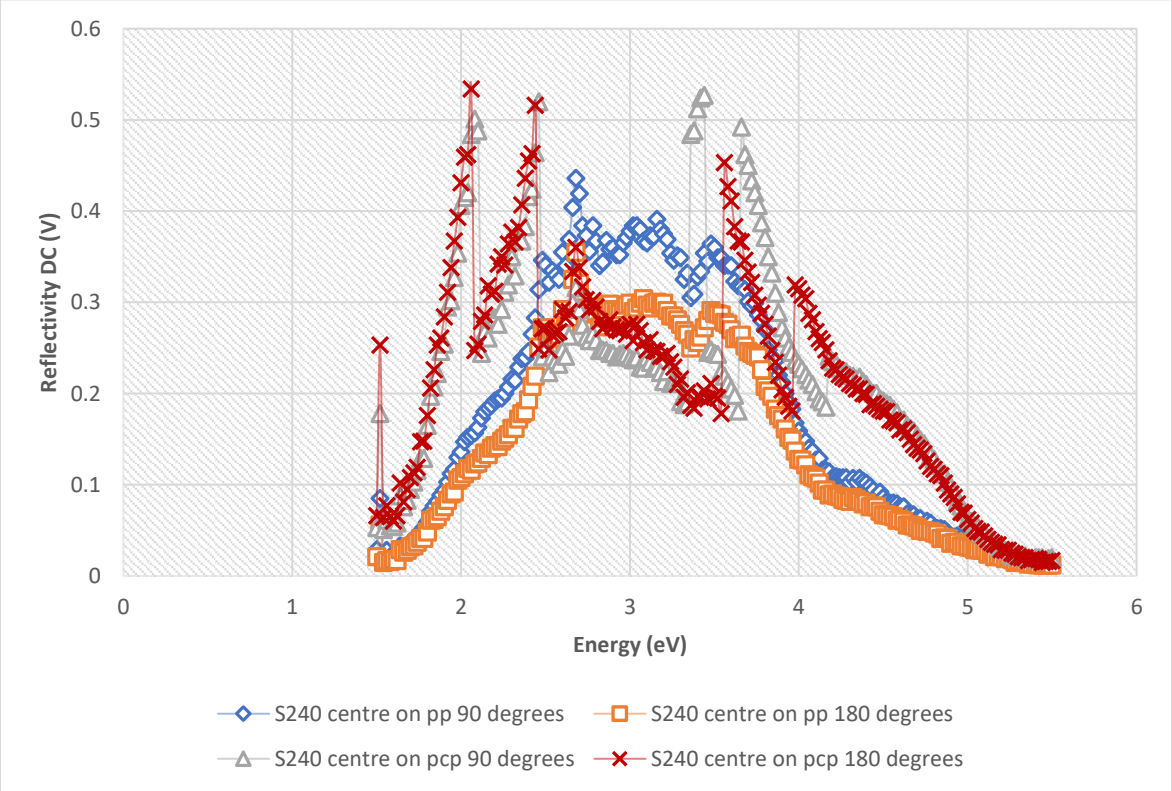

Figure A.34: Reflectivity scans of the centre of evaporated drops of S240 (0.1%) (aq) on a pcp and pp substrate in two orthogonal directions

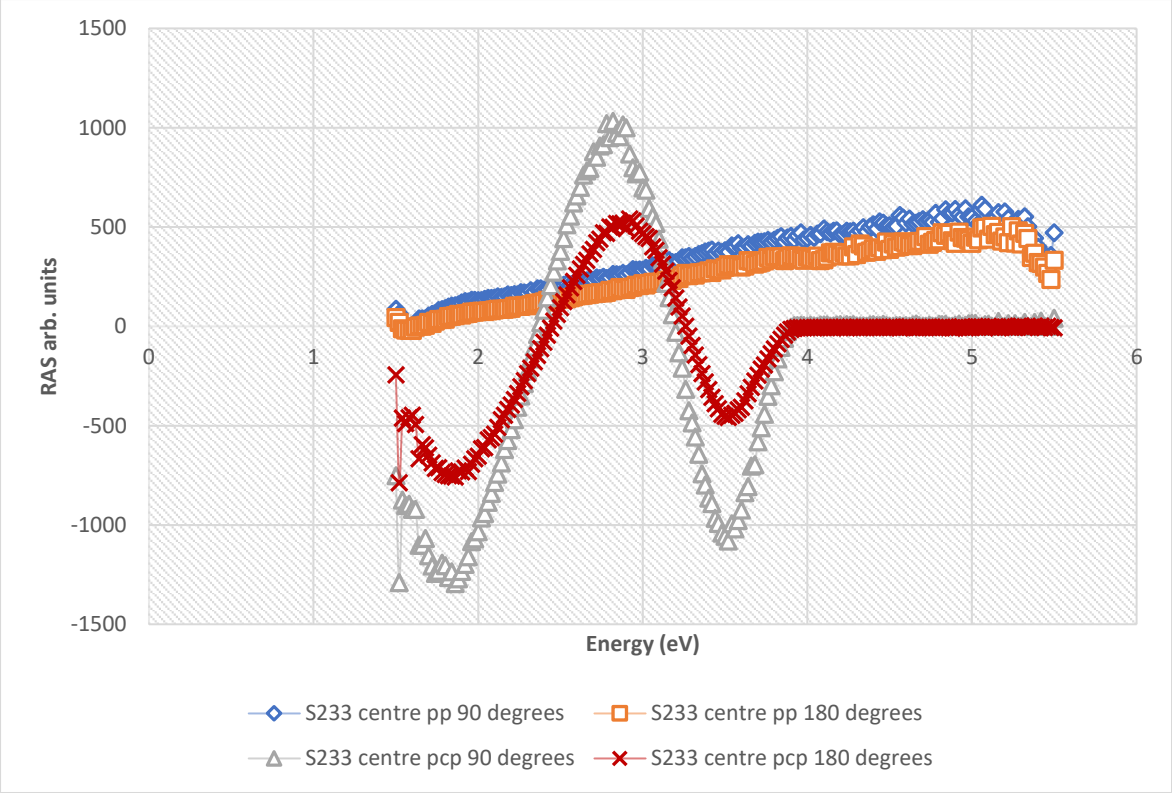

Figure A.35: RAS scans of the centre of an evaporated drop of S233 (0.1%) (aq) on a pp and pcp substrate.

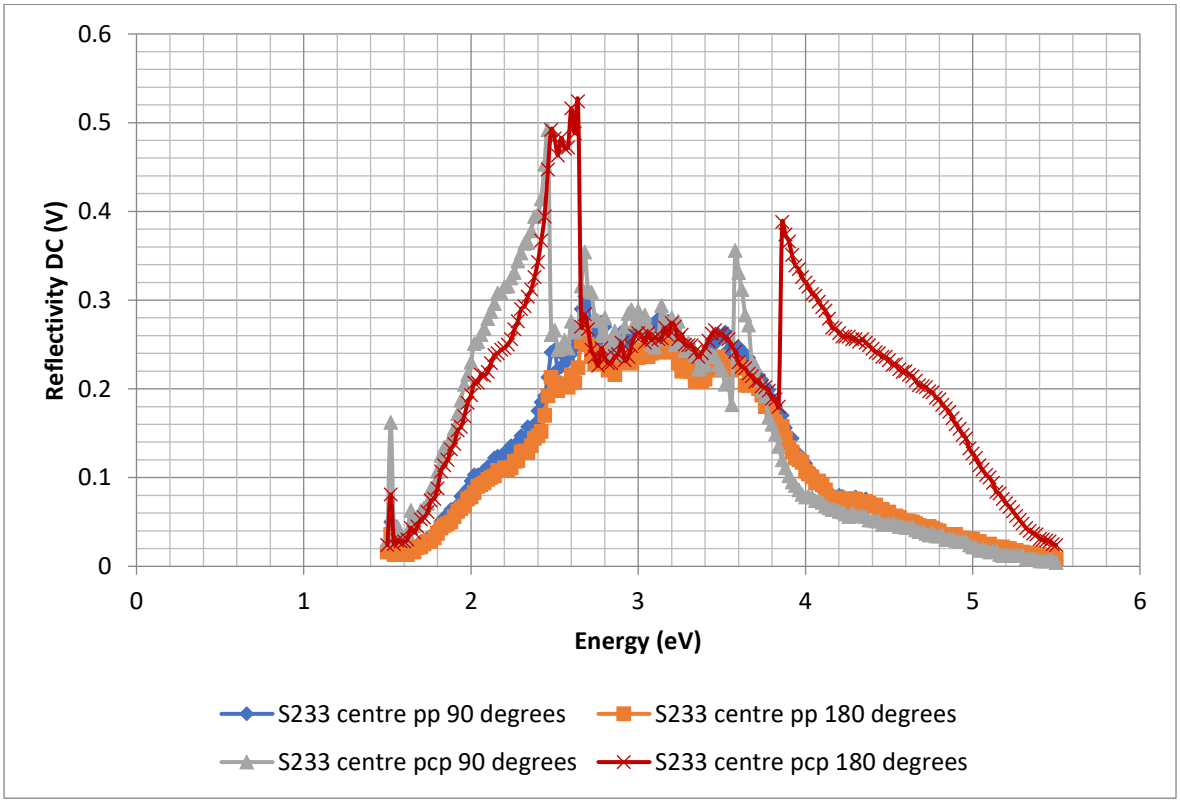

Figure A.36: Reflectivity scans of the centre of an evaporated drop of S233 (0.1%) (aq) on a pcp and pp substrate

Appendix B - In this appendix all GISAXS images are shown which have spots on the vertical flares, count versus time graphs are also shown revealing the time region where those GISAXS images are taken. These results were used in the analysis of chapter 5. At the end of the appendix are images of an inclined flare on the GISAXS images which is caused by the refraction of the X-ray beam through the liquid/air interface of the drop. The diagonal flare gives an idea of the shape of the free surface of the drop near the contact point.

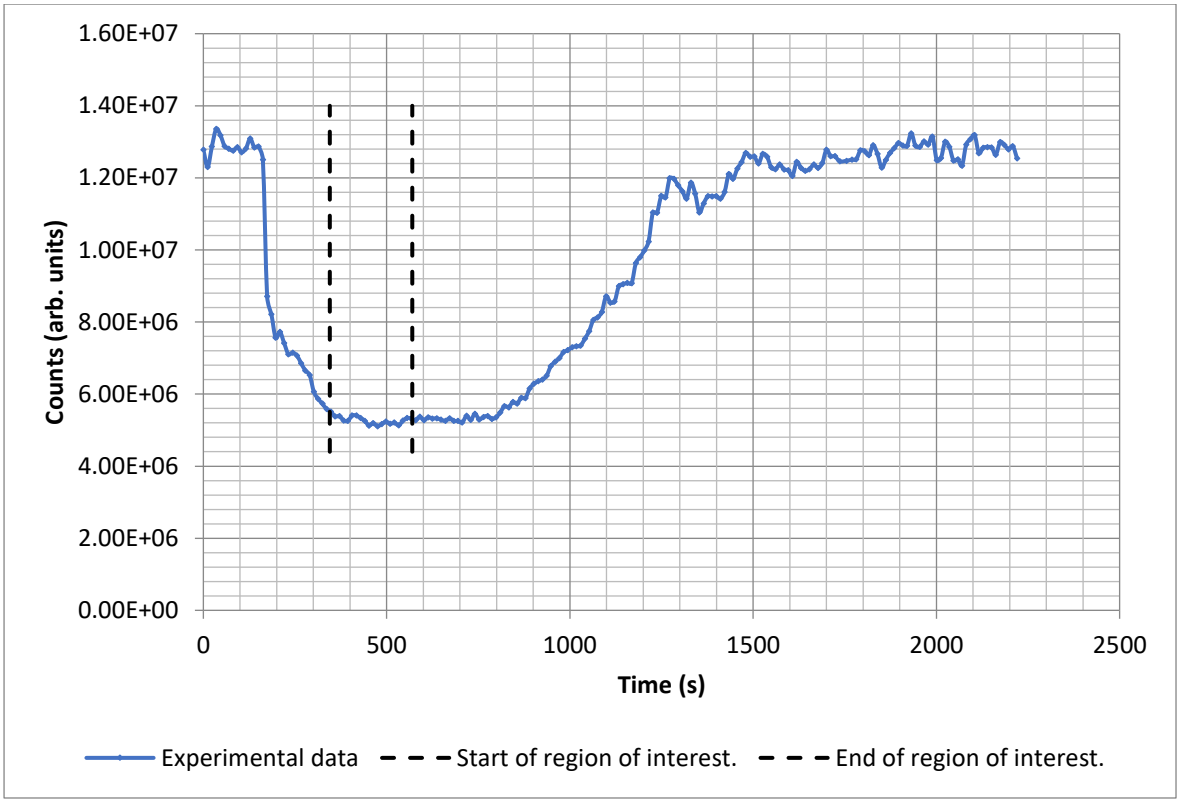

Figure B.1: Count versus time graph for drop of S240 (0.1%) (aq) spreading on pp substrate for run 1.27.

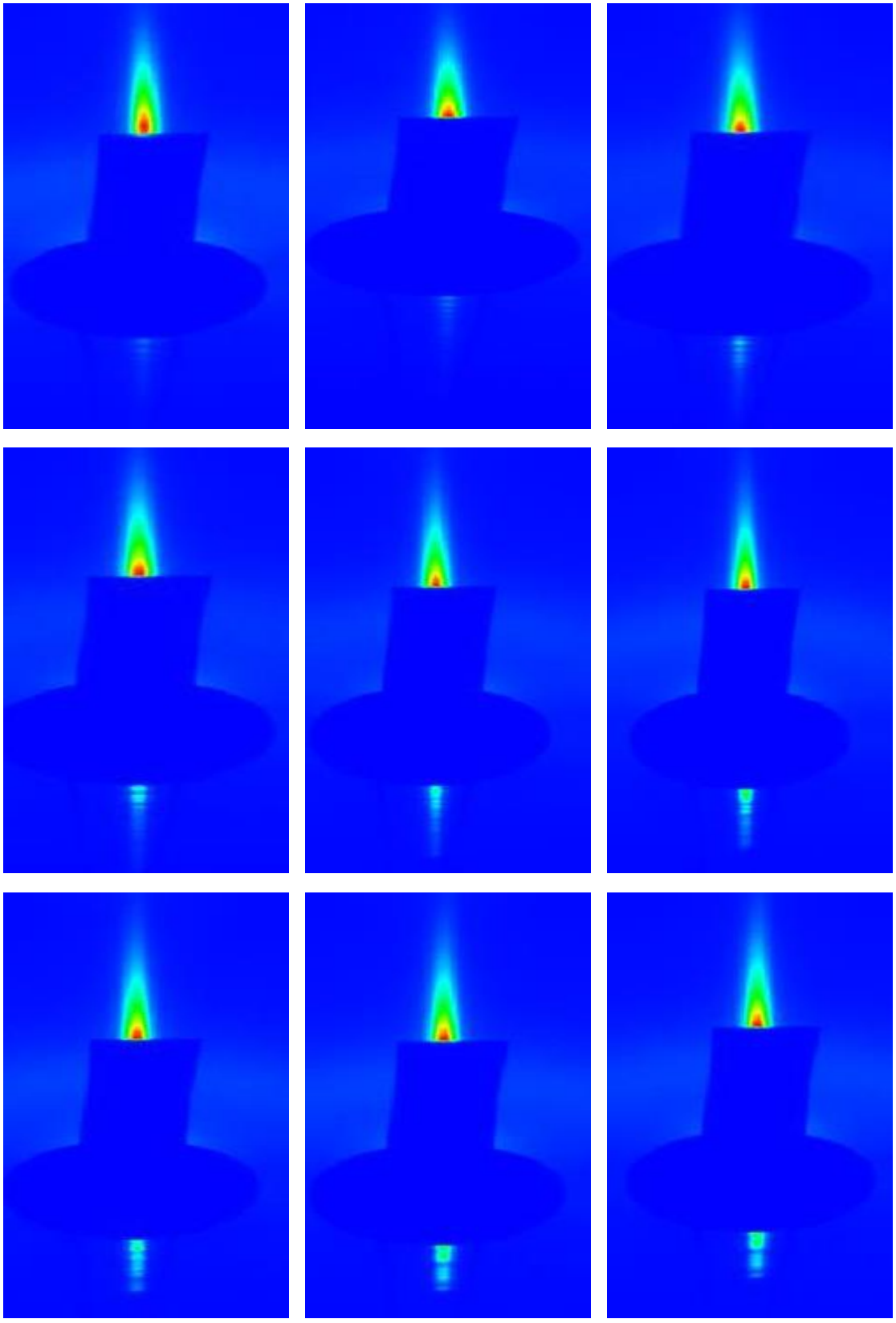

Figure B.2: Run 1.27 GISAXS image of S240 (0.1%) (aq) superspreading solution on polypropylene substrate showing periodic spots on bottom vertical flare.

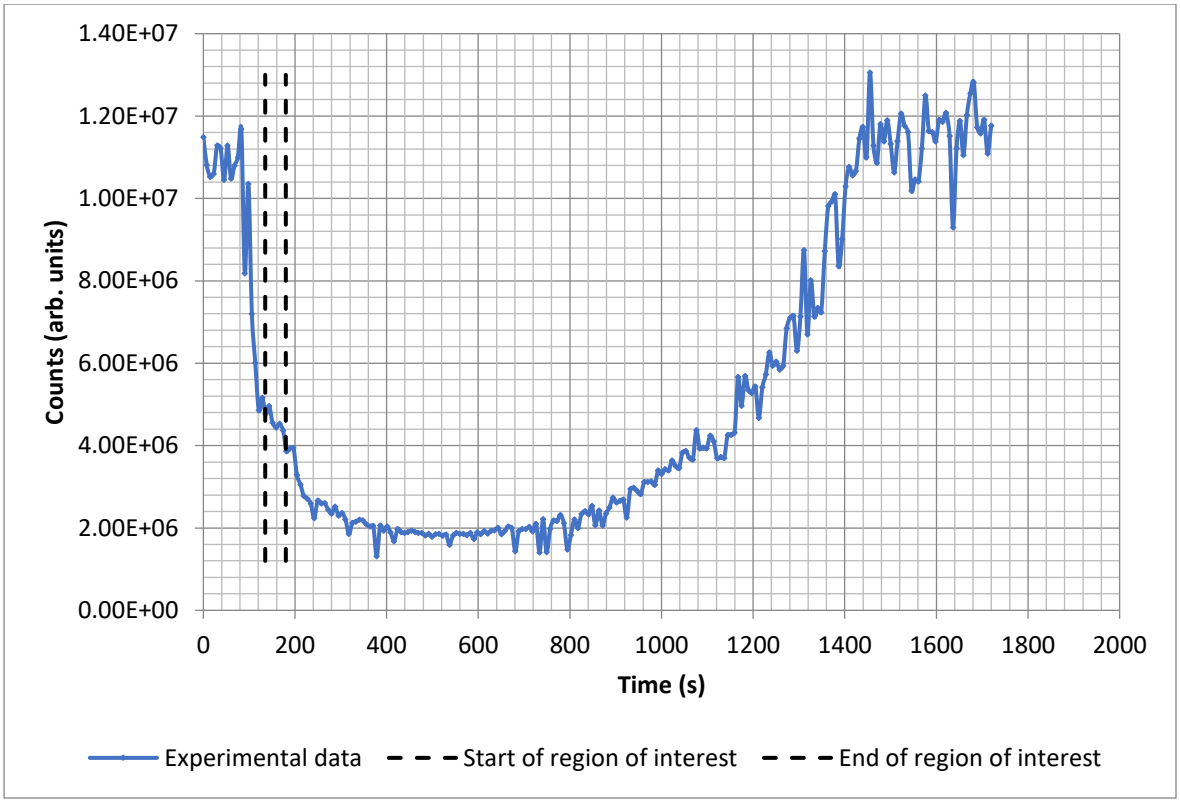

Figure B.3: Count versus time graph for drop of S240 (0.1%) (aq) spreading on pp substrate for run 1.28.

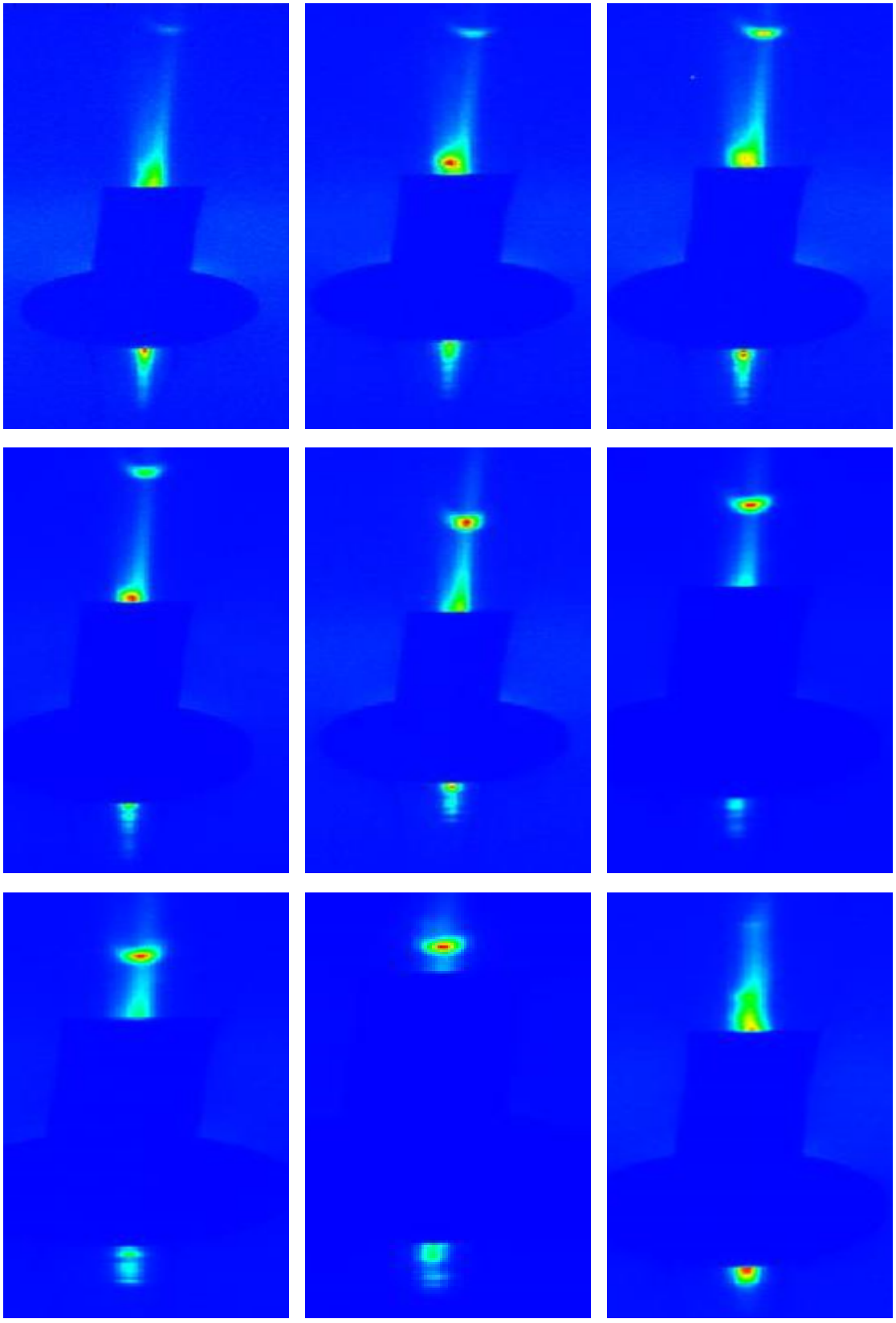

Figure B.4: GISAXS image of S240 (0.1%) (aq) superspreading solution on polypropylene substrate showing periodic spots on both bottom and top vertical flare. Run 1.28

.

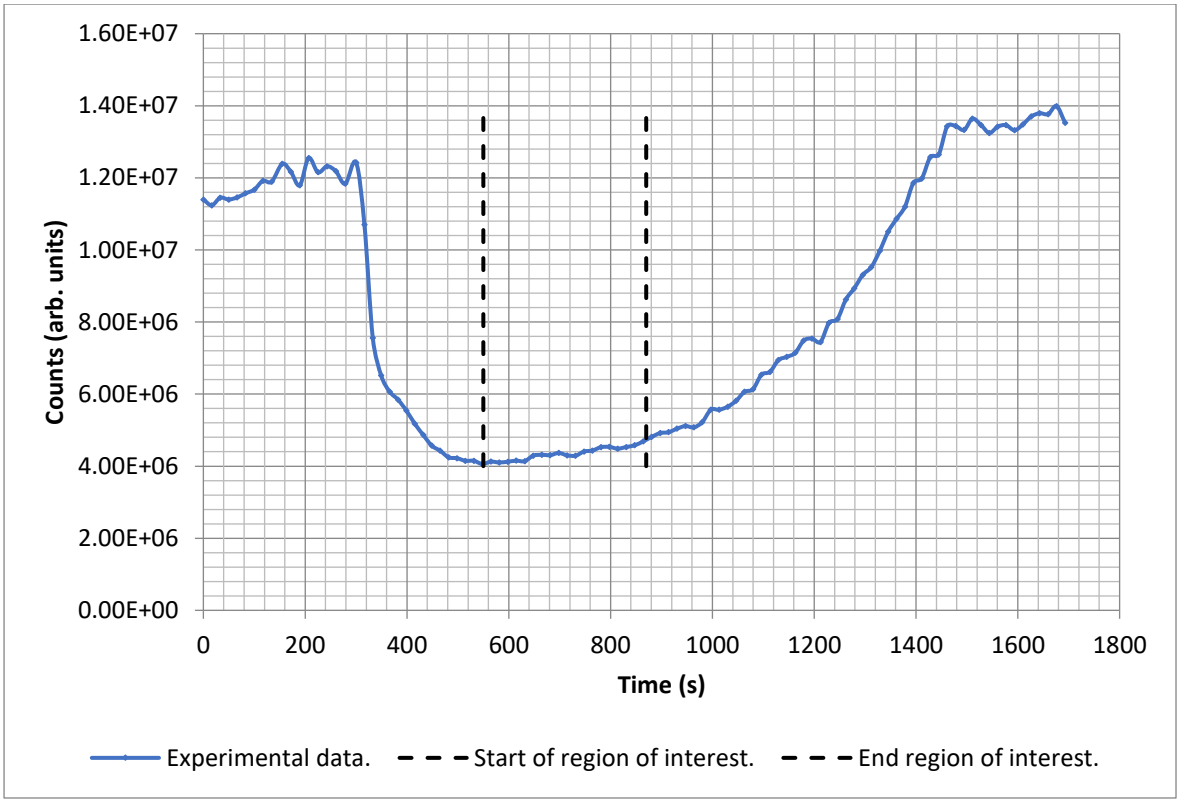

Figure B.5: Count versus time graph for drop of S240 (0.1%) (aq) spreading on pp substrate for run 1.29

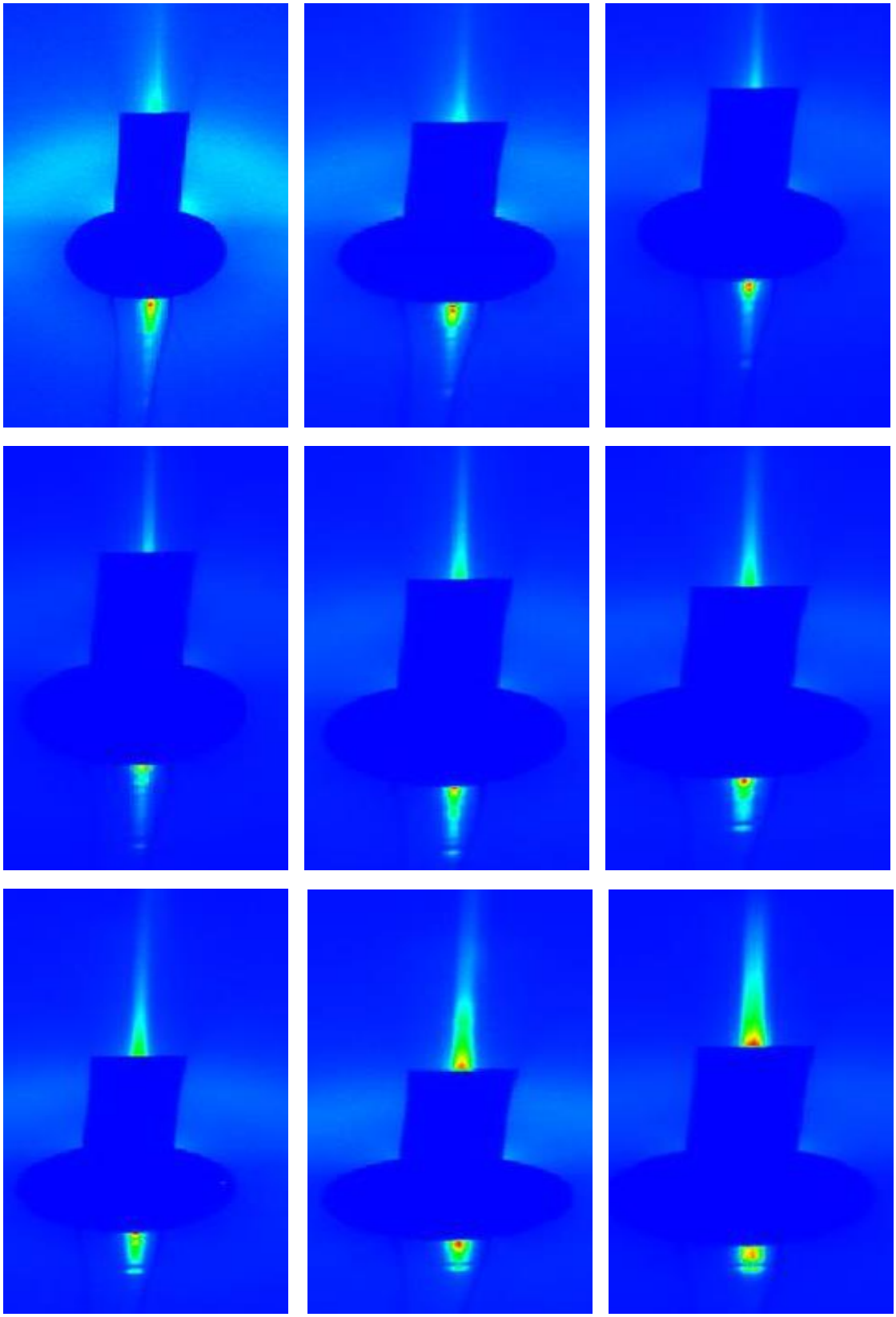

Figure B.6: GISAXS image of S240 (0.1%) (aq) superspreading solution on polypropylene substrate showing periodic spots on bottom vertical flare. Run 1.29.

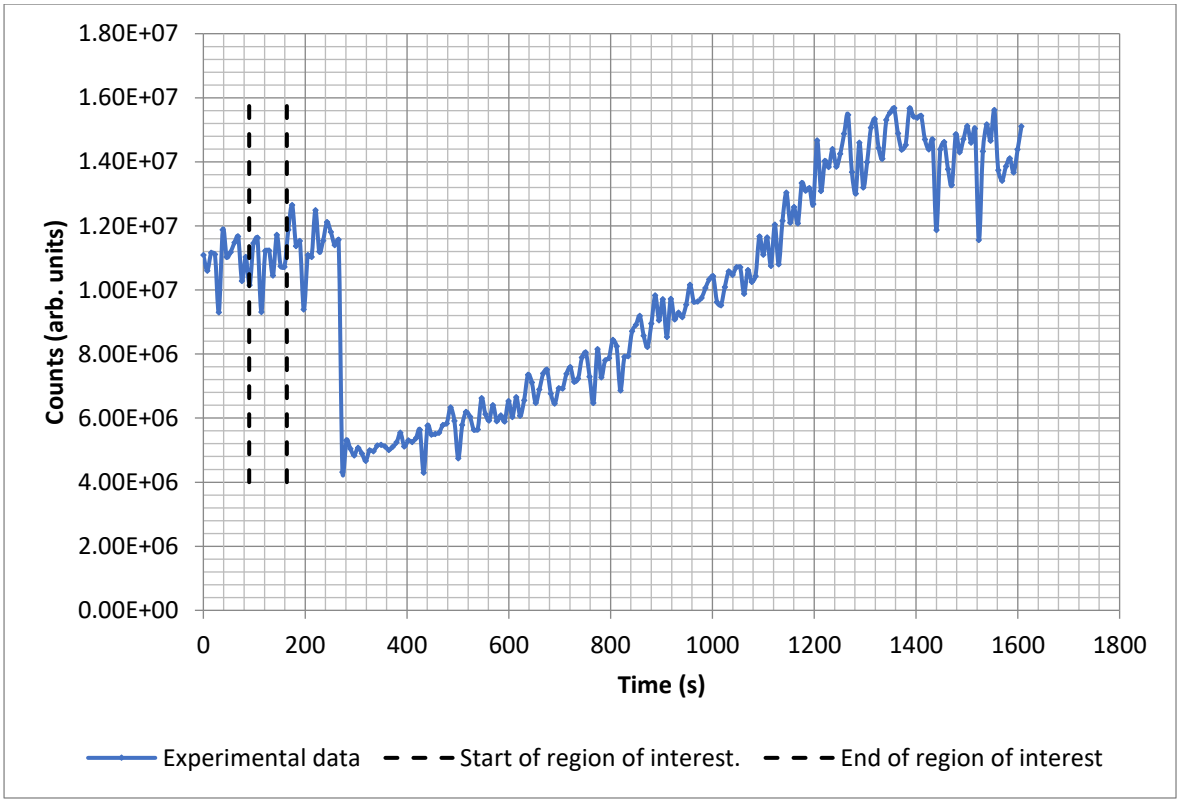

Figure B.7: Count versus time graph for drop of S240 (0.1%) (aq) spreading on pp substrate for run 1.30.

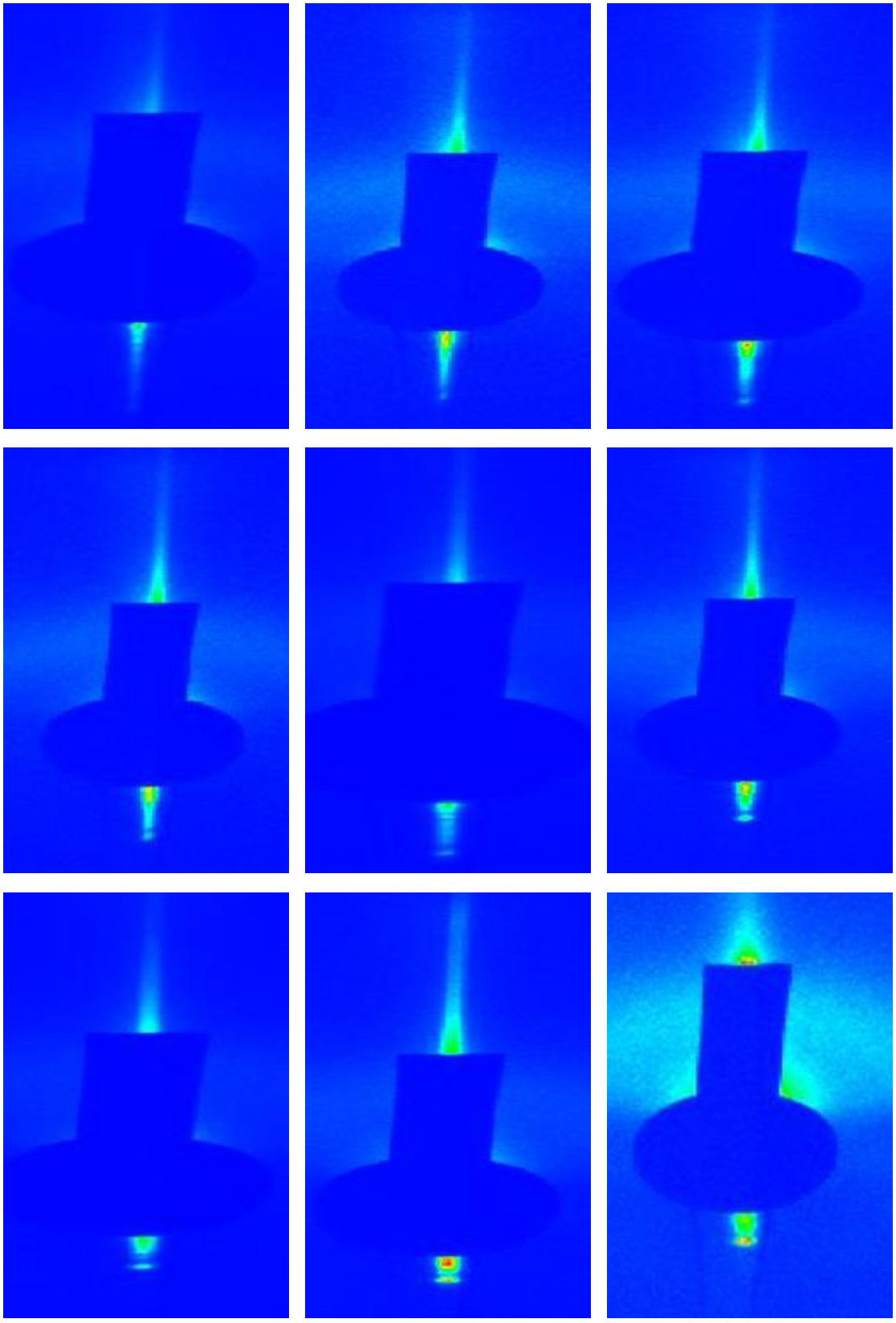

Figure B.8: GISAXS image of S240 (0.1%) (aq) superspreading solution on polypropylene substrate showing periodic spots on both bottom flare. Run 1.30.

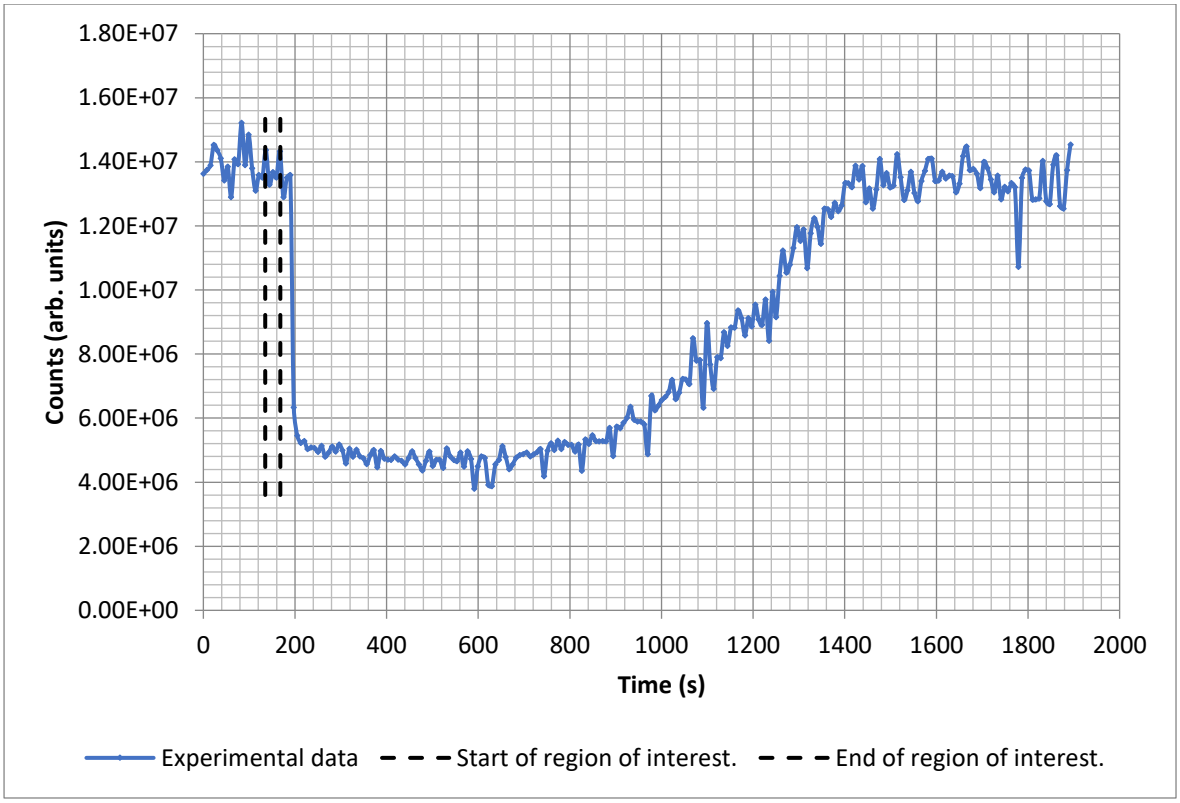

Figure B.9: Count versus time graph for drop of S240 (0.1%) (aq) spreading on pp substrate for run 1.31.

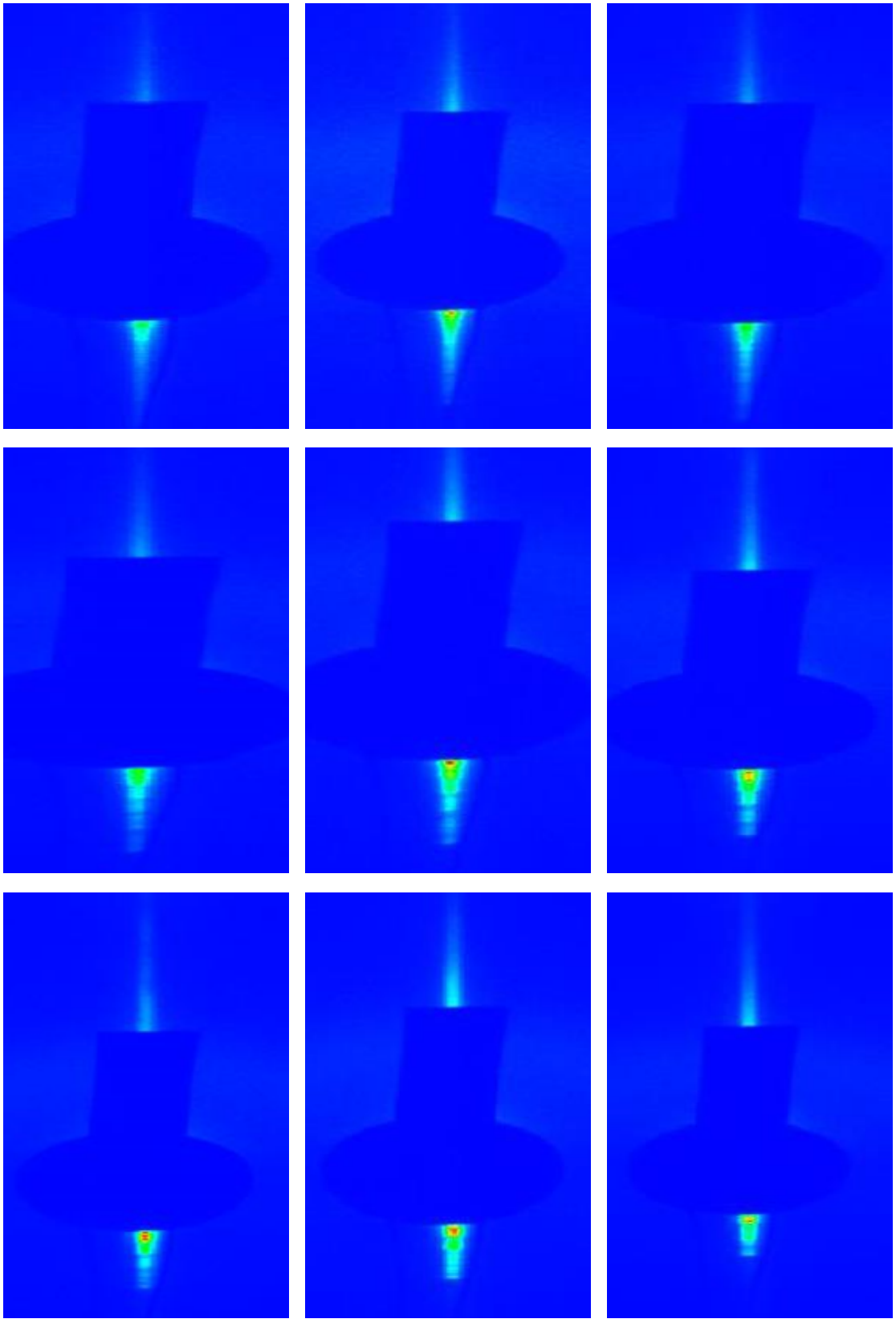

Figure B.10: GISAXS image of S240 (0.1%) (aq) superspreading solution on polypropylene substrate showing periodic spots on both bottom flare. Run 1.31

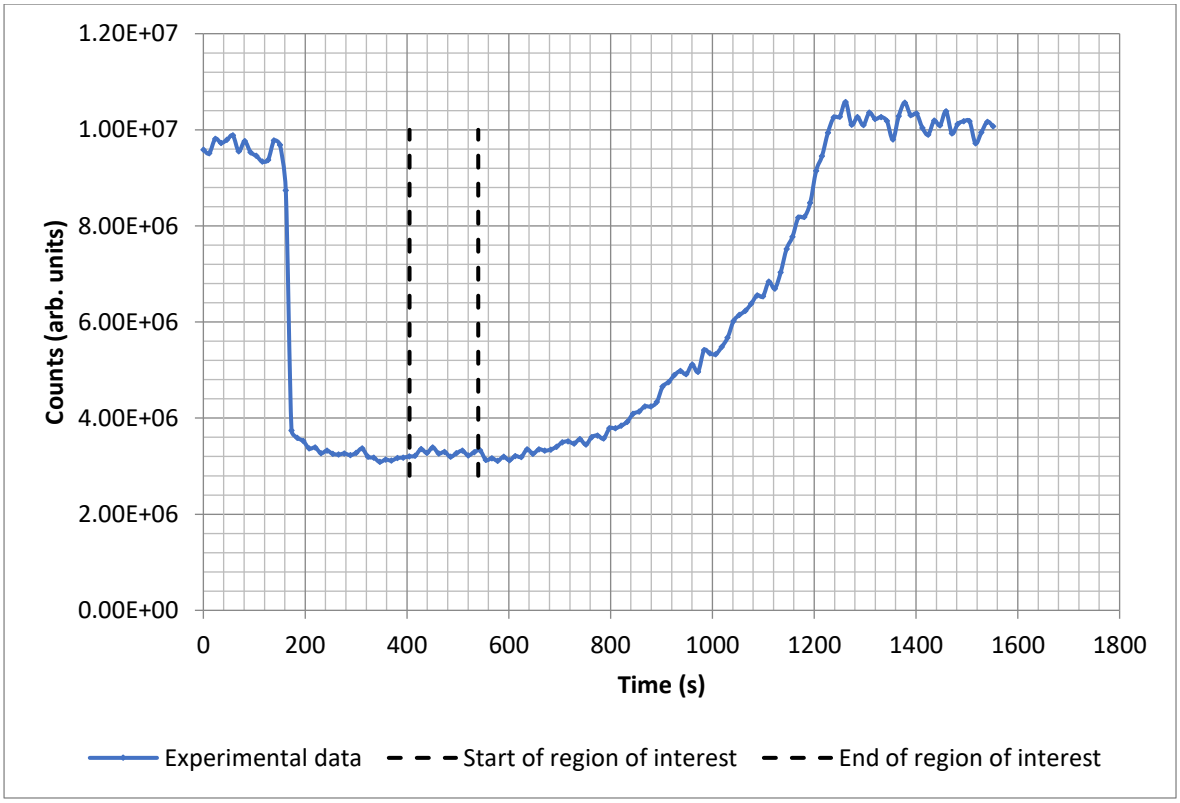

Figure B.11: Count versus time graph for drop of S233 (0.1%) (aq) spreading on pp substrate for run 1.33.

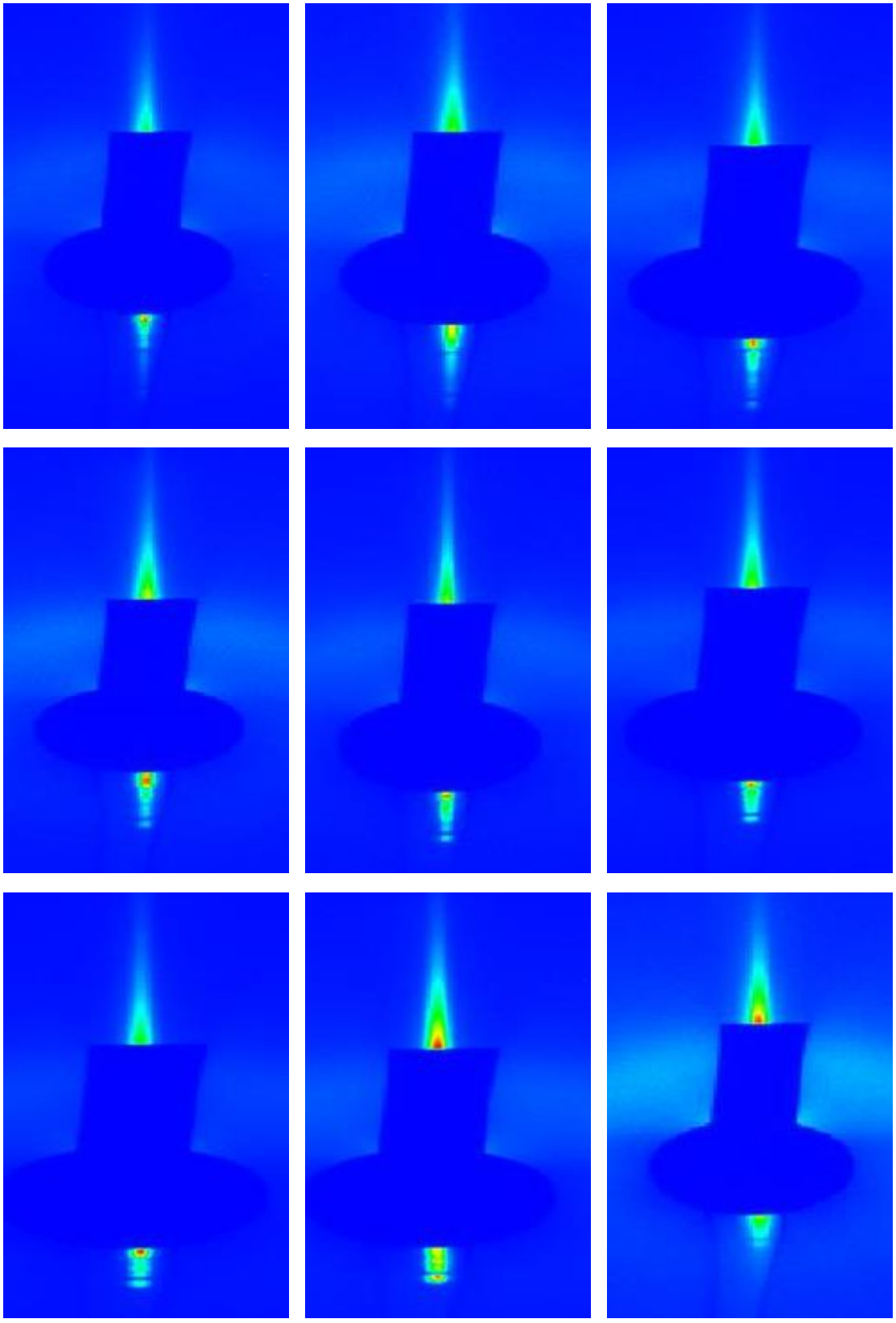

Figure B.12: GISAXS image of S233 (0.1%) (aq) superspreading solution on polypropylene substrate showing periodic spots on bottom flare. Run 1.33.

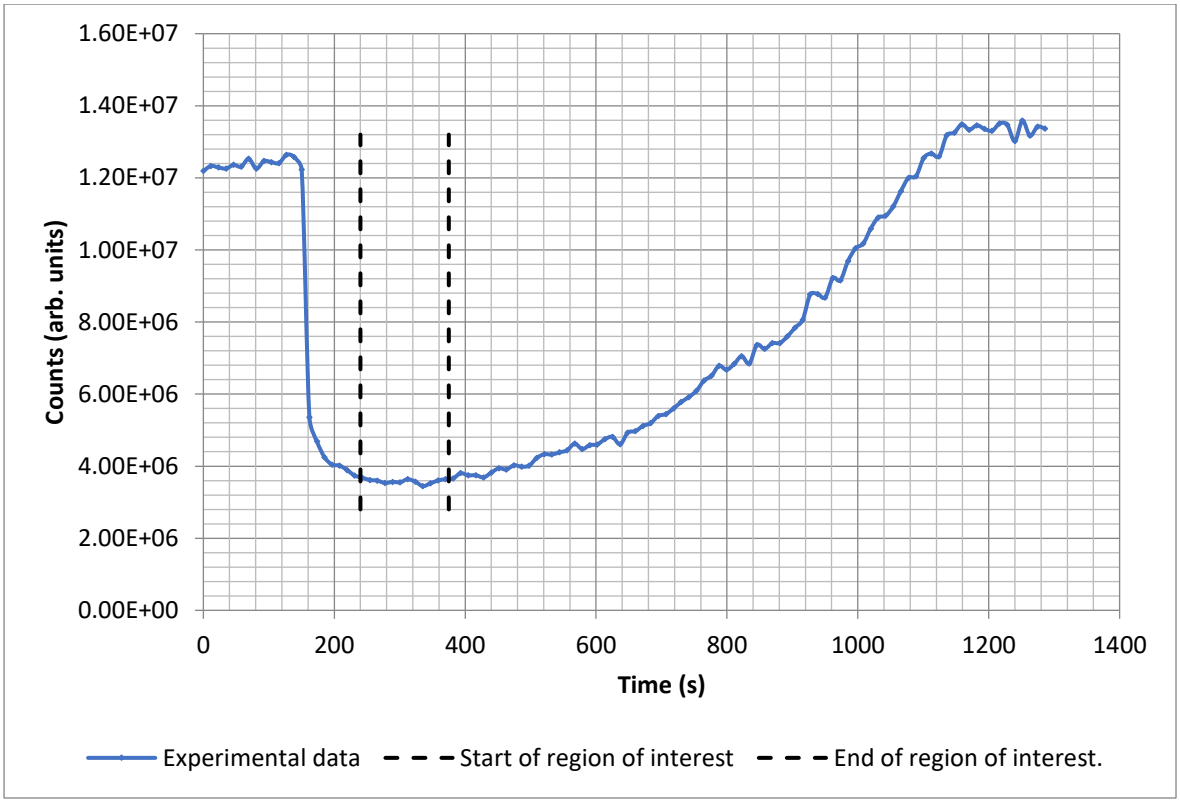

Figure B.13: Count versus time graph for drop of S233 (0.1%) (aq) spreading on pp substrate for run 1.34.

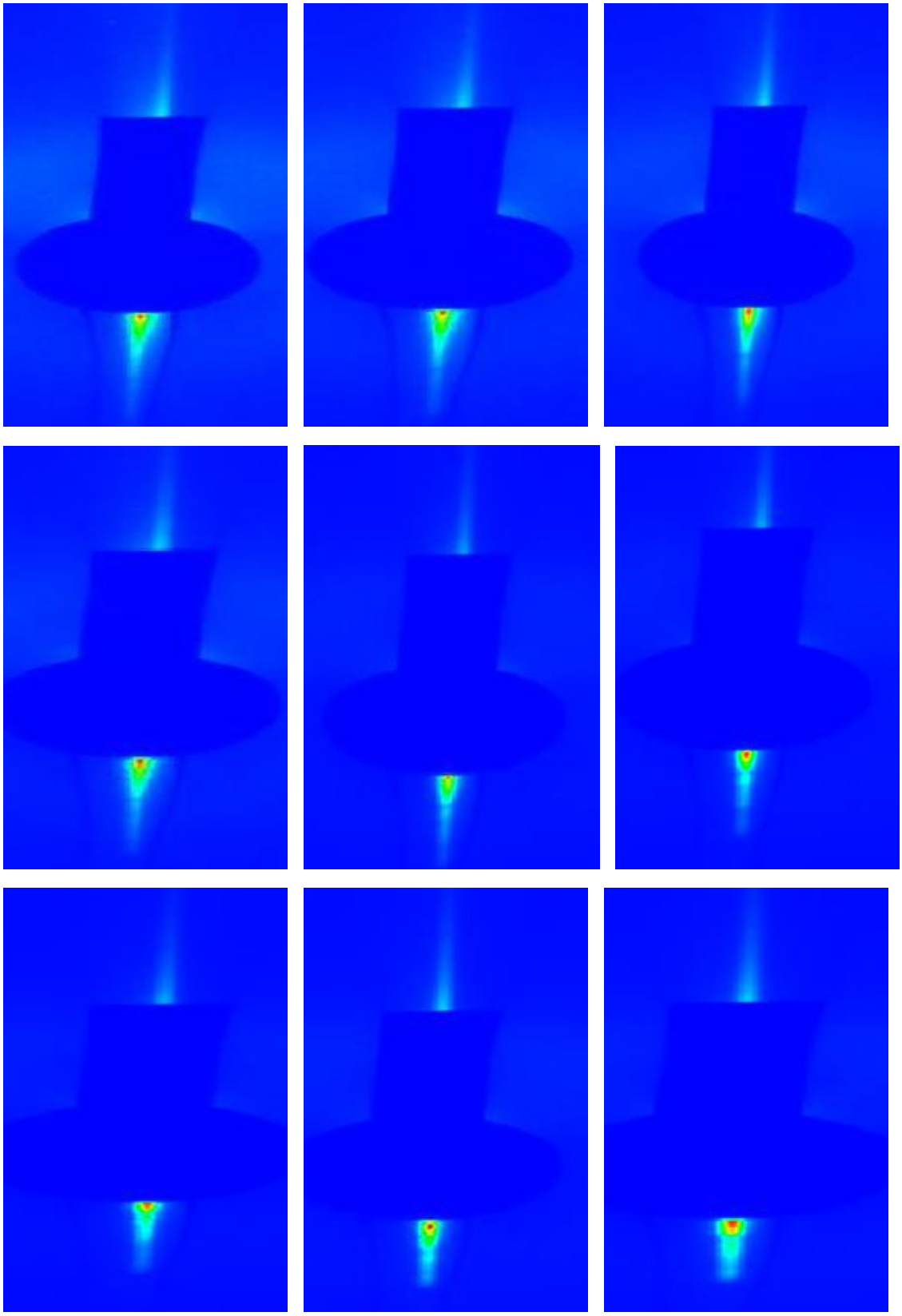

Figure B.14: GISAXS image of S233 (0.1%) (aq) solution on polypropylene substrate showing periodic spots on bottom flare. Run 1.34.

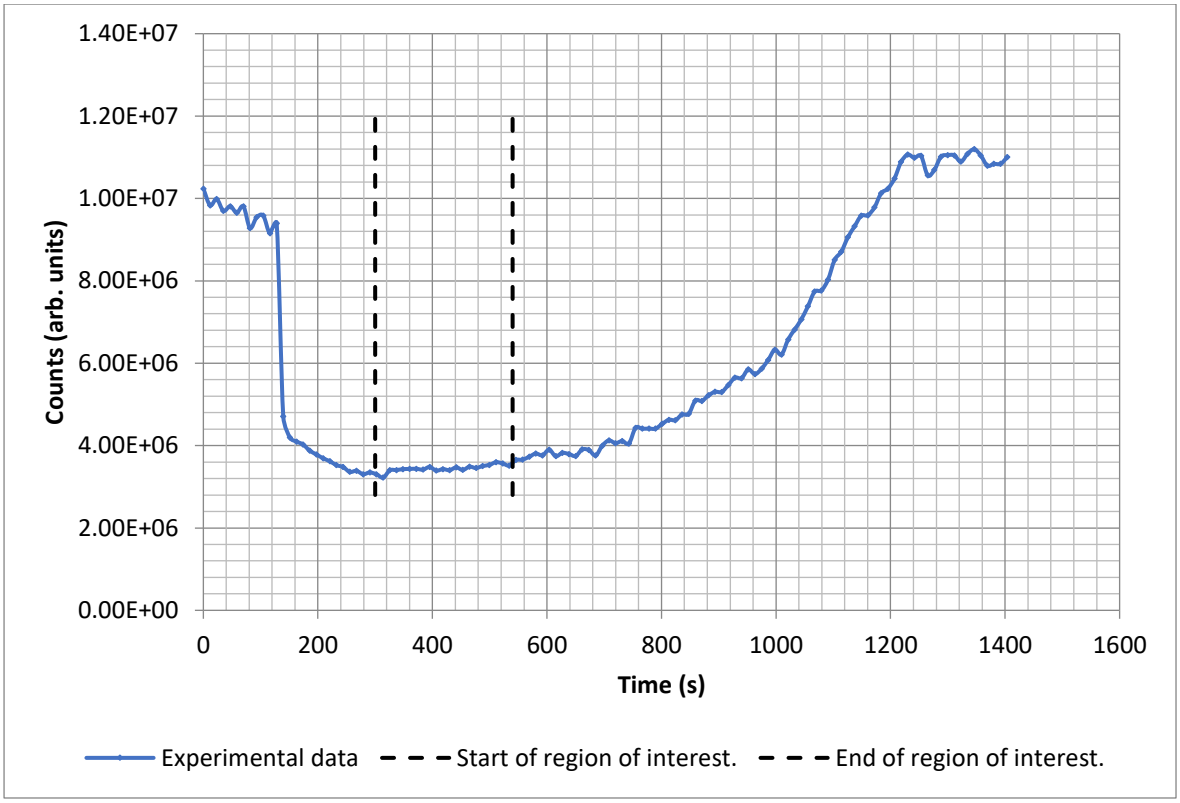

Figure B.15: Count versus time graph for drop of S233 (0.1%) (aq) spreading on pp substrate for run 1.35.

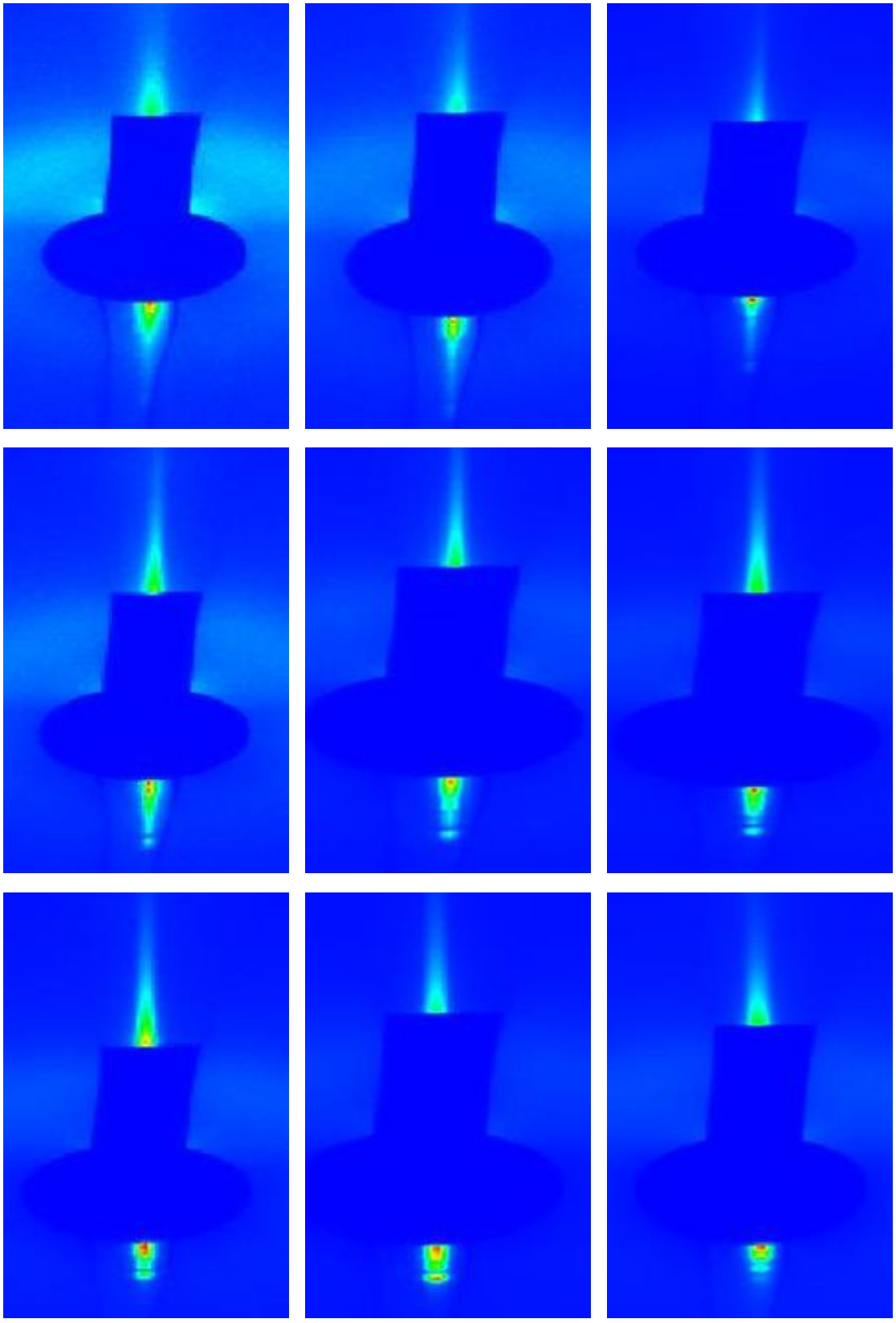

Figure B.16: GISAXS image of S233 (0.1%) (aq) superspreading solution on polypropylene substrate showing periodic spots on bottom flare. Run 1.35.

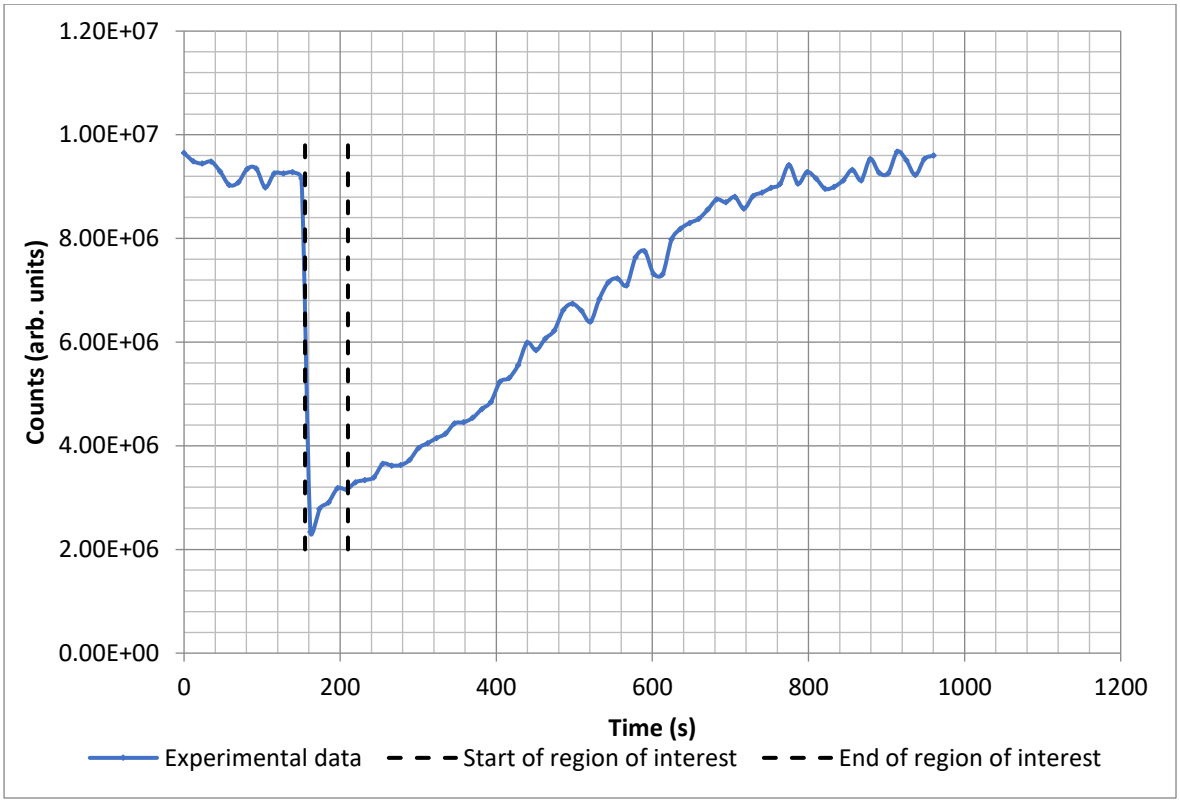

Figure B.17: Count versus time graph for drop of S233 (0.1%) (aq) spreading on pcp substrate for run 1.36.

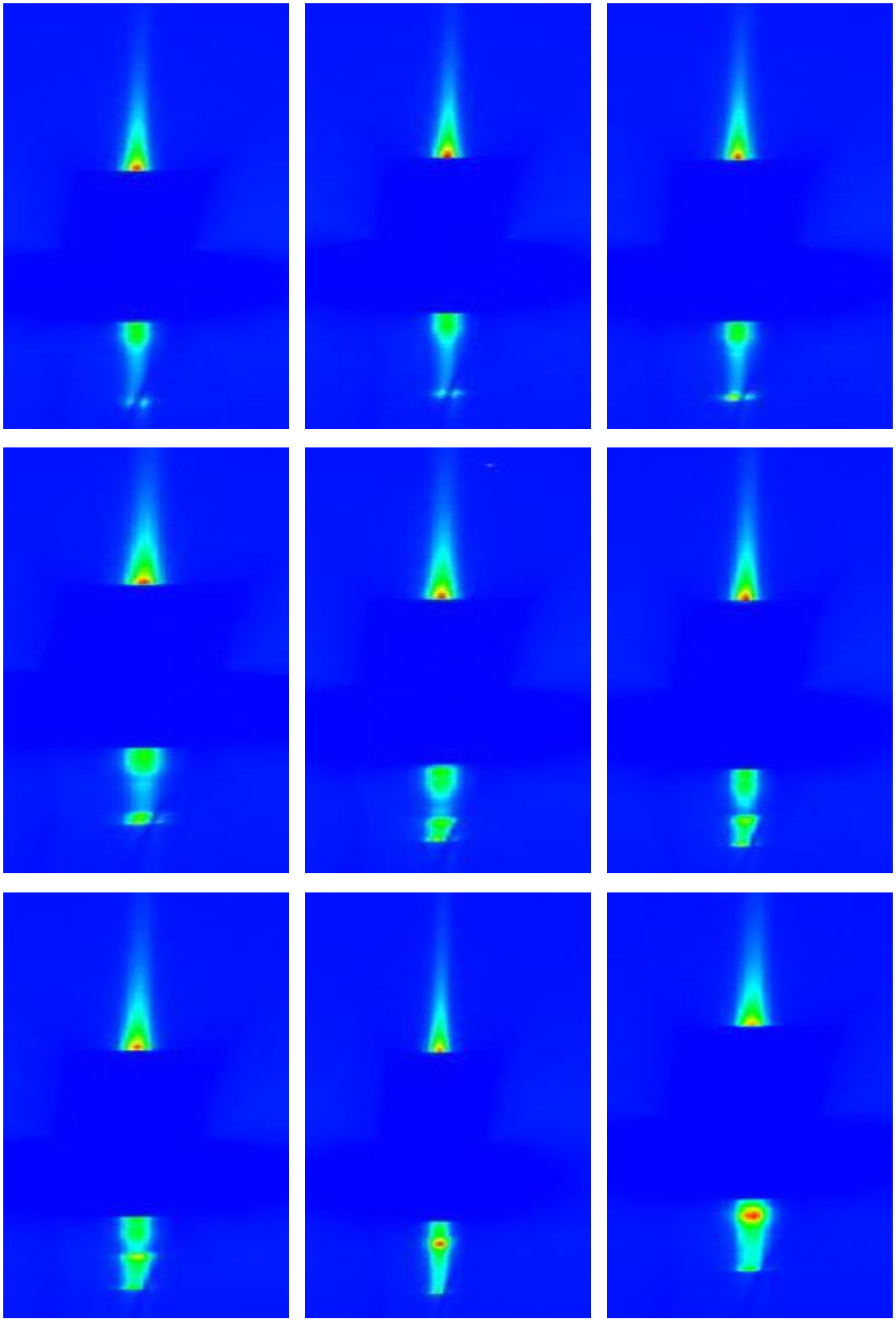

Figure B.18: GISAXS image of S233 (0.1%) (aq) superspreading solution on poly carbonate plastic sheet substrate showing periodic spots on bottom flare. Run 1.36.

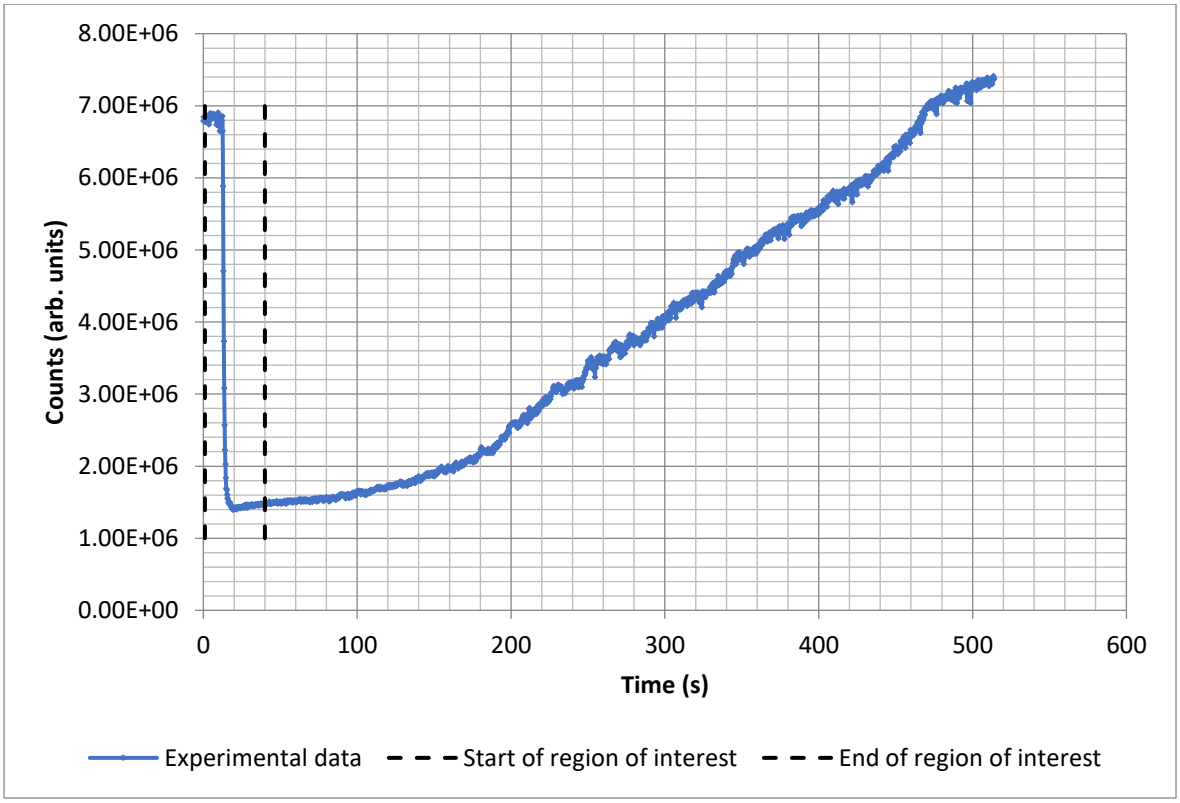

Figure B.19: Count versus time graph for drop of S240 (0.1%) (aq) spreading on a pp substrate for run 2.22.

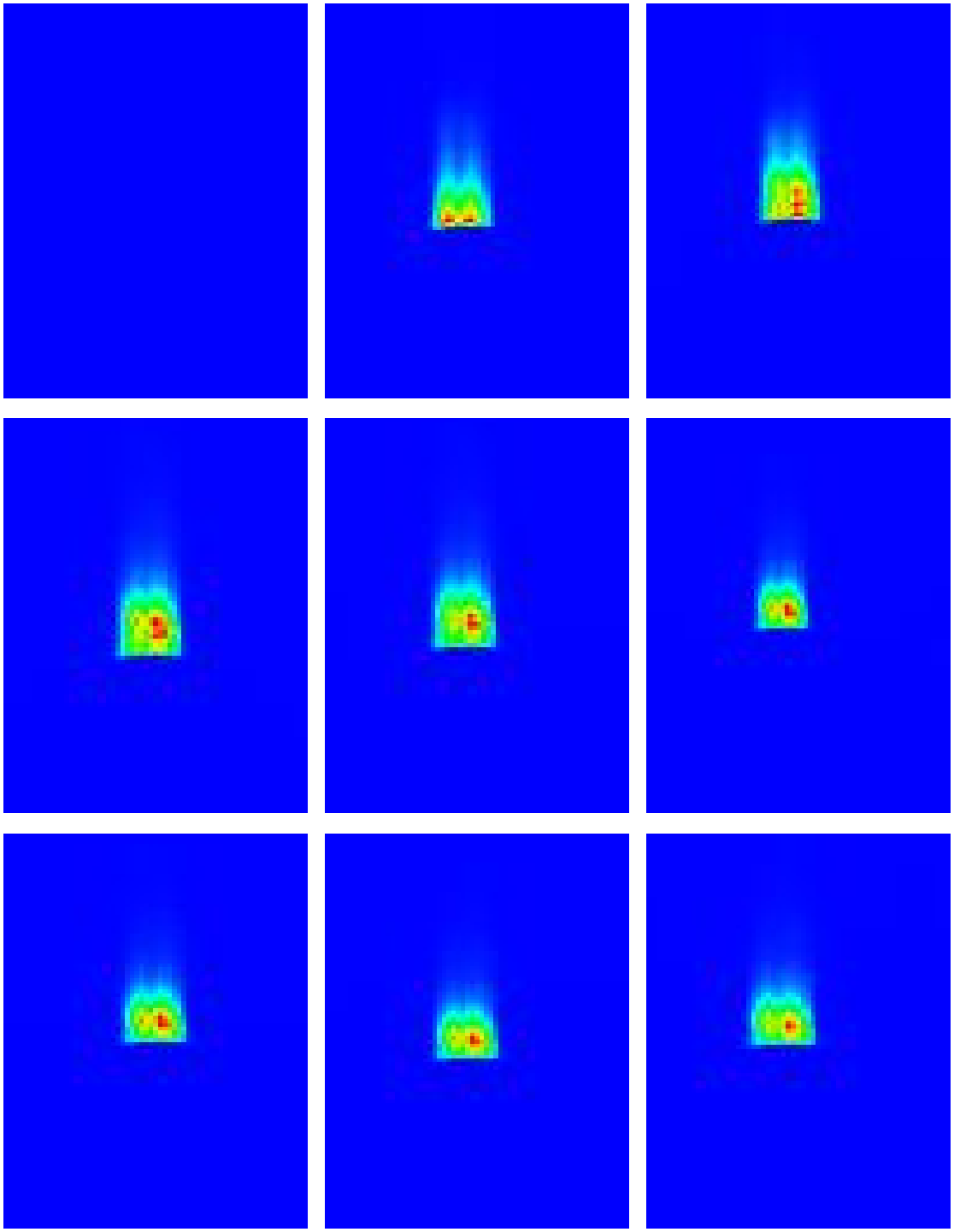

Figure B.20: GISAXS images for run 2.22 S240 (0.1%) (aq) on Polypropylene substrate, corresponds to region of interest in timescan 54.2 of 1 to 40 seconds with a time interval of 4.875 seconds between images above run 2.22

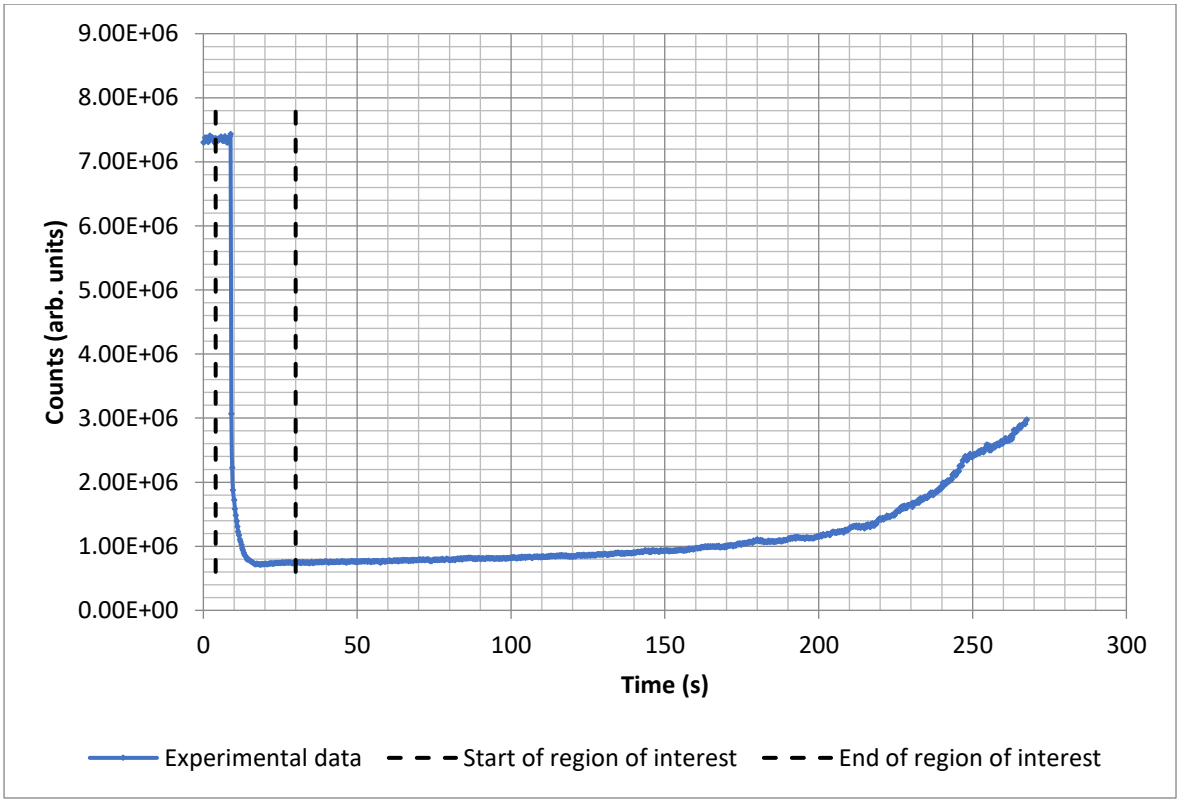

Figure B.21: Count versus time graph for drop of S240 (0.1%) (aq) spreading on a pp substrate for run 2.23

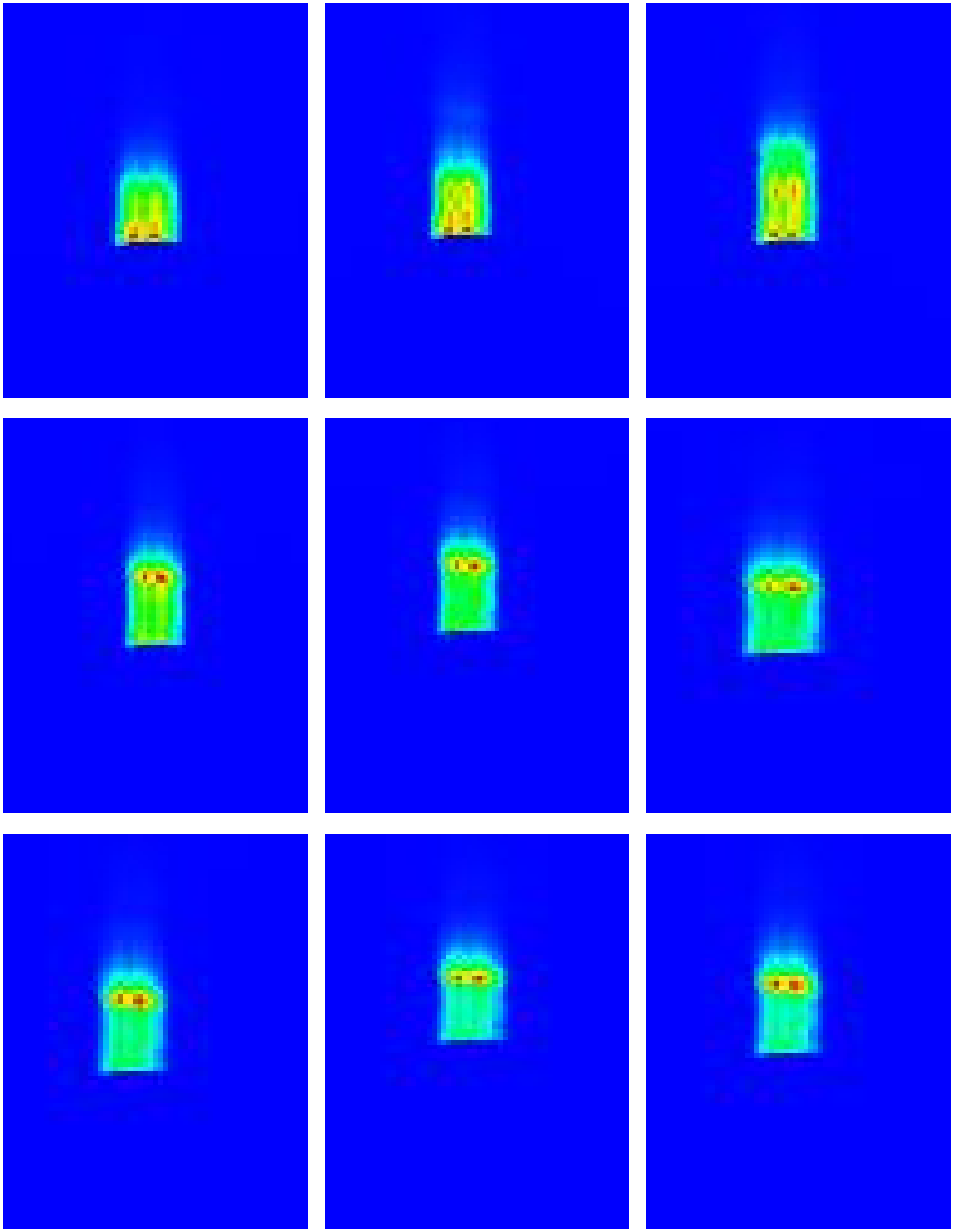

Figure B.22: GISAXS images for run 2.23 S240 (0.1%) (aq) on Polypropylene substrate, corresponds to region of interest in timescan 41.2 of 4 to 30 seconds with a time interval of 3.25 seconds between images above. Run 2.23.

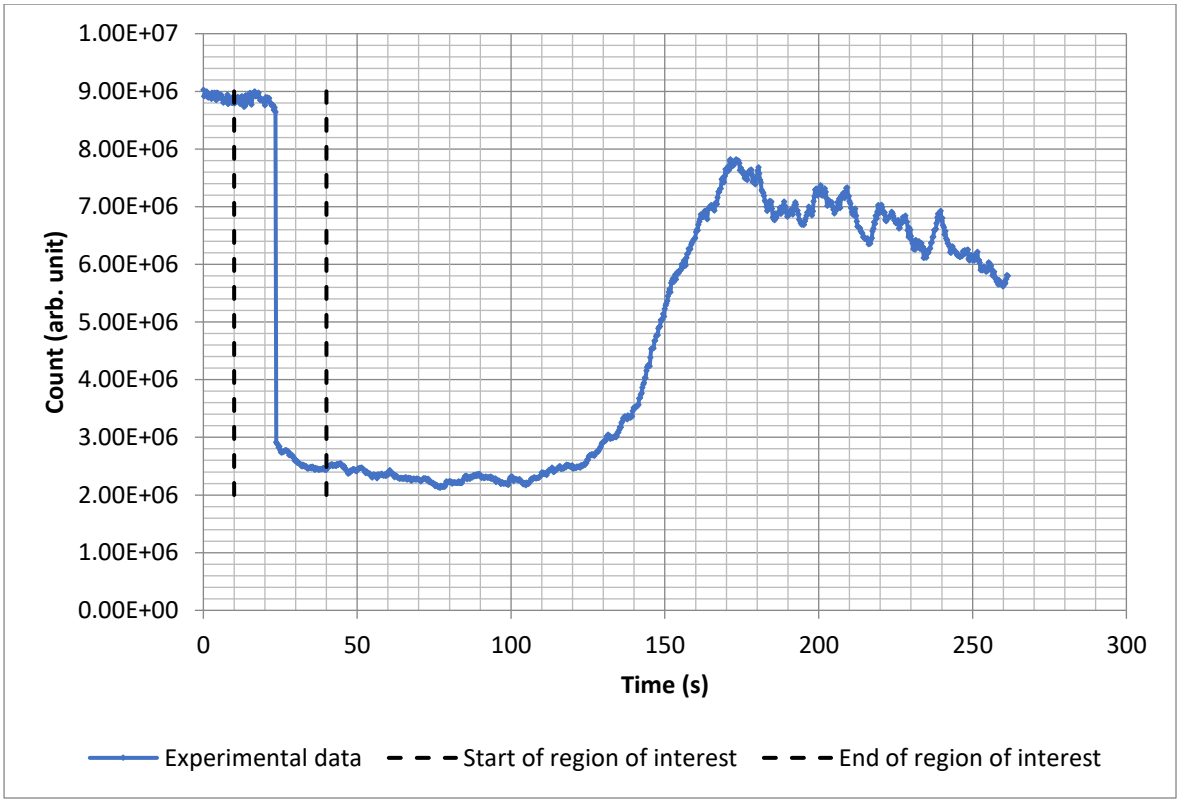

Figure B.23: Count versus time graph for drop of S240 (0.1%) (aq) spreading on ac substrate for run 2.24.

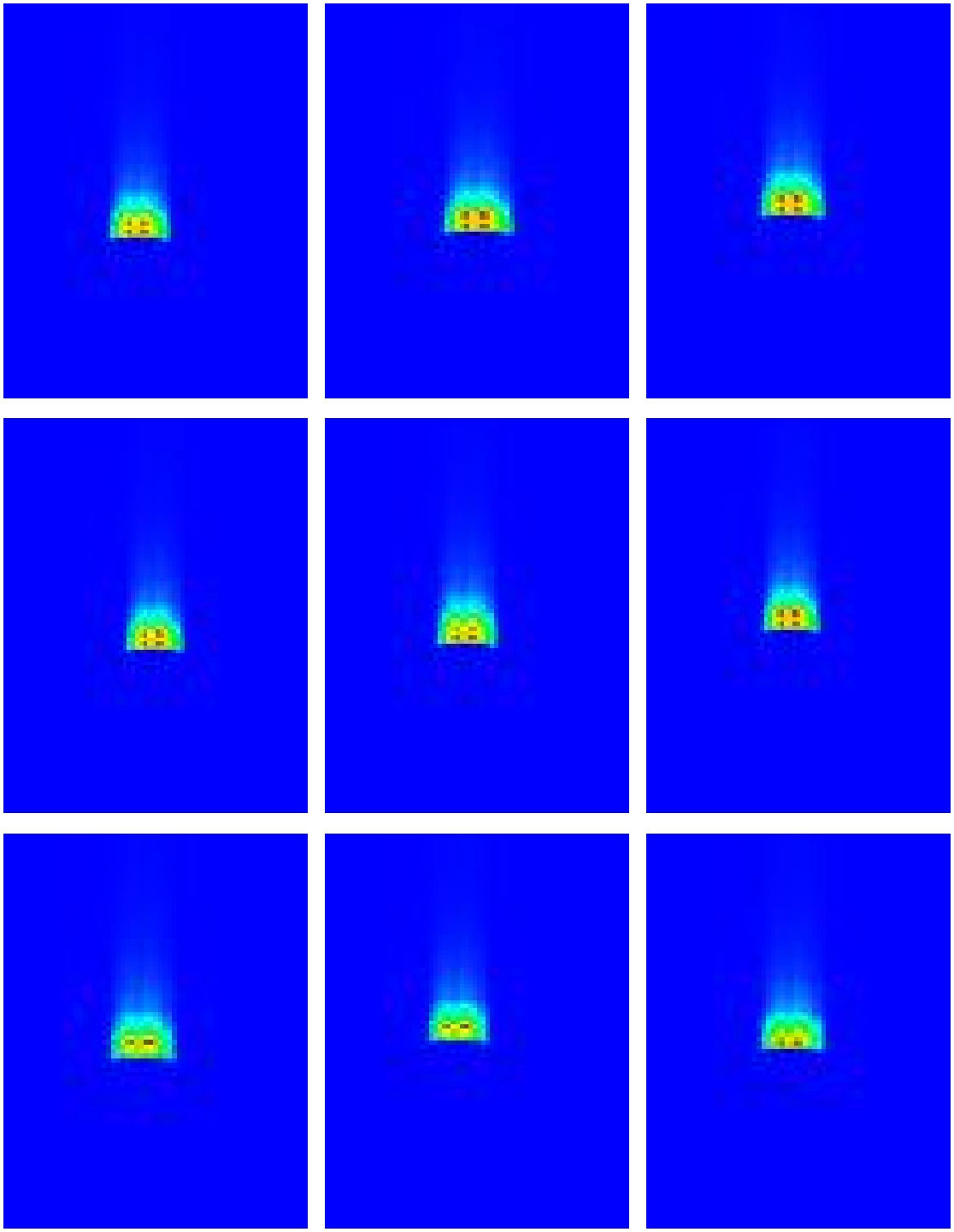

Figure B.24: GISAXS images for run 2.26 S240 (0.1%) (aq) on Acetate substrate, corresponds to region of interest in timescan 28 of 10 to 40 seconds with a time interval of 3.75 seconds between images above. Run 2.24.

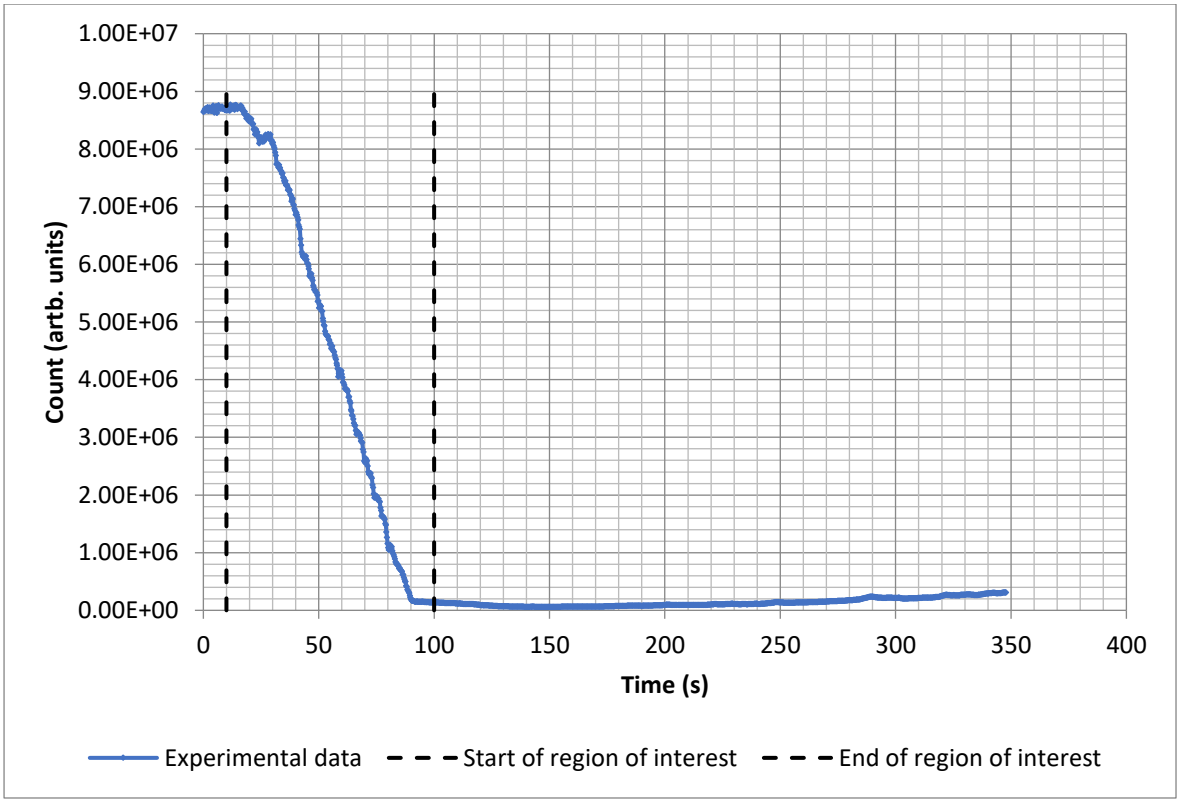

Figure B.25: Count versus time graph for drop of S240 (0.1%) (aq) spreading on ac substrate for run 2.25

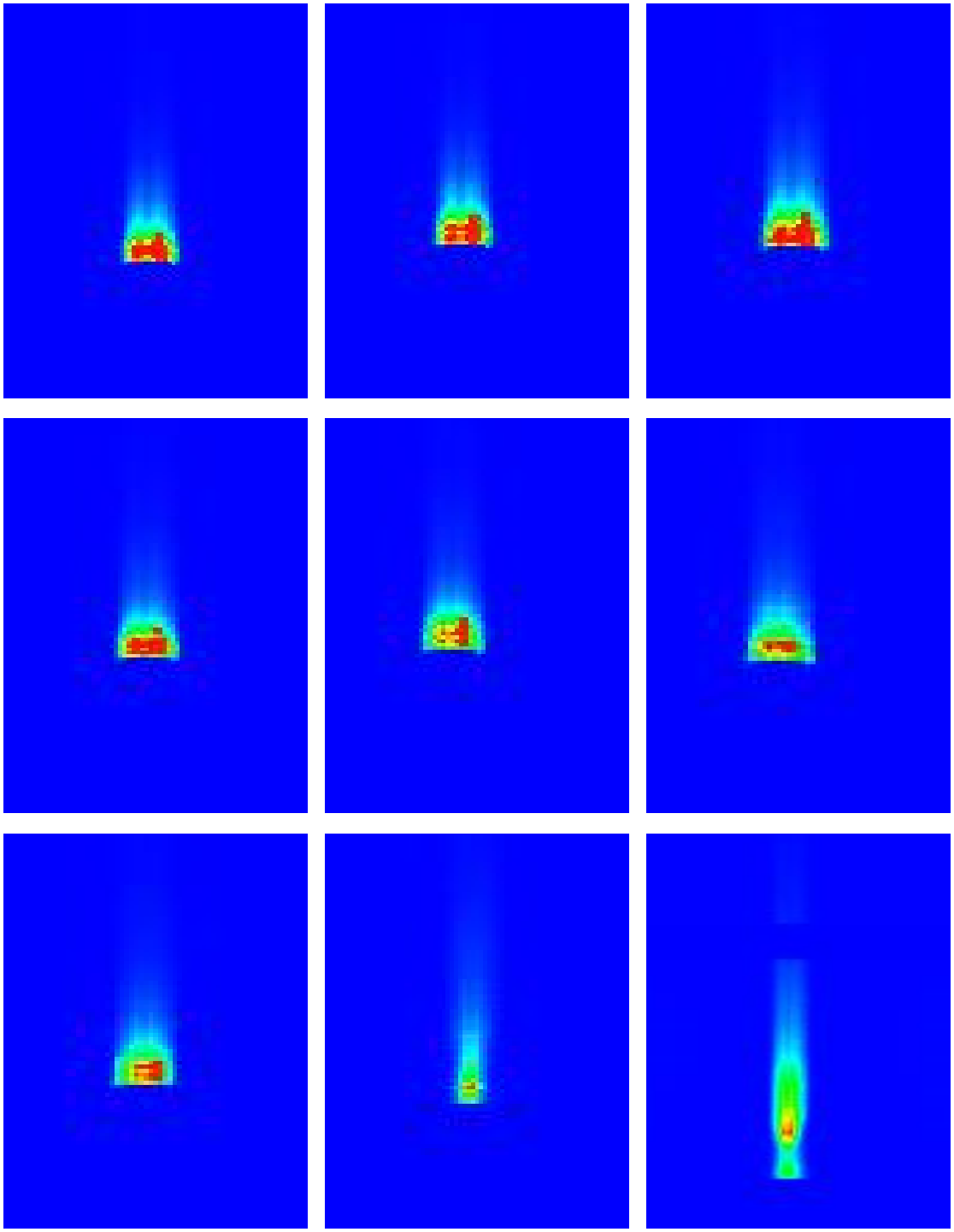

Figure B.26: GISAXS images for run 2.27 S240 (0.1%) (aq) on Acetate substrate, corresponds to region of interest in timescan 33 of 10 to 100 seconds with a time interval of 11.25 seconds between images above. Run 2.25.

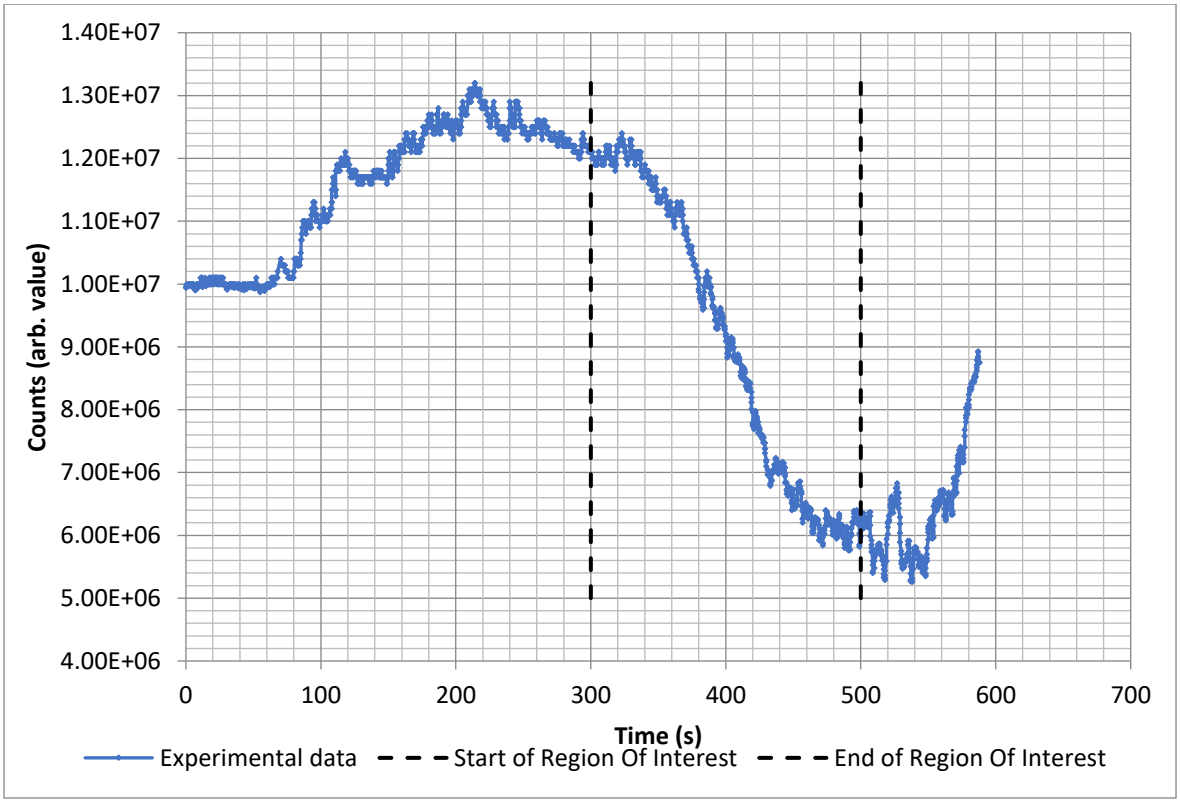

Figure B.27: Count versus time graph for drop of S233 (0.1%) (aq) spreading on ac substrate for run 2.26

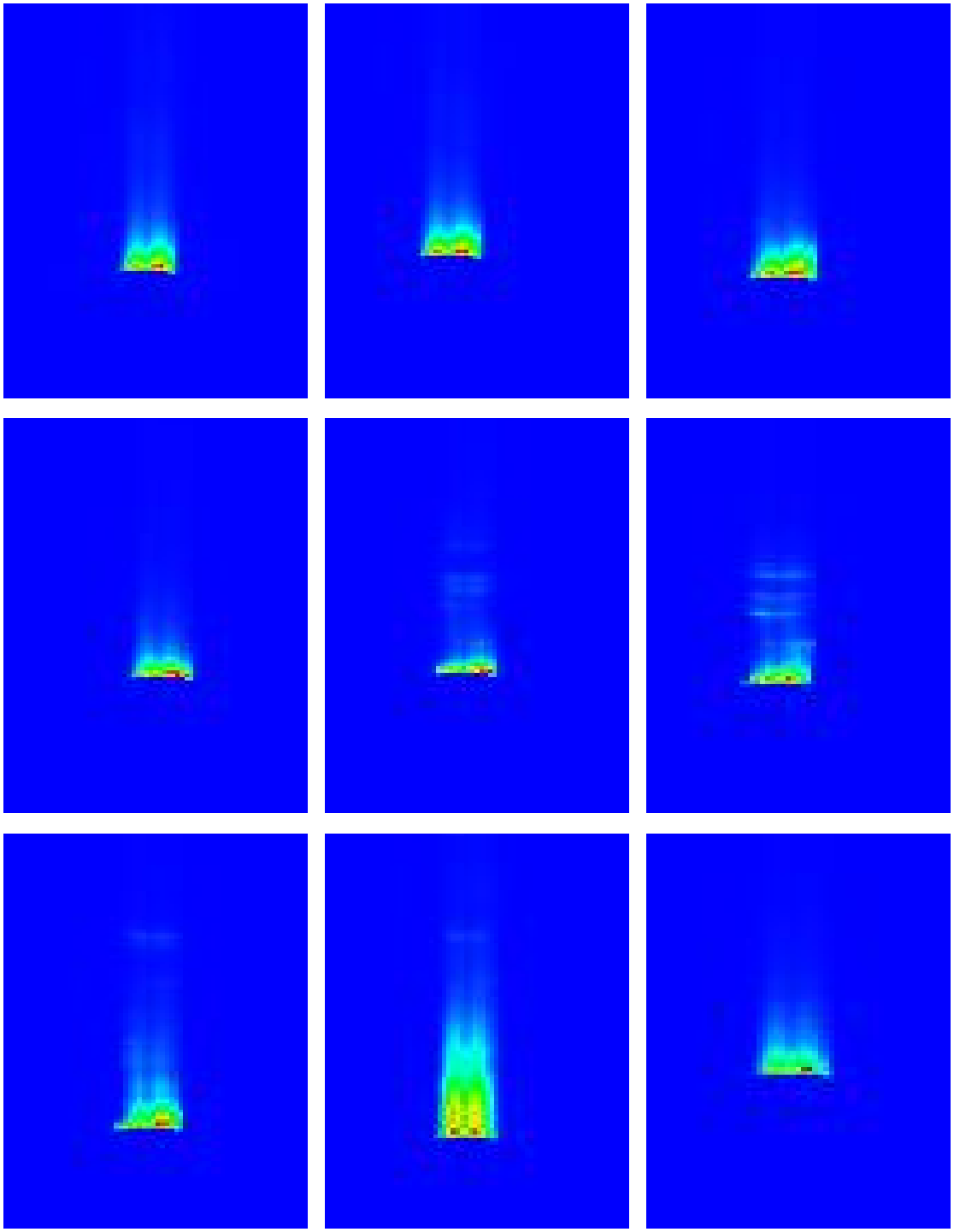

Figure B.28: GISAXS images for run 2.28 S233 (0.1%) (aq) on Acetate substrate, corresponds to region of interest in timescan 41 of 300 to 500 seconds with a time interval of 25 seconds between images above. Run 2.26.

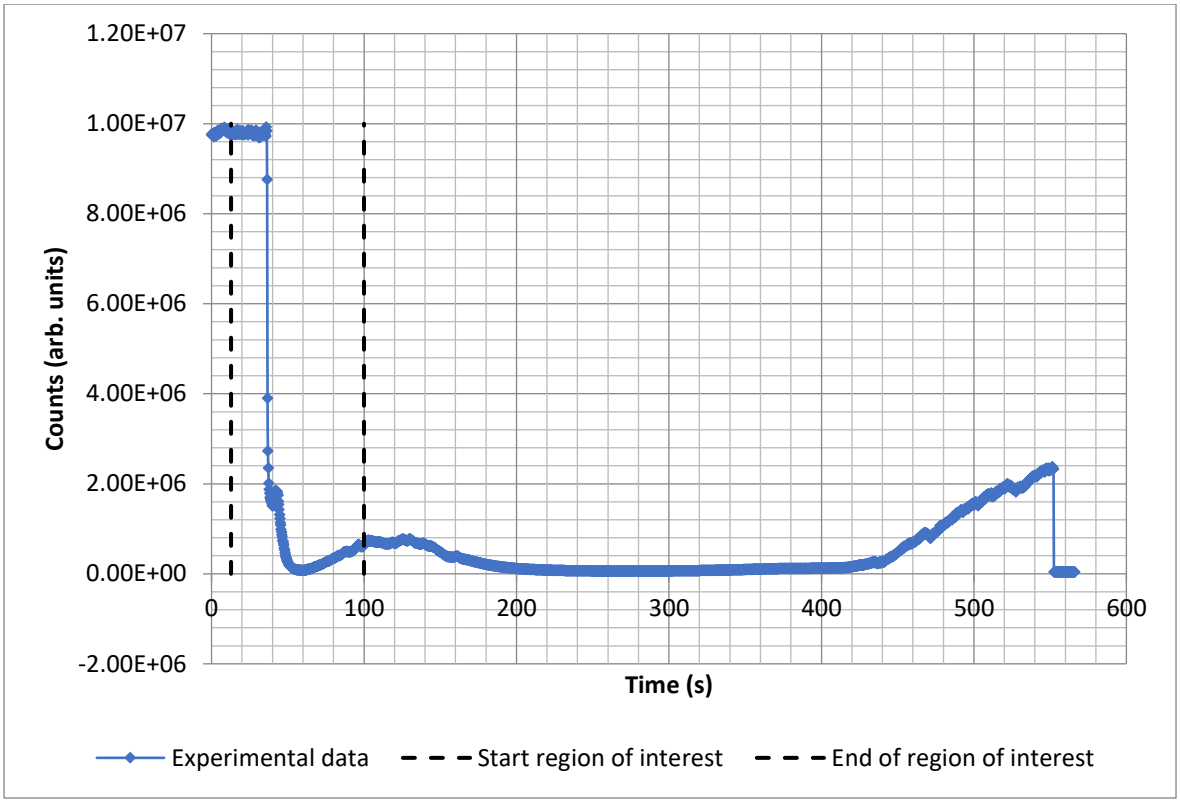

Figure B.29: Count versus time graph for drop of S233 (0.1%) (aq) spreading on ac substrate for run 2.27

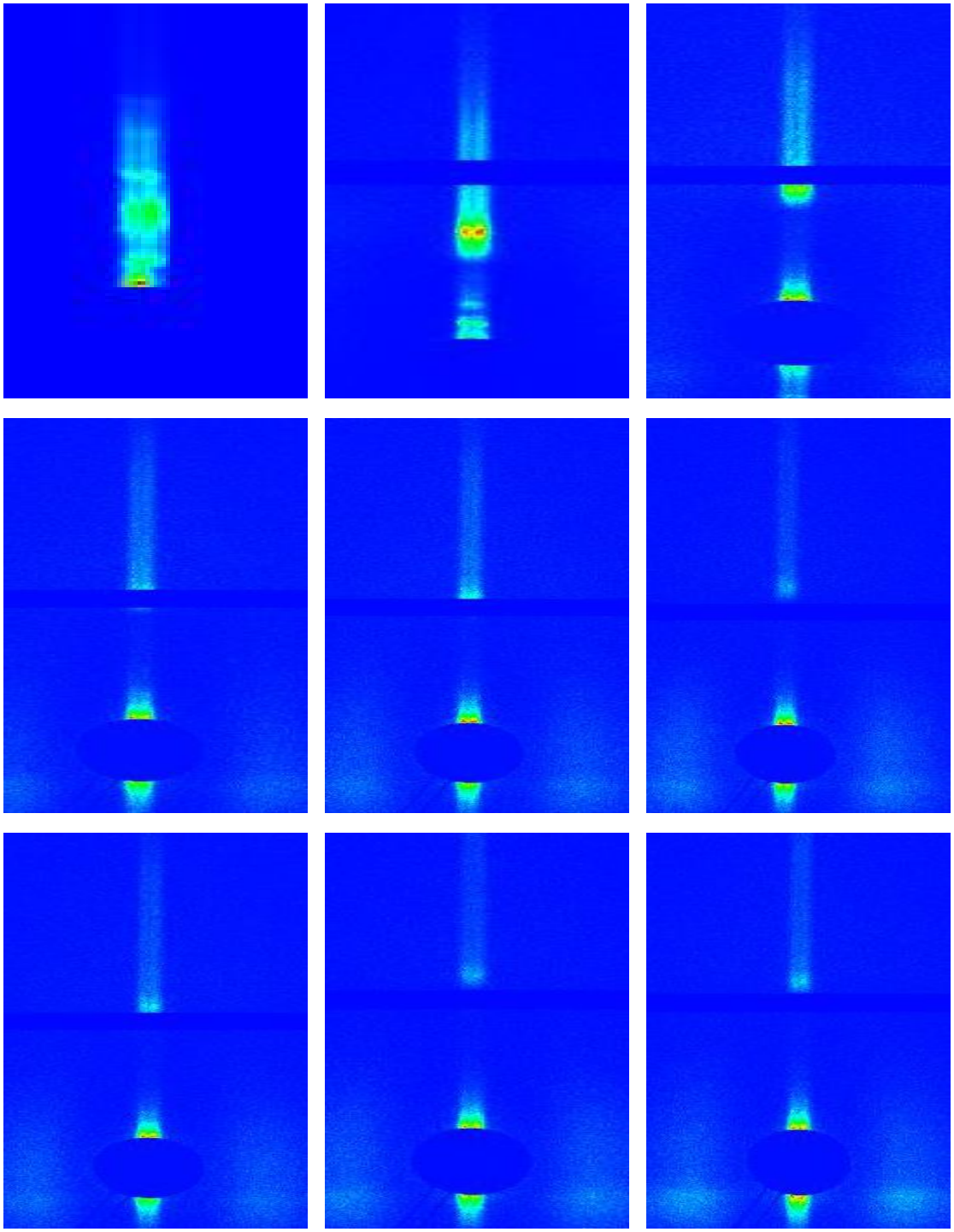

Figure B.30: GISAXS images for run 2.29 S233 (0.1%) (aq) on Acetate substrate, corresponds to region of interest in timescan 42 of 12.8 to 100 seconds with a time interval of 10.9 seconds between images above. Run 2.27

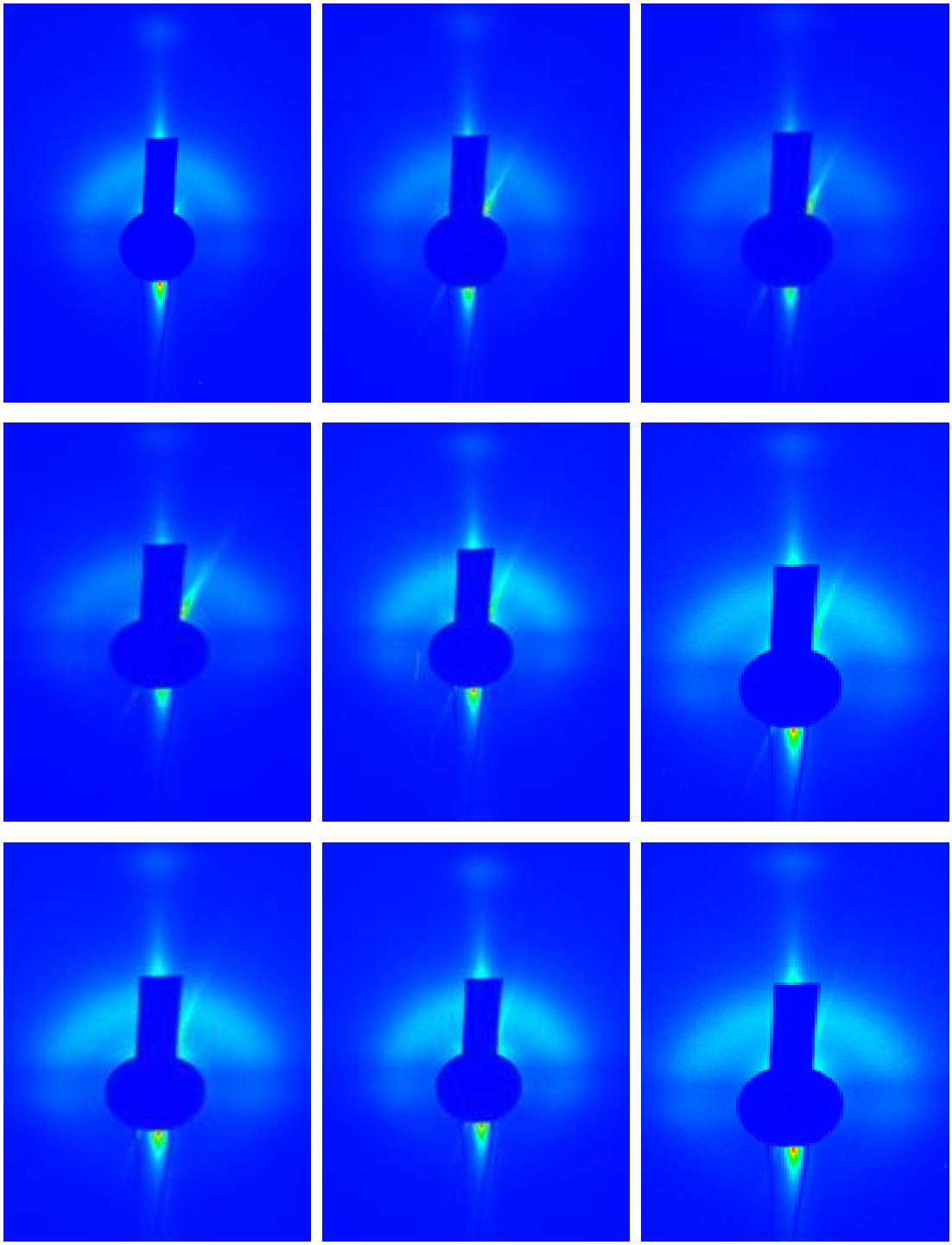

Figure B.31: Example GISAXS spectra showing diagonal flare for drop of S240 (0.1%) (aq) spreading on a pcp substrate.

Example of diagonal flares on the side of the beamstop and what this means physically.

The inclined flare is caused by the refraction of the X-ray beam through the liquid/air interface of the drop. The diagonal flare gives an idea of the shape of the free surface of the drop near the contact point. However what particular point on the liquid/air interface that the X-ray beam is refracted by a small angle is not known.

Bibliography

(1) Venzmer J. (2011), Superspreading - 20years of physicochemical research. Current Opinion in Colloid and Interface Science 16 (4): 335-343

(2) Ananthapadmanabhan K, Goddard E, Chandar P. (1990), A study of the solution, interfacial and wetting properties of silicone surfactants. Colloids and Surfaces 44: 281-297.

(3) Ruckenstein E, (2012), Superspreading: A possible mechanism. Colloids and Surfaces A Physiochemical and Engineering Aspects 412: 36-37.

(4) Zabkiewicz JA, Gaskin RE, Balneaves (1985), Effect of additives on foilar wetting and uptake of glysphosate into gorse. Application and Biology. Southcombe (ed) British Crop Protection Council UK.

(5) Rosen MJ. (2004), Surfactants and interfacial phenomena. third edition ed.: John Wiley & sons; 2004.

(6) Israelachvili J, MItchell D, Ninham B. (1976), Theory of self-assembly of hydrocarbon amiphiles into micelles and bilayers. Journal of the Chemical Society Faraday Transactions 2 72: 1525-1568

(7) Mitchell DJ, Ninham BW. (1981), Micelles, vesicles and microemulsions. Journal of the Chemical Society Faraday Transactions 77: 601.

(8) Halverson JD, Maldarelli C, Couzis A, Koplik J. (2009), Wetting of hydrophobic substrates by nanodroplets of aqueous trisiloxane and alkyl polyethoxylate surfactant solutions. Chamical Engineering Science 64(22): 4657-4667

(9) He M, Hill R, LIn Z, Scriven L, Davis H. (1993), Phase behaviour and microstructure of polyoxyethylene trisiloxane surfactants in aqueous solutions. Journal Physical Chemistry 97: 8820-8834.

(10) Hill R, He M, Davis H, Scriven L (1994), Comparison of the liquid crystal phase behaviour of four superwetter surfactants. Langmuir 10: 1724-1734

(11) Nikolov A, Wasan D (2011), Superspreading mechanisms: An overview. European Physical Journal Special Topics 197: 325-341.

(12) Zhu S, Miller W, Sciven L, Davis H. (1994), Superspreading of water silicone surfactant on hydrophobic surfaces. Colloids and Surfaces A: Physiochemical and Engineering Aspects 90: 63-78.

(13) Nikolov A, Wasan D, Chengara A, Koczo K, Policello G, Kolossvary I. (2002), Superspreading driven by Marangoni flow. Advanced Coloid Interface Science 96: 325-338

(14) Venzmer J, Wilkowski S. (1998), Trisiloxane Surfactants - Mechanism of spreading and wetting. In pesticide formulations and application systems American Society for testing and materials. 1347: 140-151.

(15) Hill R. (1998), Superspreading. Current Opinion Colloid Interface Science. 3: 247-254.

(16) Lin Z, Hill R, Davis M, Ward M (1994), Determination of wetting velocities of surfactant superspreaders with the quartz crystal microbalance. Langmuir 10: 4060-4068.

(17) Churaev NV, Esipova NE, HIll RM, Sobolev VD, Starov VM, Zorin Z. (2001), The superspreading effect of trisiloxane surfactant solutions. Langmuir 17: 1338-1348.

(18) Ritacco HA, Ortega F, Rubio RG, Ivanova N, Starov VM. (2010), Equilibriuim and dynamic surafce properties of trisiloxane aqueous solutions Part 1. Experimental results. Colloids and Surfaces A: Physicochemical and Engineering Aspects 365: 199-203.

(19) Hill R. (2002), Silicone surfactants - new developments. Current Opinion in Colloid Interface Science 7: 255-261.

(20) Ivanova NA, Starov VM. (2011), Wetting of low energy surfaces by aqueous surfactant solutions. Current Opinion Colloid Interface Science. 16: 285-291.

(21) Stoebe T, LIn Z, Hill, R.,Ward, M., Davis T. (1997), Enhanced spreading of aqueous films containing ethoxylated alcohol surfactant on solid substrates. Langmuir 13: 7270-7275.

(22) Svitova T., Hill RM, Smirnova Y, Stuermer A, Yakubov G. (1998), Wetting and interfacial transitions in dilute solutions of trisiiloxane surfactants. Langmuir 14: 5023-5031.

(23) Zhu X, Miller W, Scriven LE, Davis T. (1994) Journal of Colloid Surfaces 10: 4060

(24) Rafai S, Sarker D, Beregeron V, Meunier J, Bonn D (2002), Superspreading: Aqueous surfactant drops spreading on hydrophobic surfaces. Langmuir 18: 10486-10488.

(25) Tanner L. (1979), The spreading of silicone oil drops on horizontal surfaces. Journal of Physics D Applied Physics. 12: 1473.

(26) Karapetsas G, Craster RV, Matar OK. (2011), On surfactant-enhanced spreading and superspreading of liquid drops on solid surfaces. Journa; Fluid Mechanics 670: 5-37.

(27) Chengara A, Nikolov A, Wasan D. (2002), Surface tension gradient driven spreading of trisiloxane surfactant soluiton on hydrophobic solid. Colloids and Surfaces A: Physicochemical and Engineering Aspects 206: 31

(28) Kovalchuk NM, Trybala A, Arjmandi-Tash O, Starov V. (2016), Surfactant enhanced spreading experimental achievements and possible mechanisms. Advanced Colloid Interface Science. 233: 155

(29) Shen Y, Couzis A, Koplik J, Maldarelli C, Tomassone M (2005), Molecular dynamics study of the influence of surfactant structure on surfactant structure on surfactant-facilitated spreading of droplets on solid surfaces. Langmuir 21: 12160-12170.

(30) Frenkel D, Smit B, (2002), Understanding molecular simulation. . second ed.: Academic Press. London. 63-105.

(31) Lin J, Zhu M, Zheng C, Liu Z, Wang Q, Lu D, et al. (2016), Microwave assisted synthesis of trisiloxane superspreader and its superspreading behaviour on plant leave surfaces. Colloids and Surfaces A: Physicochemical and Engineering Aspects 511: 190-200

(32) Lee K, Starov V, Muchatuta T, Srikantha S (2009), Spreading of trisiloxanes over thin aqueous layers. Colloid Journal 71: 365-369.

(33) Lee KS, Starov VM. (2007), Spreading of surfactant solution over thin aqueous layers, influence of solubility and micelle disintegration. Journal Colloid Interface Science. 314: 631

(34) Department of Physics (2016), Advanced undergraduate practical physics handbook.

(35) Radulovic J, Sefaine K, Shanahan M. (2010), Dynamics of trisiloxane wetting. Effects of difusion and surface hydrophobicity. Journal Physical Chemistry C 114: 13620

(36) Tanner L (1979), The spreading of silicone oil drops on horizontal surfaces. Journal of Physics D: Applied Physics. 12: 1473.

(37) Xiang Wang. (2014) PhD thesis, Dynamic wetting of aqueous surfactant solutions on hydrophobic solids at the water sub phase. University of Darmstadt.

(38) Palumno M, Pulci O, Sole R, Marini A, Schwitters M, Haines SR, Williams KH, Martin DS, Weightman P, Butler JE (2005), Reflectance anisotropy spectroscopy of the diamond (100) - 2 × 1 surface. Evidence of strongly bound surface state excitions. Physical Review Letters 94 (8): 1-4.

(39) Weightman P, Martin D, Cole R, Farrell T. (2005), Reflection anisotropy spectroscopy**.** Reports on Progress in Physics 68(6): 1251-1341.

(40) Eaton P, West P (2010), Atomic Force Microscopy. Oxford.

(41) Williams K, Bertola V, Martin D (2016), Experimental investigation of a flowing superspreader solution using Reflectance Anisotropy Spectroscopy (RAS). Results in Physics 6: 277-279.

(42) Dane, T G.: Cresswell, P T., Pilkington GA, Lilliu, M, J E., Prescott SW, Bikonda O, et al (2013), Oligo(aniline) nanofilms: from molecular architecture to microstructure. Soft Matter 9: 10501-10511

(43) http://www.gisaxs.de/theory.html